

June 2019

Application of Pressure and Rate Transient Analyses to Stress-Sensitive Multi-Fractured Composite Systems and Compartmentalized Reservoirs

Oscar Mauricio Molina
Louisiana State University and Agricultural and Mechanical College

Follow this and additional works at: https://digitalcommons.lsu.edu/gradschool_dissertations



Part of the [Petroleum Engineering Commons](#)

Recommended Citation

Molina, Oscar Mauricio, "Application of Pressure and Rate Transient Analyses to Stress-Sensitive Multi-Fractured Composite Systems and Compartmentalized Reservoirs" (2019). *LSU Doctoral Dissertations*. 4938.

https://digitalcommons.lsu.edu/gradschool_dissertations/4938

This Dissertation is brought to you for free and open access by the Graduate School at LSU Digital Commons. It has been accepted for inclusion in LSU Doctoral Dissertations by an authorized graduate school editor of LSU Digital Commons. For more information, please contact gradetd@lsu.edu.

**APPLICATION OF PRESSURE AND RATE TRANSIENT ANALYSES TO
STRESS-SENSITIVE MULTI-FRACTURED COMPOSITE SYSTEMS AND
COMPARTMENTALIZED RESERVOIRS**

A Dissertation

Submitted to the Graduate Faculty of the
Louisiana State University and
Agricultural and Mechanical College
in partial fulfillment of the
requirements for the degree of
Doctor of Philosophy

in

The Department of Petroleum Engineering

by

Oscar Mauricio Molina
BS, Universidad Pontificia Bolivariana, 2007
MS, Louisiana State University, 2015
August 2019

To God, our Good Father, the Giver of every good gift.

To my parents. Thank you for all the sacrifices you have made for me, I am proud and blessed to be your son. This would have not been possible without your love and support.

To Mayra. Thank you for bringing so much joy and love into my life. Thank you for being both my lover and best friend in the daring journey of life. This achievement is ours.

To Mohammed Bousaleh & Suzanne Ferguson. Thank you for the selfless, whole-hearted, unswerving support through the good and the tough times.

In memory of Denis Klimenko (1990-2017).

Acknowledgments

I want to thank Dr Mehdi Zeidouni for his mentorship, patience and support throughout the journey of my PhD. Also, I express my gratitude to Drs Mayank Tyagi, Andrzej Wojtanowicz, Richard Hughes and Patricia Persaud. Their encouragement and technical advice were both fundamental and inspirational for me.

Table of Contents

Acknowledgments	iii
List of Tables	vii
List of Figures	viii
Abstract	xvii
1 Introduction	1
1.1 Pressure Transient Analysis (PTA)	1
1.2 Proposed Applications for Pressure-Transient Analysis	5
2 Forecast of Multi-fractured Horizontal Well Performance in Stress-sensitive Formations: Constant Rate Approach.	7
2.1 Background	7
2.2 Statement of the Problem	13
2.3 Current Analytical Methods	16
2.4 Proposed Methodology	17
2.5 Mathematical Modeling	17
2.6 Pressure Transient Analysis for Constant-rate Production	36
2.7 Estimation of Average Pressure-Drawdown	42
2.8 Iterative Solution Algorithm	45
2.9 Validation Cases	48
2.10 Sensitivity Analysis	54
2.11 Effect of Wellbore Storage and Fracture Skin on Pressure Response	63
2.12 Adding Lower Limit to Reduction in Permeability and Fracture Conductivity with Pressure Decline	65
2.13 Discussion	81
2.14 Conclusions	83
3 Analytical Model to Estimate the Fraction of Frachits in a Multi-Well Pad	85
3.1 Background	85
3.2 Statement of the Problem	88
3.3 Conceptualization of the Frac Hits Model	89
3.4 Proposed Methodology	92
3.5 Mathematical Modeling—Part I: The Fluid-flow Model	94
3.6 Mathematical Model—Part II: The Frac Hits Boundary Condition	115

3.7	Analytical Solution	125
3.8	Analytical Functions for Pressure-Transient Analysis of Frac Hits	127
3.9	Validation Cases	128
3.10	Sensitivity Analysis	138
3.11	Type-Curves Analysis	185
3.12	Discussion	197
3.13	Conclusions	199
4	Effect of Anisotropic Fault Permeability Enhancement on Pressure-Transient Behavior	201
4.1	Background	201
4.2	Statement of the Problem	202
4.3	Proposed Methodology	204
4.4	Mathematical Modeling	205
4.5	Analytical Solution to the Fault Reactivation Model	210
4.6	Pressure Transient Analysis of Fault Reactivation	220
4.7	Fault Permeability Characterization after Fault Reactivation	229
4.8	Numerical Validation Examples	230
4.9	Discussion	237
4.10	Conclusions	238
5	Discussion	239
6	Conclusions	240
7	Future Work	242
7.1	Pressure-Dependent MFHW model	242
7.2	Frac Hits Model	242
7.3	Fault Reactivation Model	243
	References	245
	Appendix A Analytical Frac Hits Model	257
	A.1 General Definitions	257
	A.2 Dimensionless Parameters Group	257
	A.3 Normalized Coordinates	257
	A.4 Normalized Dimensions	258
	Appendix B Analytical Fault Reactivation Model	260
	B.1 Dimensionless Parameters Group	260

Vita	261
----------------	-----

List of Tables

2.1	Composite system properties used in the validation cases.	49
2.2	Pressure-dependent properties used in the numerical validation study. . .	49
2.3	EUR analysis for $q_{\text{well}} = 400$ STB/D as a function of d_f	53
2.4	Correction factor β as a function of F_{CDi}	55
2.5	Stress-sensitive characteristic numbers used in this analysis.	58
2.6	SRV permeability modulus values used for the sensitivity analysis. . . .	61
2.7	Comparison of well life and EUR for different pressure-dependent SRV permeability and fracture conductivity.	63
3.1	Completion and multi-well pad properties.	128
3.2	Correlation between δ_{wAB}^* and δ_{wAB} as a function of L_{AB}	139
3.3	Correlation between δ_{wAB}^* , δ_{wAB} and δ_{wAC} for $200 \leq x_f \leq 600$ ft.	147
3.4	Correlation between δ_{wAB}^* , δ_{wAB} , δ_{wAC} and x_{fB} for $x_{fA} = 200$ ft.	153
3.5	Correlation between δ_{wAB}^* , δ_{wAB} and δ_{wAC} for $C_{fA} = C_{fB}$	158
3.6	Correlation between δ_{wAB}^* , δ_{wAB} , δ_{wAC} and C_{fB} for $C_{fA} = 500$ md-ft. . . .	164
3.7	Correlation between δ_{wAB}^* , δ_{wAB} and δ_{wAC} for $k_{1A} = k_{1B}$	170
3.8	Correlation between δ_{wAB}^* , δ_{wAB} , δ_{wAC} and k_{1B} for $k_{1A} = 0.1$ md.	175
3.9	Correlation between δ_{wAB}^* , δ_{wAB} and δ_{wAC} for $25 \leq 2x_e \leq 500$ ft.	180
3.10	Estimated average properties for wells A and B in Example 1.	194
3.11	Actual MFHW properties used in Example 1.	195
3.12	Estimated average properties for MFHW in Example 2.	196
3.13	Actual MFHW properties used in Example 2.	197

List of Figures

1.1	Two of the most common types of well tests in PTA: pressure-drawdown and pressure build-up tests.	2
1.2	Diagnostic plot of rate-normalized pressure and pressure-derivative. . . .	3
1.3	Type curves for a infinite radial reservoir with wellbore storage and skin (from Bourdet et al., 1989).	4
2.1	Types of hydraulic fractures: (a) planar fracture and (b) complex fracture.	8
2.2	Types of fractures present in a hydraulically fractured stage: hydraulic fracture, fracture branching, natural fracture networks and micro-fractures.	9
2.3	Conceptualization of the trilinear flow model. Narrow spacing between fractured stages and MFHW in a multi-well pad.	10
2.4	Conceptualization of the five-region model. Fair spacing between fractured stages and MFHW in a multi-well pad.	11
2.5	Fluid-flow in a MFHW modeled as a combination of various linear flow regimes: (a) trilinear MFHW model; (b) five-region MFHW model.	12
2.6	Schematic of forces acting on the hydraulic fracture. Fluid pressure resists the effect of closure stress trying to close up the fracture. The same scenario occurs with unproped fractures in the SRV.	13
2.7	Fractional changes in SRV and fracture permeability with pore pressure. .	15
2.8	Mass balance across a differential control volume in the matrix.	20
2.9	Mass balance across a differential control volume inside the SRV.	26
2.10	Skin damage across the SRV/interface located at $x = w/2$	30
2.11	Mass balance across a differential control volume within the fracture. . .	33
2.12	Combined pressure drop near the wellbore.	39
2.13	Iterative algorithm to solve the nonlinear flow problem.	47
2.14	Transient BHP response for Case Studies 1 and 2.	50
2.15	Rate-normalized diagnostic plot for Case Study 1.	51

2.16	Rate-normalized diagnostic plot for Case Study 2.	51
2.17	Well performance forecast and EUR as a function of d_f	52
2.18	Fractional changes in fracture conductivity, SRV and matrix permeability as a function of time.	53
2.19	BHP response as a function of C_{fi} for Case Study 1.	55
2.20	BHP response as a function of C_{fi} for Case Study 2.	56
2.21	RNP response as a function of C_{fi} for Case Study 1.	56
2.22	RNP' response as a function of C_{fi} for Case Study 2.	57
2.23	RNP' response as a function of C_{fi} for Case Study 1.	57
2.24	RNP' response as a function of C_{fi} for Case Study 2.	58
2.25	BHP response as a function of d_f	59
2.26	Fractional change in F_{CD} with time as a function of d_f	60
2.27	BHP response as a function of γ_1	61
2.28	Fractional change in SRV permeability as a function of γ_1	62
2.29	BHP response as a function of γ_1 and d_f	63
2.30	RNP and RNP' as a function of s_f (without wellbore storage effects). . . .	64
2.31	Effect of wellbore storage on RNP and RNP' for $s_f = 0.5$	65
2.32	Fractional changes in SRV and fracture permeability with pore pressure. .	67
2.33	Analytical and numerical BHP responses for Case Studies 1 and 2.	69
2.34	Analytical and numerical RNP and RNP' for Case Study 1.	69
2.35	Analytical and numerical RNP and RNP' responses for Case Study 2. . .	70
2.36	Evolution of fractional reduction of average fracture conductivity, SRV and matrix permeability for Case Studies 1 and 2.	71
2.37	BHP response as a function of SRV permeability modulus and time. . . .	72
2.38	RNP and RNP' for $\gamma_1 = 1 \times 10^{-4}$ and $5 \times 10^{-3} \text{ psi}^{-1}$	73

2.39	Fractional reduction of average k_1 for $\gamma_1 = 1 \times 10^{-4}$ to 5×10^{-3} psi ⁻¹ . . .	74
2.40	BHP response as a function of stress-sensitive characteristic number; $C_{fi} = 500$ md-ft and $C_{fm} = 100$ md-ft.	75
2.41	Evolution of fractional reduction of fracture conductivity for $d_f = 1 \times 10^{-4}$ to 5×10^{-3} psi ⁻¹ . $C_{fi} = 500$ md-ft and $C_{fm} = 100$ md-ft.	76
2.42	BHP response as a function of stress-sensitive characteristic number; $C_{fi} = 100$ md-ft and $C_{fm} = 20$ md-ft.	77
2.43	RNP and RNP' responses for $d_f = 1 \times 10^{-4}$ and 5×10^{-3} psi ⁻¹ ; $C_{fi} = 500$ md-ft and $C_{fm} = 100$ md-ft.	78
2.44	Evolution of fractional reduction of fracture conductivity for $d_f = 1 \times 10^{-4}$ to 5×10^{-3} psi ⁻¹ ; $C_{fi} = 100$ md-ft and $C_{fm} = 20$ md-ft.	79
2.45	BHP response as a function of stress-sensitive characteristic number, SRV permeability modulus and time.	80
2.46	Comparison of RNP and RNP' responses for cases 3 and 4.	81
3.1	Frac hits through primary and secondary fractures allowing pressure communication between the parent well (A) and child well (B).	86
3.2	Gunbarrel view of a multi-well pad with frac hits across different target formations. In spite of being spatially separated, wells A, B and C are interconnected through frac hits.	87
3.3	A two-MFHW pad represented as two individual vessels. Operating conditions from well A (child well) do not influence performance of well B (parent well).	90
3.4	Frac hits between two MFHWs interpreted as a "valve" connecting two vessels. Valve "aperture" is controlled by $\delta_{wAB} \in [0, 1]$ while leakage rate across vessels is proportional to $\Delta p_{wAB} = \varepsilon_{AB}(p_{wB} - p_{wA})$	91
3.5	Conceptualization of the frac hits model for a three-MFHW pad system. (a) Wells A, B and C were drilled and completed in the same target zone, (b) Frac hits can be present at several fractured stages.	93
3.6	The three-MFHW-pad frac hits model based on the QLF model. Each well is modeled based on the single-fracture approach along with its corresponding equivalent per-fracture rate.	96
3.7	Definition of equivalent fracture conductivity $\overline{C_f}$ to model fluid-flow between wells A and B through primary fractures and the frac hit.	119

3.8	Case I (wells A and B) and Case II (wells A and B).	125
3.9	Pressure distribution after 67 days (no frac hits) ($d_{wAB}^* = d_{wAC}^* = 0$).	129
3.10	Analytical and numerical BHP data for $\delta_{wAB} = \delta_{wAC} = 0$.	130
3.11	Rate-normalized plot for $\delta_{wAB} = \delta_{wAC} = 0$.	130
3.12	Analytical and numerical BHP data for $\delta_{wAB} = \delta_{wAC} = 8.9 \times 10^{-4}$.	131
3.13	Rate-normalized plot for $\delta_{wAB} = \delta_{wAC} = 8.9 \times 10^{-4}$ ($\delta_{wAB}^* = \delta_{wAC}^* = 0$).	131
3.14	Pressure distribution after after 68 days for $\delta_{wAB}^* = 0.3$ and $\delta_{wAC}^* = 0.2$.	132
3.15	Analytical and numerical BHP data for $\delta_{wAB} = 0.28$ and $\delta_{wAC} = 0.18$.	133
3.16	Rate-normalized plot for $\delta_{wAB}^* = 0.3$ and $\delta_{wAC}^* = 0.2$.	133
3.17	Pressure distribution after 70 days for the case $\delta_{wAB}^* = 0.2$ and $\delta_{wAC}^* = 0.4$.	134
3.18	Analytical and numerical BHP data for $\delta_{wAB} = 0.176$ and $\delta_{wAC} = 0.36$.	135
3.19	Rate-normalized plot for $\delta_{wAB} = 0.176$ and $\delta_{wAC} = 0.36$.	135
3.20	Pressure distribution after 70 days for the scenario $\delta_{wAB}^* = 0.1$ and $\delta_{wAC}^* = 0.8$.	136
3.21	Comparison of analytical and numerical BHP data for $\delta_{wAB} = 0.089$ and $\delta_{wAC} = 0.76$.	137
3.22	Rate-normalized plot for $\delta_{wAB} = 0.089$ and $\delta_{wAC} = 0.76$.	137
3.23	Three-MFHW pad model used for sensitivity analyses.	138
3.24	Pressure distribution in the multi-well pad under study for the case $L_{AB} = 1000$ ft and $\delta_{wAB}^* = 0.4$.	140
3.25	Graphical correlation between δ_{wAB}^* and δ_{wAB} for $500 \leq L_{AB} \leq 1000$ ft and $L_{AC} = 600$ ft.	141
3.26	History-matching of BHP for $L_{AB} = 600$ ft and $\delta_{wAB}^* = 0.4$.	142
3.27	History-matching of BHP for $L_{AB} = 1000$ ft and $\delta_{wAB}^* = 0.4$.	142
3.28	Frac-hits type-curves for $L_{AB} = 500$ ft.	144
3.29	Frac-hits type-curves for $L_{AB} = 600$ ft (base case).	144

3.30	Frac-hits type-curves for $L_{AB} = 700$ ft.	145
3.31	Frac-hits type-curves for $L_{AB} = 800$ ft.	145
3.32	Frac-hits type-curves for $L_{AB} = 900$ ft.	146
3.33	Frac-hits type-curves for $L_{AB} = 1000$ ft.	146
3.34	Graphical correlation between δ_{wAB}^* and δ_{wAB} for $200 \leq x_f \leq 600$ ft. . . .	148
3.35	History-matching of BHP for $x_f = 300$ ft and $\delta_{wAB}^* = 0.5$	149
3.36	History-matching of BHP for $x_f = 600$ ft and $\delta_{wAB}^* = 0.5$	149
3.37	Frac-hits type-curves for $x_{fA} = x_{fB} = 300$ ft.	150
3.38	Frac-hits type-curves for $x_{fA} = x_{fB} = 400$ ft.	151
3.39	Frac-hits type-curves for $x_{fA} = x_{fB} = 500$ ft.	151
3.40	Frac-hits type-curves for $x_{fA} = x_{fB} = 600$ ft.	152
3.41	Graphical correlation between δ_{wAB}^* , δ_{wAB} and x_{fB} for $x_{fA} = 200$ ft. . . .	153
3.42	History-matching of BHP for $x_{fB} = 400$ ft and $\delta_{wAB}^* = 0.6$	155
3.43	History-matching of BHP for $x_{fB} = 600$ ft and $\delta_{wAB}^* = 0.6$	155
3.44	Frac-hits type-curves for $x_{fB} = 300$ ft.	156
3.45	Frac-hits type-curves for $x_{fB} = 400$ ft.	156
3.46	Frac-hits type-curves for $x_{fB} = 500$ ft.	157
3.47	Frac-hits type-curves for $x_{fB} = 600$ ft.	157
3.48	Graphical correlation between δ_{wAB}^* and δ_{wAB} for $C_{fA} = C_{fB}$	159
3.49	History-matching of BHP for $C_f = 50$ md-ft and $\delta_{wAB}^* = 0.5$	160
3.50	History-matching of BHP for $C_f = 1000$ md-ft and $\delta_{wAB}^* = 0.5$	160
3.51	Frac-hits type-curves for $C_{fA} = C_{fB} = 50$ md-ft.	162
3.52	Frac-hits type-curves for $C_{fA} = C_{fB} = 250$ md-ft.	162
3.53	Frac-hits type-curves for $C_{fA} = C_{fB} = 1000$ md-ft.	163
3.54	Frac-hits type-curves for $C_{fA} = C_{fB} = 2500$ md-ft.	163

3.55	Graphical correlation between δ_{wAB}^* , δ_{wAB} and C_{fB} for $C_{fA} = 500$ md-ft.	165
3.56	History-matching of BHP for $C_{fB} = 50$ md-ft and $\delta_{wAB}^* = 0.8$	166
3.57	History-matching of BHP for $C_{fB} = 1000$ md-ft and $\delta_{wAB}^* = 0.8$	166
3.58	Frac-hits type-curves for $C_{fB} = 50$ md-ft.	167
3.59	Frac-hits type-curves for $C_{fB} = 250$ md-ft.	168
3.60	Frac-hits type-curves for $C_{fB} = 1000$ md-ft.	168
3.61	Frac-hits type-curves for $C_{fB} = 2500$ md-ft.	169
3.62	Graphical correlation between δ_{wAB}^* and δ_{wAB} for $k_{1A} = k_{1B}$	170
3.63	History-matching of BHP for $k_1 = 0.001$ md and $\delta_{wAB}^* = 0.7$	171
3.64	History-matching of BHP for $k_1 = 1$ md and $\delta_{wAB}^* = 0.3$	172
3.65	Frac-hits type-curves for $k_{1A} = k_{1B} = 0.001$ md.	173
3.66	Frac-hits type-curves for $k_{1A} = k_{1B} = 0.01$ md.	173
3.67	Frac-hits type-curves for $k_{1A} = k_{1B} = 1$ md.	174
3.68	Graphical correlation between δ_{wAB}^* , δ_{wAB} and k_{1B} for $k_{1A} = 0.1$ md.	175
3.69	History-matching of BHP for $k_{1B} = 0.001$ md and $\delta_{wAB}^* = 0.7$	177
3.70	History-matching of BHP for $k_{1B} = 1$ md and $\delta_{wAB}^* = 0.7$	177
3.71	Frac-hits type-curves for $k_{1A} = 0.1$ md, $k_{1B} = 0.001$ md.	178
3.72	Frac-hits type-curves for $k_{1A} = 0.1$ md, $k_{1B} = 0.01$ md.	178
3.73	Frac-hits type-curves for $k_{1A} = 0.1$ md, $k_{1B} = 1$ md.	179
3.74	Graphical correlation between δ_{wAB}^* and δ_{wAB} as a function of $2x_e$	180
3.75	History-matching of BHP for $2x_e = 25$ ft and $\delta_{wAB}^* = 0.4$	181
3.76	History-matching of BHP for $2x_e = 100$ ft and $\delta_{wAB}^* = 0.4$	182
3.77	Frac-hits type-curves for $2x_{eA} = 2x_{eB} = 25$ ft.	183
3.78	Frac-hits type-curves for $2x_{eA} = 2x_{eB} = 50$ ft.	183
3.79	Frac-hits type-curves for $2x_{eA} = 2x_{eB} = 75$ ft.	184

3.80	Frac-hits type-curves for $2x_{eA} = 2x_{eB} = 100$ ft.	184
3.81	Frac-hits type-curves for $2x_{eA} = 2x_{eB} = 250$ ft.	185
3.82	Dimensionless frac-hits type-curves as a function of the lumped frac-hits skin factor S_F	189
3.83	Resulting $RNP_{AB}(t)$ and $RNP'_{AB}(t)$ for Example 1.	193
3.84	Resulting type-curves matching for assessment of frac hits in Example 1.	194
3.85	Resulting $RNP_{AB}(t)$ and $RNP'_{AB}(t)$ for Example 2.	196
3.86	Resultin type-curves matching for Example 2.	197
4.1	Different types of pressure-drawdown distribution in a compartmentalized reservoir before the onset of fault reactivation.	204
4.2	Idealization of a segmenting fault as a linear interface in a composite reservoir (Ambastha et al., 1989). Flow direction in a typical fault zone, and idealization of a compartmentalized reservoir in which the fault is modeled as a linear interface between fault blocks.	206
4.3	Material balance in the fault: steady-state flux across the fault and transient flux along the fault.	211
4.4	Dimensionless pressure response to a sudden change in across-fault permeability for $s_f = 0.1, 1, 10, 100$ and 1000 , $h_D = \eta_D = M = 1$, and $t_{sD} = 1, 10$ and 100	222
4.5	Dimensionless pressure-derivative response to $s_f = 0.1, 1, 10, 100$ and 1000 , $h_D = \eta_D = M = 1$, and $t_{sD} = 1, 10$ and 100	223
4.6	Dimensionless type-curves for across-fault permeability enhancement for $s_f = 0.1, 1, 10, 100$ and 1000 , $h_D = \eta_D = M = 1$ and $t_{sD} = 1, 10$ and 100	223
4.7	Dimensionless pressure response to $s_f = 0$ for $h_D = 1$, $M = \eta_D = 0, 0.01, 0.1, 1$ and 10 , and $t_{sD} = 1, 10$ and 100	225
4.8	Dimensionless pressure derivative response to $M = \eta_D = 0.01, 0.1, 1, 10$ and 100 for $h_D = 1$, and $t_{sD} = 1, 10$ and 100	225
4.9	Dimensionless type-curves for across-fault permeability enhancement for $h_D = 1$, $M = \eta_D = 0.01, 0.1, 1, 10$ and 100 for $t_{sD} = 1, 10$ and 100	226

4.10	Dimensionless type curves for along-across-fault permeability enhancement for $h_D = 1$, $s_f = 0$ and $M = \eta_D = 0.01, 0.1, 1, 10$ and 100 for $t_{sD} = 1, 10$ and 100	227
4.11	Dimensionless pressure-derivative response to along-across-fault permeability enhancement for $h_D = 1$, $s_f = 0$ and $M = \eta_D = 1$ for $t_{sD} = 1, 10$ and 100	228
4.12	Dimensionless type curves for simultaneous along-across-fault permeability enhancement with $s_f = 0$, $h_D = 1$, $M = \eta_D = 1$ for $t_{sD} = 1, 10$ and 100	228
4.13	Type-curves for simultaneous across-along fault permeability enhancement. Gray dashed lines correspond to the partially-communicating fault solution for $s_f = 1, 100$ and 10000 with no along-fault flow ($F_{CD} = 0$) whereas solid gray lines correspond to along-fault flow with no fault skin for $1 \leq F_{CD} \leq 10000$	230
4.14	Comparison of RNP between analytical and numerical reservoir models for $M = h_D = 1$ and $s_f = 10$	232
4.15	Comparison of RNP' between analytical and numerical reservoir models for $M = h_D = 1$ and $s_f = 10$. Boundary effects can be seen after 150 days.	232
4.16	Comparison of RNP response between analytical and numerical models for $M = 5$, $h_D = 0.5$ and $s_f = 10$	233
4.17	RNP' response for $M = 5$, $h_D = 0.5$ and $s_f = 10$. Influence of boundary effects on normalized drawdown-derivative response are less evident.	233
4.18	Pressure-dependent multipliers for across and along-fault permeability for Case Study 3.	234
4.19	RNP response of analytical solution and numerical model for Numerical Case Study 3.	235
4.20	RNP' response of analytical solution and numerical model for Numerical Case Study 3. The proposed analytical model is able to capture the signature of fault reactivation and subsequent transitional fault properties until late-time equilibrium is reached in the compartmentalized system.	236

Abstract

Pressure transient analysis (PTA) is one of the most robust and commonly interpretation tools available for reservoir characterization. Common applications of PTA include estimation of near-wellbore and reservoir properties, detection of reservoir limits and identification of depletion mechanisms. In addition, PTA allows the identification of sealing and leaky faults and the characterization of its properties, such as permeability and transmissibility hence direction of leakage within the fault.

The purpose of this dissertation is to introduce the analytical solution for pressure-transient behavior for three novel reservoir models. First, we develop the analytical model of a multi-fracture horizontal well (MFHW) with pressure-dependent rock and fluid properties to study the impact of stress-dependent rock properties in composite unconventional systems. Second, we develop the analytical model for fluid-flow in a multi-well pad with three MFHWs in which wells can be interconnected through fracture hits. Lastly, we develop an analytical model of a compartmentalized reservoir with a segmenting fault in which fault permeability changes suddenly as a consequence of fault reactivation.

Governing equations for fluid-flow are based on Darcy's law. Pressure-dependent properties for the MFHW model are assumed to vary exponentially with local pressure-drawdown. Pressure-transient solution for each reservoir model is derived with the aid of advanced mathematical solution techniques, such as Laplace-Fourier transform and related numerical inversion, and iterative algorithms. Single-phase slightly compressible fluid-flow is considered for all reservoir models. Neither turbulence nor non-Darcy flow are considered in this work. Analytical solutions are presented as diagnostic plots and type curves.

Analytical solutions were successfully validated against numerical simulation data. The resulting diagnostic plots and type-curves for well-test interpretation are presented and discussed for each case study. Various sensitivity analyses were carried out to examine the impact of several parameters of interest on pressure-transient behavior.

In particular, we find that the effects of pressure-dependent fracture conductivity and stimulated reservoir properties, in conjunction, largely influence MFHW performance in stress-sensitivity formations. Likewise, we are able to detect and assess fracture

hits by means of types-curves matching. Finally, we observe that fault reactivation can be detected on diagnostic plots as a sudden change in pressure-derivative response followed by a trend to attain late-time equilibrium.

1. Introduction

1.1. Pressure Transient Analysis (PTA)

Pressure-transient analysis (PTA), also known as well-test interpretation (Horner, 1951) or pressure-transient testing, is a dynamic well and reservoir characterization technique that focuses on interpreting the transient pressure response from a well flowing at constant rate or that had been flowing a constant rate before being shut-in (e.g. Spivey and Lee, 2013; Lee et al., 2003). The main purpose of a PTA study is to estimate reservoir features that, depending on the type and objective of the well test, may range from simple reservoir and well properties to complex reservoir features. There are two primary areas of application for PTA: productivity tests, that covers well deliverability, completion efficiency, and descriptive reservoir tests, comprising evaluation of reservoir properties, assessment of reservoir extension, and detection and identification of reservoir boundaries. The use of diagnostic plots and type-curve analysis are amongst the most valuable applications of PTA in reservoir characterization.

Amongst the various types of PTA tests, pressure drawdown (PDD) and pressure build-up (PBU) tests are the most common well tests applied in the field. In a PDD-type test, the objective (or active) well is constrained to flow at constant volumetric flow rate while wellbore pressure $p_{wf}(t)$ is being recorded. Bottomhole pressure BHP or p_{bh} can be used interchangeably with p_{wf} if wellbore storage effects (i.e. fluid compressibility inside the wellbore) are negligible. In a PBU-type test, the well is set to flow at constant volumetric flow rate q [STB/D] for a certain period and pressure would be recorded after the well is shut-in. In this case, pressure is referred to as shut-in pressure p_{ws} . Note that in both cases, q is constant, even $q = 0$ for the case of a PBU test is still a constant rate. Figure 1.1 depicts the expected wellbore pressure response from each PTA test assuming q is the same for both cases before shut-in time. The work presented in this dissertation focuses on the application of PDD tests to different reservoir models which will be discussed in the subsequent chapters.

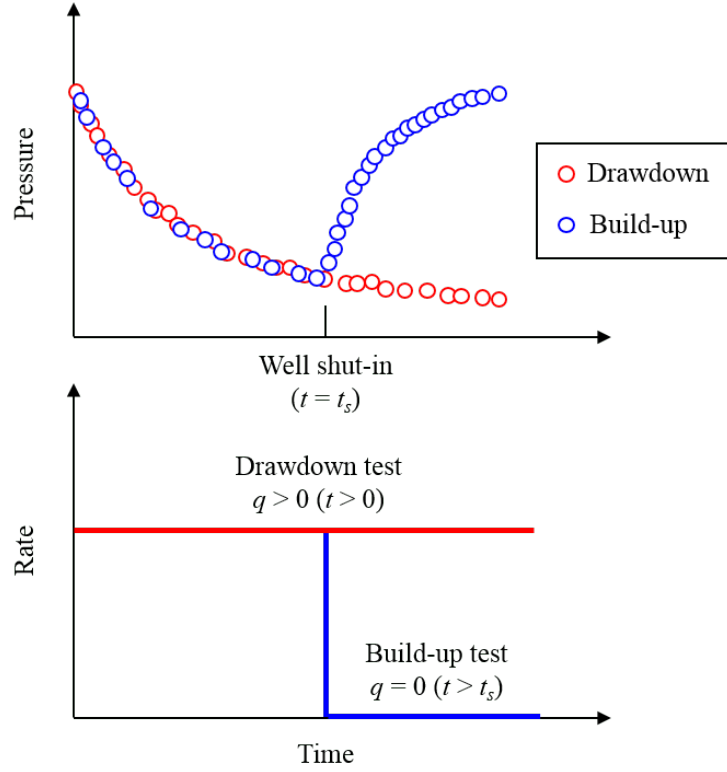


Figure 1.1: Two of the most common types of well tests in PTA: pressure-drawdown and pressure build-up tests.

Notice that Figure 1.1 do not provide much information about either the well or reservoir. In contrast, PTA diagnostic plots allow to infer and extract valuable information about wellbore, near-wellbore region and reservoir, depending on the duration of the well test. Basically, a PTA diagnostic plot displays pressure-transient data in a log-log chart. Typically, pressure-transient data are presented as pressure drawdown $\Delta p_{wf} = p_i - p_{wf}(t)$ and log-pressure-drawdown derivative $d\Delta p_{wf}(t)/d \ln t$ (Bourdet et al., 1989) versus time t [days].

PTA diagnostic plots are a powerful tool that enables the use of well-test data to detect damage or effectiveness of a stimulation job in the near-wellbore region (skin), infer the presence of sealing and leaky boundaries in the reservoir, assess the degree of interconnectivity between wells, detect the presence of natural fractures networks, infer the existence of a composite system, among others (Lee et al., 2003).

In this work, we will generate diagnostic plots from analytical and numerical data using the rate-normalized pressure (RNP [psi/STB/D]) and rate-normalized pressure-

derivative (RNP' [psi/STB/D]) (Song and Ehlig-Economides, 2011; Palacio and Blasingame, 1993). The rate-normalized parameters are defined as follows:

$$\text{RNP} = \frac{\Delta p_{wf}}{q} \quad (1.1)$$

$$\text{RNP}' = \frac{d(\Delta p_{wf}/q)}{d \ln t} \quad (1.2)$$

Note that the definition of the rate-normalized parameters applies to injector wells alike. Although both Δp_{wf} and q would be negative in this case, the resulting $\text{RNP} = \Delta p_{wf}/q$ will be positive. Figure 1.2 shows the PTA diagnostic plot, based on RNP and RNP', for infinite-acting radial flow with wellbore storage and skin damage (Bourdet et al., 1989).

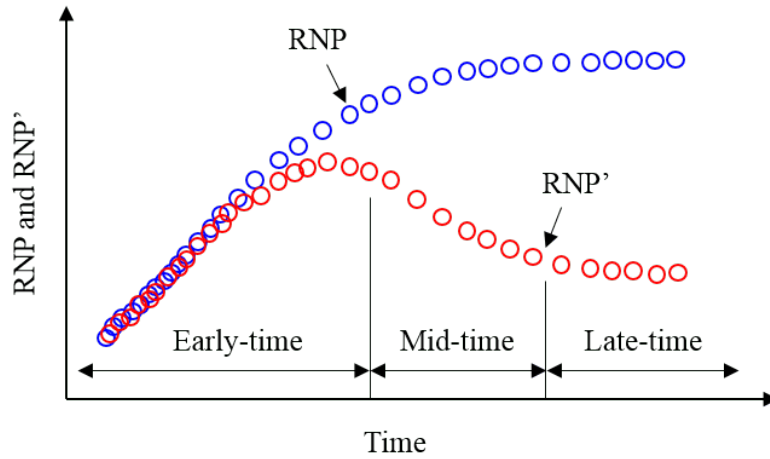


Figure 1.2: Diagnostic plot of rate-normalized pressure and pressure-derivative.

Diagnostic plots are often generated for analytical reservoir models alike. Basically, a diagnostic plot can be considered as the graphical representation of the analytical solution to the diffusivity equation (Dake, 1983) for a pre-established set of conditions in a reservoir model, including reservoir geometry (radial, rectangular, irregular) and extension (finite, semi-infinite, infinite), fluid type (slightly compressible, compressible) and types of boundaries (impervious, semi-pervious).

One of the advantages of using analytical models to generate diagnostic plots is that analytical solutions enables the analyst to examine and study the expected pressure

response to a certain reservoir/wellbore parameters without the need to run the actual well test. When one or more reservoir and/or wellbore parameters are evaluated within a given range and the resulting curves are plotted together as a set of curves describing transient pressure behavior for a particular reservoir model, the plot is called PTA type-curves plot, or simply, type curves (Gringarten, 2008; Bourdet et al., 1983; Gringarten et al., 1979).

Unlike diagnostic plots, type curves plots are based on dimensionless wellbore pressure p_{wD} (often times referred to as p_D) and dimensionless log-pressure derivative $dp_{wD}/d\ln t_D$. Dimensionless time t_D is used when pressure data is gathered from downhole gauges. Nonetheless, if pressure data is obtained from surface measurements, wellbore storage (fluid expansion inside the wellbore) and skin (formation damage/enhancement) effects must be included into the analysis, such that p_{wD} and $dp_{wD}/d\ln t_D$ are plotted against t_D/C_D , where C_D is the wellbore storage coefficient (Gringarten et al., 1979). In general, the definition of p_{wD} and t_D depends on the reservoir model and setting under evaluation (Lee et al., 2003). Figure 1.3 illustrates a typical set of type curves for an infinite radial reservoir with wellbore storage and skin.

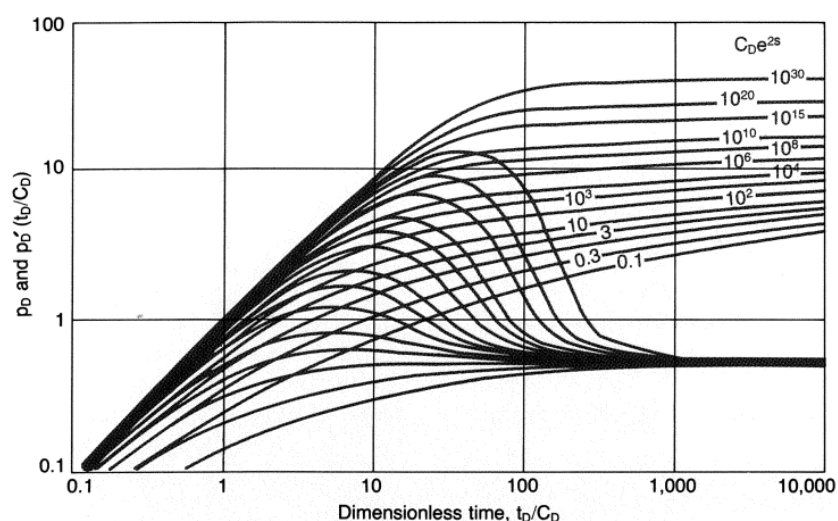


Figure 1.3: Type curves for an infinite radial reservoir with wellbore storage and skin (from Bourdet et al., 1989).

Type-curves matching is a well-known and extensively technique used for reservoir characterization purposes. The fundamental approach of type-curves matching consists of overlapping diagnostic plots from well-tests onto the type-curves graph corresponding to the reservoir model under study (Spivey and Lee, 2013; Bourdet et al.,

1989). Type-curves parameters of the reservoir model are typically dimensionless. For example, p_{wD} , t_D and C_D represent dimensionless pressure-drawdown, time and well-bore storage, respectively. Once measure transient data is fully matched against a type-curve, a matching point is chosen and reservoir properties of interest are estimated by using the analytical definitions of p_{wD} , t_D and C_D . In this dissertation, we aim to develop analytical solutions from which type-curves plots can be generated and used for reservoir characterization.

1.2. Proposed Applications for Pressure-Transient Analysis

The goal of the present work is to develop new analytical solutions for reservoir models, of high relevance to the oil and gas industry, that can be interpreted and extended to field data by means of classic PTA techniques, specifically diagnostic plots and type-curves matching. In doing so, we implement advanced mathematical techniques, like Laplace-Fourier transform coupled with iterative algorithms. Furthermore, numerical reservoir simulations are used for verification and validation purposes. In general, this dissertation focuses on the following areas of reservoir engineering:

- Forecast of MFHW performance and estimation of ultimate recovery from stress-sensitive, composite systems in which reservoir and fracture properties may vary substantially with changes in pore pressure.
- Detection of well interference effects due to fracture hits, or frac hits, and assessment of the degree of interference in a multi-well pad.
- Detection of fault reactivation and characterization of enhanced fault properties in homogeneous and heterogeneous compartmentalized reservoirs.

Chapter 2 discusses the incorporation of pressure-dependent properties into the trilinear flow model (TLF). This study assumes that the reservoir fluid is undersaturated oil hence the analytical model considers single-phase, slightly compressible fluid-flow. We discuss the origin of stress-dependency in unconventional composite systems and review the exponential pressure-dependent rock and fluid properties commonly used in the reservoir engineering literature. The governing equations as well as the boundary conditions are derived for the nonlinear problem. We further introduce an iterative algorithm to solve the nonlinear part of the model. The analytical constant-rate solution is presented in the form of diagnostic plots. Numerical simulations are carried out for validation purposes.

Chapter 3 focuses on the development of an analytical PTA model of a multi-well pad in which frac hits are present thus allowing inter-well communication. The central hypothesis of this study is that pressure across interfering wells would seek to attain a late-time equilibrium condition. This hypothesis is drawn from the first law of thermodynamics which states that, no matter the initial conditions of a system, energy will always attain a final equilibrium condition. Therefore, instead of pursuing PTA analysis of individual wells, we study the entire pad as a whole and perform typical pressure-transient techniques to transient data, which needs to be arranged in a special manner. Derivation of governing equations and frac-hits boundary conditions are detailed in this chapter. Synthetic pressure data is generated using numerical simulations for validation purposes.

Chapter 4 revisits the initial pressure-transient model for across-fault leakage upon fault reactivation proposed for this dissertation and adds two important features: simultaneous across-along-fault flow and composite reservoirs. As any analytical PTA model, the fault permeability enhancement model discussed in this chapter is intended for detection, not prediction, of fault reactivation and characterization of fault permeability enhancement. Governing equations are introduced along with the necessary boundary conditions. Laplace-Fourier transform is presented along with analytical and numerical inversion procedures. Diagnostic plots and type-curves are presented and discussed in detail for a variety of fault permeability enhancement scenarios. Numerical simulations are carried out to validate the proposed analytical model, including a case where anisotropic fault permeability is pressure-dependent and self-healing.

2. Forecast of Multi-fractured Horizontal Well Performance in Stress-sensitive Formations: Constant Rate Approach.

2.1. Background

Economic exploitation of hydrocarbons from tight and ultra-low permeability plays across the United States, such as Spraberry, Wolfcamp Shale, Avalon Shale and Bone Springs in the Permian Basin (West Texas and southeastern New Mexico), Niobrara Shale (northern Colorado and eastern Wyoming), and Woodford Shale Plays in the Anadarko Basin (Oklahoma), is nowadays a reality due to the low-cost application of hydraulic fracturing (HF) in horizontal wells. The main objective of a HF job in unconventional plays is to increase the contacted surface area of the reservoir/source rock accessed by a single horizontal well and, as such, HF is executed at various stages of the horizontal section of the well. This type of well is commonly known as multistage-fractured horizontal well or MFHW.

Several aspects should be taken into consideration to make a certain source rock or tight formation (matrix) prospective. These include total organic content (TOC), thermal maturity, reservoir pressure, brittleness, among others. Yet, the presence of natural fractures (NF) in the targeted formation may be an influential factor. For $5 \mu\text{d}$ ($= 0.005 \text{ md}$) matrix permeability, NF can be inconvenient due to fluid loss during the HF job; however, for 50 nd ($= 5 \times 10^{-6} \text{ md}$) matrix permeability, NF can be critical for hydrocarbons production (Smith and Montgomery, 2015).

The geometry of a hydraulic fracture depends on the mechanical properties of the matrix and can be either planar or complex (Cipolla and Wallace, 2014) as shown in Figure 2.1. Moreover, fracture branching induced during the HF job generates a fracture network that may interconnect micro-fractures and NF networks present in the matrix with the well, resulting in a complex fracture network that may boost well productivity (Mayerhofer et al., 2010); however, such dense fracture networks can also lead to interference between complex fractures thus hindering well productivity (Smith and Montgomery, 2015; Cipolla and Wallace, 2014).

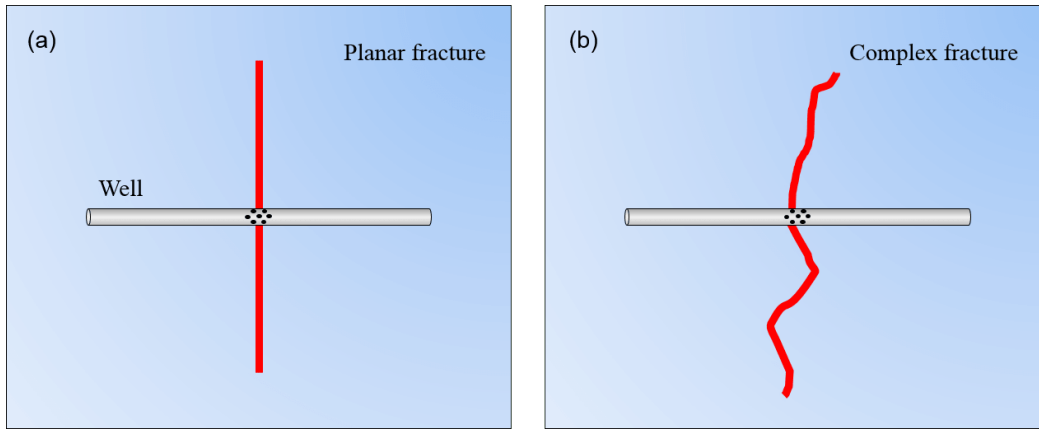


Figure 2.1: Types of hydraulic fractures: (a) planar fracture and (b) complex fracture.

In any case, fracture branching, NF and micro-fracture networks create a stimulated region around the hydraulic fracture, which is often referred to as the stimulated reservoir (or rock) volume (SRV) (Mayerhofer et al., 2010). The size of the SRV is usually estimated via microseismic mapping using observation wells located near the MFHW (Cipolla and Wallace, 2014; Warpinski, 2009; Warpinski et al., 2005; Fisher et al., 2004). Because the reservoir region around a fractured stage is composed of distinct zones—hydraulic fracture (“propped” or filled with proppant), induced-fractures network, micro-fractures and NF, and untouched matrix—rock properties are considered heterogeneous in this region. Consequently, MFHW are composite systems. Figure 2.2 depicts an illustration of the associated regions in a hydraulically fractured stage in an MFHW.

Furthermore, NF/induced-fractures networks in the SRV are generally unpropped (Wilson, 2015) hence their capacity to transport fluid from the non-stimulated (i.e. untouched) matrix into the hydraulic fracture cannot be paired to that of the hydraulic fracture itself. In addition, the flow capacity of the matrix is very low compared to that of either the SRV of hydraulic fracture. This is an important observation that needs to be accounted for in order to accurately forecast MFHW performance and estimated ultimate recovery (EUR), which are the two most important indicators of economic feasibility for developing a certain unconventional play.

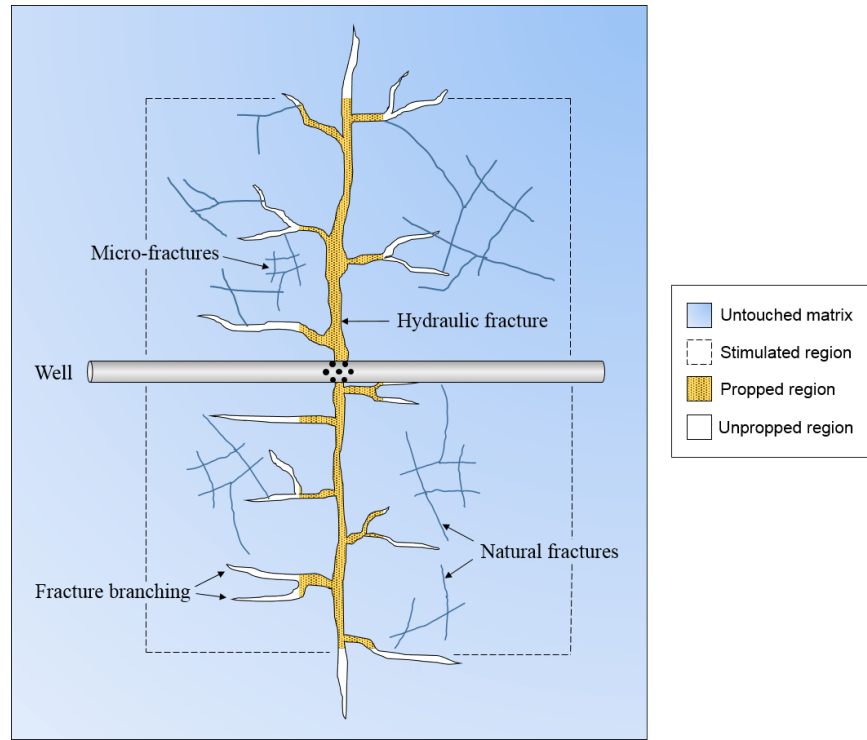


Figure 2.2: Types of fractures present in a hydraulically fractured stage: hydraulic fracture, fracture branching, natural fracture networks and micro-fractures.

In addition to the complexity posed by the uneven flow capacity in a fractured stage, conductivity of both hydraulic fracture and fracture networks in the SRV will progressively diminish as reservoir pressure declines, leading to an increase in the effective minimum horizontal stress, also known as closure stress (Smith and Montgomery, 2015). Moreover, loss in fracture conductivity in the hydraulic fracture and SRV occurs at different rates because the hydraulic fracture is propped while fracture networks in the SRV are likely not. These observations suggest that MFHW performance can be influenced by changes in stresses due to fluid withdrawal therefore they must also be considered when projecting well performance and EUR in a given shale play or tight reservoir.

Two of the most widely used analytical MFHW models are the trilinear flow (TLF) model (Brown et al., 2011) and the five-region flow (FRF) model (Stalgorova and Mattar, 2013). These models are based on the following assumptions:

- constant-rate withdrawal;
- 3-D fluid-flow modeled as a combination of several linear flows (matrix to SRV,

SRV to fracture, fracture to wellbore);

- hydraulic fractures are planar and have equal dimensions;
- complex fracture network in the SRV represented by a region of permeability orders-of-magnitude higher than matrix permeability;
- one hydraulic fracture per stage;
- hydraulic fractures have equal properties;
- fractured stages are symmetric; and,
- heterogeneous and constant rock properties.

Although similar, each analytical MFHW model is suitable for a specific field application. The TLF model, for instance, is intended for MFHWs featuring narrow spacing between fractured stages, which inherently considers that the SRV fully extends across all fractured stages, as shown in Figure 2.3. Yet, TLF can be used if this condition does not hold as long as fluid-flow in the SRV is linear transient. The FRF model, conversely, accounts for the possibility of having unstimulated rock between fractured stages, as shown in Figure 2.4, therefore is more suitable for modeling MFHWs with stimulated region with limited extent.

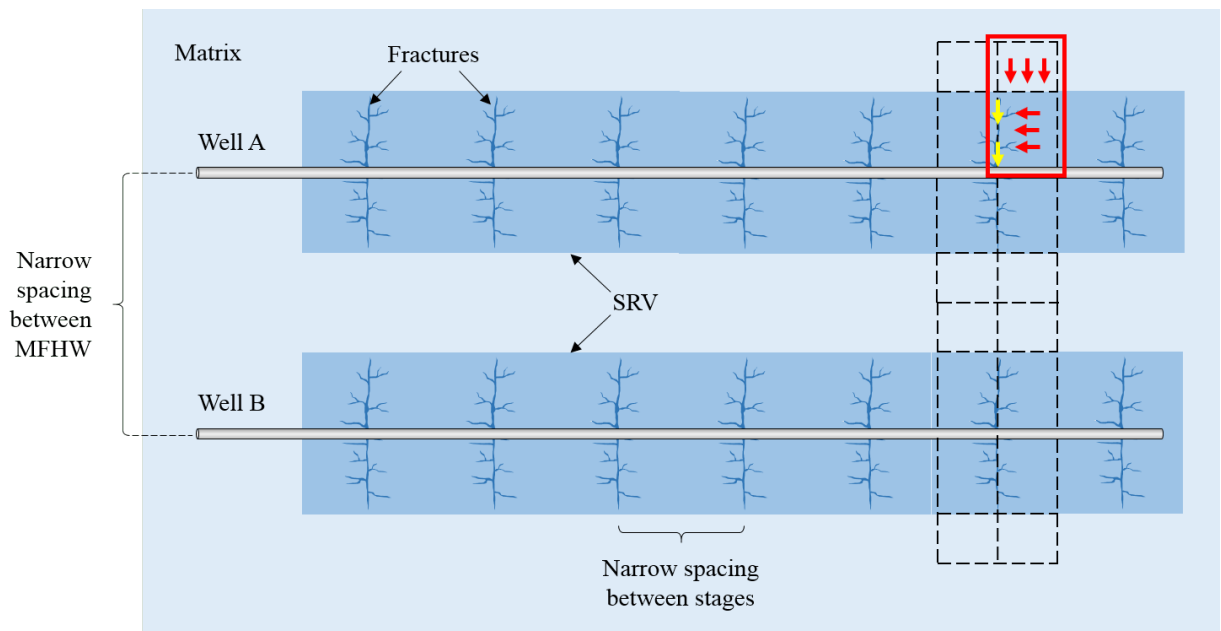


Figure 2.3: Conceptualization of the trilinear flow model. Narrow spacing between fractured stages and MFHW in a multi-well pad.

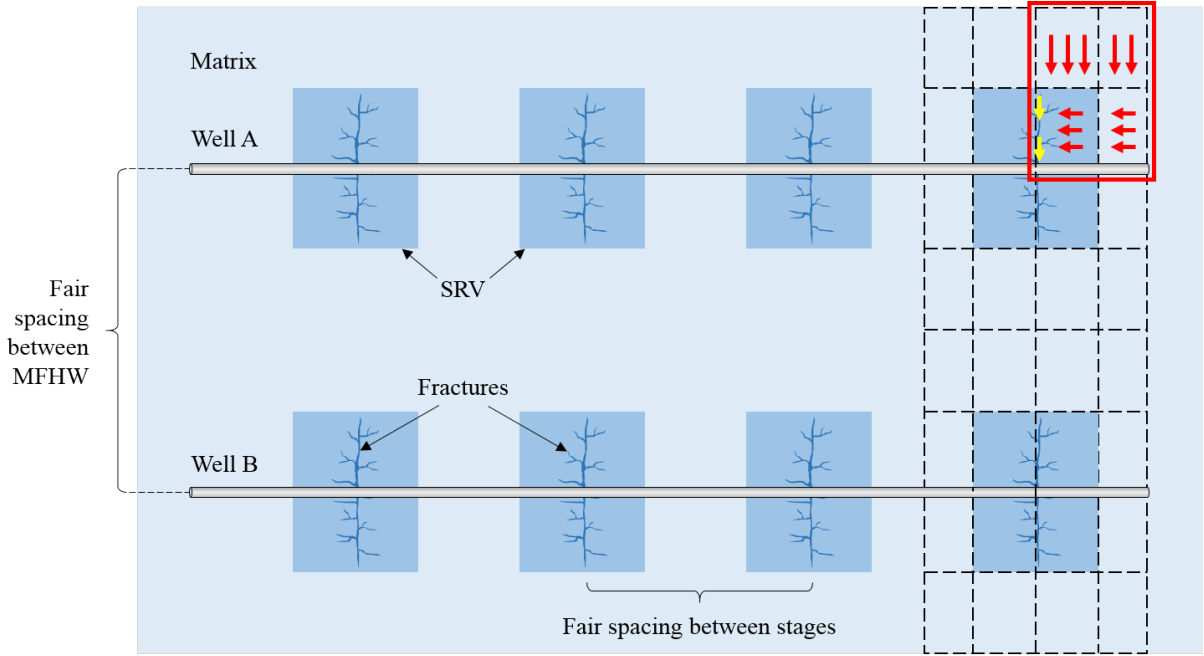
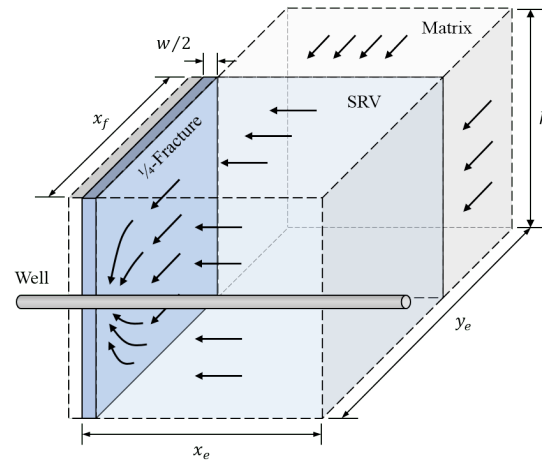


Figure 2.4: Conceptualization of the five-region model. Fair spacing between fractured stages and MFHW in a multi-well pad.

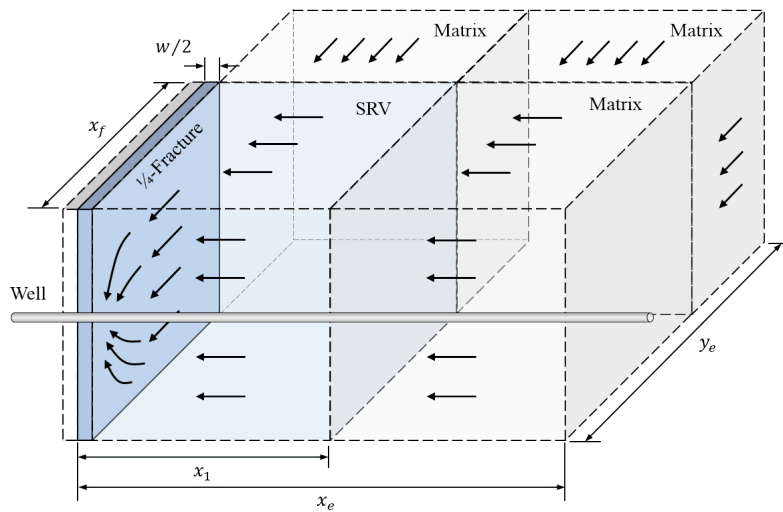
As mentioned earlier, both TLF and FRF models simplify fluid-flow from the matrix into the wellbore as the combination of several linear flow regimes. In the TLF model, for instance, fluid flows from the matrix into the SRV linearly along the y -axis. Then, fluid flows from the SRV into the fracture linearly along the x -axis. Influx from the matrix into the SRV, across the interface located at $y = x_f$, is modeled using a flux-source function. Finally, flow from the fracture towards the well occurs along the y -axis. Similar to the SRV region, influx from the SRV into the fracture, across the interface located at $x = w/2$, is modeled using another flux-source function. Figure 2.5a illustrates a schematic of the different linear flow regimes of the TLF model. The TLF includes an additional pressure loss occurring near the wellbore due to flow convergence, also known as choking skin effect (Brown et al., 2011; Stalgorova and Mattar, 2013). Similarly, the FRF model features the same linear flow regimes than the TLF plus an additional fluid influx from the untouched matrix into the SRV, as shown in Figure 2.5b.

The combined-linear-flow simplification makes both analytical MFHW model mathematically tractable. In fact, their corresponding analytical solution is found in a straightforward manner in Laplace domain. However, these expressions are too dif-

difficult to invert back into time domain analytically. Thus, numerical Laplace inversion algorithms (e.g. Zakian, 1969; Stehfest, 1970) are used to invert these solutions, which are typically derived for constant-rate production conditions. Yet, variable-rate versions of the TLF and FRF models are typically found in production data analysis software and are routinely used to estimate properties of interest, such as SRV permeability and fracture conductivity, as well as to forecast well productivity.



(a) Trilinear flow model



(b) Five-region flow model

Figure 2.5: Fluid-flow in a MFHW modeled as a combination of various linear flow regimes: (a) trilinear MFHW model; (b) five-region MFHW model.

2.2. Statement of the Problem

Among the assumptions made in deriving the fluid-flow model for the TLF and FRF, considering rock properties to be invariant with pressure may be unrealistic. Both primary and secondary fractures created during a stimulation job are kept open by fluid pressure p counteracting in-situ confining or closure stress σ_{CL} . The difference between pore pressure and closure stress is called the pressure, denoted by p_{net} (Smith and Montgomery, 2015) (Figure 2.6).

Net pressure decreases as pore pressure declines with oil production. This indicates that, over time, open fractures become more vulnerable to the action of the host rock to close them up. As a result, fracture conductivity, defined as $C_f = k_f w$, is expected to decrease as pressure declines. Conductivity of propped fractures, on the one hand, will likely decrease at a slower rate than unpropped fractures in the SRV, the reason being that proppant resists the action of closure stress. Consequently, not only fracture conductivity is expected to be sensitive to changes in pressure, but also propped and unpropped fractures lose conductivity at distinct rates. Since it is difficult to infer an average fracture width for the SRV, conductivity of unpropped fractures is often lumped into the definition of pressure-dependent SRV permeability.

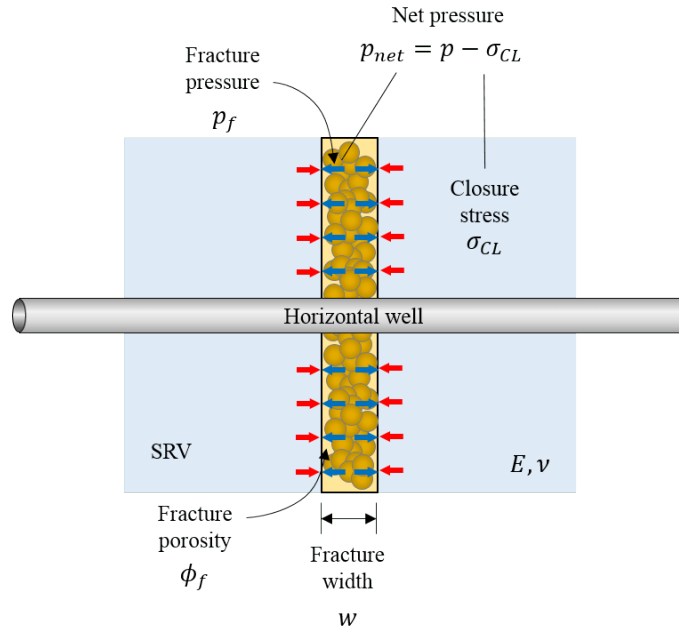


Figure 2.6: Schematic of forces acting on the hydraulic fracture. Fluid pressure resists the effect of closure stress trying to close up the fracture. The same scenario occurs with unpropped fractures in the SRV.

Productivity loss in stress-sensitive tight-oil reservoirs is therefore attributed to a gradual loss of fracture conductivity in well pads. Laboratory experiments on samples from Barnett and Haynesville shales (Cho et al., 2013; Wilson, 2015) and Huron and Marcellus shales (Chen et al., 2015; El-sgher et al., 2018) demonstrate the adverse impact of pressure depletion on fracture conductivity, particularly for unpropped fractures (Suarez-Rivera et al., 2013) which are a major contributor to SRV permeability (Cipolla et al., 2010; Guo et al., 2013; Sharma and Manchanda, 2015). A key conclusion from these studies is that conductivity of unpropped fractures reduces at a faster rate with pressure decline than propped fractures, as hypothesized earlier.

Nur and Yilmaz (1985) proposed one of the earliest exponential formulations for permeability as a function of pore pressure. Authors observed that their experimental measurements for changes in permeability with pore pressure in fracture rocks were accurately described by the following correlation:

$$k_j = k_{ji} e^{-\gamma_j \Delta p_j} \quad (2.1)$$

where the subscript j refers to a specific sample. k_{ji} is the initial fracture permeability of the sample; γ_j is the permeability modulus, and $\Delta p_j = p_i - p_j(t)$ is the change in initial pressure, equivalent to pressure-drawdown. Nur and Yilmaz (1985) stated that γ_j varies depending on rock type and fracture properties. Almost two decades later, Raghavan and Chin (2004) derived Equation 2.1 after solving the coupled geomechanics-fluid-flow governing equations based on certain simplifications of the fluid-flow model.

The exponential pressure-dependent permeability model has been widely applied in analytical modeling of unconventional wells. For instance, Cho et al. (2013) incorporated Equation 2.1 into the TLF model, via pseudo-pressure/pseudo-time, to account for overall loss of permeability with pressure decline. Likewise, Tabatabaie et al. (2016) followed the same approach to develop an analytical model to study transient linear flow in stress-sensitive formations. Both models, however, rely on a single value of γ to describe loss of permeability in the entire system. As noted earlier, this assumption may be inaccurate because propped fracture conductivity and SRV permeability decrease with pressure-drawdown at distinct rates.

Figure 2.7 illustrates the expected fractional change of permeability of the matrix (region 2), SRV (region 1) and fracture (region f) for $\gamma_2 = 5 \times 10^{-6} \text{ psi}^{-1}$ (matrix),

$\gamma_1 = 5 \times 10^{-4} \text{ psi}^{-1}$ (SRV) and $\gamma_f = 1 \times 10^{-3} \text{ psi}^{-1}$ (fracture). Here, it can be seen that more than 96% of initial matrix permeability is retained in despite the large pressure-drawdown. Thus, reduction in matrix permeability is quite negligible in this case. Contrariwise, reduction of both SRV and fracture permeability is significant. Realize, however, that these properties tend to become zero under large confining stress, which may be unrealistic. In Section 2.12, we utilize an improved exponential pressure-dependent model that sets a lower bound, or critical value, to variation in permeability with pressure decline.

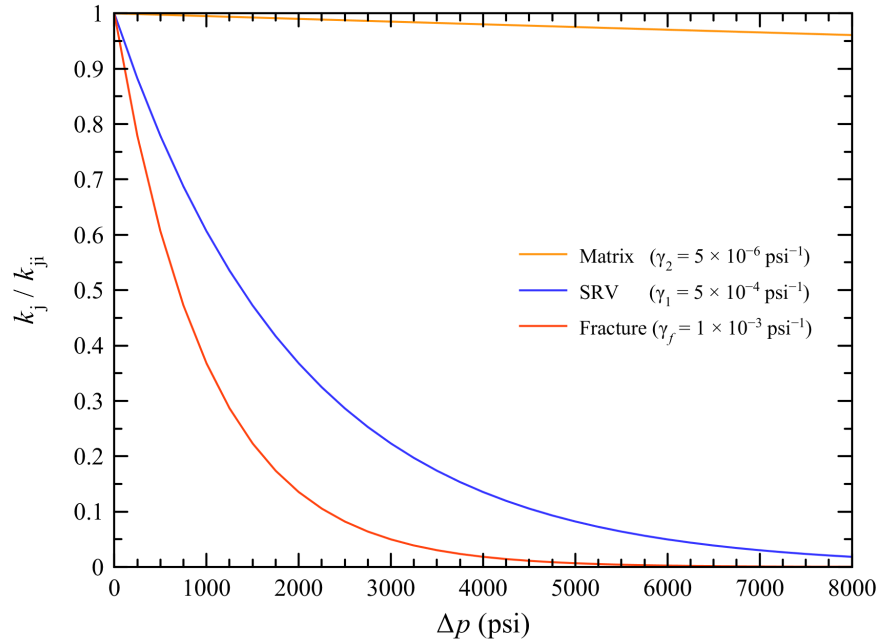


Figure 2.7: Fractional changes in SRV and fracture permeability with pore pressure.

Similar to changes in permeability with pressure, experimental results suggest that fracture conductivity closely follows an exponential relationship of the same kind (Zhang et al., 2014). As a result, the following exponential relationship for pressure-dependent fracture conductivity was proposed (Yao et al., 2016):

$$C_f = C_{fi} e^{-d_f \Delta p} \quad (2.2)$$

$C_{fi} = k_{fi} w_i$ is the initial fracture conductivity; k_{fi} and w_i are the initial fracture permeability and width, respectively; d_f is the stress-sensitive characteristic number.

In this work, we introduce an analytical MFHW model for constant-rate withdrawal that accounts for localized variations in rock properties with pressure-drawdown. Our model enables the individual assessment of the impact of pressure-dependent properties in the matrix and stimulated reservoir volume (SRV) and pressure-dependent fracture conductivity on MFHW performance, well life and expected ultimate recovery (EUR). The proposed MFHW model is based on the TLF model into which pressure-dependent properties are incorporated into each region as exponential functions of pressure-drawdown. The nonlinear solution to the governing equations is achieved by a combination of a linearization techniques, Laplace transform and an iterative nonlinear solution algorithm.

2.3. Current Analytical Methods

Several analytical MFHW models have been proposed being the TLF and FRF models the most popular. While both models consider distinct rock properties for the fracture, SRV and matrix these were originally assumed independent of changes in pore pressure. To resolve this problem, Cho et al. (2013) utilized pseudo-functions into the TLF model to study the impact of pressure-dependent permeability on productivity of a shale gas well. Similarly, Stalgorova and Mattar (2016) used pseudo-functions with the FRF model to account for permeability variations with pressure in tight oil wells. Although the dependency of permeability on pressure is incorporated into pseudo-pressure in a straightforward manner, such approach inherently assumes that permeability varies at equal rate across the composite system. Henceforth, the pseudo-pressure method may not be a reliable tool to evaluate performance of pressure-sensitive MFHWs.

Aside from these models, Luo et al. (2017) introduced a semi-analytical reservoir/fracture model for a vertical well considering pressure-dependent fracture conductivity and constant SRV permeability; matrix is not included in this model. In addition, fluid properties were assumed invariant with pressure depletion. Akin to the work of Cho et al. (2013) (TLF model with pseudo-pressure/pseudo-time), Zhu et al. (2018) introduced an exponential pressure-dependent permeability into the FRF model. Yet, none of these analytical MFHW models are able to address the possibility of assigning pressure-dependent properties individually to each region in the MFHW.

2.4. Proposed Methodology

In contrast with existing analytical MFHW models with pressure-dependent properties, we develop an analytical MFHW model for tight-oil reservoirs that allows to assign separate pressure-dependent rock properties to the fracture, SRV and matrix while accounting for changes in fluid properties with pressure. Rock and fluid properties are assumed to vary exponentially with pore pressure with respect to the reference pressure chosen to be initial reservoir pressure.

The proposed fluid-flow model is based on the TLF model for single-phase, slightly-compressible fluid flowing at constant rate. However, the inclusion of exponential pressure-dependent rock and fluid properties results in highly nonlinear partial differential equations. We linearize the resulting governing equations by assuming that certain nonlinear parameters can be approximated based on local average pressure-drawdown of each region. Since average drawdowns are initially unknown, we further implement an iterative algorithm to estimate the nonlinear parameters.

The linearized governing equations are transformed into Laplace domain and the analytical solution is inverted into time domain numerically. We use the analytical solution to the proposed MFHW model to investigate the effect of pressure dependency of fracture conductivity and SRV permeability on well performance until bubble-point pressure is reached.

Two main cases are studied in this section: (1) effect of pressure-dependent SRV permeability on well performance and (2) effect of combined pressure-dependent SRV permeability and fracture conductivity on well performance. Rock and fluid properties are taken from the liquids-rich section of the lower Eagle Ford. The proposed method is validated against synthetic data generated from a numerical MFHW model. Typical rate-normalized diagnostic plots are constructed and examined herein.

2.5. Mathematical Modeling

2.5.1 Definition of Pressure-Dependent Properties

Similar to permeability and fracture conductivity, oil properties, such as density ρ_o , formation volume factor B_o and viscosity μ_o (Chen, 2007), as well rock properties, such as porosity ϕ , also vary exponentially with pressure. These correlations are defined as:

$$\rho_o = \rho_{oi}e^{-c_o\Delta p_j} \quad (2.3)$$

$$\mu_o = \mu_{oi}e^{-c_\mu\Delta p_j} \quad (2.4)$$

$$B_o = B_{oi}e^{c_f\Delta p_j} \quad (2.5)$$

$$\phi_j = \phi_{ji}e^{-(c_r)_j\Delta p_j} \quad (2.6)$$

$$(2.7)$$

The coefficients c_o and c_μ in Equation 2.3 and 2.4, respectively, are the isothermal fluid compressibility and viscosity modulus. Note that, alike k_j , ϕ_j carries the subscript j to imply that porosity may vary at different rates across the composite system. In addition, the subscript i indicates properties measured at initial pressure. In this section, we will use $j = 2, 1, f$ to denote the matrix, SRV and fracture, respectively.

Furthermore, dividing Equation 2.2 by k_1x_f , where k_1 is the SRV permeability (given by Equation 2.1 for $j = 1$) and x_f the fracture half-length. As a result, we obtain the definition of pressure-dependent dimensionless fracture conductivity F_{CD} :

$$F_{CD} = \frac{k_{fi}w_i}{k_{1i}x_f}e^{\gamma_1\Delta p_1 - d_f\Delta p_f} \quad (2.8)$$

Unlike the definition of pressure-dependent F_{CD} proposed by Berumen and Tiab (1996), Equation 2.8 incorporates changes in SRV permeability with pressure decline.

2.5.2 Dimensionless Parameters Group

The following dimensionless parameters are introduced to normalize the linearized diffusivity equations for each region of the MFHW:

$$p_{jD} = \frac{k_{1i}h(1 - e^{-c_o^*\Delta p_j})}{141.2q'\mu_{oi}B_{oi}c_o^*} \quad (2.9)$$

$$x_D = \frac{x}{x_f} \quad (2.10)$$

$$y_D = \frac{y}{x_f} \quad (2.11)$$

$$t_D = 2.637 \times 10^{-4} \frac{k_{1i} t}{\mu_{oi} (\phi_i c_t)_1 x_f^2} \quad (2.12)$$

$$\eta_{ji} = 2.637 \times 10^{-4} \frac{k_{ji}}{\mu_{oi} (\phi_i c_t)_j} \quad (2.13)$$

$$\eta_{jD} = \frac{\eta_{ji}}{\eta_{1i}} = \frac{k_{ji}}{k_{1i}} \frac{(\phi_i c_t)_1}{(\phi_i c_t)_j} \quad (2.14)$$

The coefficient c_o^* in Equation 2.9 is defined as the difference between oil compressibility and viscosity modulus, that is, $c_o^* = c_o - c_\mu$. As such, c_o^* can be regarded as a corrected fluid compressibility. Notice that 2.9 reduces to the commonly used linear definition of dimensionless pressure shown below when c_o^* is relatively small:

$$\frac{1}{c_o^*} (1 - e^{-c_o^* \Delta p_j}) \approx \frac{1}{c_o^*} [1 - (1 - c_o^* \Delta p_j)] = \Delta p_j \quad (2.15)$$

Molina and Zeidouni (2017a) proved that c_o^* can be considered sufficiently small when $c_o^* < 10^{-6} \text{ psi}^{-1}$. In such cases, the linear approximation for Δp_j , shown above, holds.

Lastly, q' in Equation 2.9 is the equivalent per-fracture rate of the MFHW. That is, total flow rate of the MFHW divided by the number of hydraulic fractures.

2.5.3 Fluid-flow Model for Matrix (Region 2)

2.5.3.1 Governing Equation

To derive the governing equation for fluid-flow in the matrix when rock and fluid properties are sensitive to pressure, we take the differential control volume $\Delta V = hL_e \Delta y$, shown in Figure 2.8, and apply the law of mass conservation, which gives:

$$\dot{m}_{\text{in}} - \dot{m}_{\text{out}} = \frac{\partial}{\partial t} (\rho \phi_2 h L_e \Delta y) \quad (2.16)$$

Mass flux in the y -direction is given by $\dot{m}_y = \rho_o v_y A_y$ where ρ_o is the oil density, v_y the superficial fluid velocity and $A_y = hL_e$ the cross-sectional area perpendicular to the direction of flow. Replacing this condition into the material balance equation, leads to:

$$(\rho_o v_y h L_e)_y - (\rho_o v_y h L_e)_{y-\Delta y} = \frac{\partial}{\partial t} (\rho_o \phi_2 h L_e \Delta y) \quad (2.17)$$

Dividing both sides of the equation above by $h L_e \Delta y$ and letting Δy to be infinitesimally small, results in:

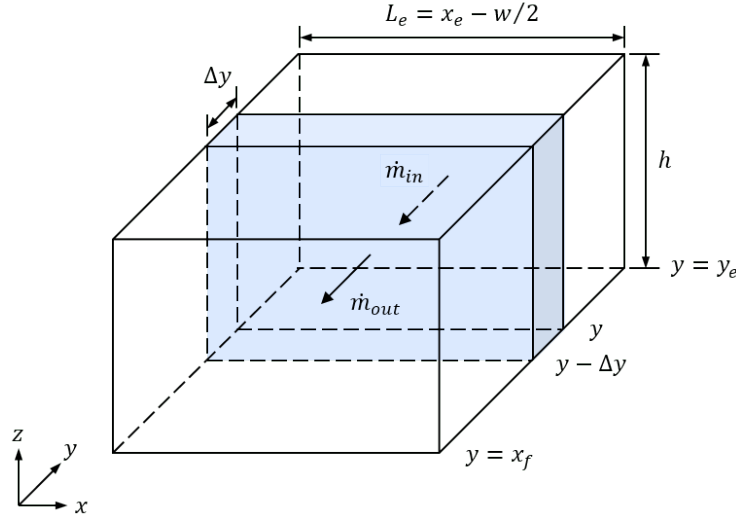


Figure 2.8: Mass balance across a differential control volume in the matrix.

$$\frac{\partial}{\partial y} (\rho v_y) = \frac{\partial}{\partial t} (\rho_o \phi_2) \quad (2.18)$$

Realize that Δp_2 decreases with increasing y then the surface velocity v_y is given, based on Darcy's law, as $v_y = -(k_2/\mu_o)(\partial \Delta p_2 / \partial y)$. Thus, the governing equation for fluid-flow in the matrix is defined in terms of Δp_2 as:

$$-\frac{\partial}{\partial y} \left(k_2 \frac{\rho}{\mu} \frac{\partial \Delta p_2}{\partial y} \right) = \frac{\partial}{\partial t} (\rho \phi_2) \quad (2.19)$$

Replacing Equation 2.3, 2.4 and 2.4 into Equation 2.19, yields:

$$\frac{\partial}{\partial y} \left(k_2 \frac{e^{-c_o^* \Delta p_2}}{\mu_{oi} B_{oi}} \frac{\partial \Delta p_2}{\partial y} \right) = \frac{(\phi c_t)_2}{B} \frac{\partial \Delta p_2}{\partial t} \quad (2.20)$$

where $c_{t2} = c_o + c_{r2}$ is the total compressibility factor of the matrix. Next, use Equation 2.1 to define k_2 as a pressure-dependent property on the left-hand side of the equation above and multiply the right-hand side by $\frac{\mu}{\mu}$, yielding

$$\frac{\partial}{\partial y} \left(e^{-\gamma_2 \Delta p_2} \frac{e^{-c_o^* \Delta p_2}}{\mu_{oi} B_{oi}} \frac{\partial \Delta p_2}{\partial y} \right) = \left(\frac{\mu_{oi} \phi_i c_t}{k_i} \right)_2 e^{-(c_\mu + c_{r2}) \Delta p_2} \frac{e^{-c_o^* \Delta p_2}}{\mu_{oi} B_{oi}} \frac{\partial \Delta p_2}{\partial t} \quad (2.21)$$

Equation 2.21 can be further recast in the following convenient form:

$$\frac{\partial}{\partial y} \left[e^{-\gamma_2 \Delta p_2} \frac{\partial}{\partial y} \left(\frac{1 - e^{-c_o^* \Delta p_2}}{\mu_{oi} B_{oi} c_o^*} \right) \right] = \frac{1}{\eta_{2i}} e^{-(c_\mu + c_{r2}) \Delta p_2} \frac{\partial}{\partial t} \left(\frac{1 - e^{-c_o^* \Delta p_2}}{\mu_{oi} B_{oi} c_o^*} \right) \quad (2.22)$$

The diffusivity coefficient of region 2 evaluated at initial reservoir conditions η_{2i} is defined (in oilfield units) as:

$$\eta_{2i} = 2.637 \times 10^{-4} \frac{k_{2i}}{\mu_{oi} (\phi_i c_t)_2} \quad (2.23)$$

Recognize that the nonlinear terms $e^{-\gamma_2 \Delta p_2}$ and $e^{-(c_\mu + c_{r2}) \Delta p_2}$ do not allow any further linearization of the governing equation above. These are strong nonlinearities that depend on both direction of flow (y) and time (t) given that $\Delta p_2 = f(y, t)$.

However, if we consider approximating these functions by evaluating them at current average pressure-drawdown $\Delta \tilde{p}_2(t)$, the directional dependency would be removed. Consequently,

$$e^{-\gamma_2 \Delta p_2} \approx e^{-\gamma_2 \Delta \tilde{p}_2} \quad (2.24)$$

$$e^{-(c_\mu + c_{r2}) \Delta p_2} \approx e^{-(c_\mu + c_{r2}) \Delta \tilde{p}_2} \quad (2.25)$$

In this manner, $e^{-\gamma_2 \Delta p_2}$ can be taken out of the partial derivative on the left-hand side of Equation 2.22 thus allowing for a partial linearization of the governing equation. As a result:

$$\frac{\partial}{\partial y} \left[\frac{\partial}{\partial y} \left(\frac{1 - e^{-c_o^* \Delta p_2}}{\mu_{oi} B_{oi} c_o^*} \right) \right] = \frac{1}{\lambda_2 \eta_{2i}} \frac{\partial}{\partial t} \left(\frac{1 - e^{-c_o^* \Delta p_2}}{\mu_{oi} B_{oi} c_o^*} \right) \quad (2.26)$$

λ_2 is a nonlinear scaling parameter, defined as

$$\lambda_2 = e^{-(\gamma_2 - c_{r2} - c_\mu) \Delta \tilde{p}_2} \quad (2.27)$$

Even though $\Delta \tilde{p}_2$ is unknown at current time, we will consider λ_2 to be a constant, so that Equation 2.26 can be solved analytically. λ_2 will be estimated iteratively, once the analytical solution to the model has been found. The iterative algorithm is explained in detail in Section 2.8.

Notice that setting $\lambda_2 = 1$ and assuming $c_o^* < 10^{-6} \text{ psi}^{-1}$ will result in the classic linear diffusivity equation for the matrix in the TLF and FRF models.

Finally, Equation 2.26 can be normalized using Equation 2.9—2.14. As a result, we get:

$$\frac{\partial^2 p_{2D}}{\partial y_D^2} = \frac{1}{\lambda_2 \eta_{2D}} \frac{\partial p_{2D}}{\partial t_D} \quad (2.28)$$

Following the assumption that λ_2 is constant, we can apply the Laplace transform upon $p_{2D}(y_D, t_D)$ over t_D on Equation 2.28, assuming that the initial pressure-drawdown in the matrix is zero (i.e. $\Delta p_2(y_D, t_D = 0) = 0$) thus $p_{1D}(y_D, t_D = 0) = 0$. This results in

$$\frac{d^2 \bar{p}_{2D}}{dy_D^2} - \frac{s}{\lambda_2 \eta_{2D}} \bar{p}_{2D} = 0 \quad (2.29)$$

where $\bar{p}_{2D}(y_D, s) = \mathcal{L} \{p_{2D}(y_D, t_D)\}$ and s is the Laplace domain parameter.

2.5.3.2 Analytical Solution

Equation 2.29 is an ordinary differential equation in Laplace domain whose analytical solution is straightforward to obtain using common solution methods, such as variation of parameters. The canonical solution to Equation 2.29 is given as

$$\bar{p}_{2D} = A_2 \cosh \left[(y_D - y_{eD}) \sqrt{\frac{s}{\lambda_2 \eta_{2D}}} \right] + B_2 \sinh \left[(y_D - y_{eD}) \sqrt{\frac{s}{\lambda_2 \eta_{2D}}} \right] \quad (2.30)$$

Figure 2.5a shows that there is a no-flux boundary at the external reservoir boundary ($y_D = y_{eD}$). This condition is mathematically expressed, in Laplace domain, as:

$$\left(\frac{d\bar{p}_{2D}}{dy_D} \right)_{y_D=y_{eD}} = 0 \quad (2.31)$$

Replacing this expression into Equation 2.30 yields $B_2 = 0$. Henceforth,

$$\bar{p}_{2D} = A_2 \cosh \left[(y_D - y_{eD}) \sqrt{\frac{s}{\lambda_2 \eta_{2D}}} \right] \quad (2.32)$$

The other boundary conditions that apply to Equation 2.32 are the following:

- (i) *Pressure continuity.* Pressure-drawdown in the matrix (Δp_2) and SRV (Δp_1) must be continuous across the SRV/matrix interface located at $y = x_f$ equivalent to $y_D = 1$ (see Figure 2.5a). Thus,

$$(\Delta p_2)_{y=x_f} = (\Delta p_1)_{y=x_f} \quad (2.33)$$

This boundary condition can be further normalized using Equation 2.9 and 2.11 which results in $(p_{1D})_{y_D=1} = (p_{2D})_{y_D=1}$. Transforming this expression into Laplace domain, leads to:

$$(\bar{p}_{1D})_{y_D=1} = (\bar{p}_{2D})_{y_D=1} \quad (2.34)$$

The integration constant A_2 is found after substituting Equation 2.34 into 2.32. Consequently, we find the specific solution, in Laplace domain, to dimensionless pressure-drawdown distribution in region 2:

$$\bar{p}_{2D} = (\bar{p}_{1D})_{y_D=1} \frac{\cosh \left[(y_D - y_{eD}) \sqrt{\frac{s}{\lambda_2 \eta_{2D}}} \right]}{\cosh \left[(1 - y_{eD}) \sqrt{\frac{s}{\lambda_2 \eta_{2D}}} \right]} \quad (2.35)$$

- (ii) *Flux continuity.* Mass must be conserved across the SRV/matrix interface ($y_D = 1$). Based on Darcy's law,

$$\left(\frac{\rho_o k_1}{\mu_o} \frac{\partial \Delta p_1}{\partial y_D} \right)_{y_D=1} = \left(\frac{\rho_o k_2}{\mu_o} \frac{\partial \Delta p_2}{\partial y_D} \right)_{y_D=1} \quad (2.36)$$

Inserting the pressure-dependent functions for ρ_o (Equation 2.3), μ_o (Equation 2.4) and k (Equation 2.1) and further normalizing Δp_1 and Δp_2 based on Equation 2.9, yields

$$\left(e^{-\gamma_1 \Delta p_1} \frac{\partial p_{1D}}{\partial y_D} \right)_{y_D=1} = \frac{k_{2i}}{k_{1i}} \left(e^{-\gamma_2 \Delta p_2} \frac{\partial p_{2D}}{\partial y_D} \right)_{y_D=1} \quad (2.37)$$

Unlike mass flux and pressure-drawdown, permeability is discontinuous across the boundary, because of the rock properties of the SRV and matrix. Therefore, the flux-continuity condition poses a new difficulty in the analytical modeling stage as the boundary condition itself is highly nonlinear. As a matter of fact, the former is the reason why the pseudo-pressure approach may not be suitable for composite pressure-dependent systems.

To overcome this issue, let us assume that $e^{-\gamma_1 \Delta p_1}$ and $e^{-\gamma_2 \Delta p_2}$ are approximately equal to the average permeability of their corresponding regions. Based on Equation 2.1, $k_1(\Delta p_1)_{y_D=1} \approx k_1(\Delta \tilde{p}_1) = k_{1i} e^{-\gamma_1 \Delta \tilde{p}_1}$ and $(k_2)_{y_D=1} \approx k_{2i} e^{-\gamma_2 \Delta \tilde{p}_2}$. As a result:

$$\left(\frac{\partial p_{1D}}{\partial y_D} \right)_{y_D=1} = \frac{k_{2i}}{k_{1i}} \frac{1}{\delta_{21}} \left(\frac{\partial p_{2D}}{\partial y_D} \right)_{y_D=1} \quad (2.38)$$

where δ_{21} is a nonlinear scaling parameter, defined by

$$\delta_{21} = e^{\gamma_2 \Delta \bar{p}_2 - \gamma_1 \Delta \bar{p}_1} \quad (2.39)$$

γ_1 and γ_2 are the permeability modulus of regions 1 and 2, respectively. Similar to λ_2 , δ_{21} is assumed as a constant initially equal to 1 and will be later estimated iteratively, as explained in Section 2.8.

Taking δ_{21} as constant and transforming Equation 2.38 into Laplace domain, gives:

$$\left(\frac{d\bar{p}_{1D}}{dy_D} \right)_{y_D=1} = \frac{k_{2i}}{\delta_{21}k_{1i}} \left(\frac{d\bar{p}_{2D}}{dy_D} \right)_{y_D=1} \quad (2.40)$$

Finally, replacing Equation 2.35 into 2.40 results in:

$$\left(\frac{d\bar{p}_{1D}}{dy_D} \right)_{y_D=1} = (\bar{p}_{1D})_{y_D=1} \frac{k_{2i}}{\delta_{21}k_{1i}} \sqrt{\frac{s}{\lambda_2 \eta_{2D}}} \tanh \left[(1 - y_{eD}) \sqrt{\frac{s}{\lambda_2 \eta_{2D}}} \right] \quad (2.41)$$

Equation 2.41 is implemented as a flux-source term in the derivation of the governing equation for fluid-flow in the SRV (region 1). This approach is comparable to that used for modeling unsteady simultaneous heat conduction and convection in fins (Bergman et al., 2011).

2.5.4 Fluid-flow Model for SRV (Region 1)

2.5.4.1 Governing Equation

We perform a mass balance across the differential control volume $\Delta V_1 = hx_f \Delta x$ in the SRV as illustrated by Figure 2.9. Aside to the mass flux along the x -axis, namely \dot{m}_{in} at x and \dot{m}_{out} at $x - \Delta x$, there is an additional mass flux, denoted by \dot{m}_2 , coming from the matrix into the SRV across the SRV/matrix boundary located at $y = x_f$.

The purpose of coupling fluid-flow from the matrix into the SRV through an influx term is to model flow in the SRV as liner flow along the x -axis. Application of a mass balance over ΔV_1 yields the following relation:

$$\dot{m}_{in} + \dot{m}_2 - \dot{m}_{out} = \frac{\partial}{\partial t} (\rho_o \phi_1 hx_f \Delta x) \quad (2.42)$$

Because $\dot{m}_{\text{in}} = (\rho_o v_x h x_f)_x$, $\dot{m}_{\text{out}} = (\rho_o v_x h x_f)_{x-\Delta x}$ and $\dot{m}_2 = (\rho_o v_y h \Delta x)_{y=x_f}$, then the mass balance over ΔV_1 becomes

$$(\rho_o v_x h x_f)_x - (\rho_o v_x h x_f)_{x-\Delta x} + (\rho_o v_y h \Delta x)_{y=x_f} = \frac{\partial}{\partial t} (\rho_o \phi_1 h x_f \Delta x) \quad (2.43)$$

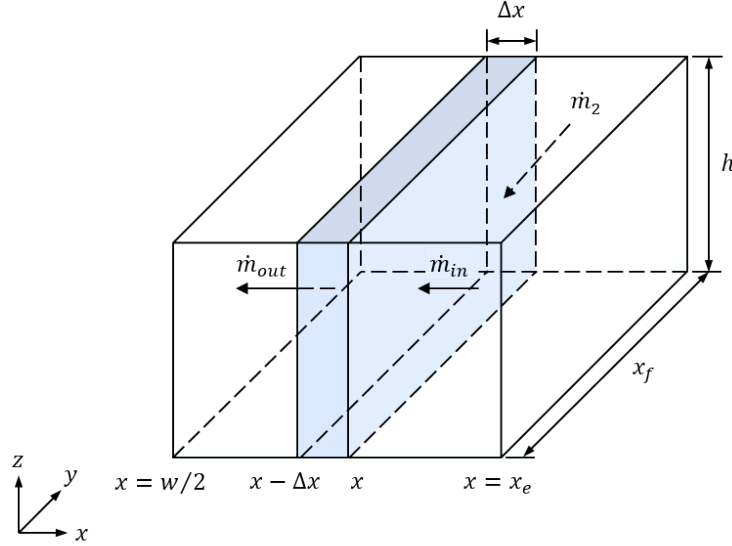


Figure 2.9: Mass balance across a differential control volume inside the SRV.

Dividing the former equation by ΔV_1 and allowing Δx to approach zero, yields

$$\frac{\partial}{\partial x} (\rho_o v_x) + \frac{1}{x_f} (\rho_o v_y)_{y=x_f} = \frac{\partial}{\partial t} (\rho_o \phi_1) \quad (2.44)$$

v_x and v_y are defined as $v_x = -(k_1/\mu_o)(\partial \Delta p_1/\partial x)$ and $v_y = -(k_1/\mu_o)(\partial \Delta p_1/\partial y)$. The negative sign is because Δp_1 and Δp_2 increases with $x > 0$ and $y > 0$, respectively. Replacing these expression into Equation 2.44 gives

$$-\frac{\partial}{\partial x} \left(\frac{\rho_o k_1}{\mu_o} \frac{\partial \Delta p_1}{\partial x} \right) - \frac{1}{x_f} \left(\frac{\rho_o k_1}{\mu_o} \frac{\partial \Delta p_1}{\partial y} \right)_{y=x_f} = \frac{\partial}{\partial t} (\rho_o \phi_1) \quad (2.45)$$

Substituting Equation 2.3, 2.4 and 2.1 into Equation 2.45, yields:

$$\begin{aligned} \frac{\partial}{\partial x} \left[e^{-\gamma_1 \Delta p_1} \frac{\partial}{\partial x} \left(\frac{1 - e^{-c_o^* \Delta p_1}}{\mu_{oi} B_{oi} c_o^*} \right) \right] + \frac{1}{x_f} \left[e^{-\gamma_1 \Delta p_1} \frac{\partial}{\partial y} \left(\frac{1 - e^{-c_o^* \Delta p_1}}{\mu_{oi} B_{oi} c_o^*} \right) \right]_{y=x_f} = \\ \frac{1}{\eta_{1i}} e^{-(c_\mu + c_{r1}) \Delta p_1} \frac{\partial}{\partial t} \left(\frac{1 - e^{-c_o^* \Delta p_1}}{\mu_{oi} B_{oi} c_o^*} \right) \end{aligned} \quad (2.46)$$

where η_{1i} is the diffusivity coefficient of region 1, evaluated at initial reservoir conditions, and defined (in oilfield units) as:

$$\eta_{1i} = 2.637 \times 10^{-4} \frac{k_{1i}}{\mu_{oi}(\phi_i c_t)_1} \quad (2.47)$$

where $c_{t1} = c_o + c_{r1}$ is the total compressibility of the SRV. Similar to the governing equation for the matrix (Equation 2.28), we can relax the strong nonlinearity posed by the exponential pressure-dependent terms onto the governing equation by assuming that these term can be evaluated at current average pressure-drawdown $\Delta \tilde{p}_1$, such that the directional dependency of these nonlinearities can be removed. In this sense, we will consider that

$$e^{-\gamma_1 \Delta p_1} \approx e^{-\gamma_1 \Delta \tilde{p}_1} \quad (2.48)$$

$$e^{-(c_\mu + c_{r1}) \Delta p_1} \approx e^{-(c_\mu + c_{r1}) \Delta \tilde{p}_1} \quad (2.49)$$

Replacing these approximations into Equation 2.46 and normalizing the resulting equation using Equation 2.9—2.14, yields

$$\frac{\partial^2 p_{1D}}{\partial x_D^2} + \left(\frac{\partial p_{1D}}{\partial y_D} \right)_{y_D=1} = \frac{1}{\lambda_1 \eta_{1D}} \frac{\partial p_{1D}}{\partial t_D} \quad (2.50)$$

The nonlinear scaling parameter λ_1 is defined as

$$\lambda_1 = e^{-(\gamma_1 - c_{r1} - c_\mu) \Delta \tilde{p}_1} \quad (2.51)$$

Similar to λ_2 (Equation 2.27), λ_1 is initially assumed to be equal to 1 and will be later computed iteratively. This procedure is discussed in detail in Section 2.8. If λ_1 is assumed to be constant, then Equation 2.50 can be transformed into Laplace domain, resulting in:

$$\frac{d^2 \bar{p}_{1D}}{dx_D^2} + \left(\frac{d\bar{p}_{1D}}{dy_D} \right)_{y_D=1} - \frac{s}{\lambda_1 \eta_{1D}} \bar{p}_{1D} = 0 \quad (2.52)$$

where $\bar{p}_{1D}(x_D, s) = \mathcal{L} \{p_{1D}(x_D, t_D)\}$. Finally, let us substitute $(d\bar{p}_{1D}/dy_D)_{y_D=1}$ from Equation 2.52 by the influx term defined in Equation 2.40, assuming that $(\bar{p}_{1D})_{y_D=1} \equiv \bar{p}_{1D}$ because $\bar{p}_{1D} \neq f(y_D)$. Consequently,

$$\frac{d^2 \bar{p}_{1D}}{dx_D^2} - c_1(s) \bar{p}_{1D} = 0 \quad (2.53)$$

where $c_1(s)$ is a flux-source function in Laplace domain, defined by:

$$c_1(s) = \frac{s}{\lambda_1 (\eta_i)_{1D}} - \frac{k_{2i}}{\delta_{21} k_{1i}} \sqrt{\frac{s}{\lambda_2 \eta_{2D}}} \tanh \left[(1 - y_{eD}) \sqrt{\frac{s}{\lambda_2 \eta_{2D}}} \right] \quad (2.54)$$

Recognize that, although not explicitly stated, $c_1(s)$ also depends on λ_1 , λ_2 and δ_{21} . Another relevant observation about $c_1(s)$ is that setting $\lambda_1 = \lambda_2 = \delta_{21} = 1$ yields the original function $c_1(s)$ proposed by Brown et al. (2011) for the trilinear flow model with constant rock properties. This conclusion suggests that λ and δ serve as a measurement of the degree of nonlinearity of the MFHW model when rock and fluid properties are exponentially pressure-dependent.

2.5.4.2 Analytical Solution

The canonical solution to Equation 2.53 in Laplace domain can be given as

$$\bar{p}_{2D} = A_1 \cosh \left[(x_D - x_{eD}) \sqrt{c_1(s)} \right] + B_1 \sinh \left[(x_D - x_{eD}) \sqrt{c_1(s)} \right] \quad (2.55)$$

According to Figure 2.5a, there is a no-flow boundary at the external boundary of the SRV (i.e. $x_D = x_{eD}$) due to symmetry, hence:

$$\left(\frac{d\bar{p}_{1D}}{dx_D} \right)_{x_D=x_{eD}} = 0 \quad (2.56)$$

Replacing this boundary condition into Equation 2.55 yields $B_1 = 0$. Consequently,

$$\bar{p}_{1D} = A_1 \cosh \left[(x_D - x_{eD}) \sqrt{c_1(s)} \right] \quad (2.57)$$

Similar to the governing equation for fluid-flow in the matrix, additional boundary conditions apply to Equation 2.57. These conditions are:

- (i) *Fracture skin damage.* We incorporate formation damage on the fracture surface in the form of fracture skin by considering fluid-flow across a region with $k_s < k_1$ [md] near the SRV/fracture interface. The depth of penetration of formation damage is denoted as w_s [ft]. Figure 2.10 illustrates the fracture skin model.

Given that w_s is orders-of-magnitude smaller than x_e we can safely assume that fluid-flow through the damage zone is steady-state. Therefore,

$$\left(\frac{k_1}{\mu B} \frac{\partial \Delta p_1}{\partial x} \right)_{x=w/2} = \frac{k_s}{\mu_{oi} B_{oi} w_s} (\Delta p_1 - \Delta p_f)_{x=w/2} \quad (2.58)$$

Realize that fracture skin only influences early-time pressure behavior. Moreover, the across-skin pressure differential $(\Delta p_1 - \Delta p_f)_{x=w/2}$ is relatively small at early time. Hence, we make the following approximation based on Equation 2.15:

$$(\Delta p_1 - \Delta p_f)_{x=w/2} \approx \left(\frac{1 - e^{-c_o^* \Delta p_1}}{c_o^*} - \frac{1 - e^{-c_o^* \Delta p_f}}{c_o^*} \right)_{x=w/2} \quad (2.59)$$

Furthermore, assume that $k_1 \approx k_{1i} e^{-\gamma_1 \Delta \bar{p}_1}$ and $k_s \approx k_{si} e^{-\gamma_1 \Delta \bar{p}_1}$. This allows both k_1 and k_s to change at the same rate with Δp_1 at $x_D = w_D/2$. Substitution of this assumption and further normalization of Equation 2.58 yields:

$$\frac{\partial}{\partial x_D} \left(\frac{1 - e^{-c_o^* \Delta p_1}}{\mu_{oi} B_{oi} c_o^*} \right)_{x_D=w_D/2} = \frac{k_{si} x_f}{k_{1i} w_s} \left(\frac{1 - e^{-c_o^* \Delta p_1}}{\mu_{oi} B_{oi} c_o^*} - \frac{1 - e^{-c_o^* \Delta p_f}}{\mu_{oi} B_{oi} c_o^*} \right)_{x_D=w_D/2} \quad (2.60)$$

Normalization and subsequent Laplace transformation of Equation 2.60 gives:

$$(\bar{p}_{1D})_{x_D=w_D/2} = (\bar{p}_{fD})_{x_D=w_D/2} + s_f \left(\frac{d\bar{p}_{1D}}{dx_D} \right)_{x_D=w_D/2} \quad (2.61)$$

where s_f is the fracture skin damage, defined as:

$$s_f = \frac{k_{1i} d_s}{k_{si} x_f} \quad (2.62)$$

where d_s [ft] is the depth of penetration of the formation damage.

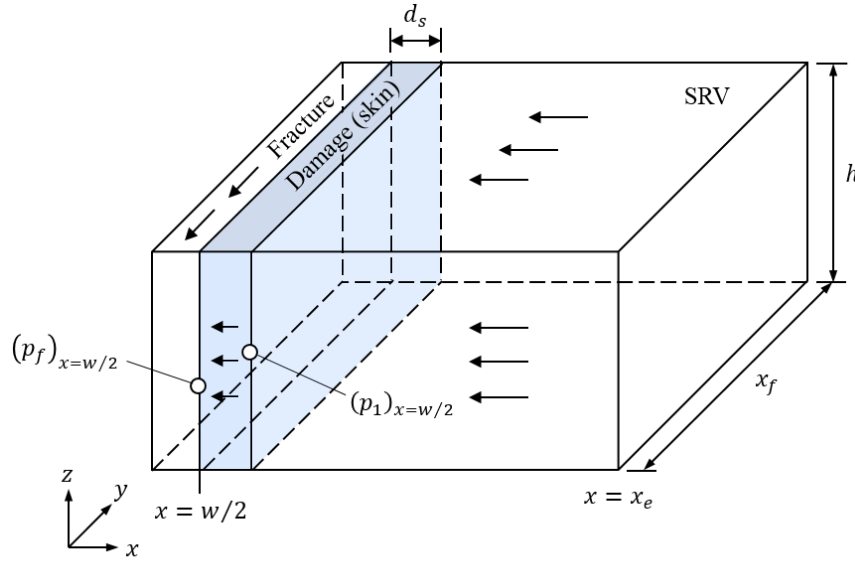


Figure 2.10: Skin damage across the SRV/interface located at $x = w/2$.

To determine the value of the integration constant A_1 , let us evaluate Equation 2.57 and its derivative with respect to x_D at $x_D = w_D/2$, which results in:

$$(\bar{p}_{1D})_{x_D=w_D/2} = A_1 \cosh \left[(w_D/2 - x_{eD}) \sqrt{c_1(s)} \right] \quad (2.63)$$

$$\left(\frac{d\bar{p}_{1D}}{dx_D} \right)_{x_D=w_D/2} = A_1 \sqrt{c_1(s)} \sinh \left[(w_D/2 - x_{eD}) \sqrt{c_1(s)} \right] \quad (2.64)$$

Combining Equation 2.63 and 2.64 with Equation 2.60 yields

$$A_1 = \frac{(\bar{p}_{fD})_{x_D=w_D/2}}{\cosh \left[(w_D/2 - x_{eD}) \sqrt{c_1(s)} \right] - s_f \sqrt{c_1(s)} \sinh \left[(w_D/2 - x_{eD}) \sqrt{c_1(s)} \right]} \quad (2.65)$$

Therefore,

$$\bar{p}_{1D} = \frac{(\bar{p}_{fD})_{x_D=w_D/2} \cosh \left[(x_D - x_{eD}) \sqrt{c_1(s)} \right]}{\cosh \left[(w_D/2 - x_{eD}) \sqrt{c_1(s)} \right] - s_f \sqrt{c_1(s)} \sinh \left[(w_D/2 - x_{eD}) \sqrt{c_1(s)} \right]} \quad (2.66)$$

$$\frac{d\bar{p}_{1D}}{dx_D} = \frac{(\bar{p}_{fD})_{x_D=w_D/2} \sqrt{c_1(s)} \sinh \left[(x_D - x_{eD}) \sqrt{c_1(s)} \right]}{\cosh \left[(w_D/2 - x_{eD}) \sqrt{c_1(s)} \right] - s_f \sqrt{c_1(s)} \sinh \left[(w_D/2 - x_{eD}) \sqrt{c_1(s)} \right]} \quad (2.67)$$

- (ii) *Flux continuity.* Mass must be conserved across the SRV/fracture interface. Therefore, based on Darcy's law, the flux-continuity boundary condition at $x_D = w_D/2$ is expressed as:

$$\left(\frac{\rho_o k_f}{\mu_o} \frac{\partial \Delta p_f}{\partial x_D} \right)_{x_D=w_D/2} = \left(\frac{\rho_o k_1}{\mu_o} \frac{\partial \Delta p_1}{\partial y_D} \right)_{x_D=w_D/2} \quad (2.68)$$

Using the pressure-dependent relationships for ρ (Equation 2.3), μ (Equation 2.4) and k (Equation 2.1), in addition to normalizing Δp_1 and Δp_f via Equation 2.9, leads to

$$\left(e^{-\gamma_f \Delta p_f} \frac{\partial p_{fD}}{\partial x_D} \right)_{x_D=w_D/2} = \frac{k_{1i}}{k_{fi}} \left(e^{-\gamma_1 \Delta p_1} \frac{\partial p_{1D}}{\partial x_D} \right)_{x_D=w_D/2} \quad (2.69)$$

Assume that $(k_f)_{x_D=w_D/2} \approx k_{fi} e^{-\gamma_f \Delta \bar{p}_f}$ and $(k_1)_{x_D=w_D/2} \approx k_{1i} e^{-\gamma_1 \Delta \bar{p}_1}$. In addition, use Equation 2.9 to normalize Δp_1 and Δp_f and transform the resulting equation into Laplace domain. The final result is given as follows:

$$\left(\frac{d\bar{p}_{fD}}{dx_D} \right)_{x_D=w_D/2} = \frac{k_{1i}}{k_{fi}} \frac{1}{e^{\gamma_1 \Delta \bar{p}_1 - \gamma_f \Delta \bar{p}_f}} \left(\frac{d\bar{p}_{1D}}{dx_D} \right)_{x_D=w_D/2} \quad (2.70)$$

For simplification purposes, we assume that oil flows linearly in the fracture along the y -axis. Thus, to eliminate the two-dimensional dependency near the SRV/fracture interface, we model flux across the interface based on a source-flux term. This flux-source term is found after replacing Equation 2.67 into 2.70:

$$\left(\frac{d\bar{p}_{fD}}{dx_D} \right)_{x_D=w_D/2} = \frac{k_{1i}/k_{fi}}{e^{\gamma_1 \Delta \bar{p}_1 - \gamma_f \Delta \bar{p}_f}} \frac{(\bar{p}_{fD})_{x_D=w_D/2} \sqrt{c_1(s)}}{\coth \left[(w_D/2 - x_{eD}) \sqrt{c_1(s)} \right] - s_f \sqrt{c_1(s)}} \quad (2.71)$$

Equation 2.71 will be implemented in the derivation of the governing equation for fluid-flow in the fracture, as discussed in the next subsection.

2.5.5 Fluid-flow Model for Fracture (Region f)

2.5.5.1 Governing Equation

The original TLF model considers a planar bi-wing fracture shaped as a rectangular slot filled with proppant. Fracture properties are assumed constant hence the geometry of the fracture is originally fixed. In reality, however, fracture width reduces over time as effective closure stress increases with pressure depletion (Smith and Montgomery, 2015).

In addition, fracture flow is considered linear along the y -axis, from the fracture tip toward the wellbore. Influx from the SRV is modeled using flux-source term approach. Based on these conditions, we carried out a mass balance over the differential control

volume $\Delta V_f = h\Delta y w/2$ located within the fracture. There are three mass fluxes associated with this control volume: \dot{m}_{in} at y , \dot{m}_{out} at $y - \Delta y$ and \dot{m}_1 at $x = w/2$, as shown by Figure 2.11. The mass balance over ΔV_f yields:

$$\dot{m}_{in} + \dot{m}_1 - \dot{m}_{out} = \frac{\partial}{\partial t} \left(\rho \phi_f h \Delta y \frac{w}{2} \right) \quad (2.72)$$

Be aware that the fracture width w is a function of Δp_f . Therefore, it cannot be taken out of any derivative without any prior assumption.

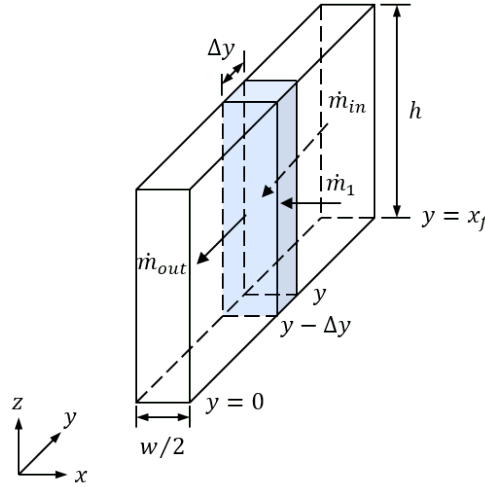


Figure 2.11: Mass balance across a differential control volume within the fracture.

Now, let us substitute $\dot{m}_{in} = (\rho_o v_y h w / 2)_y$, $\dot{m}_{out} = (\rho_o v_y h w / 2)_{y-\Delta y}$ and $\dot{m}_1 = (\rho_o v_x h \Delta y)_{x=w/2}$ into the mass balance equation. This results in:

$$\left(\rho_o v_y \frac{w}{2} h \right)_y - \left(\rho_o v_y \frac{w}{2} h \right)_{y-\Delta y} + (\rho_o v_x h \Delta y)_{x=w/2} = \frac{\partial}{\partial t} \left(\rho_o \phi_f h \Delta y \frac{w}{2} \right) \quad (2.73)$$

Dividing the equation above by $h\Delta y$ while allowing $\Delta y \rightarrow 0$, leads to

$$\frac{\partial}{\partial y} (\rho_o v_y w) + 2(\rho_o v_x)_{x=w/2} = \frac{\partial}{\partial t} (\rho_o \phi_f w) \quad (2.74)$$

Furthermore, $v_x = -(k_f / \mu_o)(\partial \Delta p_f / \partial x)$ and $v_y = -(k_f / \mu_o)(\partial \Delta p_f / \partial y)$. Substituting these expressions into the preceding equation, gives:

$$-\frac{\partial}{\partial y} \left(\frac{\rho k_f w}{\mu_o} \frac{\partial \Delta p_f}{\partial y} \right) - 2 \left(\frac{\rho_o k_f}{\mu_o} \frac{\partial \Delta p_f}{\partial x} \right)_{x=w/2} = \frac{\partial}{\partial t} (\phi_f \rho_o w) \quad (2.75)$$

Let us assume that w can be evaluated at current average drawdown such that $w \approx \tilde{w}$. Also, \tilde{w} can be taken out of any derivative if considered constant. In addition, inserting Equation 2.3, 2.6, and 2.1 into Equation 2.75, while simplifying the resulting expression, yields:

$$\begin{aligned} \frac{\partial}{\partial y} \left[e^{-d_f \Delta p_f} \frac{\partial}{\partial y} \left(\frac{1 - e^{-c_o^* \Delta p_f}}{\mu_{oi} B_{oi} c_o^*} \right) \right] + \frac{2}{\tilde{w}} \left[e^{-\gamma_f \Delta p_f} \frac{\partial}{\partial x} \left(\frac{1 - e^{-c_o^* \Delta p_f}}{\mu_{oi} B_{oi} c_o^*} \right) \right]_{x=w/2} = \\ \frac{e^{(c_{rf} - c_\mu) \Delta p_f}}{\eta_{fi}} \frac{\partial}{\partial t} \left(\frac{1 - e^{-c_o^* \Delta p_f}}{\mu_{oi} B_{oi} c_o^*} \right) \end{aligned} \quad (2.76)$$

As mentioned previously, \tilde{w} is the average fracture width at current time. The diffusivity coefficient η_{fi} is defined (in oilfield units) as:

$$\eta_{fi} = 2.637 \times 10^{-4} \frac{k_{fi}}{\mu_{oi} (\phi_i c_t)_f} \quad (2.77)$$

where $c_{tf} = c_o + c_{rf}$ is the total compressibility of the hydraulic fracture. Next, we proceed with relaxing the exponential terms inside the governing equation by assuming that they can be evaluated at current average pressure-drawdown $\Delta \tilde{p}_f$. Consequently,

$$e^{-d_f \Delta p_f} \approx e^{-d_f \Delta \tilde{p}_f} \quad (2.78)$$

$$e^{-\gamma_f \Delta p_f} \approx e^{-\gamma_f \Delta \tilde{p}_f} \quad (2.79)$$

$$e^{(c_{rf} - c_\mu) \Delta p_f} \approx e^{(c_{rf} - c_\mu) \Delta \tilde{p}_f} \quad (2.80)$$

Replacing these approximations into Equation 2.75 and normalizing the resulting equation using Equation 2.9—2.14, yields

$$\frac{\partial^2 p_{fD}}{\partial y_D^2} + \frac{2x_f}{\tilde{w}} \left(\frac{\partial p_{fD}}{\partial x_D} \right)_{x_D=w_D/2} = \frac{1}{\lambda_f \eta_{fD}} \frac{\partial p_{fD}}{\partial t_D} \quad (2.81)$$

The nonlinear scaling parameter λ_f is defined as:

$$\lambda_f = e^{-(\gamma_f - c_{rf} - c_\mu) \Delta \bar{p}_f} \quad (2.82)$$

Similar to λ_1 (Equation 2.51) and λ_2 (Equation 2.27), λ_f is initially assumed equal to 1 and will be later estimated iteratively, as discussed in Section 2.8. Furthermore, Equation 2.81 can be transformed into Laplace domain, under the assumption that λ_f is a constant, such that:

$$\frac{d^2 \bar{p}_{fD}}{dy_D^2} + \frac{2x_f}{\tilde{w}} \left(\frac{d\bar{p}_{fD}}{dx_D} \right)_{x_D=w_D/2} - \frac{s}{\lambda_f \eta_{fD}} \bar{p}_{fD} = 0 \quad (2.83)$$

where $\bar{p}_{fD}(y_D, s) = \mathcal{L} \{ p_{fD}(y_D, t_D) \}$. Finally, substitute $(d\bar{p}_{fD}/dx_D)_{x_D=w_D/2}$ by the influx term defined in Equation 2.71 while considering $(\bar{p}_{fD})_{x_D=w_D/2} \equiv \bar{p}_{fD}$ since $\bar{p}_{fD} \neq f(x_D)$. Hence,

$$\frac{d^2 \bar{p}_{fD}}{dy_D^2} - c_2(s) \bar{p}_{fD} = 0 \quad (2.84)$$

The Laplace-domain function $c_2(s)$ accounts for the influx from the SRV into the fracture. This function is defined as:

$$c_2(s) = \frac{s}{\lambda_f \eta_{fD}} - \frac{2\sqrt{c_1(s)}}{\delta_{1f} F_{CDi}} \tanh \left[(w_D/2 - x_{eD}) \sqrt{c_1(s)} \right] \quad (2.85)$$

where $F_{CDi} = C_{fi}/k_{1i}x_f$ is the initial dimensionless fracture conductivity. Moreover, δ_{1f} is a nonlinear scaling parameter arising at the SRV/fracture boundary, defined as:

$$\delta_{1f} = e^{\gamma_1 \Delta \bar{p}_1 - d_f \Delta \bar{p}_f} \quad (2.86)$$

Initially, $\delta_{1f} = 1$ and its actual value will be estimated iteratively. Also, be aware that $c_2(s)$ also depends on λ_f , δ_{1f} , λ_1 , λ_2 and δ_{21} .

Lastly, note that setting $\lambda_f = \lambda_1 = \lambda_2 = \delta_{1f} = \delta_{21} = 1$ leads to the original flux-source function $c_2(s)$ proposed by Brown et al. (2011) for constant rock and fluid properties.

2.5.5.2 Analytical Solution

The canonical solution to Equation 2.84 in Laplace domain can be given as

$$\bar{p}_{fD} = A_f \cosh \left[(y_D - 1) \sqrt{c_2(s)} \right] + B_f \sinh \left[(y_D - 1) \sqrt{c_2(s)} \right] \quad (2.87)$$

Because the fracture tip is assumed to be sealing, there is a no-flow boundary condition at $y_D = 1$, as shown in Figure 2.5a. Therefore,

$$\left(\frac{d\bar{p}_{fD}}{dy_D} \right)_{y_D=1} = 0. \quad (2.88)$$

Substitution of this boundary condition into Equation 2.84 yields $B_f = 0$ thus

$$\bar{p}_{fD} = A_f \cosh \left[(y_D - 1) \sqrt{c_2(s)} \right] \quad (2.89)$$

Furthermore, A_f depends on the production scenario under study. The next section discusses the case for constant-rate production (Section 2.6).

2.6. Pressure Transient Analysis for Constant-rate Production

The constant-rate well boundary condition for a quarter-fractured stage of the MFHW, as depicted in Figure 2.5a, is given as follows (in oilfield units):

$$q' = - \left(\frac{h}{141.2\pi\mu B} \frac{C_f}{x_f} \frac{\partial \Delta p_f}{\partial y_D} \right)_{y_D=0} \quad (2.90)$$

q' is the equivalent per-fracture rate of the well, defined as:

$$q' = \frac{q_{\text{well}}}{n_f} \quad (2.91)$$

where q_{well} and n_f are the actual production rate and number of fractured stages, respectively. Notice that a rather significant assumption made in the definition of q' is that **all** fractures are active and contribute equally to the total production of the well. Nonetheless, it may occur that well productivity is being sustained by only a few fractures. In such cases, a more accurate definition for q' would be as follows:

$$q' = \frac{q_{\text{well}}}{n_f \delta_p} \quad (2.92)$$

where $\delta_p = n_a/n_f$ is the ratio of active fractures (n_a) to total fractures (n_f). Thence, by definition, $0 < \delta_p \leq 1$. The implementation of q' as in Equation 2.92 would enable the detection of underperforming wells and actual fraction of active fractures. For the purpose of the subsequent analyses, we will assume $\delta_p = 1$.

Inserting the pressure-dependent definitions of μ_o (Equation 2.4), B_o (Equation 2.5) and C_f (Equation 2.2) into Equation 2.90, multiplying the right-hand side by k_{1i}/k_{1i} , normalizing Δp_f using Equation 2.9, and rearranging terms, gives:

$$-\frac{\pi}{F_{CDi}} = \left(e^{-d_f \Delta p_f} \frac{\partial p_{fD}}{\partial y_D} \right)_{y_D=0} \quad (2.93)$$

Let us assume that $(e^{-d_f \Delta p_f})_{y_D=0} \approx e^{-\beta d_f \Delta \tilde{p}_f}$. This approximation leads to the definition of the nonlinear scaling parameter δ_w :

$$\delta_w = e^{-d_f \beta \Delta \tilde{p}_f} \quad (2.94)$$

β is a correction factor that accounts for actual changes in $e^{-d_f \Delta p_f}$ near the wellbore. Similar to the other nonlinear parameters, δ_w is assumed equal to 1 initially and is subsequently calculated iteratively (see Section 2.8). Replacing Equation 2.94 into 2.93, yields:

$$\left(\frac{\partial p_{fD}}{\partial y_D}\right)_{y_D=0} = -\frac{\pi}{\delta_w F_{CDi}} \quad (2.95)$$

Taking the Laplace transform of Equation 2.95 gives the constant-rate well boundary condition that allows to determine A_f from Equation 2.89:

$$\left(\frac{d\bar{p}_{fD}}{dy_D}\right)_{y_D=0} = -\frac{\pi}{s\delta_w F_{CDi}} \quad (2.96)$$

Replacing the result above into the derivative of \bar{p}_{fD} with respect to y_D in Equation 2.89, yields the dimensionless pressure-drawdown distribution in the fracture:

$$\bar{p}_{fD} = \frac{\pi}{\delta_w F_{CDi}} \frac{\cosh \left[(y_D - 1) \sqrt{c_2(s)} \right]}{s \sqrt{c_2(s)} \sinh \sqrt{c_2(s)}} \quad (2.97)$$

2.6.1 Bottomhole Pressure (BHP)

As illustrated by Figure 2.12, fluid pressure at the wellbore of a fractured stage p_{bh} [psi] is equal to the fracture pressure at the origin (i.e. $y = 0$) minus the sum of all pressure drops occurring within the fracture as fluid flows into the well. This condition can be mathematically expressed as

$$p_{bh} = p_i - \Delta p_{wf} - \Delta p_s \quad (2.98)$$

where Δp_{wf} is the pressure drop due to linear flow along the fracture and Δp_s is the additional pressure drop due to flow convergence towards the wellbore (Economides et al., 2013). To derive Δp_{wf} , first evaluate Equation 2.97 at the wellbore ($y_D = 0$) to get

$$\bar{p}_{wD} = \frac{\pi}{\delta_w F_{CDi}} \frac{\coth \sqrt{c_2(s)}}{s \sqrt{c_2(s)}} \quad (2.99)$$

Then, let us invert Equation 2.99 back into time domain and use Equation 2.9 to convert the dimensionless result into units of pressure. This procedure gives

$$\Delta p_{wf} = -\frac{1}{c_o^*} \ln \left(1 - c_o^* \frac{141.2\pi q' \mu_{oi} B_{oi}}{\delta_w F_{CDi} k_{1i} h} \mathcal{L}^{-1} \left\{ \frac{\coth \sqrt{c_2(s)}}{s \sqrt{c_2(s)}} \right\} \right) \quad (2.100)$$

On the other hand, Δp_s is defined (in oilfield units) as (e.g. Economides et al., 2013)

$$\Delta p_s = \frac{141.2q' \mu_{oi} B_{oi}}{C_{fi}} \left[\ln \left(\frac{h}{2r_w} \right) - \frac{\pi}{2} \right] \quad (2.101)$$

where r_w [ft] is the wellbore radius. Combining Equation 2.100 and 2.101 with Equation 2.98, leads to

$$p_{bh} = p_i + \frac{1}{c_o^*} \ln \left(1 - c_o^* \frac{141.2\pi q' \mu_{oi} B_{oi}}{\delta_w F_{CDi} k_{1i} h} \mathcal{L}^{-1} \left\{ \frac{\coth \sqrt{c_2(s)}}{s \sqrt{c_2(s)}} \right\} \right) - \frac{141.2q' \mu_{oi} B_{oi}}{C_{fi}} \left[\ln \left(\frac{h}{2r_w} \right) - \frac{\pi}{2} \right] \quad (2.102)$$

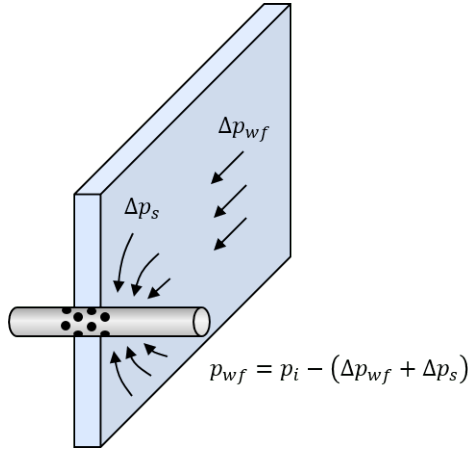


Figure 2.12: Combined pressure drop near the wellbore.

Equation 2.102 suggests that choking skin effects may be neglected when $x_f \gg h$. Contrariwise, this effect is significant when $h \gg x_f$. Nonetheless, the effect of flow convergence will only influence transient pressure response at early time. Additionally, Δp_s does not influence transient pressure-derivative behavior because Δp_s is approximately constant.

When fluid density and viscosity changes with pressure are negligible (i.e. $c_o^* < 10^{-6}$ psi⁻¹) and/or fractional changes in fracture conductivity with pressure-drawdown are

considerably large (i.e. $d_f \gg c_o^*$), Equation 2.102 can be linearized as

$$p_{bh} = p_i - \frac{141.2q'\mu_{oi}B_{oi}}{F_{CDi}k_{1i}h} \left\{ \frac{\pi}{\delta_w} \mathcal{L}^{-1} \left\{ \frac{\coth \sqrt{c_2(s)}}{s\sqrt{c_2(s)}} \right\} + \frac{h}{x_f} \left[\ln \left(\frac{h}{2r_w} \right) - \frac{\pi}{2} \right] \right\} \quad (2.103)$$

The above expression can be verified by means of the following limit:

$$\lim_{c_o^* \rightarrow 0} \left\{ \frac{1}{c_o^*} \ln(1 \pm c_o^* f(t)) \right\} = \pm f(t) \quad (2.104)$$

In practice, $c_o^* < 10^{-6} \text{ psi}^{-1}$ is sufficient to comply with the condition $c_o^* \rightarrow 0$. Furthermore, we define the rate-normalized pressure (RNP) as follows:

$$\text{RNP}(t) = \frac{p_i - p_{bh}(t)}{q'} \quad (2.105)$$

It is noteworthy to highlight that the actual definition of RNP' (Equation 1.2) is not so straightforward because all nonlinear scaling parameters λ and δ are time-dependent. The formal definition of RNP' is:

$$\begin{aligned} \frac{d\text{RNP}}{d \ln t} = & \frac{\partial(\Delta p_{bh}/q_{\text{well}})}{\partial \ln t} + \frac{t}{q_{\text{well}}} \left[\frac{\partial \Delta p_{bh}}{\partial \lambda_1} \frac{\partial \lambda_1}{\partial \Delta \tilde{p}_1} \frac{d\Delta \tilde{p}_1}{dt} + \frac{\partial \Delta p_{bh}}{\partial \lambda_2} \frac{\partial \lambda_2}{\partial \Delta \tilde{p}_2} \frac{d\Delta \tilde{p}_2}{dt} \right. \\ & + \frac{\partial \Delta p_{bh}}{\partial \lambda_f} \frac{\partial \lambda_f}{\partial \Delta \tilde{p}_f} \frac{d\Delta \tilde{p}_f}{dt} + \frac{\partial \Delta p_{wf}}{\partial \delta_w} \frac{\partial \delta_w}{\partial \Delta \tilde{p}_f} \frac{d\Delta \tilde{p}_f}{dt} \\ & \left. + \frac{\partial \Delta p_{bh}}{\partial \delta_{1f}} \left(\frac{\partial \delta_{1f}}{\partial \Delta \tilde{p}_f} \frac{d\Delta \tilde{p}_f}{dt} + \frac{\partial \delta_{1f}}{\partial \Delta \tilde{p}_1} \frac{d\Delta \tilde{p}_1}{dt} \right) + \frac{\partial \Delta p_{bh}}{\partial \delta_{21}} \left(\frac{\partial \delta_{21}}{\partial \Delta \tilde{p}_1} \frac{d\Delta \tilde{p}_1}{dt} + \frac{\partial \delta_{21}}{\partial \Delta \tilde{p}_2} \frac{d\Delta \tilde{p}_2}{dt} \right) \right] \quad (2.106) \end{aligned}$$

This equation is very intricate and impractical for well-test analysis purposes. In Section 2.8 we propose a more practical approach to estimate RNP' using converged values of RNP.

2.6.2 Well Flowing Pressure (FWP)

Bottomhole pressure (BHP) typically refers to pressure-transient data gathered at the sandface of the well. Conversely, well flowing pressure, or simply flowing pressure (FWP), refers to pressure-transient data collected at any location of the well. The reason why BHP data is preferred over FWP data in conventional wells is that BHP eliminates the effect of fluid expansion in the wellbore, known as wellbore storage (WBS) (e.g. Agarwal et al., 1970; Chen and Brigham, 1978).

Even if downhole pressure gauges are used to collect data from MFHWs, chances are that pressure-transient response will be distorted by fluid expansion along the lateral length of the well (heel to toe). In fact, it may be challenging to determine the best possible location for placing downhole gauges for well testing purposes. Therefore, it is imperative to account for WBS effects into the proposed analytical MFHW.

The normalized FWP p_{wD} can be determined analytically using the following relationship in Laplace domain (e.g Spivey and Lee, 2013):

$$p_{wD} = \mathcal{L}^{-1} \left\{ \frac{\bar{p}_{wD} + \bar{p}_{sD}}{1 + s^2 C_D (\bar{p}_{wD} + \bar{p}_{sD})} \right\} \quad (2.107)$$

\bar{p}_{wD} is given by Equation 2.99. C_D is the dimensionless wellbore storage coefficient, defined as (oilfield units) (Brown, 2009):

$$C_D = \frac{5.615C}{2\pi(\phi_i c_t)_1 h x_f^2} \quad (2.108)$$

The definition of C_D is based on a per-fracture rate normalization of pressure. If pressure is normalized using total well rate (i.e. q_{well}) then Equation 2.108 must be divided by n_f^2 . The reason for this modification is $q' \propto x_f$ consequently $q_{\text{well}} \propto n_f x_f$. Moreover, the normalized pressure drop due to choking skin effects is defined in Laplace domain as:

$$p_{sD} = \frac{k_{1i} h}{141.2 q' \mu_{oi} B_{oi} c_o^*} \left(1 - e^{-c_o^* \frac{141.2 q' \mu_{oi} B_{oi}}{k_{1i} h} \frac{h}{F_{CDi} x_f} \ln \left[\left(\frac{h}{2r_w} \right) - \frac{\pi}{2} \right]} \right) \quad (2.109)$$

Since p_{sD} is usually small, it can be approximated as:

$$p_{sD} \approx \frac{h}{x_f F_{CDi}} \ln \left[\left(\frac{h}{2r_w} \right) - \frac{\pi}{2} \right] \quad (2.110)$$

Note that rock and fluid properties are still pressure-dependent thus WBS should take this into account. Nonetheless, pressure-drawdown is quite small at early time so that variations in ρ_o are negligible. Therefore, Equation 2.107 must hold valid during the period dominated by WBS effects.

Substitution of Equation 2.99 and 2.110 into Equation 2.107 yields:

$$\bar{p}_{wD} + \bar{p}_{sD} = \frac{1}{sF_{CDi}} \left\{ \frac{\pi \coth \sqrt{c_2(s)}}{\delta_w \sqrt{c_2(s)}} + \frac{h}{x_f} \ln \left[\left(\frac{h}{2r_w} \right) - \frac{\pi}{2} \right] \right\} \quad (2.111)$$

Combining Equation 2.107 with 2.9, results in:

$$p_{wf}(t) = p_i + \frac{1}{c_o^*} \ln \left(1 - c_o^* \frac{141.2q' \mu_{oi} B_{oi}}{k_{1i} h} \mathcal{L}^{-1} \left\{ \frac{\bar{p}_{wD} + \bar{p}_{sD}}{1 + C_D s^2 (\bar{p}_{wD} + \bar{p}_{sD})} \right\} \right) \quad (2.112)$$

If $c_o^* < 10^{-6} \text{ psi}^{-1}$, then

$$p_{wf}(t) = p_i - \frac{141.2q' \mu_{oi} B_{oi}}{k_{1i} h} \mathcal{L}^{-1} \left\{ \frac{\bar{p}_{wD} + \bar{p}_{sD}}{1 + C_D s^2 (\bar{p}_{wD} + \bar{p}_{sD})} \right\} \quad (2.113)$$

2.7. Estimation of Average Pressure-Drawdown

We implement an integral-average approach to estimate the normalized average pressure-drawdown in region j . The mathematical definition of $\mathcal{L}\{\bar{p}_{jD}\}$ is given in Laplace domain as follows:

$$\mathcal{L}\{\bar{p}_{jD}\} = \frac{1}{\theta_2 - \theta_1} \int_{\theta_1}^{\theta_2} \bar{p}_{jD}(\theta, s) d\theta \quad (2.114)$$

where θ , θ_1 and θ_2 are the direction of flow and boundaries of region j , respectively.

2.7.1 Fracture

Let us replace $j = f$, $\theta = y_D$, $\theta_1 = 0$ and $\theta_2 = 1$ in Equation 2.114. Moreover, we must include the dimensionless pressure loss due to choking skin at the wellbore. In this manner, $\mathcal{L}\{\bar{p}_{fD}\}$ is defined as:

$$\mathcal{L}\{\bar{p}_{fD}\} = \int_{\theta_1=0}^{\theta_2=1} \left\{ \frac{\pi}{\delta_w F_{CDi}} \frac{\cosh[(\theta - 1)\sqrt{c_2(s)}]}{s\sqrt{c_2(s)} \sinh \sqrt{c_2(s)}} + \frac{s_c}{s} \delta(\theta) \right\} d\theta \quad (2.115)$$

where $\delta(\theta)$ indicates that the choking skin only exists at the wellbore ($\theta = 0$). Integration of the equation above yields:

$$\mathcal{L}\{\bar{p}_{fD}\} = \frac{1}{\delta_w F_{CDi}} \frac{\pi + s_c \delta_w F_{CDi} c_2(s)}{s c_2(s)} \quad (2.116)$$

Combining this result with Equation 2.9

$$\Delta \bar{p}_f(t) = -\frac{1}{c_o^*} \ln \left(1 - c_o^* \frac{141.2 q' \mu_{oi} B_{oi}}{\delta_w F_{CDi} k_{1i} h} \mathcal{L}^{-1} \left\{ \frac{\pi + s_c \delta_w F_{CDi} c_2(s)}{s c_2(s)} \right\} \right) \quad (2.117)$$

2.7.2 SRV

Normalized pressure in the SRV is given, in Laplace domain, by Equation 2.66 in Laplace domain. Yet, the term $(\bar{p}_{fD})_{x_D=w_D/2}$ on the right-hand side of the equation cannot be analytically determined because of the assumption of linear flow along the y -axis. To resolve this issue, we assume that pressure at the SRV/fracture interface is approximately equal to the average pressure in the fracture. Thus, $(\bar{p}_{fD})_{x_D=w_D/2} \approx \mathcal{L}\{\bar{p}_{fD}\}$. Replacing $(\bar{p}_{fD})_{x_D=w_D/2}$ by $\mathcal{L}\{\bar{p}_{fD}\}$ in Equation 2.66, yields:

$$\bar{p}_{1D} = \frac{\left(\frac{\pi + s_c \delta_w F_{CDi} c_2(s)}{\delta_w F_{CDi} s c_2(s)} \right) \cosh \left[(x_D - x_{eD}) \sqrt{c_1(s)} \right]}{\cosh \left[(w_D/2 - x_{eD}) \sqrt{c_1(s)} \right] + s_f \sqrt{c_1(s)} \sinh \left[(w_D/2 - x_{eD}) \sqrt{c_1(s)} \right]} \quad (2.118)$$

Substitution of Equation 2.118 into Equation 2.114 with $j = 1$, $\theta = x_D$, $\theta_1 = w_D/2$ and

$\theta_2 = x_{eD}$, while recognizing that $x_{eD} - w_D/2 \approx x_{eD}$, gives

$$\mathcal{L}\{\tilde{p}_{1D}\} = \frac{F_1(s)}{\delta_w F_{CDi} x_{eD}} \quad (2.119)$$

where

$$F_1(s) = \frac{\pi + s_c \delta_w F_{CDi} c_2(s)}{s c_2(s) \sqrt{c_1(s)} \left\{ \coth \left(x_{eD} \sqrt{c_1(s)} \right) - s_f \sqrt{c_1(s)} \right\}} \quad (2.120)$$

Finally, the average pressure-drawdown in the SRV is given by:

$$\Delta \tilde{p}_1(t) = -\frac{1}{c_o^*} \ln \left(1 - c_o^* \frac{141.2 q' \mu_{oi} B_{oi}}{\delta_w F_{CDi} k_{1i} h x_{eD}} \mathcal{L}^{-1} \{F_1(s)\} \right) \quad (2.121)$$

2.7.3 Matrix

Similar to the SRV region, $(\bar{p}_{1D})_{y_D=1}$ cannot be explicitly determined because of the linear flow assumption made when deriving \bar{p}_{1D} . Yet, we can make the approximation $(\bar{p}_{1D})_{y_D=1} \approx \mathcal{L}\{\tilde{p}_{1D}\}$. Replacing Equation 2.119 into 2.35 yields:

$$\bar{p}_{2D} = \frac{1}{\delta_w F_{CDi} x_{eD}} \frac{F_1(s) \cosh \left[(y_{eD} - y_D) \sqrt{\frac{s}{\lambda_2 \eta_{2D}}} \right]}{\cosh \left[(y_{eD} - 1) \sqrt{\frac{s}{\lambda_2 \eta_{2D}}} \right]} \quad (2.122)$$

Replacing Equation 2.122 into Equation 2.114 with $j = 2$, $\theta = y_D$, $\theta_1 = 1$ and $\theta_2 = y_{eD}$ yields:

$$\mathcal{L}\{\tilde{p}_{2D}\} = \frac{F_2(s)}{\delta_w F_{CDi} x_{eD} (y_{eD} - 1)} \quad (2.123)$$

where

$$F_2(s) = \frac{F_1(s) \sqrt{\lambda_2 \eta_{2D}}}{\sqrt{s}} \tanh \left[(y_{eD} - 1) \sqrt{\frac{s}{\lambda_2 \eta_{2D}}} \right] \quad (2.124)$$

Finally,

$$\Delta \tilde{p}_2(t) = -\frac{1}{c_o^*} \ln \left(1 - c_o^* \frac{141.2q' \mu_{oi} B_{oi}}{\delta_w F_{CDi} k_{1i} h x_{eD} (y_{eD} - 1)} \mathcal{L}^{-1} \{F_2(s)\} \right) \quad (2.125)$$

2.8. Iterative Solution Algorithm

In this section, we introduce the successive substitution iterative algorithm which enables the estimation of the nonlinear scaling parameters λ and δ at current time t . Here, we use t^n and $t^{n+1} = t + \Delta t$ to represent previous and current time steps, respectively. The iterative procedure explained next is based on current-time estimations, hence the superscript $n + 1$ will be dropped. The superscripts v and $v + 1$ denote current and previous iteration level, respectively.

The iterative algorithm is initialized by setting $\lambda_f^v = \lambda_1^v = \lambda_2^v = \delta_w^v = \delta_{1f}^v = \delta_{21}^v = 1$, at iteration level $v = 0$. This results in $\Delta \tilde{p}_f^v = \Delta \tilde{p}_1^v = \Delta \tilde{p}_2^v = 0$. Next, $\Delta \tilde{p}_f^{v+1}$, $\Delta \tilde{p}_1^{v+1}$ and $\Delta \tilde{p}_2^{v+1}$ are estimated using Equation 2.117, 2.121 and 2.125, respectively. This result is subsequently used to λ_f^{v+1} (Equation 2.82), λ_1^{v+1} (Equation 2.51), λ_2^{v+1} (Equation 2.27), δ_w^{v+1} (Equation 2.94), δ_{1f}^{v+1} (Equation 2.86) and δ_{21}^{v+1} (Equation 2.39). Finally, we estimate the relative error ε at current iteration level $v + 1$, using the following equation:

$$\varepsilon^{(v+1)} = \max \left\{ \left| \frac{\lambda_j^{(v+1)} - \lambda_j^{(v)}}{\lambda_j^{(v)}} \right|, \left| \frac{\delta_w^{(v+1)} - \delta_w^{(v)}}{\delta_w^{(v)}} \right|, \left| \frac{\delta_{1f}^{(v+1)} - \delta_{1f}^{(v)}}{\delta_{1f}^{(v)}} \right|, \left| \frac{\delta_{21}^{(v+1)} - \delta_{21}^{(v)}}{\delta_{21}^{(v)}} \right| \right\} \quad (2.126)$$

where $j = f, 1, 2$. The iterative algorithm would have achieved convergence when $\varepsilon^{v+1} \leq \text{tol}$ where tol is a certain tolerance level, which we set to 10^{-5} .

Once the iterative algorithm has converged for current time step calculations, we use converged values of λ_j^{v+1} , δ_w^{v+1} and δ_{jk}^{v+1} to estimate either BHP^{n+1} (Equation 2.102) or FWP^{n+1} (Equation 2.112). Rate-normalized pressure-derivative is estimated as:

$$\text{RNP}^{n+1} = \frac{1}{q'} \left(\frac{\Delta p_{wf}^{n+1} - \Delta p_{wf}^n}{\ln t^{n+1} - \ln t^{n-1}} \right) \quad (2.127)$$

The main drawback of this method is that Δp_{wf}^{n+1} must be computed for fairly small time steps in order to get representative values for RNP' that would allow the identification of flow regimes and other features by means of PTA diagnostic plots. Furthermore, average properties in the composite system can be estimated as follows:

$$\tilde{k}_j = k_{ji} e^{-\gamma_j \Delta \bar{p}_j(t)} \quad (2.128)$$

$$\tilde{\phi}_j = \phi_{ji} e^{-c_{rj} \Delta \bar{p}_j(t)} \quad (2.129)$$

$$\tilde{C}_f = C_{fi} e^{-d_f \Delta \bar{p}_f} \quad (2.130)$$

$$\tilde{F}_{CD} = \frac{\tilde{C}_f}{\tilde{k}_1 x_f} \quad (2.131)$$

The pseudo-code of the iteration algorithm is presented in Figure 2.13. For efficiency purposes, we suggest using λ_j^{v+1} , δ_w^{v+1} and δ_{jk}^{v+1} as the initial guesses for the subsequent time step. That is, $\lambda_j^{v,n+1} = \lambda_j^{v+1,n}$, $\delta_w^{v,n+1} = \delta_w^{v+1,n}$, $\delta_{1f}^{v,n+1} = \delta_{1f}^{v+1,n}$ and $\delta_{21}^{v,n+1} = \delta_{21}^{v+1,n}$.

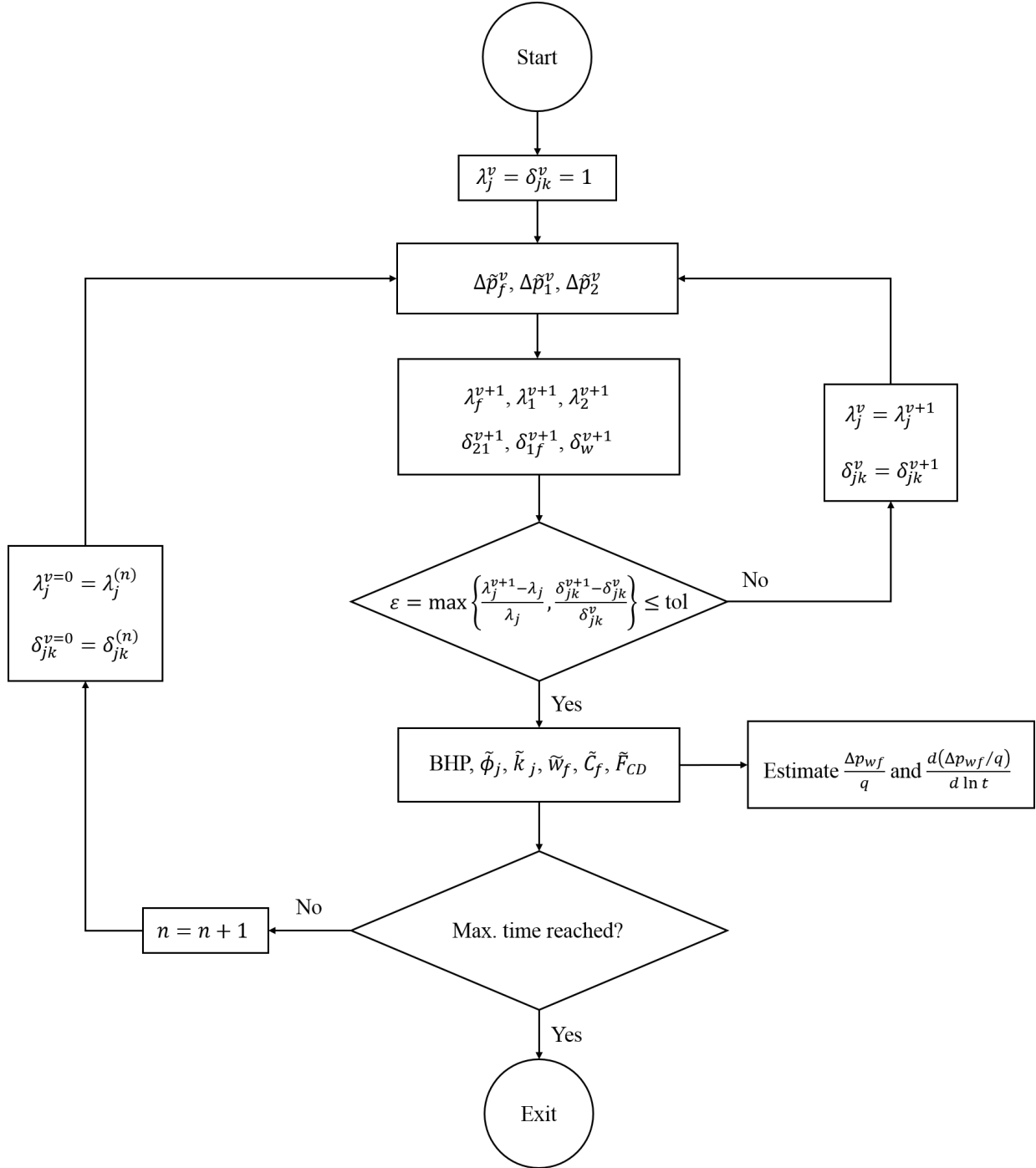


Figure 2.13: Iterative algorithm to solve the nonlinear flow problem.

2.9. Validation Cases

We setup a numerical simulation model of a MFHW with 20 fractured stages flowing at $q_{\text{well}} = 400$ STB/D or $q' = 20$ STB/D/fracture. Wellbore radius is $r_w = 0.25$ ft. We make the following assumptions about the MFHW model: (1) single-phase oil flow, (2) constant and uniform initial reservoir pressure, (3) reservoir rock volume between fractures is fully stimulated, (4) WBS effects are ignored ($C_D = 0$), and (5) stress-dependent rock properties are accurately represented by exponential functions of local pressure-drawdown.

The 3-D simulation model was built on CMG IMEX. The numerical model features a mesh refinement near the SRV/fracture interface to avoid potential numerical convergence issues due to sudden changes in flow direction and highly contrasting permeability values varying with pressure decline.

Reservoir properties are adapted from the lower Eagle Ford shale (Orangi et al., 2011; Cerón et al., 2013). Fracture width is considered constant. Table 2.1 summarizes reservoir (matrix), SRV and fracture properties used in this section. These properties are given at initial reservoir conditions ($p_i = 6500$ psi). Given that $k_f \propto w^2$ then we can safely assume that $\gamma_f \approx d_f$.

We examine two validation case studies in which we examine the effect of rock compressibility, permeability modulus and stress-dependent characteristic number on MFHW performance. Pressure-dependent properties of the MFHW are given in Table 2.2. In addition, we neglect fracture skin damage in the aforementioned case studies. We benchmark the analytical solution to synthetic pressure data and discuss the following comparison plots:

- Bottomhole pressure (BHP)
- Rate-normalized pressure (RNP) and pressure-derivative (RNP')
- Evolution of fractional reduction in permeability and fracture conductivity

Analysis of results show that the proposed analytical solution is in excellent agreement with numerical data (see Figure 2.14). Likewise, RNP and RNP' responses are in excellent agreement with simulation results. The maximum number of iterations per time step was 4.

Table 2.1: Composite system properties used in the validation cases.

Reservoir properties	
Matrix permeability, k_{2i} [md]	0.00073
Matrix porosity, ϕ_{2i} [—]	0.049
SRV permeability, k_{1i} [md]	1
SRV porosity, ϕ_{1i} [—]	0.1
Net pay thickness, h [ft]	100
Reservoir width, $2y_e$ [ft]	2000
Initial reservoir pressure, p_i [psi]	6500
Oil properties	
API density	42
Formation volume factor, B_{oi} [rb/STB]	1.3534
Viscosity, μ_{oi} [cP]	0.58
Compressibility, c_o [psi ⁻¹]	4.8×10^{-6}
Bubble-point pressure, p_{bp} [psi]	1000
Hydraulic fracture properties	
Fracture conductivity, C_{fi} [md-ft]	500
Proppant pack porosity, ϕ_{fi} [—]	0.35
Distance between fractured stages, $2x_e$ [ft]	500
Fracture half-length, x_f [ft]	200

Table 2.2: Pressure-dependent properties used in the numerical validation study.

Property	Matrix	SRV	Fracture	
			Case Study 1	Case Study 2
Rock compressibility, c_r [psi ⁻¹]	5×10^{-7}	1×10^{-6}	1×10^{-4}	1×10^{-4}
Permeability modulus, γ [psi ⁻¹]	2×10^{-6}	5×10^{-5}	—	—
Stress-sensitive number, d_f [psi ⁻¹]	—	—	8×10^{-4}	1×10^{-3}

PTA diagnostic plots for Case Studies 1 and 2 are presented in Figure 2.15 and 2.16, respectively. For both cases, we observe the typical transient response from a MFHW:

- Bilinear flow (fracture + SRV). Characterized by a 1/4-slope in the RNP'.
- Linear flow (SRV). A 1/2-slope in RNP' indicates the occurrence of this regime.
- Transitional flow (SRV + matrix). Often called boundary-dominated flow (BDF). Identified by the \sim unit slope and matching RNP and RNP'.

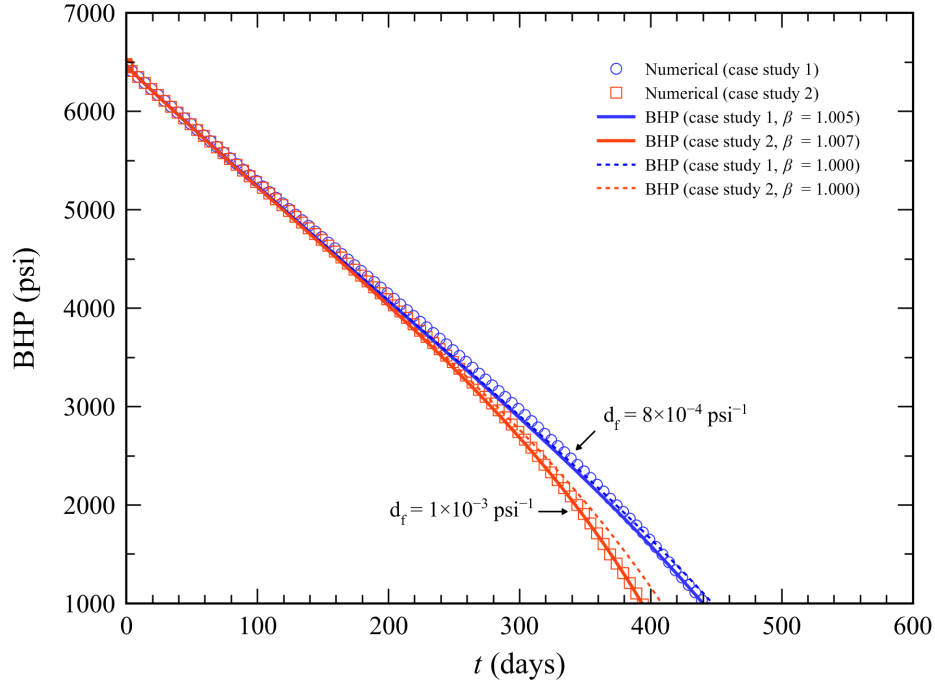


Figure 2.14: Transient BHP response for Case Studies 1 and 2.

In addition to the flow regimes typically encountered in the analysis of MFHW performance, we found a fourth flow regime marked by a rapid nonlinear separation between the RNP and RNP' taking place at late time ($t \approx 160$ days), which indicates the onset of severe loss of fracture conductivity and SRV permeability with pressure decline. This means that, up to that time, and even though initial fracture conductivity had been considerably lost, it would still be enough to produce oil at the prescribed constant per-fracture rate.

The onset of pressure-dependent effect is seen in Figure 2.14 as the kick-off point where the BHP curves depart from each other. In essence, we conclude that stress-dependent effects due to γ_1 and d_f , given the values from Table 2.2, are negligible for $t < 160$ days; however, they strongly dominate pressure-transient response when $t > 160$ days. In other words, if the MFHW was set to produce at constant rate for 160 days then stress-dependency effects on fracture conductivity would not be relevant.

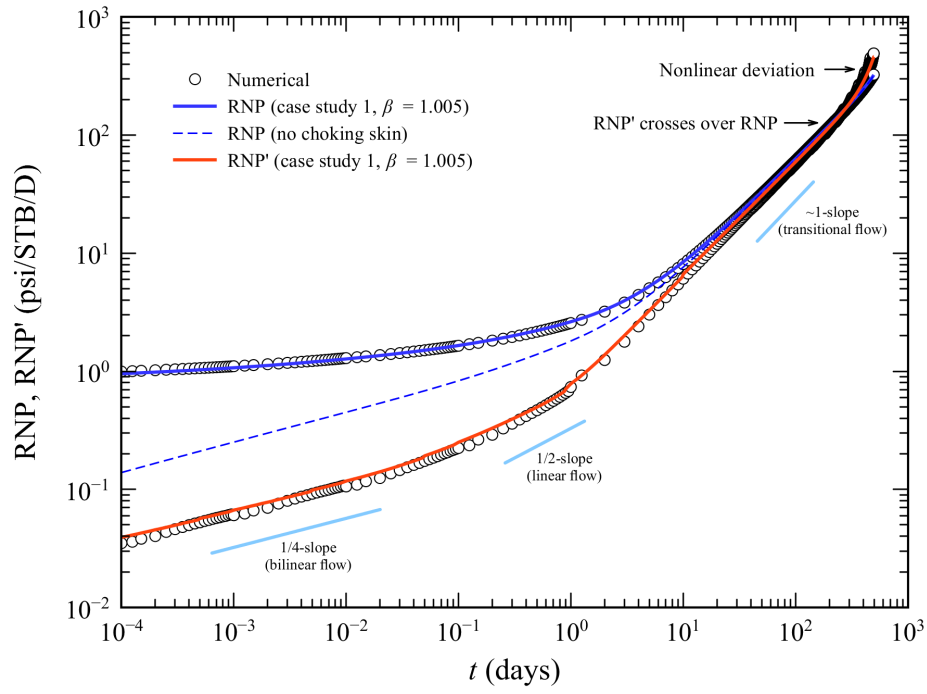


Figure 2.15: Rate-normalized diagnostic plot for Case Study 1.

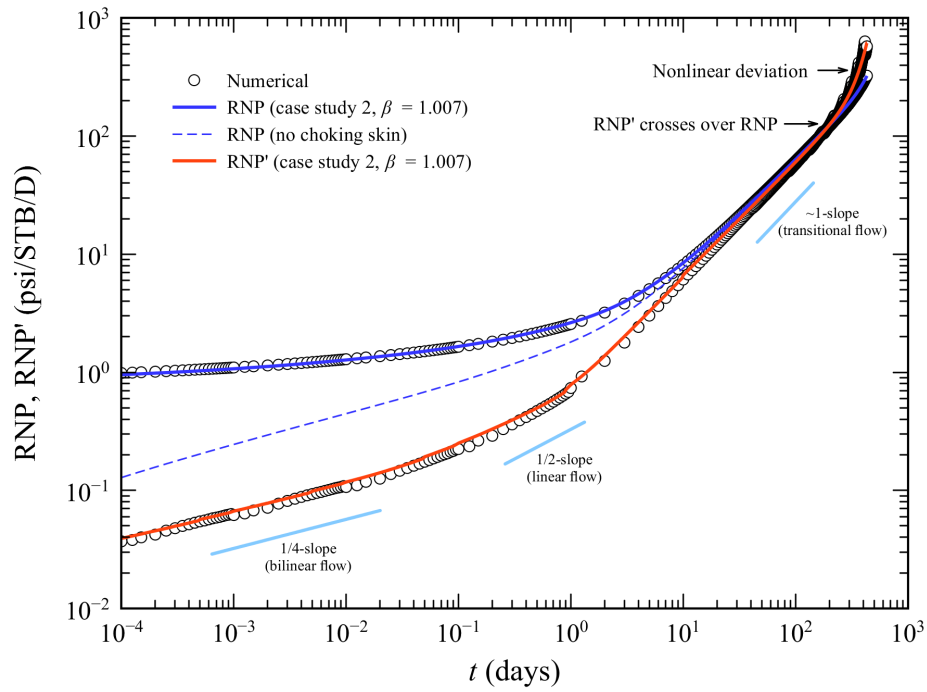


Figure 2.16: Rate-normalized diagnostic plot for Case Study 2.

An important matter due to pressure-dependent fracture conductivity and SRV permeability is how to accurately forecast well productivity and estimate oil recovery until reaching bubble-point pressure conditions.

To illustrate this point, suppose that well-test data for 50 days of constant-rate production from the MFHW in discussion is available. Based on this data, we are required to forecast well performance and EUR until abandonment pressure is reached at which point production scheme switches to constant pressure or artificial lift is installed.

Figure 2.17 presents MFHW performance forecast for various values of d_f . The ultimate recovery for constant-rate production is calculated as $EUR = q_{well} \times t_{final}$ [STB] where t_{final} [days] is the time at which bottomhole pressure reaches abandonment pressure, in this case, BHP = 1000 psi. This plot allows to conclude that uniqueness of both well performance forecast and EUR largely depend upon completion performance. Notice that the less well-test data is available data the less accurate the well performance forecast hence EUR. Analysis of results are summarized in Table 2.3.

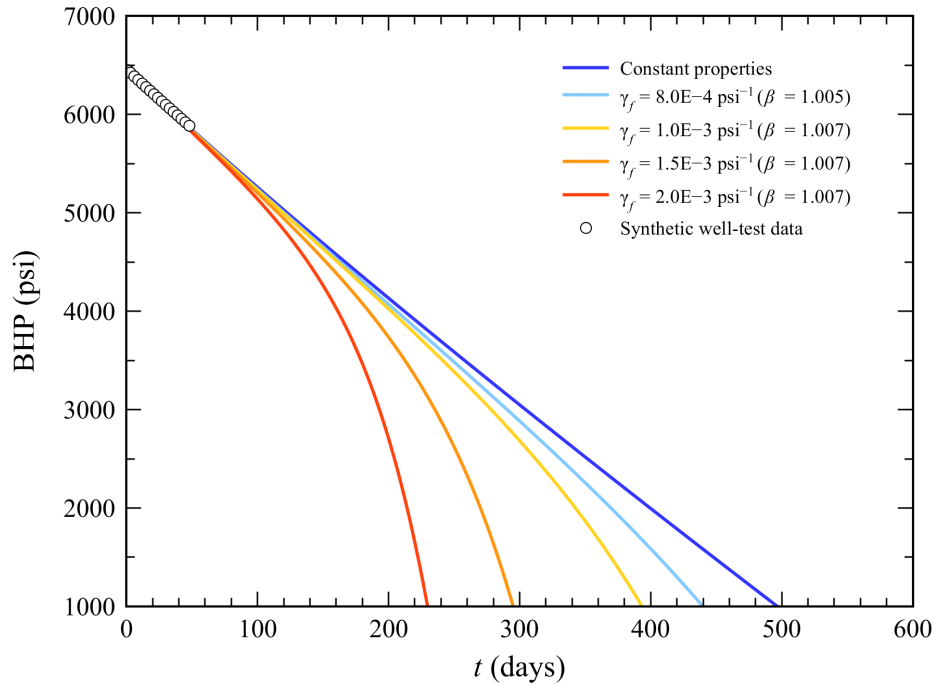


Figure 2.17: Well performance forecast and EUR as a function of d_f .

Given the results from Table 2.3, reservoir engineers should consider accounting for variations in fracture conductivity with pressure decline as to make better decisions in

Table 2.3: EUR analysis for $q_{\text{well}} = 400$ STB/D as a function of d_f .

d_f [psi ⁻¹]	Onset of nonlinear effects [days]	t_{final} [days]	EUR [MSTB]	Error [%]
$\leq 1 \times 10^{-4}$	—	496	198.4	—
8.0×10^{-4}	160	440	176	12.7
1.0×10^{-3}	155	395	158	25.6
1.5×10^{-3}	47	295	118	68.1
2.0×10^{-3}	43	230	92	115.6

regard well life, anticipate well stimulation (e.g. re-fracturing), installation of artificial lift technology, or well abandonment.

Figure 2.18 compares the fractional reduction in matrix, SRV and fracture permeability for Case Studies 1 and 2. It is evident that reduction in fracture conductivity is the fastest, dropping by 50% of its initial value after 80 and 60 days of constant-rate withdrawal for $d_f = 8 \times 10^{-4}$ and 1×10^{-3} psi⁻¹, respectively. Also, note that SRV permeability decline almost linearly with time whereas matrix permeability remains essentially constant throughout.

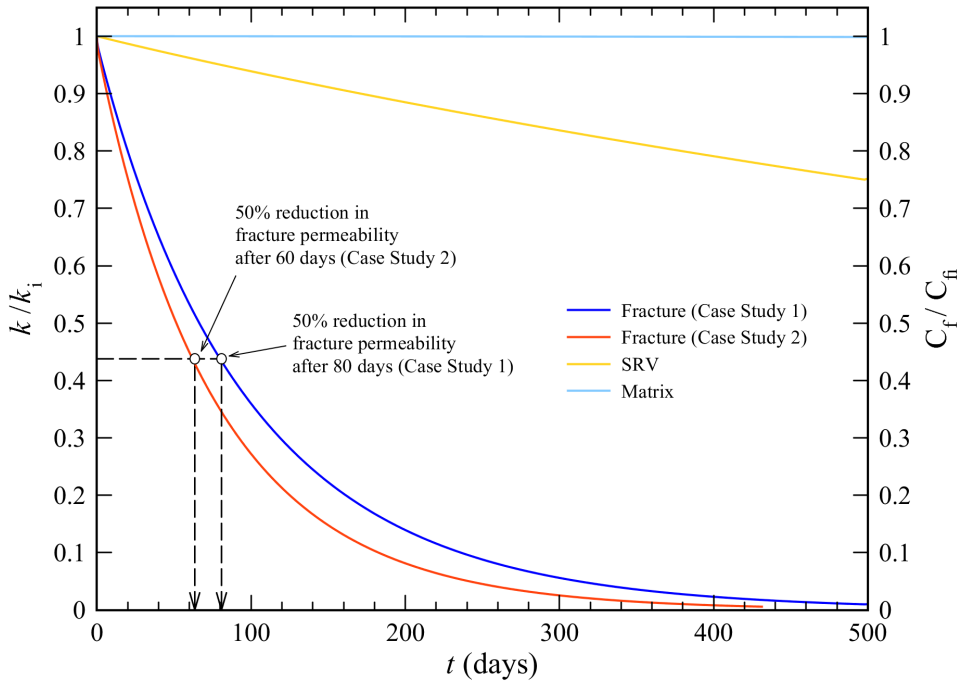


Figure 2.18: Fractional changes in fracture conductivity, SRV and matrix permeability as a function of time.

2.10. Sensitivity Analysis

2.10.1 Impact of Initial Fracture Conductivity on Well Performance

As pointed out by Smith and Montgomery (2015), SRV conductivity $k_1 x_f$ is the ability of the formation to feed hydrocarbons into the fracture whereas the fracture conductivity is the ability of fracture to carry that fluid into the wellbore. Therefore, both $k_1 x_f$ and C_{fi} should be taken into consideration during the design of a hydraulic fracturing job to avoid unnecessarily large initial fracture conductivity, which may significantly increase the overall cost of the treatment.

In this section, we study the impact of C_{fi} on well performance, considering $C_{fi} = 50, 500, 2000, 5000$ and 10000 md-ft for the case studies analyzed in the previous section. The values of C_{fi} chosen for the study in this section are aligned with typical values for different types of proppant commonly used in hydraulic fracturing jobs (e.g. Zhang et al., 2014). Given that $k_{1i} = 1$ md and $x_f = 200$ ft then $F_{CDi} = 0.25, 2.5, 10, 25$ and 50 .

Figure 2.19 shows that the analytical model is in good agreement with numerical data for bottomhole pressure response. Note that the impact of initial fracture conductivity on MFHW performance when fracture conductivity is pressure-dependent is notorious when $F_{CDi} < 10$ whereas it is almost imperceptible when $F_{CDi} \geq 10$. In other words, the effect of a pressure-dependent fracture conductivity will not influence MFHW performance if $F_{CDi} \geq 10$. Figure 2.20 shows that the analytical model is in excellent agreement with numerical simulation data. Likewise, the RNP plot shows an excellent early-to-mid time match for all values of F_{CDi} (Figure 2.21).

Similarly, Figure 2.21 shows that the RNP for an initially low fracture conductivity translates into a higher convergence skin which may mask early-time bi-linear flow regime, particularly when $F_{CDi} < 10$. This pressure-transient response can also be observed in Figure 2.22 exhibits a similar behavior.

RNP' exhibits an early-time mismatch when $F_{CDi} = 0.25$ in Case Study 1, as depicted by (Figure 2.23). This misfit may be due to the occurrence of a long transitional flow between the SRV/fracture bilinear and SRV linear regimes. Interestingly, all drawdown-derivative curves converge to ≈ 0.4 psi/STB/D at $t = 1$ day regardless of the value of F_{CDi} . Other than that, the analytical model is in excellent agreement with numerical data. Moreover, similar to Figure 2.21, nonlinear effects due to a pressure-dependent fracture conductivity can be detected at late-time only when $F_{CDi} < 10$.

RNP' in Case Study 2 also exhibits early-time mismatch when $F_{CDi} = 0.25$ (Figure 2.24). This mismatch may be due to the transitional flow regime discussed earlier, which cannot be capture by a combined linear flow model. Finally, similar to the previous case study, all pressure drawdown-derivative curves converge to ≈ 0.4 psi/STB/D at $t = 1$ day when $F_{CDi} \geq 2.5$. Values of β for various dimensionless fracture conductivity values are summarized in Table 2.4.

Table 2.4: Correction factor β as a function of F_{CDi} .

	β vs F_{CDi}				
	0.25	2.5	10	25	50
Case study 1	1.025	1.005	1.000	0.997	0.995
Case study 2	1.030	1.007	1.002	1.000	0.998

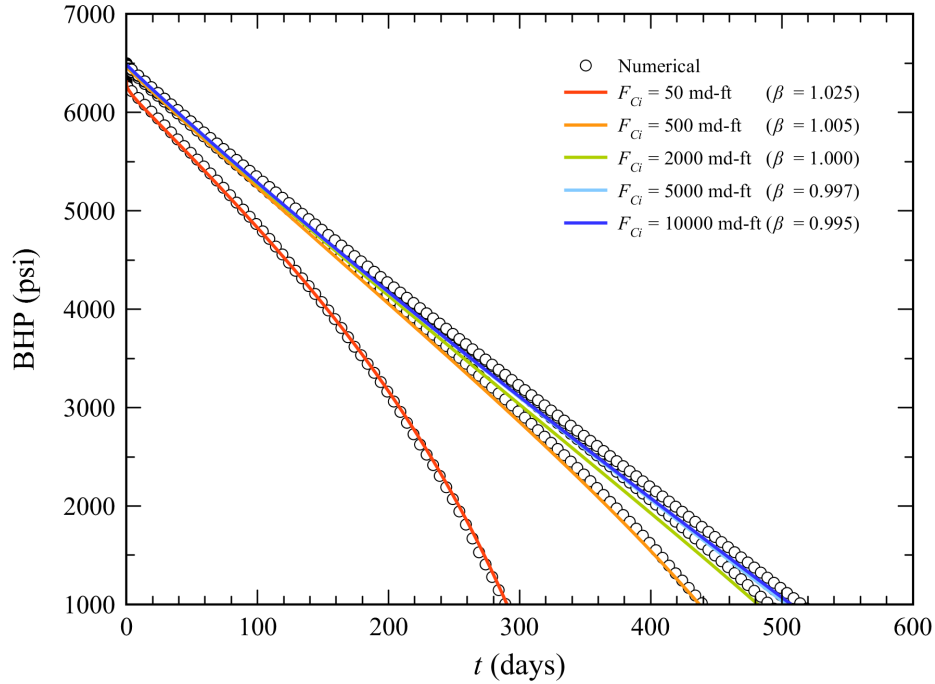


Figure 2.19: BHP response as a function of C_{fi} for Case Study 1.

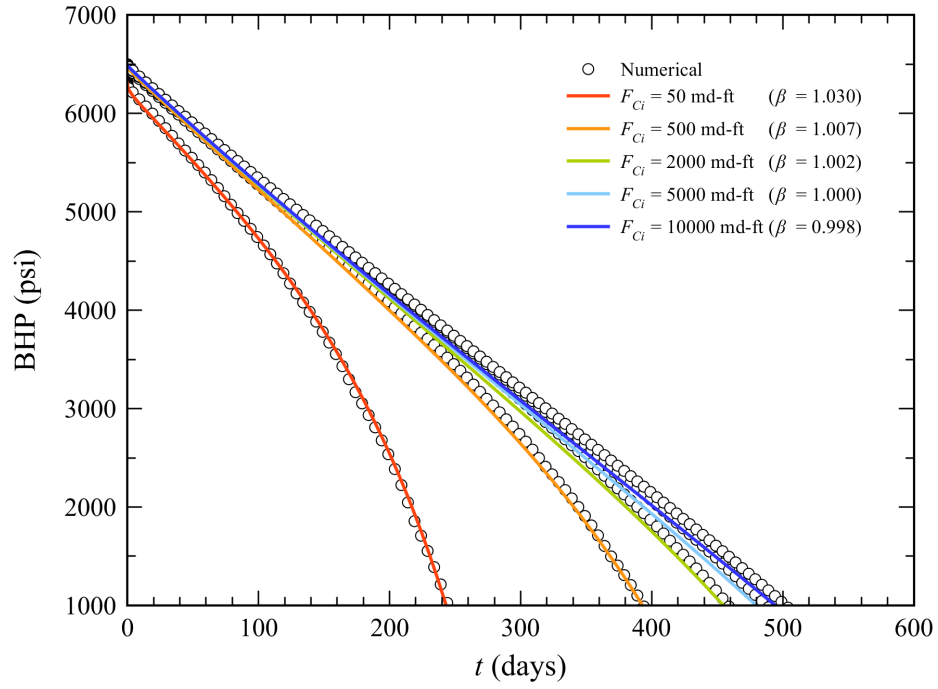


Figure 2.20: BHP response as a function of C_{fi} for Case Study 2.

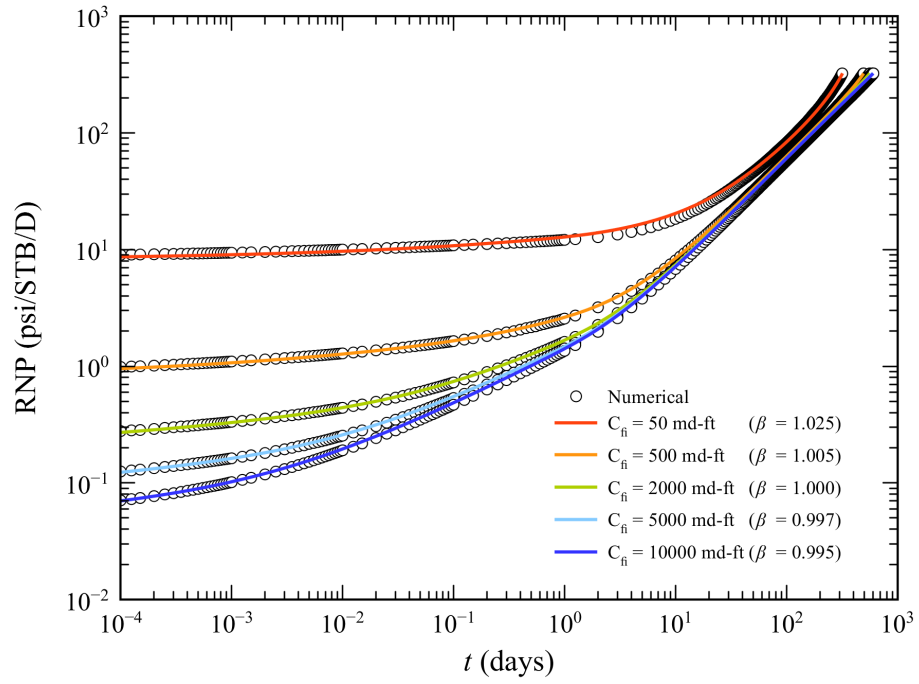


Figure 2.21: RNP response as a function of C_{fi} for Case Study 1.

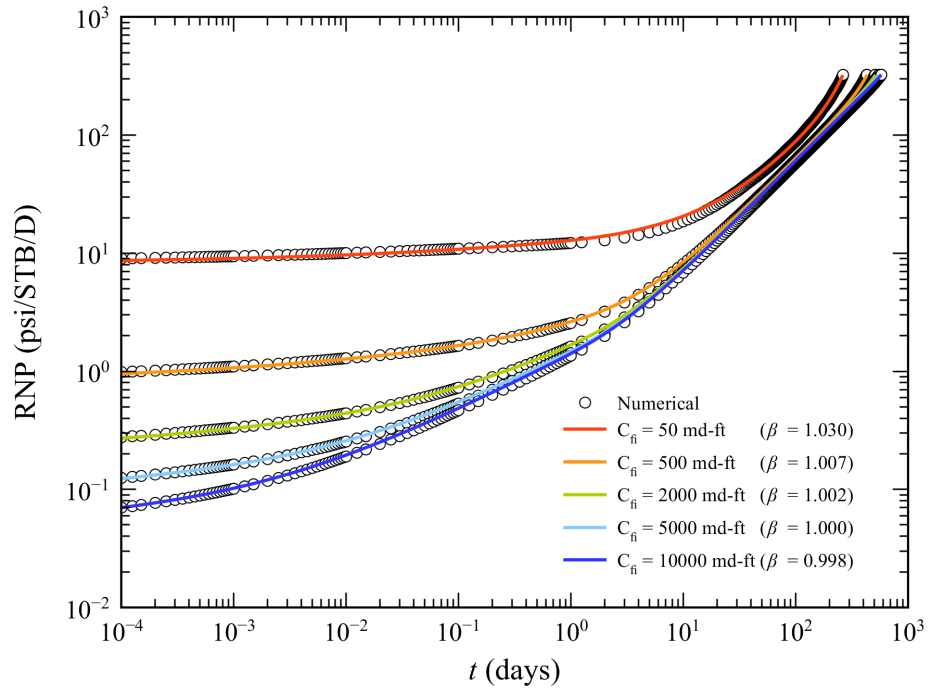


Figure 2.22: RNP' response as a function of C_{fi} for Case Study 2.

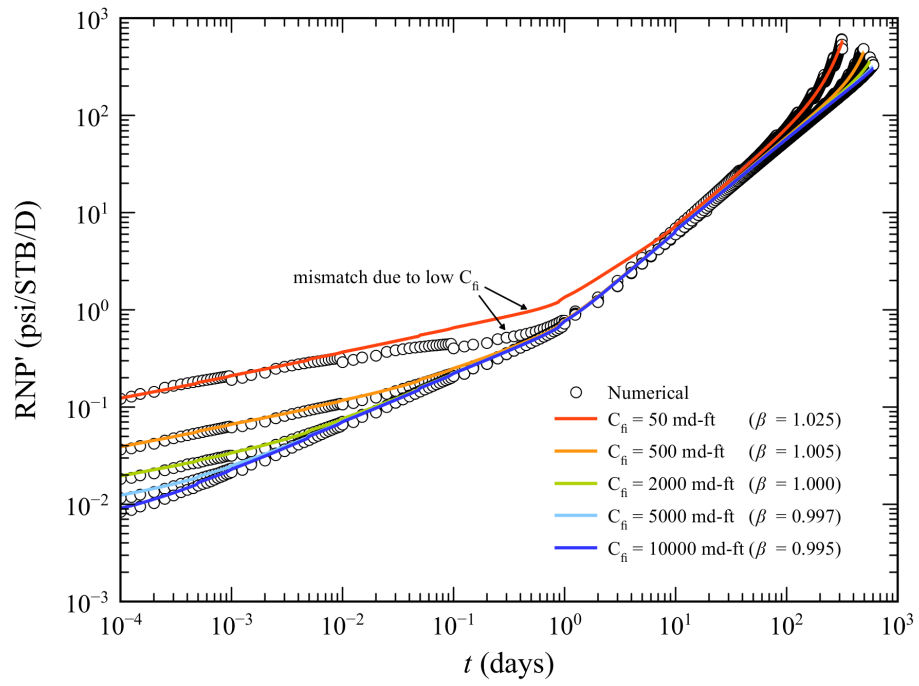


Figure 2.23: RNP' response as a function of C_{fi} for Case Study 1.

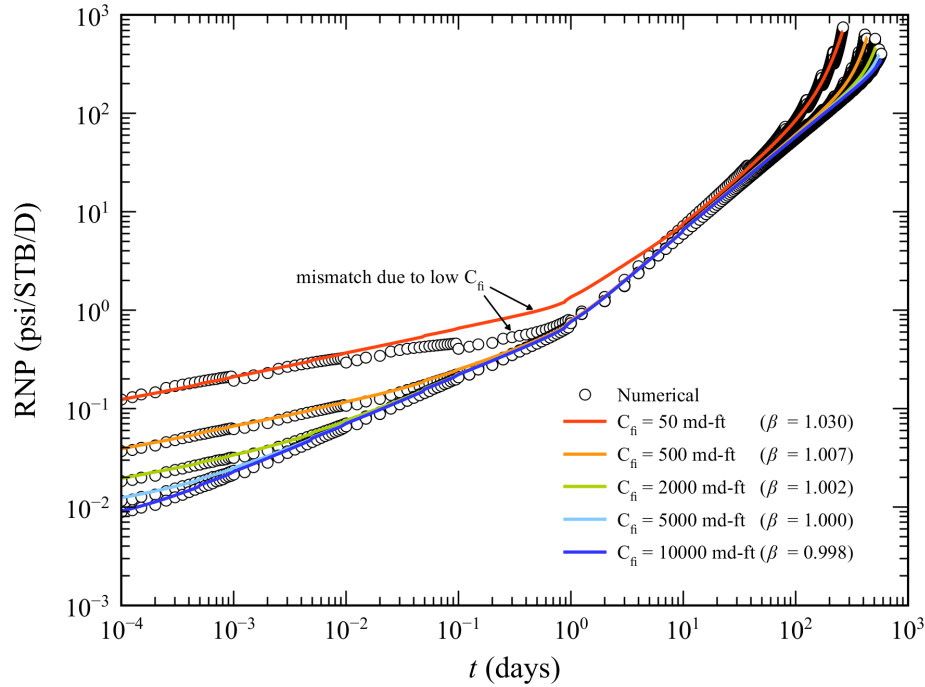


Figure 2.24: RNP' response as a function of C_{fi} for Case Study 2.

2.10.2 Impact of Pressure-Dependent Fracture Conductivity on Well Performance

This section examines the impact of pressure dependency of fracture conductivity on pressure-transient behavior. The sensitivity analysis is performed for typical values of the stress-sensitive characteristic number of common proppant agents (e.g. Yao et al., 2016) (see Table 2.5). Matrix and SRV properties are considered constant in this analysis therefore $C_f/C_{fi} = F_{CD}/F_{CDi}$. Furthermore, $\beta = 0.995$ for $d_f \leq 4 \times 10^{-4} \text{ psi}^{-1}$ and $\beta = 1.005$ for $d_f > 4 \times 10^{-4} \text{ psi}^{-1}$. Reservoir, fluid and MFHW properties are taken from Table 2.1.

Table 2.5: Stress-sensitive characteristic numbers used in this analysis.

Modulus [psi^{-1}]	Scenario 1	Scenario 2	Scenario 3	Scenario 4	Scenario 5	Scenario 6
d_f	6×10^{-5}	1×10^{-4}	4×10^{-4}	1×10^{-3}	2×10^{-3}	3×10^{-3}
Well life [days]	496	495	495	400	238	165
EUR [MSTB]	198.4	198	198	160	95.2	66

Figure 2.25 illustrates well performance forecast for various d_f . The baseline for this analysis is the constant properties case which sets the expected life of the well to 594

days. Interestingly, almost the same performance forecast is yielded for $d_f \leq 4 \times 10^{-4} \text{ psi}^{-1}$, which suggests that reduction of initial fracture conductivity with pressure decline would not significantly affect well performance. This observation is supported by the predicted well lives from Table 2.5 (up to Scenario 3) as compared to the baseline forecast.

Yet, the baseline forecast could be overly optimistic if the dependency of fracture conductivity on average fracture pressure-drawdown is ignored when $d_f > 4 \times 10^{-4} \text{ psi}^{-1}$. It is evident from Table 2.5 that well life can be largely affected by a decreasing fracture conductivity. Likewise, EUR for these cases would be substantially lower than the baseline EUR hence potentially resulting in misleading reservoir economic analysis of the shale oil prospect.

In summary, the present analysis demonstrated that a pressure-sensitive fracture conductivity would affect well performance and future production estimates only if its stress-dependent characteristic value is considerably large. In this study, we find that $d_f > 4 \times 10^{-4} \text{ psi}^{-1}$ is sufficiently large to adversely affect production forecast and EUR. Therefore, engineers should be aware that variations in initial fracture conductivity under high confining stress may negatively impact expected well performance.

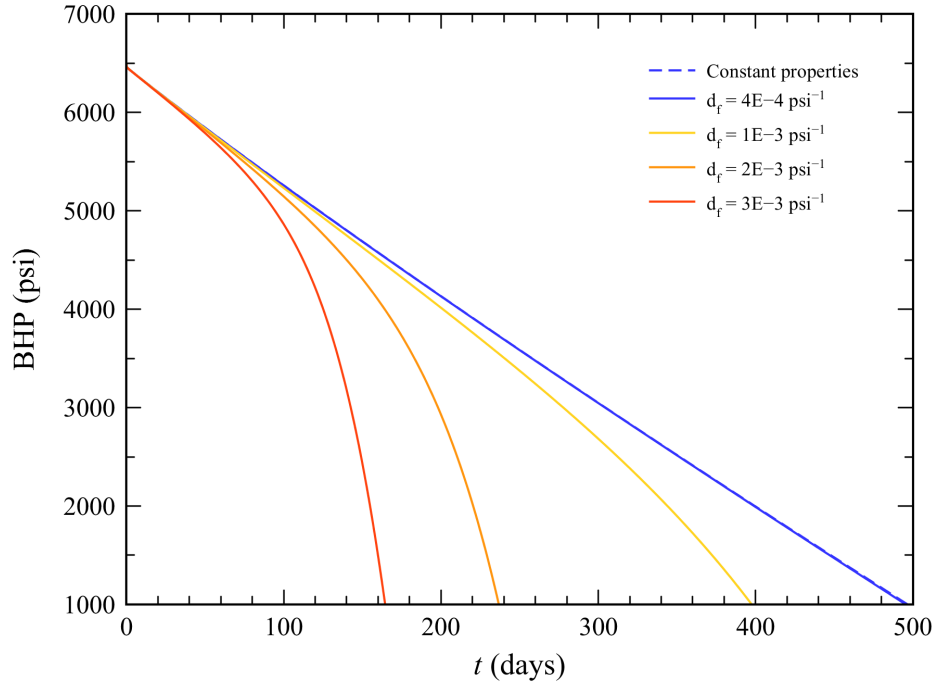


Figure 2.25: BHP response as a function of d_f .

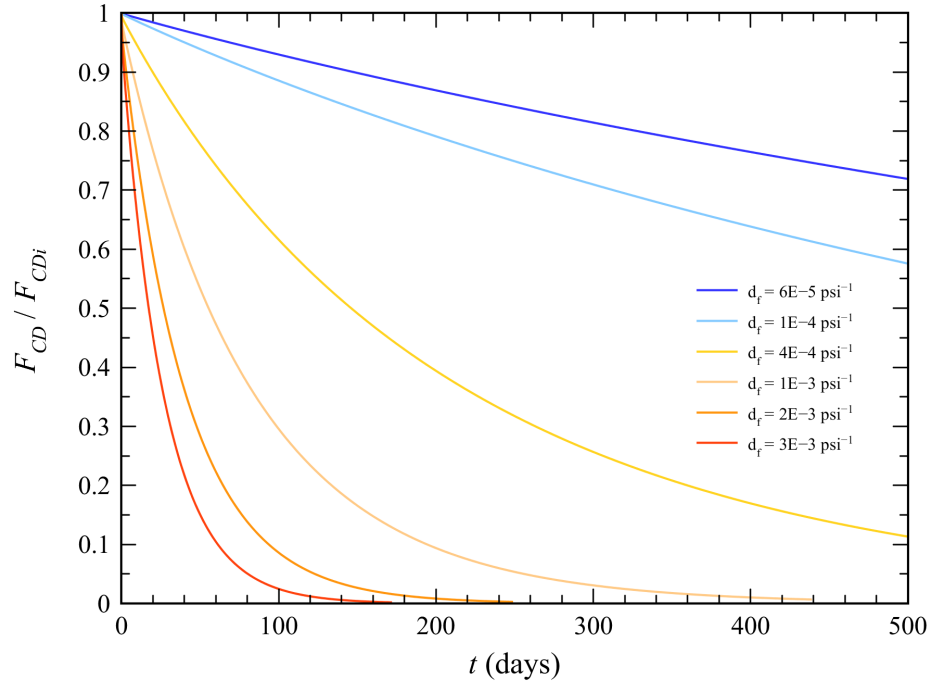


Figure 2.26: Fractional change in F_{CD} with time as a function of d_f .

Another interesting conclusion drawn from Figure 2.26 is, even though fracture conductivity would reduce rapidly with increasing pressure-drawdown, fracture conductivity is still enough to deliver 20 STB/D per fractured stage. Nonetheless, fracture conductivity loss is substantially higher when $d_f > 4 \times 10^{-4} \text{ psi}^{-1}$ thus the well is no longer able to maintain a constant per-fracture flow rate. This explains why well life reduces drastically in such cases.

2.10.3 Impact of Pressure-Dependent SRV Permeability on Well Performance

We discussed in Section 2.1 that SRV permeability is primarily due to fracture branching and induced/reactivated natural fractures and micro-fractures networks. Unfortunately, these fractures are often too narrow to get propped during the stimulation job (Sharma and Manchanda, 2015) (Figure 2.1). Therefore, an increasing confining stress can lead to an orders-of-magnitude reduction in SRV permeability (Guo et al., 2013). As such, it is necessary to consider the impact of loss of SRV permeability with pressure decline on MFHW performance. Here we consider constant rock properties in the matrix and fracture, and examine pressure-transient behavior to various values of γ_1 . Reservoir, fluid and system properties are taken from Table 2.2.

Forecast of well life and EUR until reaching bubble-point pressure are summarized in Table 2.6. Notice that these results are similar to those in Table 2.5. This indicates that the impact of pressure-dependent fracture and SRV are comparable when $\gamma_1 \approx d_f$. Figure 2.27 illustrates BHP response as a function of γ_1 . On the one hand, MFHW performance and EUR would not be substantially affected if $\gamma_1 < 5 \times 10^{-4} \text{ psi}^{-1}$. On the other hand, they may be largely affected when $\gamma_1 > 5 \times 10^{-4} \text{ psi}^{-1}$, leading to a sensible overestimation of well performance and EUR if pressure-dependency of SRV permeability is neglected.

Table 2.6: SRV permeability modulus values used for the sensitivity analysis.

	Scenario 1	Scenario 2	Scenario 3	Scenario 4	Scenario 5	Scenario 6
$\gamma_1 [\text{psi}^{-1}]$	6×10^{-5}	1×10^{-4}	4×10^{-4}	1×10^{-3}	2×10^{-3}	3×10^{-3}
Well life [days]	496	490	485	388	230	160
EUR [MSTB]	198.4	196	194	155.2	92	64

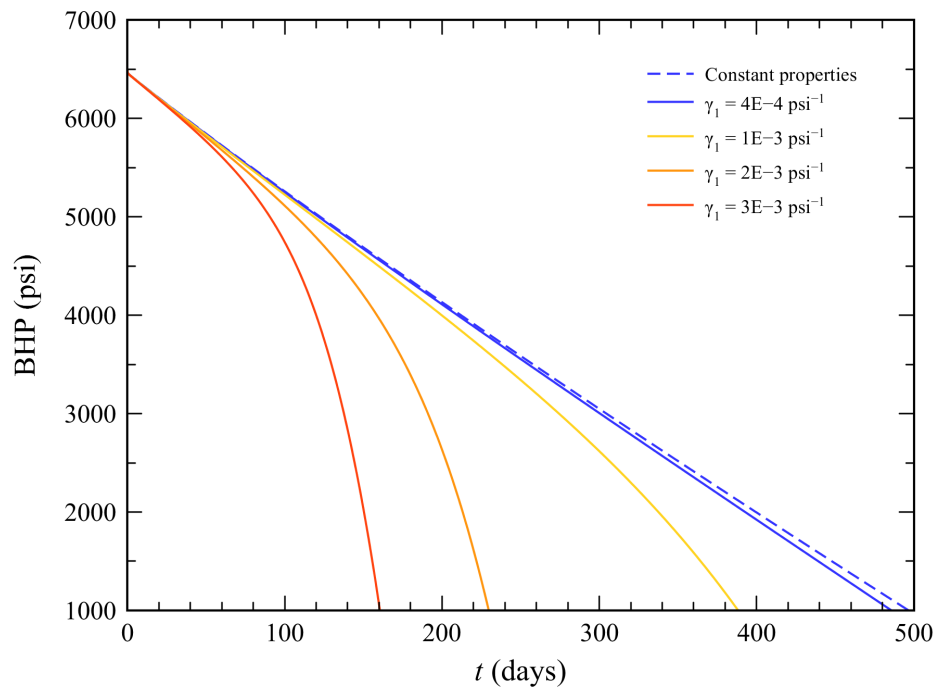


Figure 2.27: BHP response as a function of γ_1 .

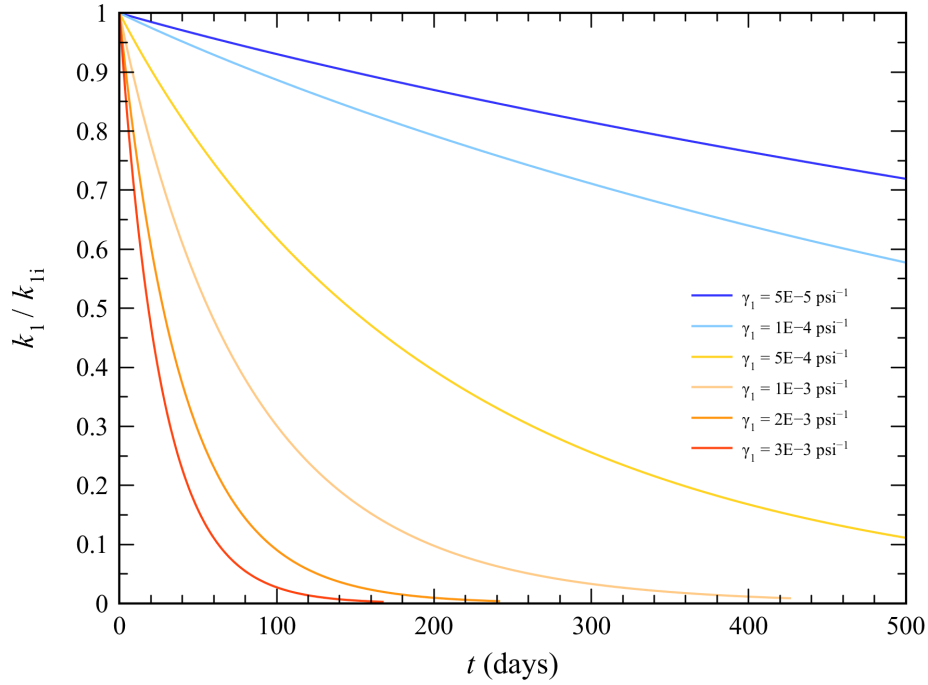


Figure 2.28: Fractional change in SRV permeability as a function of γ_1 .

Unlike hydraulic fracture conductivity, which is designed and controlled by proppant type and concentration, SRV permeability cannot be prescribed and/or estimated solely based on proppant properties. Therefore, if transient BHP response exhibits nonlinear behavior, even though d_f is relatively low by design ($< 4 \times 10^{-4} \text{ psi}^{-1}$), then sensitivity of SRV permeability to pressure decline may potentially be the cause of such behavior.

Another case of interest is that when both SRV permeability and fracture conductivity are both highly sensitive to pressure decline. Table 2.7 summarizes the forecast and EUR results for constant rock properties (baseline case), pressure-dependent SRV permeability only ($\gamma_1 = 1 \times 10^{-3} \text{ psi}^{-1}$ and $d_f < 4 \times 10^{-4} \text{ psi}^{-1} \approx 0$), pressure-dependent fracture conductivity only ($d_f = 1 \times 10^{-3} \text{ psi}^{-1}$ and $\gamma_1 < 4 \times 10^{-4} \text{ psi}^{-1} \approx 0$) and simultaneous pressure-dependent fracture conductivity and SRV permeability ($\gamma_1 = d_f = 1 \times 10^{-3} \text{ psi}^{-1}$).

Figure 2.28 shows expected BHP response for all scenarios of pressure-sensitive SRV permeability. Notice that BHP response for the case of when pressure-dependent SRV is dominant over pressure-sensitive fracture conductivity yields similar results as the case of fracture conductivity being more sensitive to pressure decline than SRV perme-

ability. However, well performance is largely impacted when both SRV permeability and fracture conductivity are largely sensitive to pressure decline.

Table 2.7: Comparison of well life and EUR for different pressure-dependent SRV permeability and fracture conductivity.

	Scenario 1	Scenario 2	Scenario 3	Scenario 4
γ_1 [psi ⁻¹]	$< 4 \times 10^{-4}$	1×10^{-3}	$< 4 \times 10^{-4}$	1×10^{-3}
d_f [psi ⁻¹]	$< 4 \times 10^{-4}$	$< 4 \times 10^{-4}$	1×10^{-3}	1×10^{-3}
Well life [days]	496	388	397	331
EUR [MSTB]	198.4	155.2	158.8	132.4

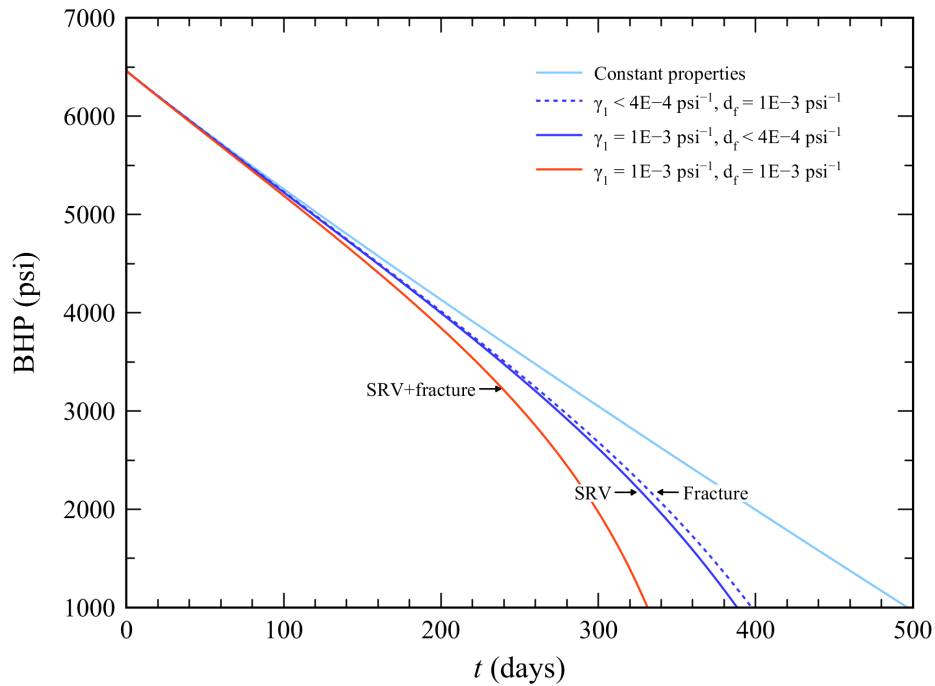


Figure 2.29: BHP response as a function of γ_1 and d_f .

2.11. Effect of Wellbore Storage and Fracture Skin on Pressure Response

So far we have studied the impact of changes in rock properties with pressure decline on BHP. In this section, we examine pressure-transient response considering WBS effects and fracture skin damage ($s_f > 0$). In particular, we focus on the use of diagnostic plots to investigate the signature transient response to the presence of fracture skin

in conjunction with WBS. Rock, fluid and system properties are taken from Table 2.1 assuming $d_f = \gamma_f = 8 \times 10^{-4} \text{ psi}^{-1}$.

Figure 2.30 shows the rate-normalized diagnostic plot for $0.005 \leq s_f \leq 5$ neglecting WBS effects. Note that RNP' is more sensitive than RNP to s_f ; however, fracture skin influences RNP response when $s_f > 0.5$. As seen in this diagnostic plot, the transient signature of fracture skin occurs at early time; its duration depends on the value of s_f , such that the higher the skin the longer the signature response.

In general, transient response of rate-normalized parameters is similar to that of a well with WBS and skin damage, with the exception that RNP and RNP' do not coincide at early time. Additionally, the slope of RNP' at early time is $1/2$, indicative of linear flow in the fracture.

Figure 2.31 shows the effect of WBS on pressure-transient response for $s_f = 0.5$. Type-curves were generated for various C_D . Numerical data correspond to BHP. RNP' exhibits two humps due to choking skin and fracture skin, when C_D is relatively small; yet, high C_D would mask fracture skin effects.

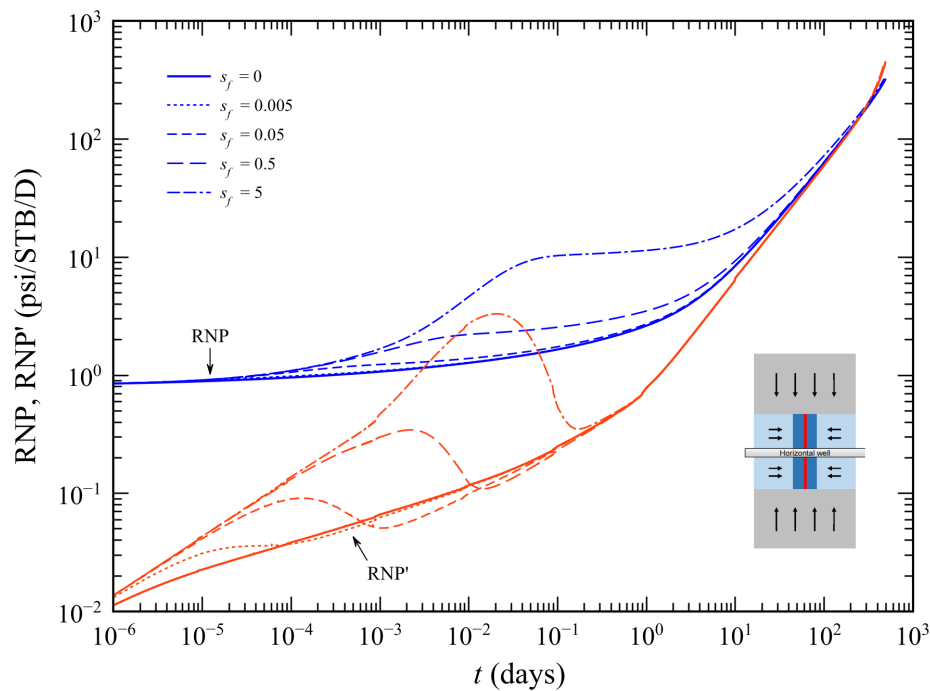


Figure 2.30: RNP and RNP' as a function of s_f (without wellbore storage effects).

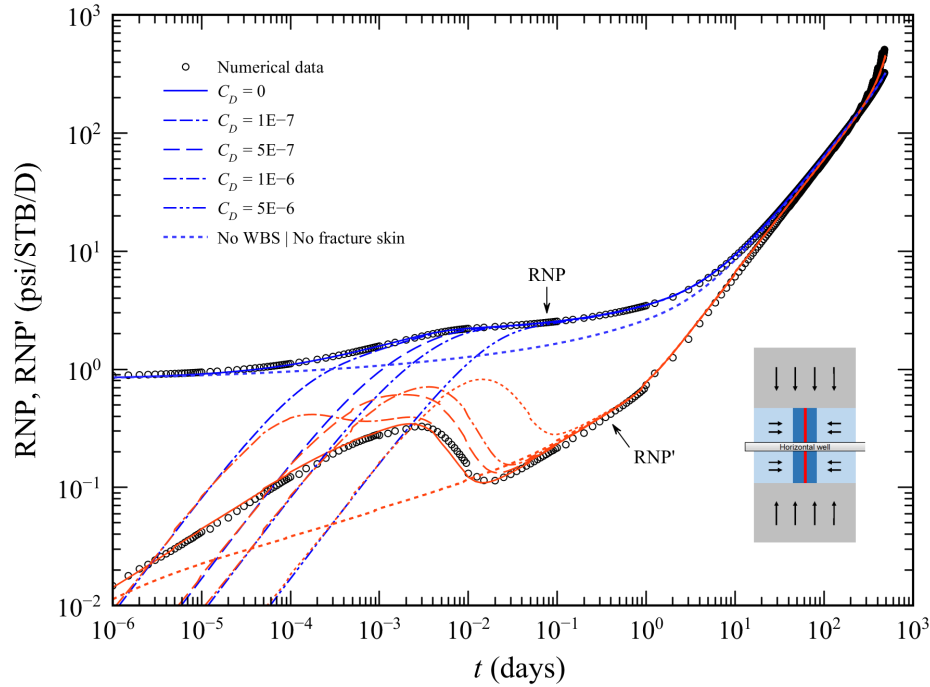


Figure 2.31: Effect of wellbore storage on RNP and RNP' for $s_f = 0.5$.

2.12. Adding Lower Limit to Reduction in Permeability and Fracture Conductivity with Pressure Decline

In Equation 2.1 we introduced an exponential function correlating reduction in permeability with increasing pressure decline. This exponential formulation, however, can be troublesome in situations where γ is sufficiently large to induce a rapid drop in permeability at low-to-moderate pressure-drawdown. As such, initial permeability will rapidly approach zero. For instance, SRV permeability may drop to a value lower than the intact matrix permeability. Evidently, this may not be physically sound.

To overcome this potential pitfall, we introduce in this section an improved exponential formulation for pressure-sensitive permeability (Luo et al., 2017). This formulation features a critical value, or lower bound, denoted by k_{jm} , beyond which initial permeability k_{ji} cannot decrease with pressure any more and behaves steady state. This lower bound can be regarded as the retained permeability under high confining stress. In this approach, pressure-dependent permeability is defined as:

$$k_j = k_{ji} \left[1 - (1 - k_{jm}/k_{ji})(1 - e^{-\gamma_j \Delta p_j}) \right] \quad (2.132)$$

Similarly, fracture conductivity has been observed to reduced from its initial value, C_{fi} , to a critical value beyond which it behaves steady state (Abass et al., 2009; Palisch et al., 2007; Weaver et al., 2010). Henceforth, we adopt the following formulation for changes in fracture conductivity with pressure-drawdown in the fracture:

$$C_f = C_{fi} \left[1 - (1 - C_{fm}/C_{fi})(1 - e^{-d_f \Delta p_f}) \right] \quad (2.133)$$

Inserting Equation 2.132 and 2.133 into the analytical model previously developed in Section 2.5 leads to new definitions of the nonlinear scaling parameter λ_j , as follows:

$$\lambda_f = \left[1 - (1 - C_{fm}/C_{fi})(1 - e^{-d_f \Delta \tilde{p}_f}) \right] e^{(c_{rf} + c_\mu) \Delta \tilde{p}_f} \quad (2.134)$$

$$\lambda_1 = \left[1 - (1 - k_{1m}/k_{1i})(1 - e^{-\gamma_1 \Delta \tilde{p}_1}) \right] e^{(c_{r1} + c_\mu) \Delta \tilde{p}_1} \quad (2.135)$$

$$\lambda_2 = \left[1 - (1 - k_{2m}/k_{2i})(1 - e^{-\gamma_2 \Delta \tilde{p}_2}) \right] e^{(c_{r2} + c_\mu) \Delta \tilde{p}_2} \quad (2.136)$$

Similarly, the nonlinear scaling parameters arising at the SRV/fracture and SRV/matrix interfaces are redefined as:

$$\delta_{1f} = \frac{1 - (1 - C_{fm}/C_{fi})(1 - e^{-d_f \Delta \tilde{p}_f})}{1 - (1 - k_{1m}/k_{1i})(1 - e^{-\gamma_1 \Delta \tilde{p}_1})} \quad (2.137)$$

$$\delta_{21} = \frac{1 - (1 - k_{1m}/k_{1i})(1 - e^{-\gamma_1 \Delta \tilde{p}_1})}{1 - (1 - k_{2m}/k_{2i})(1 - e^{-\gamma_2 \Delta \tilde{p}_2})} \quad (2.138)$$

Lastly, the nonlinear scaling factor δ_w in the constant-rate boundary condition is redefined as:

$$\delta_w = \beta \left[1 - (1 - C_{fm}/C_{fi})(1 - e^{-d_f \Delta \tilde{p}_f}) \right] \quad (2.139)$$

where β is a correction factor that accounts for the fact that near-wellbore properties change at a faster rate than overall fracture properties with pressure decline. We have observed that $\beta = 1.03$ gives accurate results for $20 \leq C_{fi} \leq 1000$ md-ft.

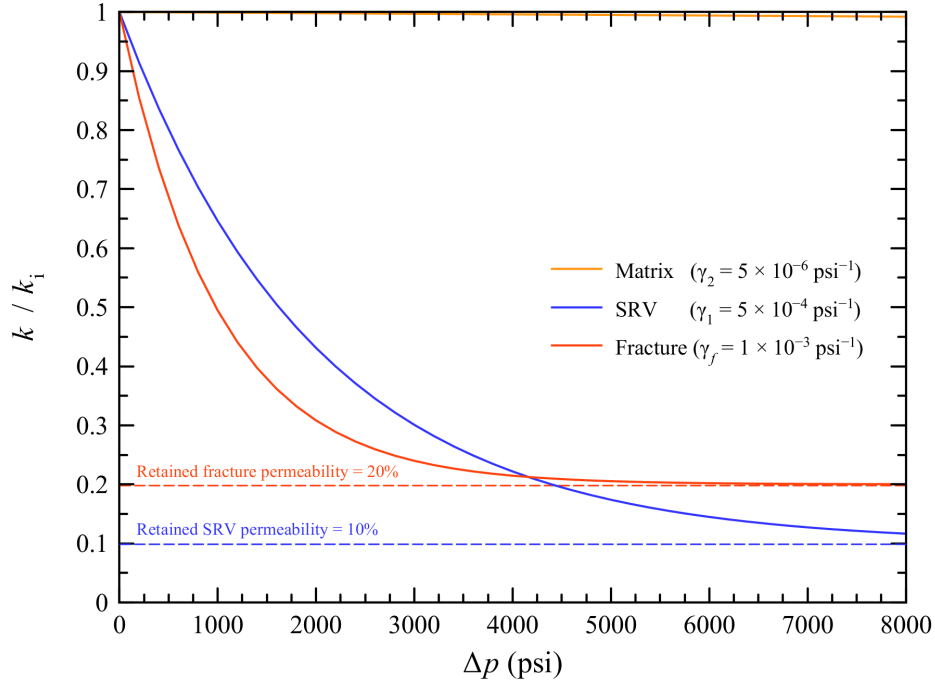


Figure 2.32: Fractional changes in SRV and fracture permeability with pore pressure.

To validate the analytical MFHW model with exponential pressure-dependent properties, we use the numerical model from the previous section. Two simulation case studies are examined. Initial and retained fracture conductivity are 500 and 100 md-ft, respectively. For Case Study 1, we consider that SRV permeability is more sensitive to pressure decline than fracture conductivity thus we assign $\gamma_1 = 2 \times 10^{-3} \text{ psi}^{-1}$ and $d_f = 1 \times 10^{-4} \text{ psi}^{-1}$. Conversely, we consider in Case Study 2 that fracture conductivity is more sensitive to pressure decline than SRV permeability, hence we define $\gamma_1 = 1 \times 10^{-4} \text{ psi}^{-1}$ and $d_f = 2 \times 10^{-3} \text{ psi}^{-1}$.

First, we compare BHP response given by our analytical model against the original TLF model (constant properties) and numerical BHP data. Next, we compare the rate-normalized pressure and pressure-derivative response given by our analytical model against the TLF model and numerical data. Finally, we examine the evolution of fractional reduction of SRV permeability and fracture conductivity for each case study.

Figure 2.33 shows the comparison between BHP responses for both numerical case studies. To begin with, our model is in excellent agreement with numerical data regardless of whether fracture conductivity or SRV permeability is most sensitive parameter to pressure decline. Second, the TLF model fails to accurately capture the expected BHP response from either case study. Also note that neglecting the effect of pressure on rock properties will result in an accurate forecast of well performance until bubble-point pressure conditions are reached. For instance, the TLF model predicts that bubble-point pressure will be reached after more than 800 days of constant rate production. Nonetheless, we observe that the onset time of two-phase flow (i.e. oil and gas) actually depends on variations in SRV permeability and fracture conductivity with time. Our model predicts that bubble-point pressure conditions will be reached in the MFHW after 640 and 730 days for Case Study 1 and 2, respectively, which are aligned with numerical data.

Lastly, note that the late-time BHP decline rate for Case Study 2 is almost equal to that given by the TLF model, indicating that variation in rock properties with pressure decline is quite negligible and does not influence late-time behavior of the system. Conversely, BHP decline rate for Case Study 2 is higher than the other cases. This difference may be due to the presence of non-negligible changes in rock properties with pressure decline at late time which, at the same time, points out to a slow rate of stabilization in those properties.

Figure 2.34 shows the rate-normalized pressure and pressure-derivative responses given by our analytical model compared to the original TLF model and numerical data for Case Study 1. The diagnostic plot shows that the three approaches give essentially the same pressure-transient response at early times. In fact, $1/4$ -slope (bilinear, SRV/fracture) and $1/2$ -slope (linear, SRV) flow regimes can be easily identified. Yet, nonlinear effects, due to pressure-dependent properties, begin to influence pressure-transient response after only 1 day of constant rate withdrawal; thereon, the TLF model departs from the transient response expected from either case study. Moreover, note that boundary-dominated flow (BDF) behavior is apparent between 70 and 250 days. Then, RNP and RNP' depart again from each other, which may be indicative of SRV permeability being close to reaching steady-state conditions. This presumption is also confirmed by Figure 2.36 where it can be seen that fractional reduction in SRV permeability would become nearly flat after 260 days.

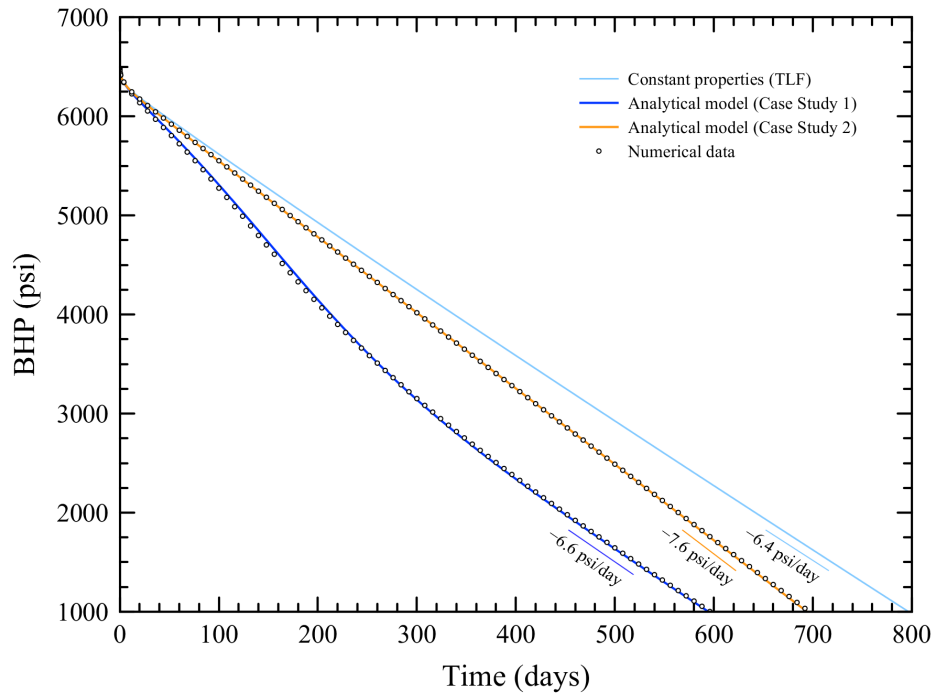


Figure 2.33: Analytical and numerical BHP responses for Case Studies 1 and 2.

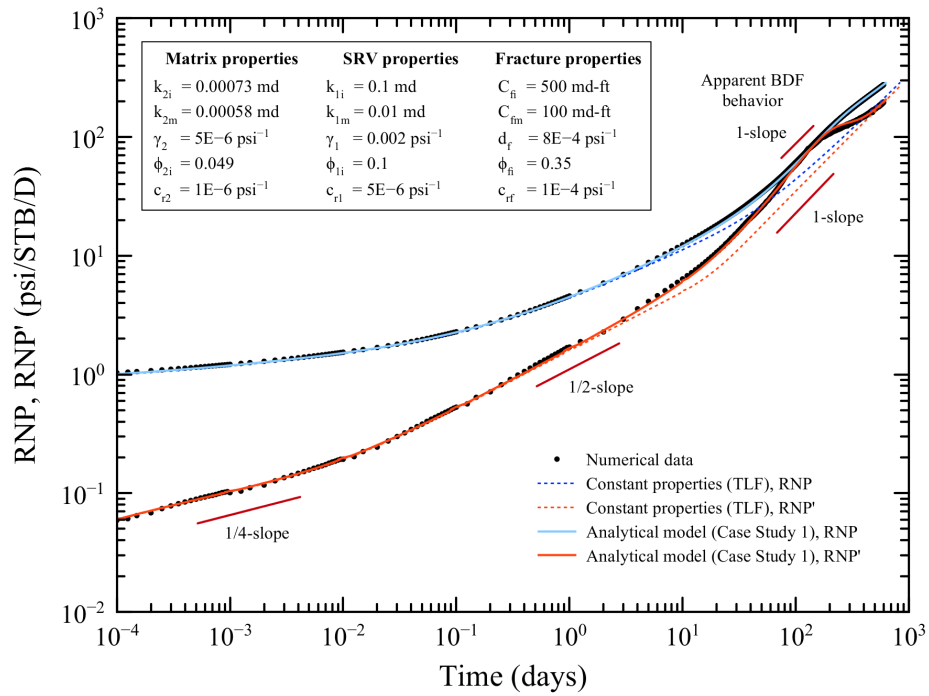


Figure 2.34: Analytical and numerical RNP and RNP' for Case Study 1.

Figure 2.35 shows the rate-normalized diagnostic plot corresponding to Case Study 2. Realize that, even though SRV permeability and fracture conductivity are both sensitive to pressure decline, it is hard to detect their impact on pressure-transient behavior solely based on this plot, primarily because of the log-scale. However, notice that the TLF model deviates from our analytical model and numerical data after around 20 days of constant-rate withdrawal. From that point onward, RNP and RNP' of the TLF exhibit a unit-slope behavior whereas RNP and RNP' of the pressure-dependent MFHW model form a slope slightly higher than 1, indicative of higher BHP decline rate, as shown in Figure 2.33.

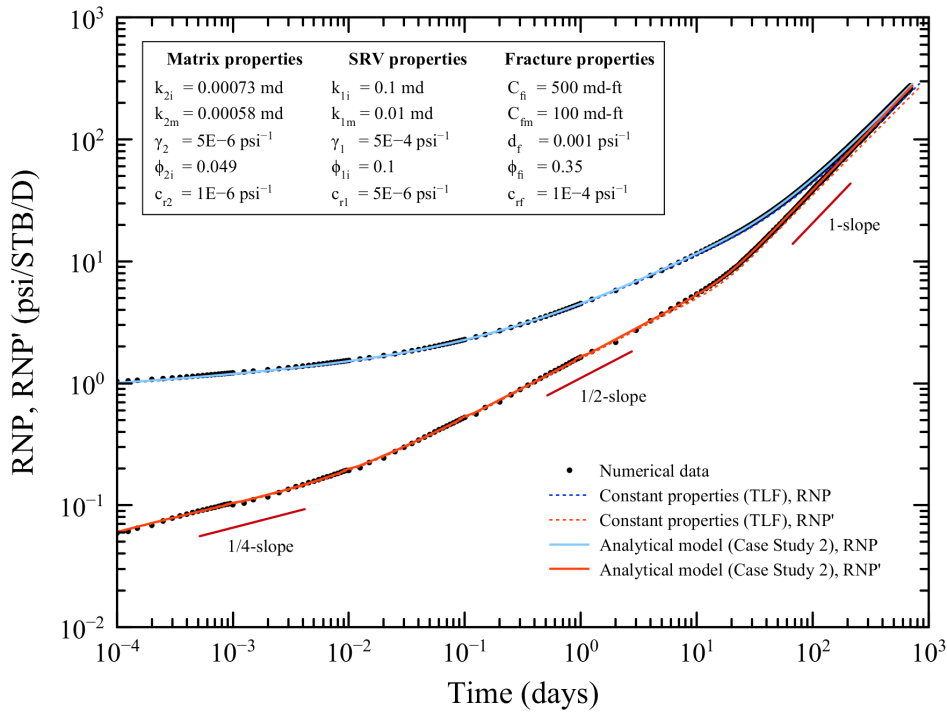


Figure 2.35: Analytical and numerical RNP and RNP' responses for Case Study 2.

The fact that early-time pressure response is not affected by the pressure-sensitive fracture conductivity suggests that, although conductivity is being lost rapidly with time, it is still enough for the well to flow at the prescribed constant rate. In this view, initial fracture conductivity may play a significant role in forecasting well productivity. This issue will be explored in more detail later in this section.

Figure 2.36 shows the evolution of fractional reduction in average fracture conductivity (C_f/C_{fi}), SRV permeability (k_1/k_{1i}) and matrix permeability (k_2/k_{2i}). Fracture conduc-

tivity and SRV permeability for Case Study 1 would have respectively been reduced by roughly 50% and 70% after 100 days of constant-rate withdrawal. Moreover, SRV permeability will fully reach steady-state after 300 days. Fracture conductivity, on the other hand, will plateau toward its critical value after 400 days. Evolution of fractional changes in fracture conductivity and SRV permeability is reversed in Case Study 2, where it can be seen that fracture conductivity has been reduced by 50% after 100 days of constant-rate production whereas SRV permeability still retains 70% of its initial value. While fracture conductivity reaches steady-state 400 days, SRV permeability does not exhibit any trend towards steady-state response; however, loss of initial SRV permeability is quite significant (50%) after 220 days.

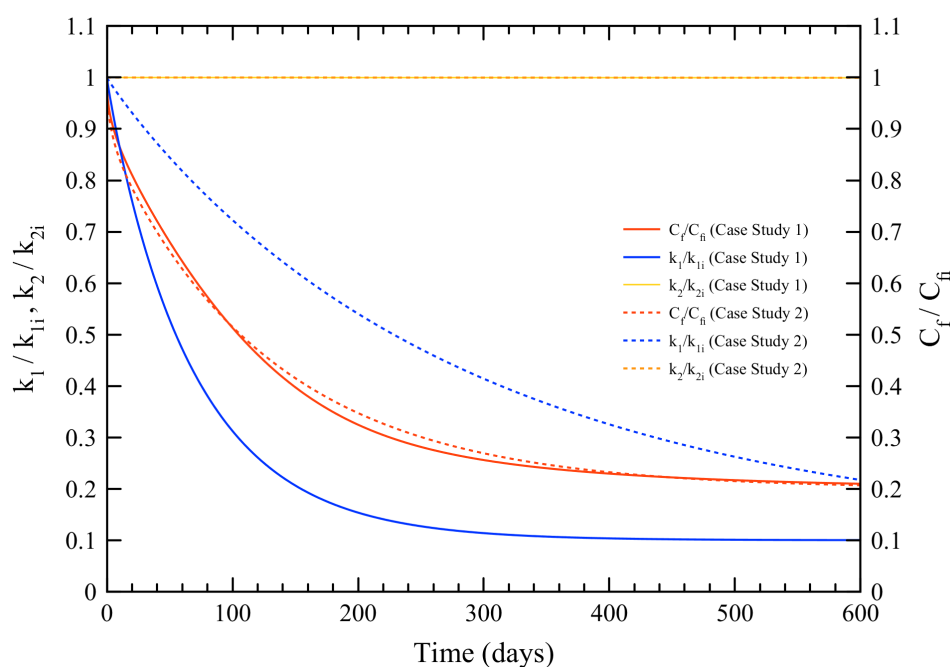


Figure 2.36: Evolution of fractional reduction of average fracture conductivity, SRV and matrix permeability for Case Studies 1 and 2.

2.12.1 Impact of Pressure-Dependent SRV Permeability on Well Performance

In this case study, we assume that matrix permeability and fracture conductivity are constant while SRV permeability vary with pressure decline. We aim to examine pressure-transient response to the cases $\gamma_1 = 1 \times 10^{-4}$, 4×10^{-4} , 1×10^{-3} , 2×10^{-4} , 3×10^{-4} and 5×10^{-4} psi^{-1} . Reservoir, fluid and MFHW properties are taken from the

previous case studies. Figure 2.37 shows the transient BHP response given by our analytical model as a function of the SRV permeability modulus and time. BHP response given by the TLF model is also included in Figure 2.37. Note that the BHP response given by our analytical model is close to the TLF model when the dependency of SRV permeability on pressure is quite small ($\gamma_1 = 1 \times 10^{-4} \text{ psi}^{-1}$). In this case, both approaches estimate the onset of two-phase flow effects, due to reaching bubble-point pressure, to be > 800 days. However, the TLF model fails to capture expected BHP response as the dependency of SRV permeability on pressure decline becomes stronger. Recognize that BHP follows two distinct depletion paths when $\gamma_1 > 2 \times 10^{-3} \text{ psi}^{-1}$. In the first stage, BHP exhibits a steep decline with time followed by a late-time trend towards achieving a stabilized decline rate, which is presumably dominated by the steady state, or critical, SRV permeability. This transient BHP behavior is evident for the case $\gamma_1 = 5 \times 10^{-3} \text{ psi}^{-1}$.

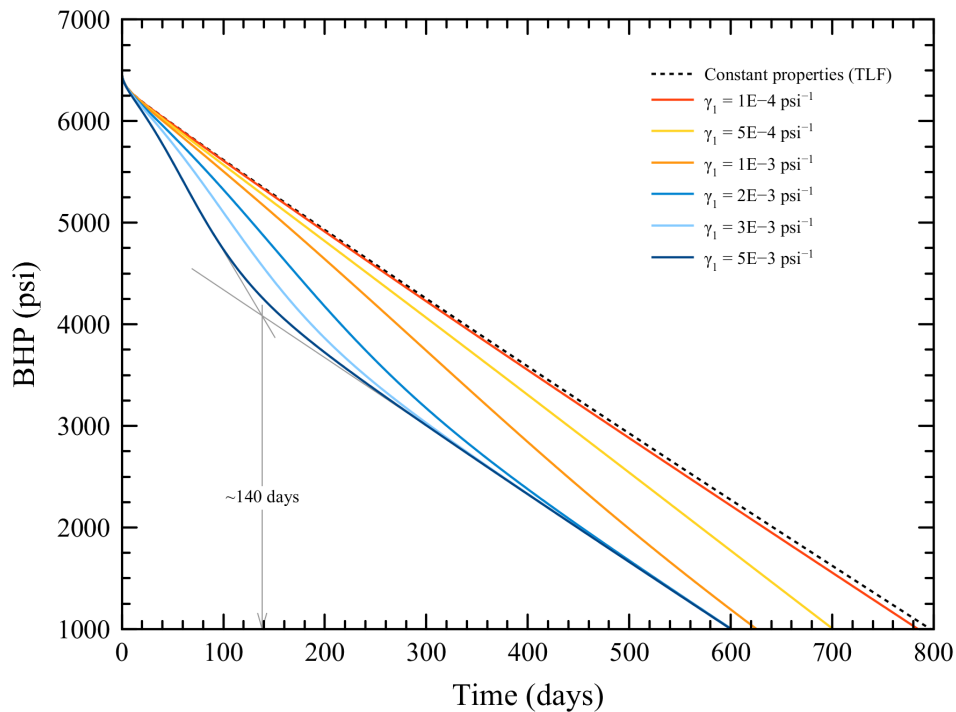


Figure 2.37: BHP response as a function of SRV permeability modulus and time.

In order to determine whether such change in decline rate is dominated by the critical SRV permeability, we draw a straight line with a slope equal to that of the mid-times decline rate. Similarly, we draw another line with a slope equal to that of the late-times

decline rate. Both straight lines are extended until they intersect and the time at which the intersection occurs is read from the x -axis, which is around 140 days for $\gamma_1 = 5 \times 10^{-3} \text{ psi}^{-1}$. Interestingly, Figure 2.39 shows that SRV permeability achieves steady state roughly after 140 days of constant-rate production for this case, which coincides with the time at which the change in slope in BHP decline is seen on Figure 2.37. In addition, realize that an increasing permeability modulus results in early reaching of bubble-point pressure under constant-rate production. Although the onset of two-phase flow effects dramatically reduces with increasing γ_1 , it does not seem to vary sensibly when γ is relatively large (e.g. $> 2 \times 10^{-3} \text{ psi}^{-1}$).

Figure 2.38 compares RNP and RNP' given by our analytical model for $\gamma_1 = 1 \times 10^{-4}$ and $5 \times 10^{-3} \text{ psi}^{-1}$ against the TLF model. We see that pressure-dependent SRV permeability does not influence early-time pressure response of the MFHW. This conclusion is quite understandable as early-time behavior is dominated by fracture conductivity. As such, we are able to easily identify the 1/4-slope (bilinear, SRV/fracture) and 1/2-slope (linear, SRV) flow regimes in the plot. Our analytical model and the TLF model coincide when $\gamma_1 = 1 \times 10^{-4} \text{ psi}^{-1}$, indicating that loss of SRV permeability with pressure decline is negligible.

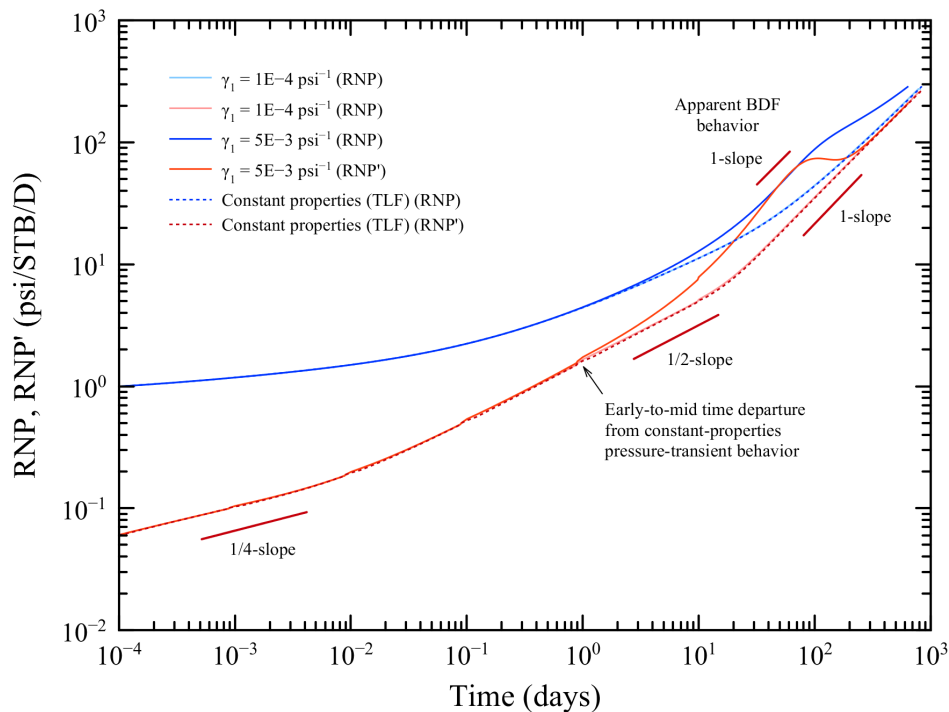


Figure 2.38: RNP and RNP' for $\gamma_1 = 1 \times 10^{-4}$ and $5 \times 10^{-3} \text{ psi}^{-1}$.

This conclusion was previously drawn after comparing BHP responses from Figure 2.37. Yet, pressure-dependent SRV permeability largely influences pressure-transient response of the MFHW only after 1 day of constant-rate production when $\gamma_1 = 5 \times 10^{-3} \text{ psi}^{-1}$. Note that RNP sharply increases until joining RNP' response, forming a unit-slope trend, or apparent boundary-dominated flow (BDF) regime, between 40 and 80 days. The apparent BDF gradually dissipates until RNP joins the response of the TLF model, indicating the reach of an actual stabilized rate of decline.

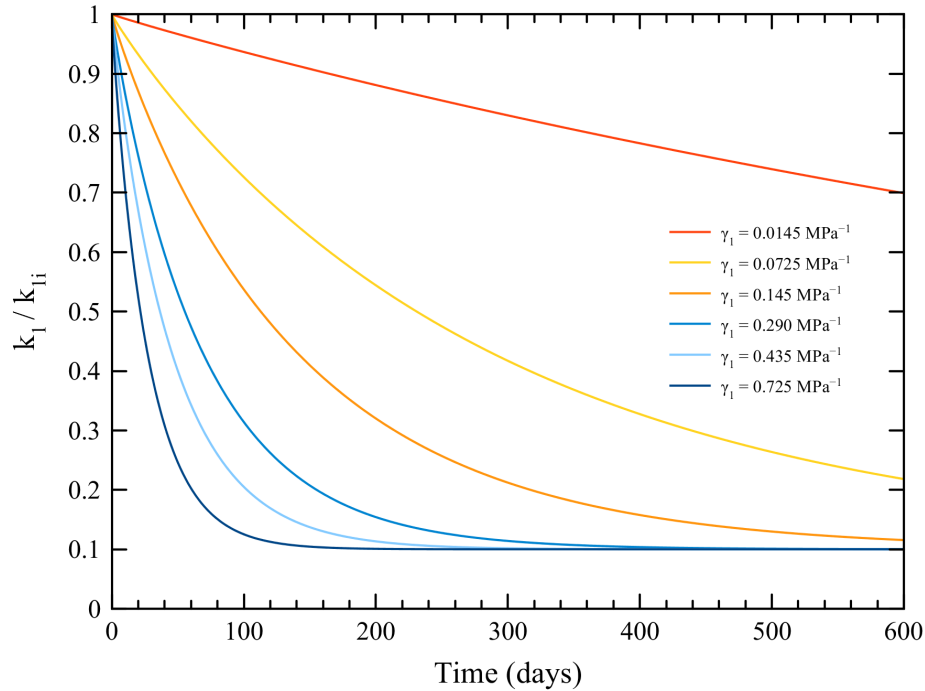


Figure 2.39: Fractional reduction of average k_1 for $\gamma_1 = 1 \times 10^{-4}$ to $5 \times 10^{-3} \text{ psi}^{-1}$.

2.12.2 Impact of Pressure-Dependent Fracture Conductivity on Well Performance

The objective of this section is to study the influence of initial fracture conductivity and stress-sensitive characteristic number of pressure-transient response and well performance. Here, SRV and matrix permeability are considered constant. Two case studies are designed for pressure-transient analysis in this section. The first case study assumes an initial and critical fracture conductivity of 500 and 100 md-ft, respectively; this means that 20% of the in-place conductivity is retained under high confining stress conditions. The second scenario studies the effect of low initial and critical fracture conductivity, 100 and 20 md-ft, respectively. Similar to SRV permeability in the previ-

ous section, we study low-to-high stress-sensitive characteristic numbers in both case studies ($d_f = 1 \times 10^{-4}, 5 \times 10^{-4}, 1 \times 10^{-3}, 2 \times 10^{-3}, 3 \times 10^{-4}$ and

Figure 2.40 shows the expected BHP response as a function of d_f and time for $C_{fi} = 500$ md-ft and $C_{fm} = 100$ md-ft. BHP response of the TLF model is included in this plot. Remarkably, even though fracture conductivity can largely decrease with pressure decline, as illustrated by Figure 2.41, expected BHP response does not vary considerably with respect to that given by the TLF model for constant properties. This deduction indicates that critical fracture conductivity, equal to the conductivity retained under high confining stress conditions, plays a major role in maximizing the long-term yield of a MFHW. This means that an initial fracture conductivity of 100 md-ft would have been sufficient to produce the MFHW under study at preset constant rate of 20 STB/D/fracture if dependency of both fracture conductivity and SRV permeability on pressure decline is negligible.

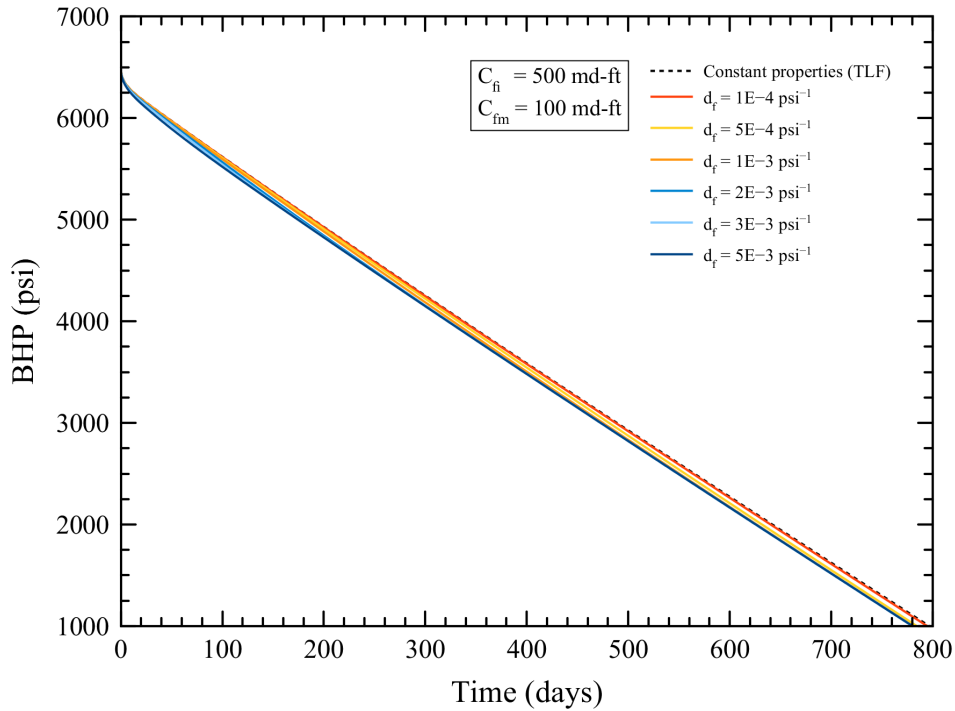


Figure 2.40: BHP response as a function of stress-sensitive characteristic number; $C_{fi} = 500$ md-ft and $C_{fm} = 100$ md-ft.

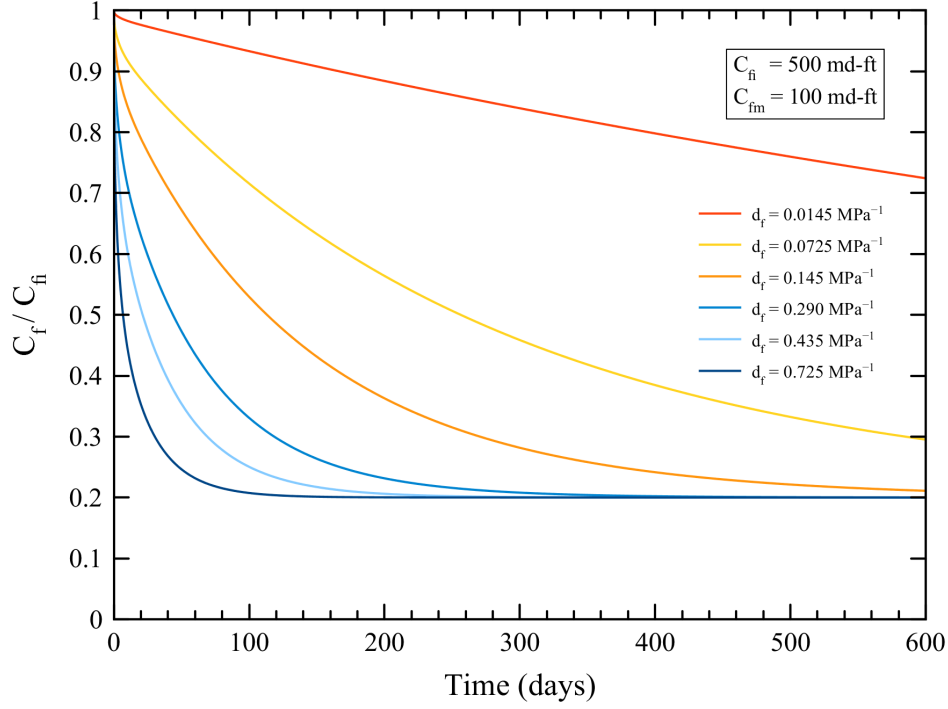


Figure 2.41: Evolution of fractional reduction of fracture conductivity for $d_f = 1 \times 10^{-4}$ to $5 \times 10^{-3} \text{ psi}^{-1}$. $C_{fi} = 500 \text{ md-ft}$ and $C_{fm} = 100 \text{ md-ft}$.

Figure 2.42 shows the transient BHP response as a function of d_f and time for $C_{fi} = 100 \text{ md-ft}$ and $C_{fm} = 20 \text{ md-ft}$. Unlike the previous scenario, in which initial fracture conductivity was relatively high, BHP seems to be negatively affected by increasing d_f when initial fracture conductivity is relatively low. Note the similarity in BHP responses between Figure 2.37 and Figure 2.42. In particular, recognize that BHP stems tend to attain late-time stabilized pressure decline rate, as clearly seen for $d_f > 1 \times 10^{-3} \text{ psi}^{-1}$. Additionally, the onset of bubble-point pressure effects is reached earlier as sensitivity of fracture conductivity to pressure decline increases.

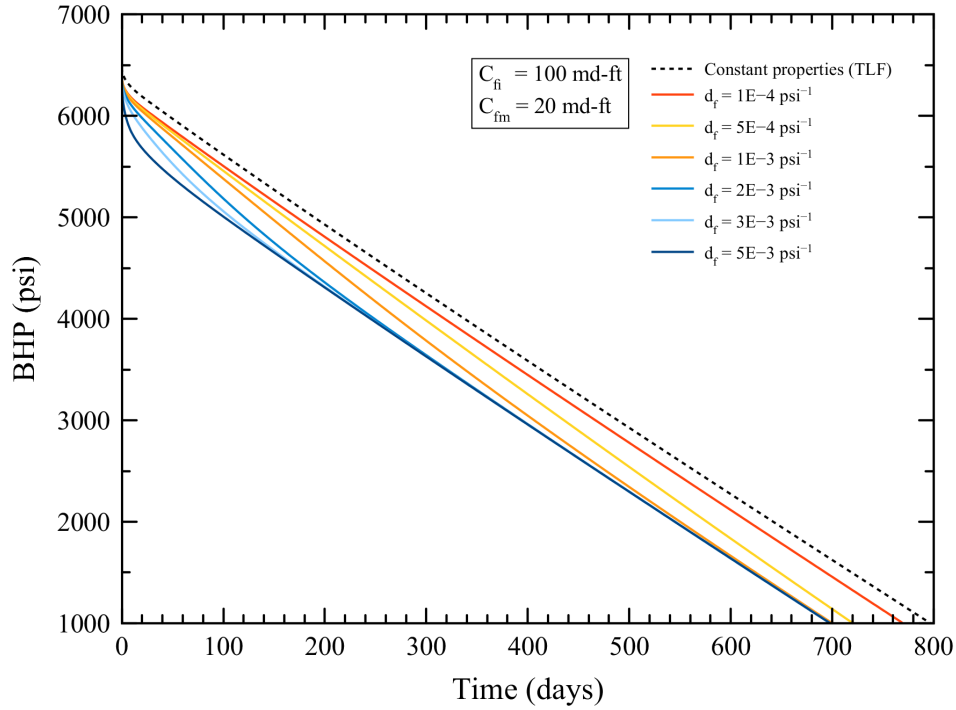


Figure 2.42: BHP response as a function of stress-sensitive characteristic number; $C_{fi} = 100$ md-ft and $C_{fm} = 20$ md-ft.

Figure 2.43 shows the RNP and RNP' responses for $d_f = 1 \times 10^{-4}$ and 5×10^{-3} psi^{-1} , as well as the TLF model. To begin with, observe that pressure-dependent and TLF models are in close agreement when $d_f = 1 \times 10^{-4}$ psi^{-1} . This result indicates that, in this case, sensitivity of fracture conductivity to pressure-drawdown is negligible. On the contrary, there is an evident mismatch between models when $d_f = 1 \times 10^{-4}$ psi^{-1} . Therefore, fracture conductivity is highly sensitive to pressure decline in this case. Notably, both RNP and RNP' responses are higher than the TLF model. In addition, RNP' response does not exhibit the bilinear SRV/fracture flow regime (1/4-slope behavior) expected at early time. Moreover, linear flow in the SRV (1/2-slope behavior) occurs between 0.4 and 14 days (earlier than expected) and is followed by a transitional flow regime toward attaining late-time equilibrium. This late-time behavior is too displayed by the RNP.

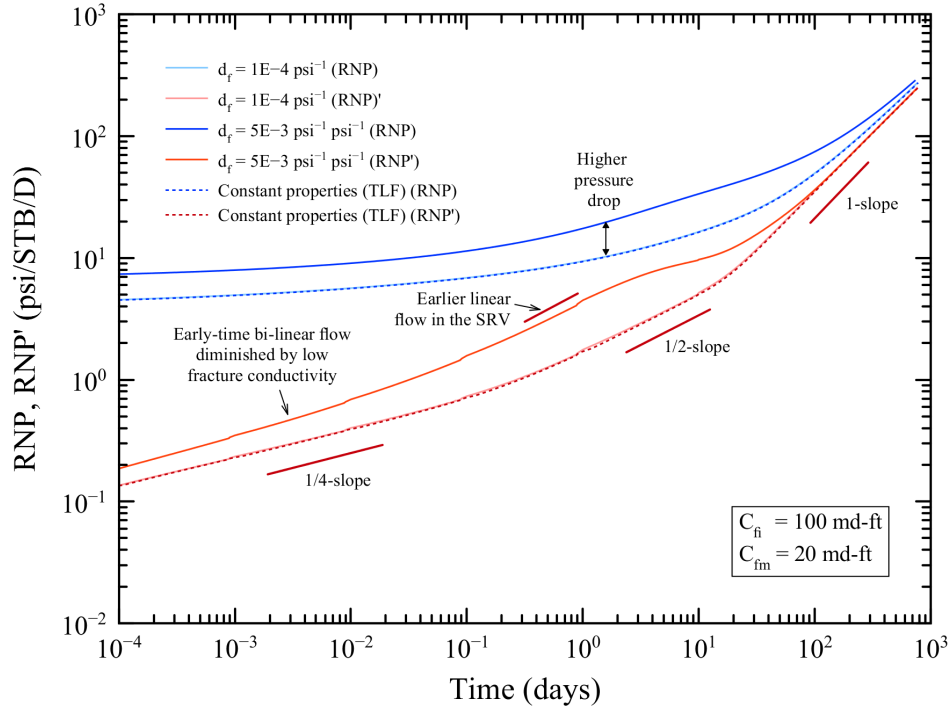


Figure 2.43: RNP and RNP' responses for $d_f = 1 \times 10^{-4}$ and $5 \times 10^{-3} \text{ psi}^{-1}$; $C_{fi} = 500 \text{ md-ft}$ and $C_{fm} = 100 \text{ md-ft}$.

Figure 2.44 shows the evolution of fractional reduction of fracture conductivity for $d_f = 1 \times 10^{-4}$ to $5 \times 10^{-3} \text{ psi}^{-1}$ as a function of time. Realize that initial fracture conductivity drops by 50% after 10, 30 and 100 days of constant-rate withdrawal when $d_f = 3 \times 10^{-3}$, 2×10^{-3} and $1 \times 10^{-3} \text{ psi}^{-1}$, respectively. Nonetheless, note that fracture conductivity drop to almost its critical value within 50 days when $d_f = 5 \times 10^{-3} \text{ psi}^{-1}$. The latter result may be the cause of the higher RNP and RNP' responses, observed in Figure 2.43.

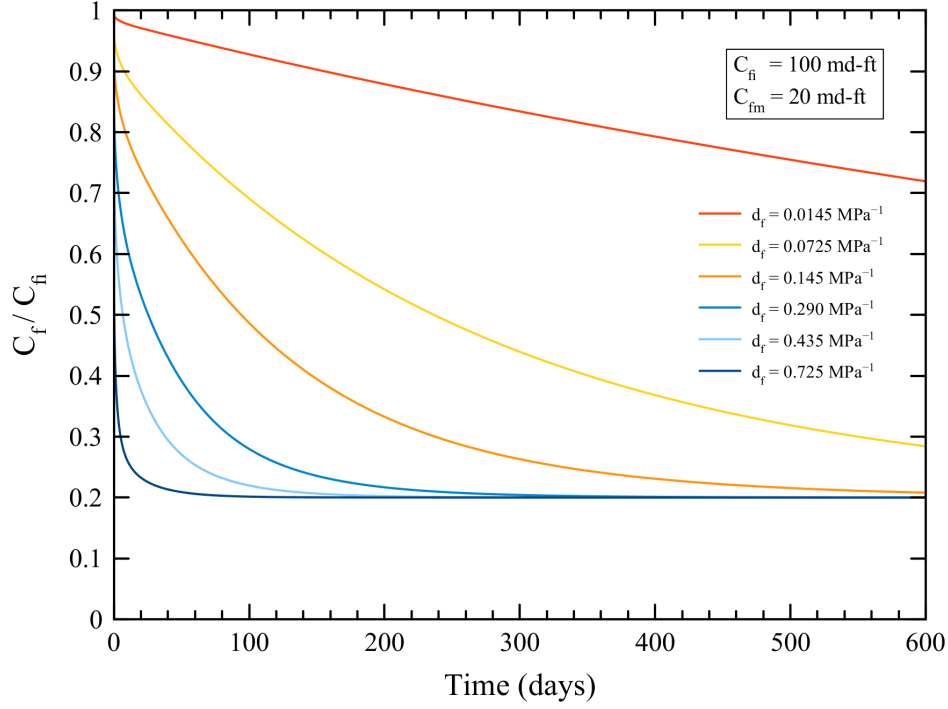


Figure 2.44: Evolution of fractional reduction of fracture conductivity for $d_f = 1 \times 10^{-4}$ to $5 \times 10^{-3} \text{ psi}^{-1}$; $C_{fi} = 100 \text{ md-ft}$ and $C_{fm} = 20 \text{ md-ft}$.

2.12.3 Impact of Simultaneous Pressure-Dependent SRV Permeability and Fracture Conductivity on Well Performance

In this section, we examine pressure-transient behavior for the following scenarios:

- Case 1: $\gamma_1 = 5 \times 10^{-4} \text{ psi}^{-1}$ and $d_f = 5 \times 10^{-4} \text{ psi}^{-1}$
- Case 2: $\gamma_1 = 1 \times 10^{-3} \text{ psi}^{-1}$ and $d_f = 5 \times 10^{-4} \text{ psi}^{-1}$
- Case 3: $\gamma_1 = 1 \times 10^{-3} \text{ psi}^{-1}$ and $d_f = 1 \times 10^{-3} \text{ psi}^{-1}$
- Case 4: $\gamma_1 = 3 \times 10^{-3} \text{ psi}^{-1}$ and $d_f = 1 \times 10^{-3} \text{ psi}^{-1}$

We assume $\gamma_2 = 5 \times 10^{-6} \text{ psi}^{-1}$. Initial and retained fracture conductivities are 100 and 20 md-ft, respectively. In case 1 fracture conductivity is more sensitive to pressure decline than SRV permeability. Case 2 is the opposite version of case 1. In Case 3 fracture conductivity and SRV permeability vary at equal rate with pressure-drawdown, resembling the pseudo-pressure approach. Lastly, Case 4 relates to the more realistic situation where, although rock properties are pressure-dependent, SRV permeability drops faster with pressure decline than fracture conductivity (Suarez-Rivera et al., 2013).

Figure 2.45 illustrates the expected BHP responses for the four cases along with the TLF model response. As in previous cases, the TLF model fails to capture actual pressure behavior due to the assumption of constant properties. Notice that BHP response for cases 2 and 3 are substantially different; however, BHP response of cases 2 and 3 is somewhat similar. However, BHP response from Case 4 is intricate and involves the equilibration of SRV permeability and fracture conductivity at different times.

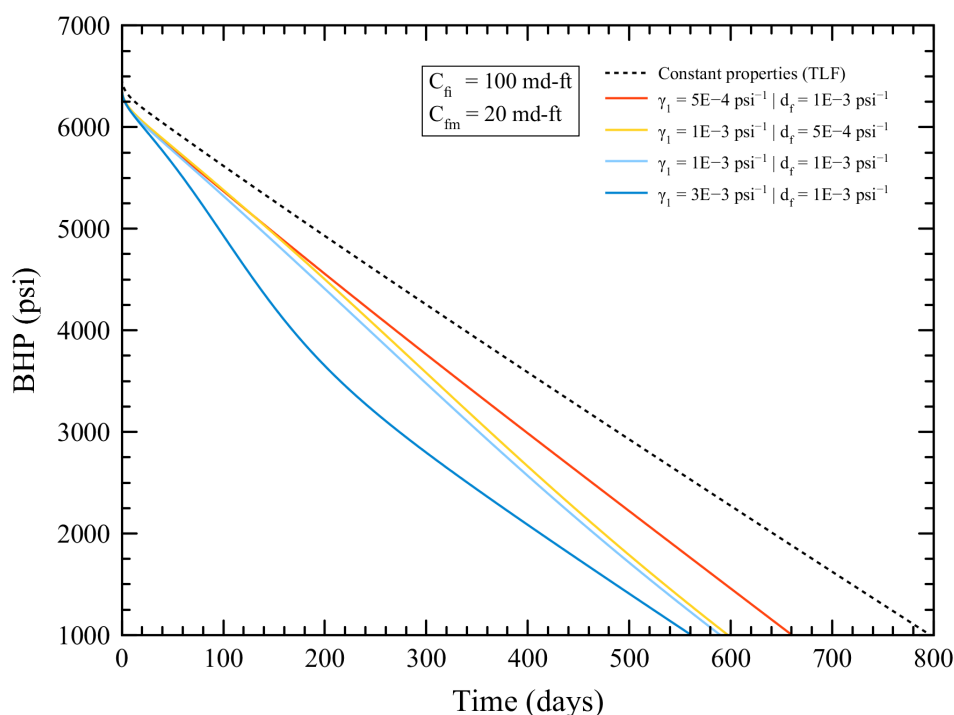


Figure 2.45: BHP response as a function of stress-sensitive characteristic number, SRV permeability modulus and time.

Figure 2.46 shows RNP and RNP' responses for cases 3 and 4. Note that the TLF model seems again off from the expected pressure-transient response. Actually, RNP and RNP' for cases 3 and 4 are slightly higher than that of the TLF, which indicates early loss of fracture conductivity, as discussed in the previous section. Moreover, the linear flow regime in the SRV for the pressure-dependent cases is shorter than expected. Specifically, RNP' of case 4 promptly increases to join its RNP counterpart, both exhibiting a unit-slope during a short period, which may be indicative of an apparent BDF regime. Finally, RNP and RNP' split up. This also occurs with RNP and RNP' responses for case 3; however, the apparent BDF slowly dissipates.

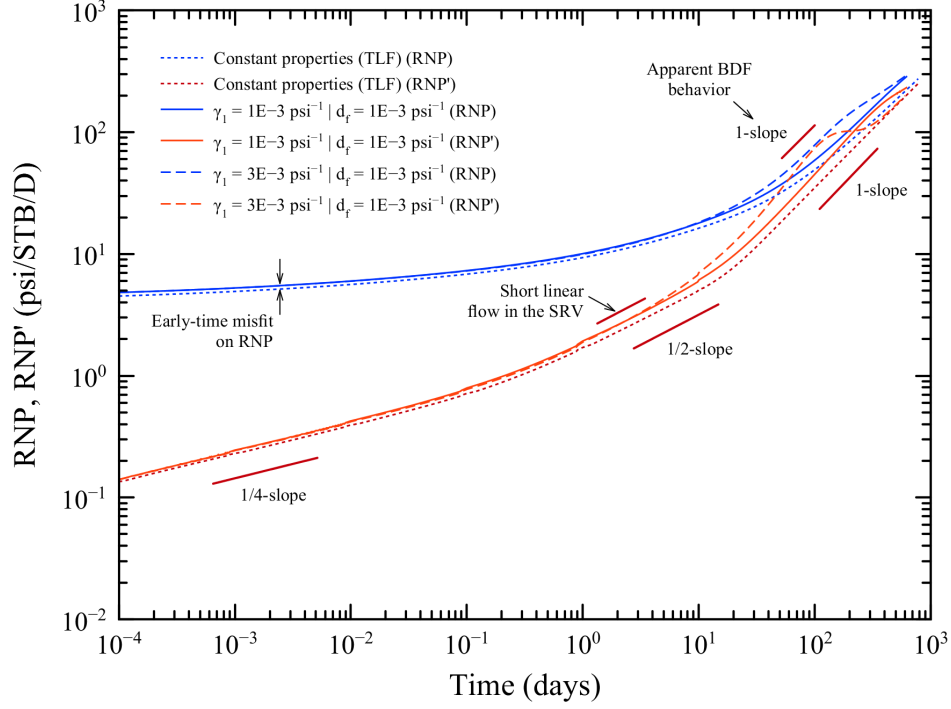


Figure 2.46: Comparison of RNP and RNP' responses for cases 3 and 4.

Finally, prediction of the onset of two-phase flow effects due to reaching bubble-point pressure in the MFHW is not sensibly different between cases 1, 2 and 3. Nevertheless, as discussed earlier, highly pressure-sensitive SRV permeability can lead to a steep drop in BHP until it reaches its final equilibrium, or critical, permeability value.

2.13. Discussion

We propose an analytical model that incorporates localized variations in rock and fluid properties with pressure depletion to examine their impact on expected performance of multi-fractured horizontal wells. Pressure-dependent properties are modeled as exponential functions of local pressure-drawdown, which allows assigning unique pressure-dependent rock properties to the different regions of the MFHW (i.e. matrix, SRV and fracture). In this manner, we are able to model the more realistic case where SRV and fracture properties vary with pressure at different rates. Such behavior cannot be captured with the application of pseudo-functions which unfortunately are common ground for most of the analytical MFHW models available in the literature.

One interesting observation made in this study is that pressure-dependent properties do not affect pressure-transient behavior or well performance during early-to-mid-times production when initial fracture conductivity is relatively large (> 500 md-ft), even if it is highly sensitive to pressure decline. On the other hand, we observe that dependency of SRV permeability on pressure decline can largely affect both pressure response and performance of the MFHW. We observe that the characteristic BHP response to this case is complex and involves changes in the rate at which BHP declines with time. We further proposed a simple straight-line method to determine the time at which SRV permeability had reached its critical value. Furthermore, effect of pressure decline on SRV permeability may induce a unit-slope response of RNP and RNP', or apparent BDF regime, during mid to late times while SRV permeability reaches steady state. Likewise, we observe that low initial fracture conductivity causes a positive shift in RNP and RNP' responses with respect to the TLF model, indicative of high-rate loss of fracture conductivity at very early times which continues until it reaches its steady state, or critical, value. This value is often referred to as the retained fracture conductivity under high confining stress.

Note that our analytical model does not apply to single-phase compressible flow and multi-phase flow. Nevertheless, as the proposed analytical solution method involves an iterative algorithm, it may be feasible to develop a more generalized governing equation in which rock and fluid properties do not necessarily exhibit exponential behavior with pressure-drawdown. In such case, instead of defining nonlinear scaling parameters, the (normalized) diffusivity coefficient would become pressure-dependent and will be up-dated iteratively as pressure depletion progresses.

In addition, wellbore storage (WBS) effects can be quite significant in MFHWs particularly when the lateral length is considerably large (e.g. > 5000 ft). Fortunately, WBS effects can be readily incorporated into the analytical solution derived in this paper by following the method proposed by Brown (2009). Constant-rate production may itself be a limitation to the application of our analytical MFHW model for production forecast. Long-term yield and EUR of a MFHW are typically estimated by means of rate-transient analysis (RTA) which implies the use of constant-pressure and/or variable-rate/variable-pressure conditions.

2.14. Conclusions

We developed an analytical MFHW model, based on the TLF model, where rock and fluid properties vary exponentially with pressure decline. Unlike existing analytical MFHW models that use pseudo-pressure/pseudo-time to account for pressure-dependent properties, our model allows assigning individual rock properties to each of the regions of the MFHW. That is, matrix, SRV and fracture are assigned a unique set of pressure-dependent properties. In this manner, we model the more realistic scenario where SRV permeability, mainly due to the presence of unpropped fractures, declines faster with pressure-drawdown than fracture conductivity. As such, our analytical model enables assessing the impact of simultaneous decline in SRV permeability and fracture conductivity with pressure depletion on well performance forecast and estimation of onset of two-phase flow effects due to reaching bubble-point pressure.

Our model uses the assumption of single-phase, slightly-compressible fluid-flow in the MFHW hence it is not able to handle multi-phase flow due to either pressure dropping below bubble-point pressure of co-produced water flowing along with oil. Given this limitation, we rather focused on examining pressure-transient behavior and well performance up to reaching bubble-point pressure conditions. The introduction of the exponential definition for normalized pressure, in conjunction with the definition of nonlinear scaling parameters, enabled the linearization of the governing equations for the composite system. The analytical pressure-transient solution is found in Laplace domain and it is inverted back into time domain numerically. We introduce an iterative algorithm to estimate the nonlinear scaling parameters, local average pressure-drawdowns and BHP, simultaneously.

Our pressure-dependent MFHW model was successfully validated against numerical simulations. We observed that the sensitivity of SRV permeability to pressure decline can largely affect well performance, leading to an early reaching of bubble-point pressure in the MFHW. Foremost, simultaneous reduction in fracture conductivity and SRV permeability with pressure decline, the latter exhibiting a faster decline trend, significantly reduce the expected yield of a MFHW. Therefore, it is necessary to account for the fact that fracture conductivity and SRV permeability vary at different rates with pressure-drawdown in order to make more realistic estimation of well productivity and performance forecast, at least, until the composite system reaches bubble-point pressure.

In general, our analytical MFHW model with pressure-dependent rock and fluid properties delivers accurate prediction of pressure- transient behavior and well life when constant-rate production and single-phase flow conditions are ensued in the MFHW.

3. Analytical Model to Estimate the Fraction of Frachits in a Multi-Well Pad

3.1. Background

Tightening well spacing while pumping larger hydraulic fracturing jobs was deemed as the most practical solution to maximize recovery and boost revenue from shale plays in North America. However, drilling infill (or child) wells too close to depleted offset (or parent) wells may actually have an adverse impact on long-term productivity and safety of the multi-well pad. The pressure-depleted region surrounding the parent well acts as a pressure sink that "attracts" hydraulic fractures from the infill well, thus allowing pressure communication between infill and offset wells. This process is known as fracture-driven interactions (FDI), more commonly referred to as fracture hits or "frac hits" (Jacobs, 2017a).

Frac hits relate to the propagation of hydraulic fractures from child wells into other existing fractures, either primary or secondary, from neighboring wells (Lawal et al., 2013). This mode of well interference may result in temporary or permanent loss of productivity (King et al., 2017; Garza et al., 2019). In addition, because of the potentially high-pressure difference between offset and infill wells, frac hits may induce blow-outs from offset wells (Jacobs, 2017b). In general, frac hits can occur through either primary (hydraulic) or secondary fractures (natural/induced fracture network) (Jia et al., 2017; Frohne and Mercer, 1984). Figure 3.1 shows a schematic of the two types of frac hits between infill and offset wells.

The degree of severity of the pressure connectivity is directly related to the number of fractured stages in communication. The key physical mechanisms responsible for the generation of frac hits are stress shadowing (Peirce and Bungler, 2015; Daneshy, 2014) and poroelastic effects (Seth et al., 2019), both due to substantial differences in zonal reservoir pressure across wells. The difference in pressure between wells is due to the offset wells being depleted, typically 6 to 12 months, before infill wells are drilled and completed.

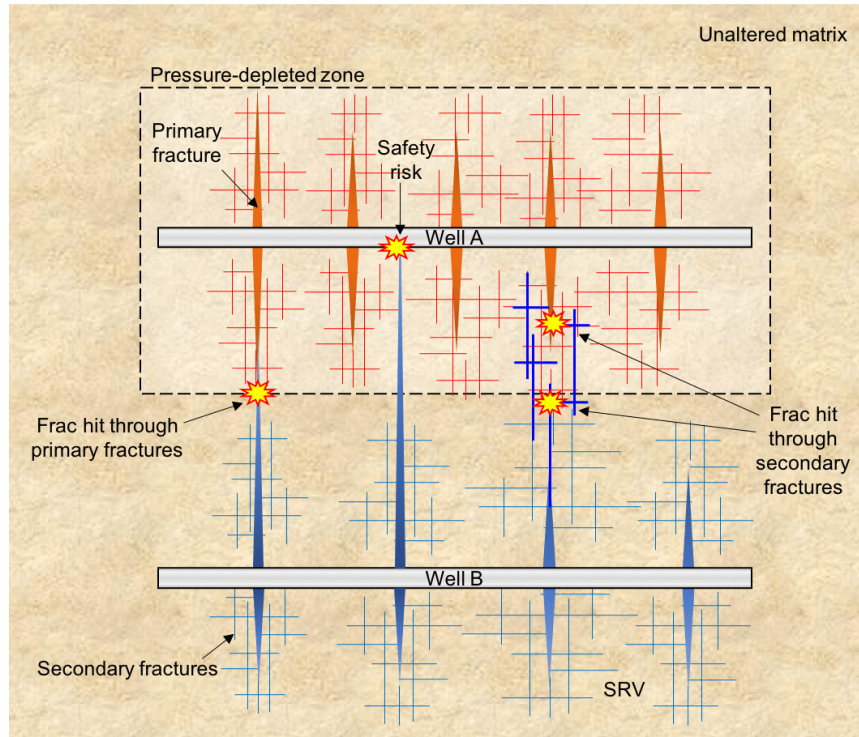


Figure 3.1: Frac hits through primary and secondary fractures allowing pressure communication between the parent well (A) and child well (B).

Frac hits not only happen between MFHWs landed in the same low-perm formation but also across stacked pay zones. When treatment pressure in the infill well overcomes the stress barrier segmenting a stacked formation play, primary fractures are allowed to grow along and across the path of least resistance. In this case, this path is the pressure-depleted region surrounding the parent wells (Minkoff et al., 2003; Roussel and Sharma, 2010; Huang et al., 2019). Figure 3.2 shows the gunbarrel view, or wine-rack configuration, of a multi-well pad with frac hits covering two stacked pay zones.

As mentioned earlier, frac hits are a major concern for two reasons. First, they are a serious safety risk to field operations. Second, frac hits have a negative impact on infill well performance and ultimate recovery in multi-well pads. For these reasons, shale oil and gas operators, service companies and regulatory agencies have been working closely to develop methods and procedures aimed at predicting or, at least, mitigating the occurrence of frac hits when MFHWs are tightly spaced.

Recently, several techniques aimed at mitigating frac hits during the completion of infill wells have delivered positive results. One of such techniques is pressure recharge of offset wells (e.g. Gala et al., 2018; Jacobs, 2018). The working principle of this method

is the repressurization of the parent well to compensate for the increase in effective stresses. Bommer et al. (2017) reported the successful application of offset-well repressurization in a six-well zipper project in the Bakken Formation.

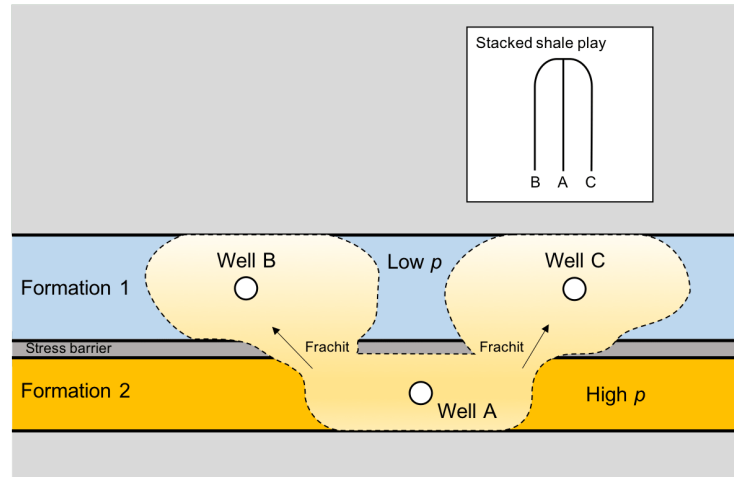


Figure 3.2: Gunbarrel view of a multi-well pad with frac hits across different target formations. In spite of being spatially separated, wells A, B and C are interconnected through frac hits.

Preventive refracturing of parent wells is another method for protection against frac hits (King et al., 2017). Garza et al. (2019) discuss the application of refrac treatments pumped into offset wells before drilling and completing infill wells. Authors assert that preventive refracs reduce the chances of getting loss of productivity in offset wells and improves the performance of the child well.

Far-field diversion is another frac hits prevention method in which diverters are deployed into the child well during the hydraulic fracturing job. The objective of is to prevent uncontrolled length growth of the newly-created hydraulic fractures toward depleted zones around offset wells. Zhang et al. (2019) presented a statistical analysis in which wells impacted by far-field diverters exhibit an increment in EUR compared to offset wells. Other similar studies have also reported positive results for the implementation of far-field diversion (Vidma et al., 2018,0; Rodionov et al., 2017).

Aside from these preventive techniques, there have been other methods trialed in the field, including leaving the offset well open to flow during the fracturing job, shutting in the well (short or long term) and monitoring pressure response while the infill well is fractured (King et al., 2017). In despite of these techniques, reports of the occurrence of frac hits continue to grow across US basins.

3.2. Statement of the Problem

Several methods for detection and assessment of impact of frac hits on well performance and estimated ultimate recovery (EUR) have been proposed in the literature. Ajani and Kelkar (2012) examined fracture data and production data from 179 wells in the Arkoma basin and estimated the loss of gas production due to frac hits. Authors concluded that offset wells were impacted by child wells. Lawal et al. (2013) and Yadav and Motealleh (2017) implemented rate-transient analysis (RTA) specialized plots combined with straight-line analysis, to study the impact of frac hits on well productivity and EUR. However, none of these studies quantify the actual number of frac hits.

Sardinha et al. (2014) used pre-flowback pressure data from 10 MFHWs in the Horn River basin to assess the overall connectivity in the pad. Authors estimated the ratio of total number of recorded pressure hits to the total number of possible pressure hits between two wells. Awada et al. (2016) proposed a workflow for the identification of well interference mechanism and subsequent numerical simulation modeling to accurately estimate the impact of frac hits on well productivity. In their work, authors assert that MFHWs must be isolated from their pads or “gathering systems” to be able to diagnose interference effects accurately. Authors recommend well shut-ins to examine pressure behavior in offset wells in response to operational changes in the active MFHW.

Molina and Zeidouni (2017b) introduced an analytical pressure-transient analysis (PTA) model to detect and assess the fraction of frac hits between two MFHWs without the need for any shut-ins; however, wells must be flowing at constant rate. Authors introduced the degree of well interference coefficient δ_w , defined as the ratio of frac hits to the total number of possible frac hits, as a history-matching parameter. The main drawback from this approach is that another interference coefficient should be known beforehand; this coefficient is strongly dependent on wells’ dimensions and properties.

Numerical models have also been proposed. These models often add more layers of complexity to the problem, like non-planar or complex fractures in stacked plays (e.g., Cao et al., 2017; Marongiu-Porcu et al., 2015; Tang et al., 2017; Yu et al., 2018). The application of such models, however, is restricted to proprietary software and requires the numerical model to be fed with specialized information from the multi-well pad (well profile, fracture network/density, direction and magnitude of in-situ stresses, etc.)

The objective of this chapter is to develop an analytical model that can be used to detect well interference effects due to frac hits and estimate the fraction of frac hits be-

tween MFHWs based on the application of PTA to a generalized MFHW model, where fluid-flow is approximated by a combination of several linear-flow regimes. In such model, frac hits are modeled as a boundary condition that allows inter-well pressure communication through primary fractures. Pressure connectivity is governed by the fraction of frac hits in the infill well (δ_{wAB}) and the bottomhole-pressure differential $\Delta p_{wAB} = |\Delta p_{wA} - \Delta p_{wB}|$, where $\Delta p_{wj} = p_i - p_{wj}(t)$ is the pressure-drawdown of well $j = A, B$.

δ_{wAB} is used as the history-matching parameter between the analytical solution and synthetic pressure data, generated via numerical simulations. The proposed model considers single-phase, slightly compressible fluid-flow in a multi-well pad in which fractures are planar and wells are perfectly parallel to each other. Moreover, MFHWs are landed in the same pay. The analytical solution to the frac hits model is derived in Laplace domain and inverted into time domain numerically (Stehfest, 1970). Different sensitivity analyses are performed and history-matched rate-normalized type-curves are presented and discussed for each case study.

3.3. Conceptualization of the Frac Hits Model

Pressure communication through the matrix in ultra-low perm formations is negligible when primary fracture and frac hits conductivity is relatively high (e.g. >100 md-ft) (Yu et al., 2016). Therefore, if MFHWs are fairly spaced in a multi-well pad, each well would function as an isolated “vessel” that operates independent from others. From this perspective, and in the absence of frac hits, multi-well pads can be deemed as gathering systems for several isolated vessels. The concept of independent vessels for two multi-fractured wells is depicted in Figure 3.3.

If frac hits are present, on the other hand, MFHW performance becomes inter-well-dependent. Since pressure communication takes place through the frac hits, interfering wells eventually become branches of a unitized well pad. In this case, the assumption of wells operating as independent vessels does not hold anymore. More importantly, changes in the operating conditions of a well influence interconnected wells.

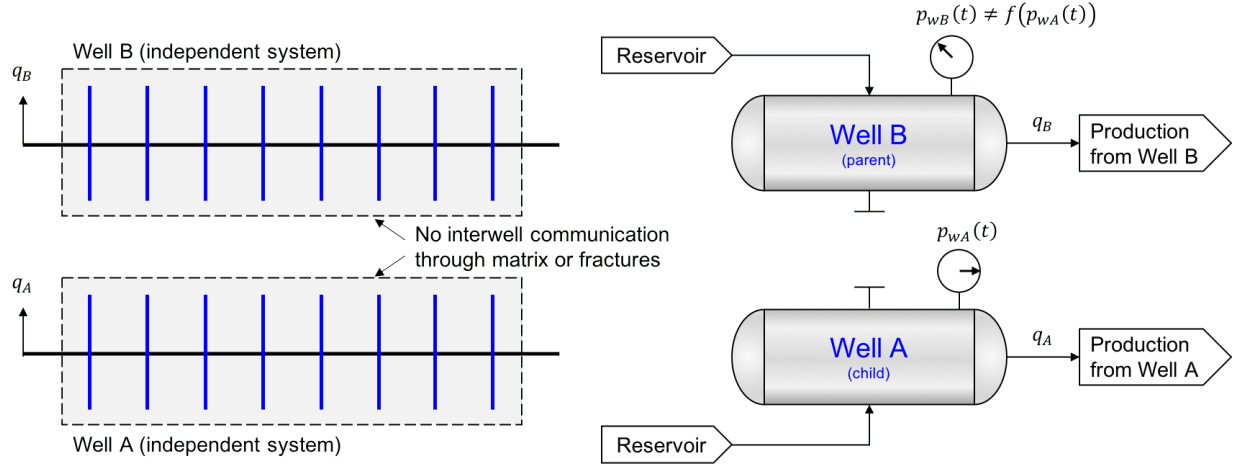


Figure 3.3: A two-MFHW pad represented as two individual vessels. Operating conditions from well A (child well) do not influence performance of well B (parent well).

From a thermodynamics perspective, total energy in a multi-well pad will tend reach an equilibrium condition with its surroundings. Under the presumption of interfering wells becoming branches of a unitized pad, we hypothesize that pressure, as a form of energy density (i.e. energy per unit volume), will ultimately equilibrate across interfering wells. Hence, in the presence of frac hits, $\Delta p_{wAB}(t) = |\Delta p_{wA}(t) - \Delta p_{wB}(t)|$ should exhibit a tendency to plateau toward its final equilibrium condition. On the contrary, $\Delta p_{wAB}(t)$ will continue to grow in the absence of any form of pressure communication.

Figure 3.4 conceptualizes frac hits as a “valve” connecting vessels A and B. The “aperture” of this valve, defined as $0 \leq \delta_{wAB} \leq 1$, is directly proportional to the fraction of frac hits. $\delta_{wAB} = 0$ indicates no frac hits; $0 < \delta_{wAB} < 1$ indicates partial pressure communication; and, $\delta_{wAB} = 1$ indicates full frac hits (i.e. all fractures between wells A and B are in communication). Furthermore, we define $\Delta p_{wAB}(t) = \varepsilon_{AB}(p_{wB}(t) - p_{wA}(t))$ while assuming that the leakage rate across interfering wells is proportional to $\Delta p_{wAB}(t)$. ε_{AB} sets the direction of flow as follows: $\varepsilon_{AB} = 1$ if $q_A > q_B$; otherwise, $\varepsilon_{AB} = 0$.

Realize that the speed at which pressure stabilizes across wells A and B in Figure 3.4 depends on the aperture of the valve. Hence, the rate of stabilization must be a function of δ_{wAB} because the higher δ_{wAB} the faster $\Delta p_{wAB}(t)$ will reach equilibrium. Therefore, δ_{wAB} makes possible to both detect frac hits and assess the fraction of frac hits between wells A and B. This is the fundamental hypothesis of the analytical frac hits model developed in this chapter.

Here, we assume that wells have equal number of fractured stages, with one hydraulic fracture per stage (frac-sleeve-type completion). Moreover, fractures are planar. We too consider that frac hits conductivity is equal to the average fracture conductivity of well A. Furthermore, we assume that wells are landed in the same formation (Figure 3.5a). Lastly, transience effects within frac hits are assumed negligible.

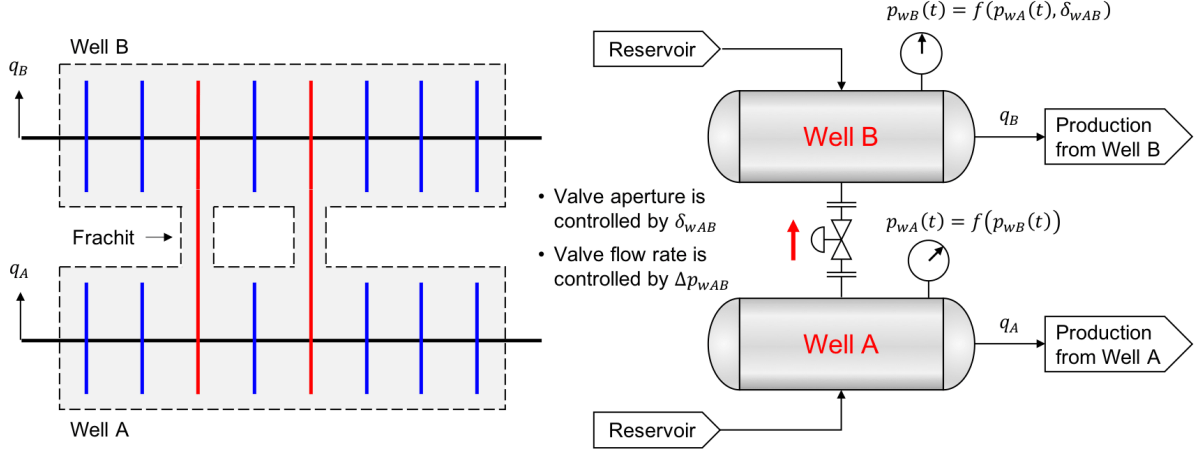


Figure 3.4: Frac hits between two MFHWs interpreted as a “valve” connecting two vessels. Valve “aperture” is controlled by $\delta_{wAB} \in [0, 1]$ while leakage rate across vessels is proportional to $\Delta p_{wAB} = \varepsilon_{AB}(p_{wB} - p_{wA})$.

In reality, MFHWs can have different number of primary fractures. Consequently, it is both sound and convenient to define δ_w on a per-well basis rather than on a global basis. In this sense, let us define δ_{wAj} as the ratio of total frac hits between wells A and j, $(n_{fh})_{Aj}$, where well j is located immediately next to well A (Figure 3.5b), to the total number of primary fractures in well A, n_{fA} :

$$\delta_{wAj} = \frac{(n_{fh})_{Aj}}{n_{fA}} \quad (3.1)$$

The former definition can be readily extended to wells $j = B$ and C using well A as the reference point:

$$\delta_{wAj} = \frac{(n_{fh})_{Aj}}{n_{fj}} = \frac{(n_{fh})_{Aj}}{n_{fA}} \times \frac{n_{fA}}{n_{fj}} = \delta_{wAj} \left(\frac{n_{fA}}{n_{fj}} \right) \quad (3.2)$$

As an example, consider the two-MFHW system discussed earlier and further suppose

that $n_{fA} = 50$ and $n_{fB} = 65$. According to Equation 3.2, $\delta_{wBA} = 0.769\delta_{wAB}$. This result is sound as, although the number of frac hits is equal in both wells, the degree of well interference of well B must be smaller as it has more fractures than well A.

Equation 3.1 and 3.2 will be used in the derivation of the frac hits boundary condition for the fluid-flow model, described in Section 3.6.

3.4. Proposed Methodology

We develop an analytical single-phase, fluid-flow model for a three-MFHW pad in an oil-rich low-perm formation. Since MFHWs are landed in the same pay, frac hits are only allowed between wells A and B and wells A and C (Figure 3.5b). As such, well A is defined as the reference MFHW in the pad. Rock and fluid properties are considered constant and independent of changes in pressure.

We introduce the quad-linear flow (QLF) model for each MFHW as the basis of the fluid-flow model of the multi-well pad. Unlike the trilinear flow (TLF) model (Brown et al., 2011) or five-region flow (FRF) model (Stalgorova and Mattar, 2013), in which well dimensions must be symmetric, QLF model can easily handle asymmetric well dimensions. Moreover, QLF accounts for two different fluxes coming from the matrix into the SRV of each well (Figure 3.6). Another novelty introduced with the QLF model is the availability of two boundary conditions, each located at the inner and outer fracture tip. In this manner, we can assign to each fracture tip either a frac-hit-type or a no-flux boundary condition. This procedure is discussed in detail in Section 3.5.

Earlier we discussed that a stabilization trend in $\Delta p_{wAB}(t)$ would be a clear indication of inter-well communication due to frac hits. Consequently, we define $\Delta p_{wAC}(t) = \varepsilon_{AC}(p_{wC}(t) - p_{wA}(t))$, with $\varepsilon_{AC} = 1$ if $q_A > q_C$ and 0 otherwise, as the parameter that allows the detection frac hits between wells A and C. The goal is to find analytical expressions for $p_{wA} = f(t, \delta_{wAB}, \delta_{wAC})$, $p_{wB} = f(t, \delta_{wAB})$ and $p_{wC} = f(t, \delta_{wAC})$ for which classical PTA techniques, such as diagnostic plots and type-curves analysis, can be applied to detect and estimate the fraction of frac hits in a multi-well pad. We define the following rate-normalized parameters that will be used for PTA analysis:

$$\text{RNP}_{Aj} = \varepsilon_{Aj} \frac{\Delta p_{wA}(t) - \Delta p_{wj}(t)}{q'_t} \equiv \frac{\Delta p_{wAj}(t)}{q'_t} \quad (3.3)$$

$$\text{RNP}'_{Aj} = \frac{1}{q'_t} \frac{d\Delta p_{wAj}(t)}{d \ln t} \quad (3.4)$$

In the equations above, q'_t is the total equivalent per-fracture production rate of the multi-well pad, as defined in Equation 3.6.

Frac hits are artificially created in the numerical model by interconnecting primary fractures between wells A-B and A-C. We denote the actual fraction of frac hits by δ_{wAB}^* and δ_{wAC}^* . Validation of the model is carried out by history-matching the analytical solution with numerical data. Since the fractions of frac hits of the numerical model are known, we compare the history-matched values of δ_{wAB} and δ_{wAC} against δ_{wAB}^* and δ_{wAC}^* and compare how accurate would the estimation of frac hits be by means of the analytical model.

Subsequently, we evaluate the sensitivity of δ_{wAB} and δ_{wAC} to relevant reservoir and well properties, such as distance between MFHWs, fracture half-length, fracture conductivity, SRV permeability and distance between fractured stages.

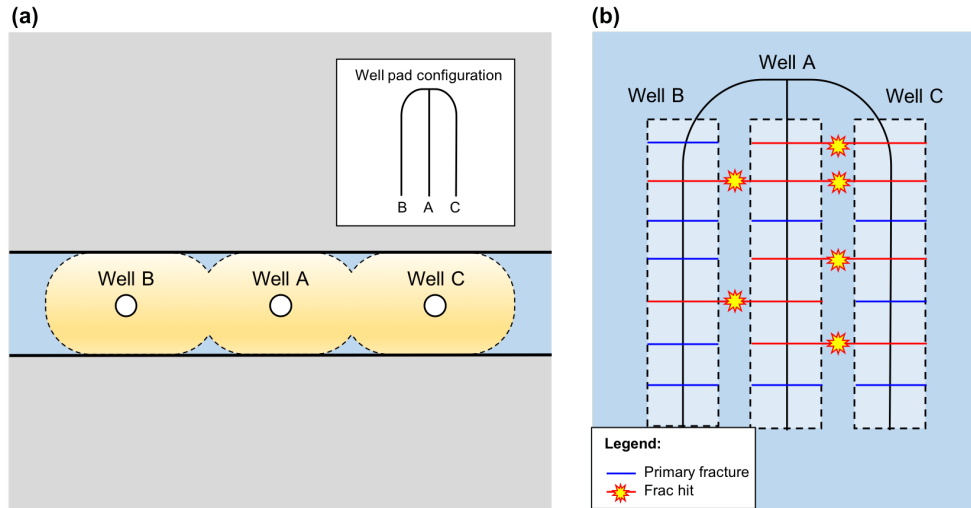


Figure 3.5: Conceptualization of the frac hits model for a three-MFHW pad system. (a) Wells A, B and C were drilled and completed in the same target zone, (b) Frac hits can be present at several fractured stages.

3.5. Mathematical Modeling—Part I: The Fluid-flow Model

3.5.1 General Remarks

Alike the TLF and FRF fluid-flow models for MFHWs, the proposed analytical approach is based on modeling MFHW as a well with a single primary fracture using the equivalent per-rate approach. This simplification assumes that all primary fractures of a MFHW can be represented by a single fracture with equivalent per-fracture flow rate, defined as $q'_j = (q_{\text{well}})_j / n_{fj}$ [STB/D/fracture]. The most significant assumption behind this definition of q'_j is that all primary fractures in well j are active and flowing at the same rate.

Now, suppose that, due to some operational issue constraint, some stages were shut-in during the collection of pressure-transient data from the pad. Although current analytical MFHW models (i.e. TLF and FRF) cannot accommodate for such scenario, we introduce a more accurate definition for q'_j that enables accounting for isolated stages in our model, as follows:

$$q'_j = \left(\frac{q_{\text{well}}}{\delta_p n_f} \right)_j \quad (3.5)$$

where $0 < \delta_p \leq 1$ is the fraction of fractures in well j that were active during the gathering of pressure data. Following this definition, we define the total equivalent per-fracture flow rate from the three-MFHW pad under discussion:

$$q'_t = \left(\frac{q_{\text{well}}}{\delta_p n_f} \right)_A + \left(\frac{q_{\text{well}}}{\delta_p n_f} \right)_B + \left(\frac{q_{\text{well}}}{\delta_p n_f} \right)_C \quad (3.6)$$

We setup the analytical fluid-flow model based on the single-fracture and per-fracture equivalent rate approached using the definition of q'_j given by Equation 3.5. A schematic of the multi-MFHW pad under analysis is presented in Figure 3.6.

Note from Figure 3.6 that fluid-flow across each single-fracture well is modeled as the combination of four separate linear flows. We call this flow modeling approach the quad-linear flow model or QLF. The four combined-linear flow regimes are:

- Matrix to SRV (outer matrix, Oj)
- Matrix to SRV (inner matrix Ij)
- SRV to fracture ($1j$)
- Fracture to well (fj)

$j = A, B$ and C . In general, we can say that the fluid-flow model for the three-MFHW scenario is simply the result of assembling three QLF wells together. The distance from well j to the outermost boundary in the x -axis is dictated by the average half-distance between fractured stages on each MFHW. The outermost boundary with respect to the y -axis on wells B and C are given by the well site configuration of the pad in the formation.

Because wells B and C are placed at different locations with respect to well A , we conveniently define a coordinate system to simplify the process of deriving the governing equations and boundary conditions for each well. To begin with, we align all wells at $x = 0$ thus we can use the x -axis to define horizontal coordinates for all wells. With respect to the y -axis, we provide each well with its own y -axis relative to the original y -axis in well A . In summary:

$$x_A = x_B = x_C = x \quad (3.7)$$

$$y_A = y \quad (3.8)$$

$$y_B = y - L_{AB} \quad (3.9)$$

$$y_C = y + L_{AC} \quad (3.10)$$

L_{AB} is the distance between wells A and B and L_{AC} between wells A and C . Note that wells B and C are conveniently located at $y_B = 0$ and $y_C = 0$, respectively. Normalized Cartesian coordinates are presented in Section A.3.1 and Section A.3.2.

An important issue arises when defining which portion of the inner matrix between wells A and B , also between wells A and C , would be drained by each well. The depth of investigation into this region depends on several parameters, including fracture half-length (x_{fj}), SRV permeability (k_{1j}), and per-fracture flow rate (q'_j).

However, assigning a dynamic inner matrix boundary to each well would introduced undesired nonlinearities that largely jeopardize the practicality of the model. Instead,

we assume that the maximum depth of investigation accessed by well j into the inner matrix region between wells A and j is proportional to the half-fracture length of each well. A no-flux boundary condition will be assigned at each of these boundaries.

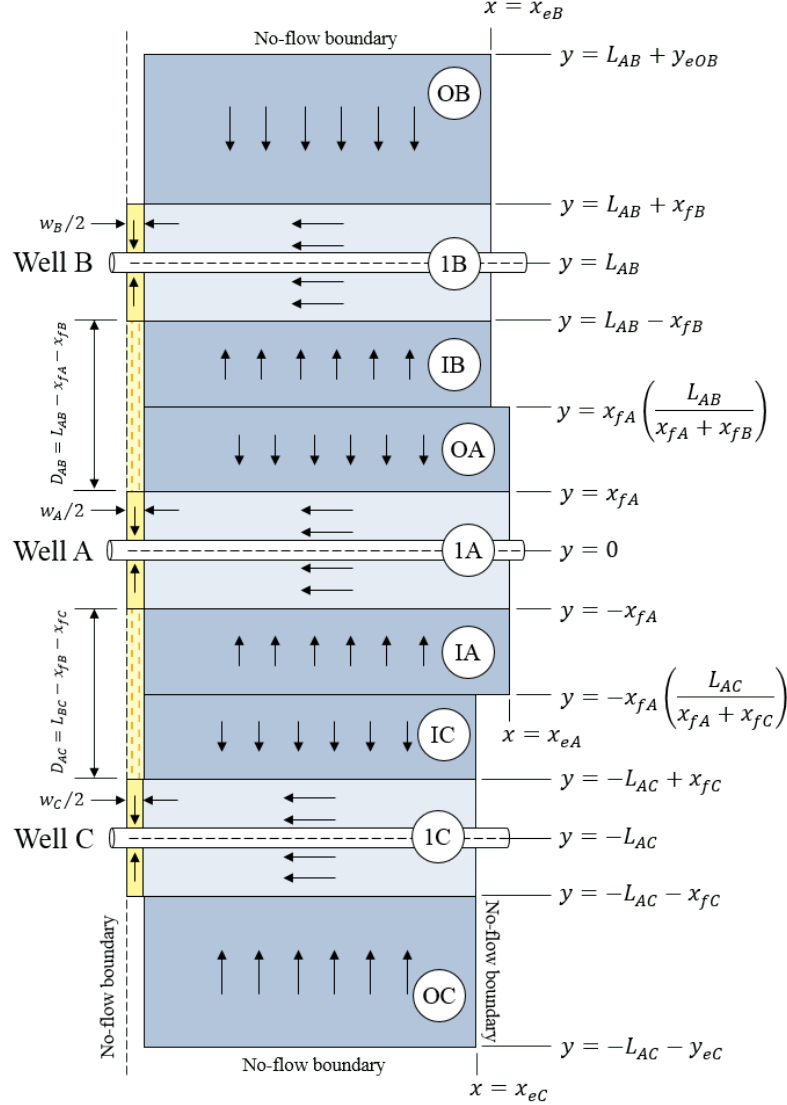


Figure 3.6: The three-MFHW-pad frac hits model based on the QLF model. Each well is modeled based on the single-fracture approach along with its corresponding equivalent per-fracture rate.

For instance, the outer matrix (y_{eOA}) and inner matrix (y_{eIA}) boundaries of well A are, respectively, defined as:

$$y_{eOA} = x_{fA} + [L_{AB} - (x_{fA} + x_{fB})] \frac{x_{fA}}{x_{fA} + x_{fB}} = x_{fA} \left(\frac{L_{AB}}{x_{fA} + x_{fB}} \right) \quad (3.11)$$

$$y_{eIA} = x_{fA} + [L_{AC} - (x_{fA} + x_{fC})] \frac{x_{fA}}{x_{fA} + x_{fC}} = x_{fC} \left(\frac{L_{AC}}{x_{fA} + x_{fC}} \right) \quad (3.12)$$

Similar expressions for normalized dimensions and distances for wells A, B and C are given in Section A.4.1, Section A.4.2 and Section A.4.3, respectively.

3.5.2 General Assumptions

The following assumptions were made in the development of the QLF model: (1) single-phase, slightly-compressible flow, (2) constant rock and fluid properties, (3) homogeneous initial pressure across the multi-well pad, (4) planar hydraulic fractures, (5) MFHW can be modeled as a single-fracture well with an equivalent per-rate flow, defined as total flow rate divided by number of fractured stages, (6) flow from the untouched matrix into the wellbore can be approximated as a combination of four linear-flow regimes, (7) SRV is modeled as a rectangular region with permeability orders-of-magnitude higher than matrix permeability, (8) frac hits only occur between hydraulic fractures, and (9) all hydraulic fractures contribute equally (i.e. $\delta_{pA} = \delta_{pB} = \delta_{pC} = 1$).

Additionally, we assume frac hits can only happen between primary fractures of neighboring wells. As such, we do not consider the case of well interference effects due to the interaction between primary fractures and SRV of neighboring wells. Similarly, we ignore fluid-flow from the inner matrix region between wells into the fracture segment that connects primary fractures.

3.5.3 Derivation of Governing Equations

The general governing equation for 2-D porous flow of slightly-compressible fluid with constant rock and fluid properties is given by (Dake, 1983):

$$\frac{\partial^2 \Delta p_{rj}}{\partial x^2} + \frac{\partial^2 \Delta p_{rj}}{\partial y_j^2} + Q_{rj} \mu B = \frac{1}{\eta_j} \frac{\partial \Delta p_{rj}}{\partial t} \quad (3.13)$$

where Q_j is a general flux-sink term. We use Q_j to model the constant-rate well boundary condition in the fracture, in this manner freeing up two boundary conditions to be used when solving the governing equation for each fracture region. Additionally, r refers to the specific region in well j , i.e. matrix ($j = I, O$), SRV ($j = 1$) and fracture ($j = f$). Equation 3.13 can be written in dimensionless form as:

$$\frac{\partial^2 p_{rjD}}{\partial x_D^2} + \frac{\partial^2 p_{rjD}}{\partial y_{jD}^2} + Q_{rjD} = \frac{1}{\eta_{jD}} \frac{\partial p_{rjD}}{\partial t_D} \quad (3.14)$$

Assuming initial pressure is initially equal and constant throughout the system ($p_{rjD} = 0$ at $t_D = 0$), Equation 3.14 can be transformed into Laplace domain, which gives

$$\frac{\partial^2 \bar{p}_{rjD}}{\partial x_D^2} + \frac{\partial^2 \bar{p}_{rjD}}{\partial y_{jD}^2} + Q_{rjD} - \frac{s}{\eta_{jD}} \bar{p}_{rjD} = 0 \quad (3.15)$$

The normalized quantities p_{rjD} , x_D , y_{jD} , t_D and η_{jD} in Equation 3.14 are described in Appendix A.

3.5.3.1 Matrix (Regions I and O)

Fluid-flow in the matrix regions, both inner our outer, is assumed to be one-dimensional (i.e. linear) with respect to the y_j -axis. Therefore, the x_D component of Equation 3.15 can be neglected. This simplification leads to

$$\frac{d^2 \bar{p}_{rjD}}{dy_{jD}^2} - \frac{s}{\eta_{mD}} \bar{p}_{rjD} = 0 \quad (3.16)$$

where $r = I$ and O refers to the inner and outer matrix regions, respectively (see Figure 3.6). The subscript m in the dimensionless diffusivity coefficient indicates it is defined based on matrix properties.

3.5.3.2 SRV (Region 1)

The dimensionless governing equation for fluid-flow in the SRV region is given in Laplace domain as:

$$\frac{\partial^2 \bar{p}_{1jD}}{\partial x_D^2} + \frac{\partial^2 \bar{p}_{1jD}}{\partial y_{jD}^2} - \frac{s}{\eta_{1jD}} \bar{p}_{1jD} = 0 \quad (3.17)$$

Flow is assumed linear with respect to the x -axis in this region hence $\bar{p}_{1jD} \neq f(y_{jD})$. However, notice from Figure 3.6 that there are two external influxes coming into the SRV through the SRV/matrix interfaces. These boundaries are located at $y_{jD} = x_{fjD}$ and $y_{jD} = -x_{fjD}$.

The assumption $p_{1jD} \neq f(y_{jD})$ enables the integration of Equation 3.17 with respect to y_{jD} within the interval $y_{jD} \in [-x_{fjD}, x_{fjD}]$:

$$\int_{-x_{fjD}}^{x_{fjD}} \frac{\partial^2 \bar{p}_{1jD}}{\partial x_D^2} dy_{jD} + \int_{-x_{fjD}}^{x_{fjD}} \frac{\partial^2 \bar{p}_{1jD}}{\partial y_{jD}^2} dy_{jD} - \frac{s}{\eta_{1jD}} \int_{-x_{fjD}}^{x_{fjD}} \bar{p}_{1jD} dy_{jD} = 0 \quad (3.18)$$

As a result,

$$\frac{\partial^2 \bar{p}_{1jD}}{\partial x_D^2} + \frac{1}{2x_{fjD}} \left[\left(\frac{\partial \bar{p}_{1jD}}{\partial y_{jD}} \right)_{y_{jD}=x_{fjD}} - \left(\frac{\partial \bar{p}_{1jD}}{\partial y_{jD}} \right)_{y_{jD}=-x_{fjD}} \right] - \frac{s}{\eta_{1jD}} \bar{p}_{1jD} = 0 \quad (3.19)$$

Mass must be conserved across SRV/matrix boundaries. Therefore, assuming that both matrix and SRV properties are isotropic and homogeneous across regions, we derive the following flux-continuity relationships:

$$\left(\frac{\partial p_{1jD}}{\partial y_{jD}} \right)_{y_{jD}=x_{fjD}} = \frac{k_m}{k_{1j}} \left(\frac{\partial p_{OjD}}{\partial y_{jD}} \right)_{y_{jD}=x_{fjD}} \quad (3.20)$$

$$\left(\frac{\partial p_{1jD}}{\partial y_{jD}} \right)_{y_{jD}=-x_{fjD}} = \frac{k_m}{k_{1j}} \left(\frac{\partial p_{IjD}}{\partial y_{jD}} \right)_{y_{jD}=-x_{fjD}} \quad (3.21)$$

Transforming Equation 3.20 and 3.21 into Laplace domain and replacing the resulting expressions into Equation 3.19 yields

$$\frac{d^2 \bar{p}_{1jD}}{dx_D^2} + \frac{k_m/k_{1j}}{2x_{fjD}} \left[\left(\frac{d\bar{p}_{OjD}}{dy_{jD}} \right)_{y_{jD}=x_{fjD}} - \left(\frac{d\bar{p}_{IjD}}{dy_{jD}} \right)_{y_{jD}=-x_{fjD}} \right] - \frac{s}{\eta_{1jD}} \bar{p}_{1jD} = 0 \quad (3.22)$$

The flux-source terms $\left(\frac{d\bar{p}_{OjD}}{dy_{jD}} \right)_{y_{jD}=x_{fjD}}$ and $\left(\frac{d\bar{p}_{IjD}}{dy_{jD}} \right)_{y_{jD}=-x_{fjD}}$ will be ultimately determined based on the analytical solution for the inner and outer matrix regions for each individual well in the multi-well pad.

3.5.3.3 Fracture (Region f)

Fluid flow in the fracture is assumed one-dimensional along the y -axis. Well is modeled as a infinitesimal sink located at $y_{jD} = 0$. The governing equation for the fracture region in well j is given (in oilfield units) by

$$\frac{\partial^2 \Delta p_{fj}}{\partial x^2} + \frac{\partial^2 \Delta p_{fj}}{\partial y_j^2} + \frac{2\pi \times 141.2 q'_j \mu B}{k_{fj} w_j h} \delta(y_j) = \frac{1}{\eta_{fj}} \frac{\partial \Delta p_{fj}}{\partial t} \quad (3.23)$$

where q'_j [STB/D/fracture] is the per-fracture rate of well j (see Equation 2.92). Normalization, and subsequent transformation, of Equation 3.23 into Laplace domain, yields

$$\frac{\partial^2 \bar{p}_{fjD}}{\partial x_D^2} + \frac{\partial^2 \bar{p}_{fjD}}{\partial y_{jD}^2} + \frac{2\pi q'_{jD}}{s(F'_{CD})_j} \delta(y_{jD}) - \frac{s}{\eta_{fjD}} \bar{p}_{fjD} = 0 \quad (3.24)$$

Integration of Equation 3.23 with respect to x_D for $x_D \in [0, w_{jD}/2]$, leads to:

$$\int_0^{w_{jD}/2} \frac{\partial^2 \bar{p}_{fjD}}{\partial x_D^2} dx_D + \int_0^{w_{jD}/2} \frac{\partial^2 \bar{p}_{fjD}}{\partial y_{jD}^2} dx_D + \int_0^{w_{jD}/2} \left\{ \frac{2\pi q'_{jD}}{(F'_{CD})_j} \delta(y_{jD}) - \frac{s}{\eta_{fjD}} \bar{p}_{fjD} \right\} dx_D = 0 \quad (3.25)$$

Performing the integration with respect to x_D above, yields

$$\frac{d^2 \bar{p}_{fjD}}{dy_{jD}^2} + \frac{2}{w_{jD}} \left[\left(\frac{d\bar{p}_{fjD}}{dx_D} \right)_{x_D=w_{jD}/2} - \left(\frac{d\bar{p}_{fjD}}{dx_D} \right)_{x_D=0} \right] + \frac{2\pi q'_{jD}}{s(F'_{CD})_j} \delta(y_{jD}) - \frac{s}{\eta_{fjD}} \bar{p}_{fjD} = 0 \quad (3.26)$$

There are two boundary conditions within the range of integration: (1) axisymmetric condition (i.e. no-flow boundary) at $x_D = 0$, and (2) flux continuity across the SRV/fracture interface located at $x_D = w_{jD}/2$. These conditions are:

$$\left(\frac{\partial p_{fjD}}{\partial x_D} \right)_{x_D=0} = 0 \quad (3.27)$$

$$\left(\frac{\partial p_{fjD}}{\partial x_D} \right)_{x_D=w_{jD}/2} = \frac{k_{1j}}{k_{fj}} \left(\frac{\partial p_{1jD}}{\partial x_D} \right)_{x_D=w_{jD}/2} \quad (3.28)$$

Transforming these boundary conditions into Laplace domain and inserting them into Equation 3.27, results in:

$$\frac{d^2 \bar{p}_{fjD}}{dy_{jD}^2} + \frac{2k_{1jD}}{(F'_{CD})_j} \left(\frac{d\bar{p}_{1jD}}{dx_D} \right)_{x_D=w_{jD}/2} + \frac{2\pi q'_{jD}}{s(F'_{CD})_j} \delta(y_{jD}) - \frac{s}{\eta_{fjD}} \bar{p}_{fjD} = 0 \quad (3.29)$$

The flux-source term $\left(\frac{\partial \bar{p}_{1jD}}{\partial x_D} \right)_{x_D=w_{jD}/2}$ is later determined for each well in the pad.

3.5.4 Analytical Solution for Fluid-flow in Well A

3.5.4.1 Outer Matrix (Region OA)

The dimensionless pressure distribution in Laplace domain for Region OA ($r = O, j = A$), denoted by \bar{p}_{OAD} , is determined after finding the general solution to Equation 3.16:

$$\bar{p}_{OAD} = A_{OA} \cosh \left[(y_D - y_{eOAD}) \sqrt{\frac{s}{\eta_{mD}}} \right] + B_{OA} \sinh \left[(y_D - y_{eOAD}) \sqrt{\frac{s}{\eta_{mD}}} \right] \quad (3.30)$$

As discussed in Section 3.5.1, we assume that y_{eOAD} (Equation A.17) is the deepest

normalized distance the pressure disturbance from well A would reach into the matrix region between wells A and B (see Figure 3.6). Therefore, we prescribe a no-flow boundary condition at $y_D = y_{eOAD}$, given by

$$\left(\frac{d\bar{p}_{OAD}}{dy_D} \right)_{y_D=y_{eOAD}} = 0 \quad (3.31)$$

Replacing Equation 3.31 into 3.30, leads to:

$$\bar{p}_{OAD} = A_{OA} \cosh \left[(y_D - y_{eOAD}) \sqrt{\frac{s}{\eta_{mD}}} \right] \quad (3.32)$$

$$\frac{d\bar{p}_{OAD}}{dy_D} = A_{OA} \sqrt{\frac{s}{\eta_{mD}}} \sinh \left[(y_D - y_{eOAD}) \sqrt{\frac{s}{\eta_{mD}}} \right] \quad (3.33)$$

There are two additional boundary conditions that allows connecting the outer matrix region with the SRV in well A. These boundary conditions are:

- (i) *Pressure continuity.* Pressure hence must be continuous across the matrix/SRV interface located at $y_D = 1$. This condition must also hold true in Laplace domain. Thus, in dimensionless form, we get:

$$(\bar{p}_{OAD})_{y_D=1} = (\bar{p}_{1AD})_{y_D=1} \quad (3.34)$$

We derive the following relationships by substituting Equation 3.34 into 3.32:

$$\bar{p}_{OAD} = (\bar{p}_{1AD})_{y_D=1} \frac{\cosh \left[(y_D - y_{eOAD}) \sqrt{\frac{s}{\eta_{mD}}} \right]}{\cosh \left[(1 - y_{eOAD}) \sqrt{\frac{s}{\eta_{mD}}} \right]} \quad (3.35)$$

$$\frac{d\bar{p}_{OAD}}{dy_D} = (\bar{p}_{1AD})_{y_D=1} \frac{\sqrt{\frac{s}{\eta_{mD}}} \sinh \left[(y_D - y_{eOAD}) \sqrt{\frac{s}{\eta_{mD}}} \right]}{\cosh \left[(1 - y_{eOAD}) \sqrt{\frac{s}{\eta_{mD}}} \right]} \quad (3.36)$$

- (ii) *Flux continuity*. Mass must be conserved across the matrix/SRV interface located at $y_D = 1$. This condition is mathematically defined, in Laplace domain, as:

$$\left(\frac{d\bar{p}_{OAD}}{dy_D} \right)_{y_D=1} = \frac{k_{1A}}{k_m} \left(\frac{d\bar{p}_{1AD}}{dy_D} \right)_{y_D=1} \quad (3.37)$$

Replacing Equation 3.36 into 3.37, yields

$$\left(\frac{d\bar{p}_{1AD}}{dy_D} \right)_{y_D=1} = (\bar{p}_{1AD})_{y_D=1} \frac{k_m}{k_{1j}} \sqrt{\frac{s}{\eta_{mD}}} \tanh \left[(1 - y_{eAOD}) \sqrt{\frac{s}{\eta_{mD}}} \right] \quad (3.38)$$

Equation 3.38 will be implemented as a flux-source function during the derivation of the analytical solution for fluid-flow in the SRV of well A.

3.5.4.2 Inner Matrix (Region IA)

The analytical solution to Equation 3.16 for Region IA ($r = O, j = A$) is given by

$$\bar{p}_{IAD} = A_{IA} \cosh \left[(y_D + y_{eIAD}) \sqrt{\frac{s}{\eta_{mD}}} \right] + B_{IA} \sinh \left[(y_D + y_{eIAD}) \sqrt{\frac{s}{\eta_{mD}}} \right] \quad (3.39)$$

Similar to Region IA, we consider that y_{eIAD} (Equation A.18) is the deepest dimensionless distance the pressure disturbance from well B would reach into the matrix region between wells A and C (see Figure 3.6). The corresponding no-flow boundary condition at $y_D = y_{eIAD}$ is defined as:

$$\left(\frac{d\bar{p}_{IAD}}{dy_D} \right)_{y_D=y_{eIAD}} = 0 \quad (3.40)$$

Replacing Equation 3.40 into 3.39 gives:

$$\bar{p}_{IAD} = A_{IA} \cosh \left[(y_D + y_{eIAD}) \sqrt{\frac{s}{\eta_{mD}}} \right] \quad (3.41)$$

$$\frac{d\bar{p}_{IAD}}{dy_D} = A_{IA} \sqrt{\frac{s}{\eta_{mD}}} \sinh \left[(y_D + y_{eIAD}) \sqrt{\frac{s}{\eta_{mD}}} \right] \quad (3.42)$$

Alike Region OA , the following two boundary conditions allow pressure communication hence fluid-flow across the inner matrix region and SRV in well A:

- (i) *Pressure continuity.* Pressure must be continuous across the matrix/SRV interface so that dimensionless pressure in the matrix and SRV are equal at $y_D = -1$. This boundary condition is given in Laplace domain as:

$$(\bar{p}_{IAD})_{y_D=-1} = (\bar{p}_{1AD})_{y_D=-1} \quad (3.43)$$

Replacing Equation 3.43 into 3.41, and solving for A_{IA} , yields:

$$\bar{p}_{IAD} = (\bar{p}_{1AD})_{y_D=-1} \frac{\cosh \left[(y_D + y_{eIAD}) \sqrt{\frac{s}{\eta_{mD}}} \right]}{\cosh \left[(-1 + y_{eIAD}) \sqrt{\frac{s}{\eta_{mD}}} \right]} \quad (3.44)$$

$$\frac{d\bar{p}_{IAD}}{dy_D} = (\bar{p}_{1AD})_{y_D=-1} \frac{\sqrt{\frac{s}{\eta_{mD}}} \sinh \left[(y_D + y_{eIAD}) \sqrt{\frac{s}{\eta_{mD}}} \right]}{\cosh \left[(-1 + y_{eIAD}) \sqrt{\frac{s}{\eta_{mD}}} \right]} \quad (3.45)$$

- (ii) *Flux continuity.* Flux leaving the inner matrix region must be equal to the flux entering the SRV through the interface located at $y_D = -1$. Therefore,

$$\left(\frac{d\bar{p}_{IAD}}{dy_D} \right)_{y_D=-1} = \frac{k_{1A}}{k_m} \left(\frac{d\bar{p}_{1AD}}{dy_D} \right)_{y_D=-1} \quad (3.46)$$

Replacing Equation 3.46 into Equation 3.45 gives:

$$\left(\frac{d\bar{p}_{1AD}}{dy_D} \right)_{y_D=-1} = (\bar{p}_{1AD})_{y_D=-1} \frac{k_m}{k_{1A}} \sqrt{\frac{s}{\eta_{2D}}} \tanh \left[(-1 + y_{eAID}) \sqrt{\frac{s}{\eta_{2D}}} \right] \quad (3.47)$$

Equation 3.47 will be used as a flux-source during the derivation of the analytical solution for fluid-flow in the SRV of well A.

3.5.4.3 SRV (Region 1A)

The derivation of the governing equation for fluid-flow in the SRV was discussed in Section 3.5.3.2 and its one-dimensional form in Laplace domain is given by Equation 3.22.

Realize that the two flux-source functions required for finding the desired specific solution to Equation 3.22 were found in the previous section. Therefore, we proceed with replacing Equation 3.38 and 3.47 into Equation 3.22 while operating under the assumption that $(\bar{p}_{1AD}) \neq f(y_D)$. In this manner, we arrive at the following governing equation for the SRV region:

$$\frac{d^2 \bar{p}_{1AD}}{dx_D^2} - c_{1A}(s) \bar{p}_{1AD} = 0 \quad (3.48)$$

The flux-source function $c_{1A}(s)$ describing total influx from the matrix (inner and outer regions) into the SRV is defined as:

$$c_{1A}(s) = \frac{s}{\eta_{1AD}} - \frac{k_m/k_{1A}}{2} \sqrt{\frac{s}{\eta_{mD}}} \left\{ \tanh \left[(1 - y_{eOAD}) \sqrt{\frac{s}{\eta_{mD}}} \right] + \tanh \left[(1 - y_{eIAD}) \sqrt{\frac{s}{\eta_{mD}}} \right] \right\} \quad (3.49)$$

The general solution to Equation 3.48 is given by

$$\bar{p}_{1AD} = A_{1A} \cosh \left[(x_D - x_{eAD}) \sqrt{c_{1A}(s)} \right] + B_{1A} \sinh \left[(x_D - x_{eAD}) \sqrt{c_{1A}(s)} \right] \quad (3.50)$$

Notice from Figure 3.6 that there is a no-flow boundary at $x_D = x_{eAD}$ due to symmetry conditions due to the assumption that all stages are identical. This boundary condition is defined as:

$$\left(\frac{d\bar{p}_{1AD}}{dx_D} \right)_{x_D=x_{eD}} = 0 \quad (3.51)$$

Further substitution of Equation 3.51 into 3.50 leads to:

$$\bar{p}_{1AD} = A_{1A} \cosh \left[(x_D - x_{eAD}) \sqrt{c_{1A}(s)} \right] \quad (3.52)$$

$$\frac{d\bar{p}_{1AD}}{dx_D} = A_{1A} \sqrt{c_{1A}(s)} \sinh \left[(x_D - x_{eAD}) \sqrt{c_{1A}(s)} \right] \quad (3.53)$$

Two additional boundary conditions apply to the SRV region. These are related to the pressure discontinuity due to the presence of fracture skin damage at the SRV/fracture interface and flux continuity across that interface. These are described next.

- (i) *Fracture skin damage.* Pressure is discontinuous across the SRV/fracture interface ($x_D = w_{AD}/2$) due to the presence of a low-conductivity region (i.e. fracture skin damage). The derivation of such boundary condition was introduced in Section 2.5.4.2 thus we herein adapt that result into the model in discussion. The pressure-discontinuity boundary condition is given by (see Equation 2.61)

$$(\bar{p}_{fAD})_{x_D=w_{AD}/2} = (\bar{p}_{1AD})_{x_D=w_{AD}/2} - s_{fA} \left(\frac{d\bar{p}_{1AD}}{dx_D} \right)_{x_D=w_{AD}/2} \quad (3.54)$$

where the fracture skin damage s_{fA} (Equation 2.62) is defined as:

$$s_{fA} = \frac{k_{1A}d_s}{k_s x_{fA}} \quad (3.55)$$

Here, d_s and k_s refer to the depth of penetration of formation damage into the SRV and permeability of the damage zone, respectively.

We are able to fully determine the integration constant A_{1A} by replacing Equation 3.54 into Equation 3.52 and 3.53 and solving the resulting system of equations. This yields:

$$\bar{p}_{1AD} = \frac{(\bar{p}_{fAD})_{x_D=w_{AD}/2} \cosh \left[(x_D - x_{eAD}) \sqrt{c_{1A}(s)} \right]}{\cosh \left[(w_{AD}/2 - x_{eAD}) \sqrt{c_{1A}(s)} \right] - s_{fA} \sqrt{c_{1A}(s)} \sinh \left[(w_{AD}/2 - x_{eAD}) \sqrt{c_{1A}(s)} \right]} \quad (3.56)$$

$$\frac{d\bar{p}_{1AD}}{dx_D} = \frac{(\bar{p}_{fAD})_{x_D=w_{AD}/2} \sqrt{c_{1A}(s)} \sinh \left[(x_D - x_{eAD}) \sqrt{c_{1A}(s)} \right]}{\cosh \left[(w_{AD}/2 - x_{eAD}) \sqrt{c_{1A}(s)} \right] - s_{fA} \sqrt{c_{1A}(s)} \sinh \left[(w_{AD}/2 - x_{eAD}) \sqrt{c_{1A}(s)} \right]} \quad (3.57)$$

Recognize that pressure continuity would be recovered simply by setting $s_{fA} = 0$. In this manner, Equation 3.54 becomes $(\bar{p}_{fAD})_{x_D=w_{AD}/2} = (\bar{p}_{1AD})_{x_D=w_{AD}/2}$.

- (ii) *Flux continuity.* Mass influx coming into the fracture must be equal to the mass influx leaving the SRV. Thus, mass must be conserved across the matrix/SRV interface, located at $y_D = 1$. This statement is mathematically expressed as:

$$\left(\frac{d\bar{p}_{1AD}}{dx_D} \right)_{x_D=w_{AD}/2} = \frac{k_{fA}}{k_{1A}} \left(\frac{d\bar{p}_{fAD}}{dx_D} \right)_{x_D=w_{AD}/2} \quad (3.58)$$

Substitution of Equation 3.58 into 3.57 gives

$$\left(\frac{d\bar{p}_{fAD}}{dx_D} \right)_{x_D=w_{AD}/2} = \frac{(k_{1A}/k_{fA})(\bar{p}_{fAD})_{x_D=w_{AD}/2} \sqrt{c_{1A}(s)}}{\coth \left[(w_{AD}/2 - x_{eAD}) \sqrt{c_{1A}(s)} \right] - s_{fA} \sqrt{c_{1A}(s)}} \quad (3.59)$$

Analogous to the matrix flux-source functions, Equation 3.59 will be used for the derivation of the governing equation for one-dimensional fluid-flow in the fracture.

3.5.4.4 Fracture (Region fA)

The governing equation for 1-D flow in the fracture was derived in Section 3.5.3.3; however, the influx term was yet to be determined. This flux-source function was just derived in the previous section. Therefore, we can proceed with substituting Equation 3.59 into 3.29 under the assumption that $(\bar{p}_{fAD}) \neq f(x_D)$. As a result,

$$\frac{d^2 \bar{p}_{fAD}}{dy_D^2} - c_{2A}(s) \bar{p}_{fAD} = -\frac{2\pi q'_{AD}}{s(F'_{CD})_A} \delta(y_D) \quad (3.60)$$

where $c_{2A}(s)$ is a flux-source function, defined in Laplace domain as:

$$c_{2A}(s) = \frac{s}{\eta_{fAD}} - \frac{2\sqrt{c_{1A}(s)}/(F'_{CD})_A}{\coth \left[(w_{AD}/2 - x_{eAD})\sqrt{c_{1A}(s)} \right] - s_{fA}\sqrt{c_{1A}(s)}} \quad (3.61)$$

Because the constant-rate well condition has been embedded into the governing equation in the form of a line-source term, two boundary conditions are available for tailoring the specific solution to Equation 3.60.

Given the nature of the problem in discussion, both boundary conditions should relate to pressure communication between well A and wells B and C due to frac hits. The derivation of the "leaky" boundary condition that represents frac hits is detailed in Section 3.6. At this point, though, let us simply define the following set of "dummy" flux boundary conditions at the fracture tips:

$$\left(\frac{d\bar{p}_{fAD}}{dy_D} \right)_{y_D=1} = F_{AB}(s) \quad (3.62)$$

$$\left(\frac{d\bar{p}_{fAD}}{dy_D} \right)_{y_D=-1} = F_{AC}(s) \quad (3.63)$$

Using Equation 3.62 and 3.63 to find the analytical solution to Equation 3.60, and evaluating the resulting expression at $y_D = 0$ (i.e. wellbore), yields

$$(\bar{p}_{fAD})_{y_D=0} = \frac{\pi q'_{AD}}{(F'_{CD})_A} \frac{\coth \sqrt{c_{2A}(s)}}{s\sqrt{c_{2A}(s)}} + \frac{1}{2} [F_{AB}(s) - F_{AC}(s)] \frac{\operatorname{csch} \sqrt{c_{2A}(s)}}{\sqrt{c_{2A}(s)}} \quad (3.64)$$

Recognize that operating conditions of well A would be fully independent from other wells if $F_{AB}(s) = F_{AC}(s) = 0$; however, if $F_{AB}(s) \neq 0$ then interference between wells A and C is taking place. Likewise, $F_{AC}(s) \neq 0$ may indicate pressure communication between wells A and C.

3.5.5 Analytical Solution for Fluid-flow in Well B

The derivation of the analytical solution for fluid-flow in all regions of well B is analogous to those in well A. Thus, we will provide the analytical expressions for the final solutions and flux-source functions whenever needed. Also, we will explain any difference related to boundary conditions with respect to those in well A.

3.5.5.1 Outer Matrix (Region OB)

According to Figure 3.6, well B is bounded by well A and the reservoir limit. As such, the size of the outer matrix region is given by the distance from well B to the outer matrix boundary. In dimensionless form, this distance is defined as y_{eOBD} (Equation A.23). Also, there is a no-flow boundary at $y_{BD} = y_{eOBD}$ thus $\left(\frac{d\bar{p}_{OBD}}{dy_{BD}}\right)_{y_{BD}=y_{eOBD}} = 0$.

Application of the former boundary condition while realizing that Region OB only exists for $x_{fBD} \leq y_{BD} \leq y_{eOBD}$, leads to the analytical solution to Equation 3.16 for $r = O$ and $j = B$:

$$\bar{p}_{OBD} = (\bar{p}_{1BD})_{y_{BD}=x_{fBD}} \frac{\cosh \left[(y_{BD} - y_{eOBD}) \sqrt{\frac{s}{\eta_{mD}}} \right]}{\cosh \left[(x_{fBD} - y_{eOBD}) \sqrt{\frac{s}{\eta_{mD}}} \right]} \quad (3.65)$$

The flux-source function later used to model influx from the outer matrix into the SRV is defined as:

$$\left(\frac{d\bar{p}_{1BD}}{dy_{BD}}\right)_{y_{BD}=x_{fBD}} = (\bar{p}_{1BD})_{y_{BD}=x_{fBD}} \frac{k_m}{k_{1B}} \sqrt{\frac{s}{\eta_{mD}}} \tanh \left[(x_{fBD} - y_{eOBD}) \sqrt{\frac{s}{\eta_{mD}}} \right] \quad (3.66)$$

3.5.5.2 Region IB (Inner Matrix)

There exists a no-flow boundary between wells A and B located at $y_{BD} = -y_{eIBD}$ (Equation A.24) henceforth $\left(\frac{d\bar{p}_{IBD}}{dy_{BD}}\right)_{y_{BD}=-y_{eIBD}} = 0$. Using this boundary condition to find the desired solution to Equation 3.16 for $j = B$ and $r = I$, and recognizing that $-y_{eIBD} \leq y_{BD} \leq -x_{fBD}$, leads to:

$$\bar{p}_{IBD} = (\bar{p}_{1BD})_{y_{BD}=-x_{fBD}} \frac{\cosh \left[(y_{BD} + y_{eIBD}) \sqrt{\frac{s}{\eta_{mD}}} \right]}{\cosh \left[(-x_{fBD} + y_{eIBD}) \sqrt{\frac{s}{\eta_{mD}}} \right]} \quad (3.67)$$

The flux-source term associated with influx from this region into the SRV is given by

$$\left(\frac{d\bar{p}_{1BD}}{dy_{BD}} \right)_{y_{BD}=-x_{fBD}} = (\bar{p}_{1BD})_{y_{BD}=-x_{fBD}} \frac{k_m}{k_{1B}} \sqrt{\frac{s}{\eta_{mD}}} \tanh \left[(-x_{fBD} + y_{eIBD}) \sqrt{\frac{s}{\eta_{mD}}} \right] \quad (3.68)$$

3.5.5.3 SRV (Region 1B)

We substitute Equation 3.68 and 3.66 into 3.16 to find the 1-D governing equation for fluid-flow in the SRV. Assuming that $\bar{p}_{1BD} \neq f(y_D)$, Equation 3.16 becomes

$$\frac{d^2 \bar{p}_{1BD}}{dx_D^2} - c_{1B}(s) \bar{p}_{1BD} = 0 \quad (3.69)$$

where $c_{1B}(s)$ is the matrix-to-SRV flux-source function, defined in Laplace domain as:

$$c_{1B}(s) = \frac{s}{\eta_{1BD}} - \frac{k_m/k_{1B}}{2x_{fBD}} \sqrt{\frac{s}{\eta_{mD}}} \left\{ \tanh \left[(x_{fBD} - y_{eOBD}) \sqrt{\frac{s}{\eta_{mD}}} \right] + \tanh \left[(x_{fBD} - y_{eIBD}) \sqrt{\frac{s}{\eta_{mD}}} \right] \right\} \quad (3.70)$$

The analytical solution to dimensionless pressure distribution in the SRV of well B is given by

$$\bar{p}_{1BD} = \frac{(\bar{p}_{fBD})_{x_D=w_{BD}/2} \cosh \left[(x_D - x_{eBD}) \sqrt{c_{1B}(s)} \right]}{\cosh \left[(w_{BD}/2 - x_{eBD}) \sqrt{c_{1B}(s)} \right] - s_{fB} \sqrt{c_{1B}(s)} \sinh \left[(w_{BD}/2 - x_{eBD}) \sqrt{c_{1B}(s)} \right]} \quad (3.71)$$

where s_{fB} is the fracture skin damage of well B. The following expression will be used to determine the flux-source function corresponding to the SRV/fracture interface:

$$\left(\frac{d\bar{p}_{fBD}}{dx_D}\right)_{x_D=w_{BD}/2} = \frac{(k_{1B}/k_{fB})(\bar{p}_{fBD})_{x_D=w_{BD}/2}\sqrt{c_{1B}(s)}}{\coth\left[(w_{BD}/2 - x_{eBD})\sqrt{c_{1B}(s)}\right] - s_{fB}\sqrt{c_{1B}(s)}} \quad (3.72)$$

3.5.5.4 Fracture (Region fB)

To derive the 1-D governing equation for fluid-flow in the fracture along the y_{BD} -axis, we replace Equation 3.72 into 3.29 operating under the assumption that $(\bar{p}_{fBD}) \neq f(x_D)$. This yields

$$\frac{d^2\bar{p}_{fBD}}{dy_{BD}^2} - c_{2B}(s)\bar{p}_{fBD} = 0 \quad (3.73)$$

where the flux-source function $c_{2B}(s)$ is defined as

$$c_{2B}(s) = \frac{s}{\eta_{fBD}} - \frac{2x_{fBD}\sqrt{c_{1B}(s)}/(F'_{CD})_B}{\coth\left[(w_{BD}/2 - x_{eBD})\sqrt{c_{1B}(s)}\right] - s_{fB}\sqrt{c_{1B}(s)}} \quad (3.74)$$

Because the constant-rate well condition is embedded into the governing equation as a line-source function, we have two boundary conditions available to fully determine the specific analytical solution to Equation 3.73 for well B.

One of such boundary conditions must be a no-flow boundary located at the outer fracture tip located at $y_{BD} = x_{fBD}$. The other one must allow pressure communication between wells A and wells B, due to frac hits at $y_{BD} = -x_{fBD}$ (see Figure 3.6). The derivation of this "leaky" boundary conditions is detailed in Section 3.6. At this point, nonetheless, let us simply define a "dummy" flux boundary condition for the inner fracture tip. Henceforth, the two flux boundary conditions associated with the fracture region are:

$$\left(\frac{d\bar{p}_{fBD}}{dy_{BD}}\right)_{y_D=x_{fBD}} = 0 \quad (3.75)$$

$$\left(\frac{d\bar{p}_{fBD}}{dy_{BD}}\right)_{y_D=-x_{fBD}} = F_{BA}(s) \quad (3.76)$$

The analytical solution to Equation 3.60 evaluated at the wellbore ($y_D = 0$), based on the former boundary conditions, is given as

$$(\bar{p}_{fBD})_{y_{BD}=0} = \frac{\pi q'_{BD}}{(F'_{CD})_B} \frac{\coth(x_{fBD} \sqrt{c_{2B}(s)})}{s \sqrt{c_{2B}(s)}} - \frac{1}{2} F_{BA}(s) \frac{\operatorname{csch}(x_{fBD} \sqrt{c_{2B}(s)})}{\sqrt{c_{2B}(s)}} \quad (3.77)$$

$F_{BA}(s) \neq 0$ indicates pressure communication between wells A and B due to frac hits. Conversely, $F_{BA}(s) = 0$ indicates that production from well B is not affected by well A.

3.5.6 Analytical Solution for Fluid-flow in Well C

3.5.6.1 Outer Matrix (Region OC)

The outer matrix region of well C is bounded by the reservoir at $y_{CD} = -y_{eOCD}$ (see Figure 3.6) therefore a no-flux boundary condition must be imposed there. The analytical solution to Equation 3.16 for $r = O$ and $j = C$ is found to be

$$\bar{p}_{OBD} = (\bar{p}_{1BD})_{y_{BD}=-x_{fBD}} \frac{\cosh \left[(y_{CD} + y_{eOCD}) \sqrt{\frac{s}{\eta_{mD}}} \right]}{\cosh \left[(-x_{fCD} + y_{eOCD}) \sqrt{\frac{s}{\eta_{mD}}} \right]} \quad (3.78)$$

The flux associated with flow continuity between the outer matrix and SRV is based on the pressure gradient evaluated at $y_{CD} = -x_{fCD}$, given by

$$\left(\frac{d\bar{p}_{1CD}}{dy_{CD}} \right)_{y_{CD}=-x_{fCD}} = (\bar{p}_{1CD})_{y_{CD}=-x_{fCD}} \frac{k_m}{k_1} \sqrt{\frac{s}{\eta_{mD}}} \tanh \left[(-x_{fCD} + y_{eOCD}) \sqrt{\frac{s}{\eta_{mD}}} \right] \quad (3.79)$$

3.5.6.2 Inner Matrix (Region IC)

The analytical solution for dimensionless pressure in Region *IB* is denoted as

$$\bar{p}_{ICD} = (\bar{p}_{1CD})_{y_{CD}=x_{fCD}} \frac{\cosh \left[(y_{CD} - y_{eICD}) \sqrt{\frac{s}{\eta_{mD}}} \right]}{\cosh \left[(x_{fCD} - y_{eICD}) \sqrt{\frac{s}{\eta_{mD}}} \right]} \quad (3.80)$$

Similar to the outer matrix region, the flux associated with flow continuity between the inner matrix and SRV is based on the pressure gradient evaluated at $y_{CD} = x_{fCD}$, given by

$$\left(\frac{d\bar{p}_{1CD}}{dy_{CD}} \right)_{y_{CD}=x_{fCD}} = (\bar{p}_{1CD})_{y_{CD}=x_{fCD}} \frac{k_m}{k_{1C}} \sqrt{\frac{s}{\eta_{mD}}} \tanh \left[(x_{fCD} - y_{eICD}) \sqrt{\frac{s}{\eta_{mD}}} \right] \quad (3.81)$$

3.5.6.3 SRV (Region 1C)

The 1-D governing equation for fluid-flow in the SRV is yielded from Equation 3.22 under the assumption that $\bar{p}_{1BD} \neq f(y_{BD})$:

$$\frac{d^2 \bar{p}_{1CD}}{dx_D^2} - c_{1C}(s) \bar{p}_{1CD} = 0 \quad (3.82)$$

where the flux-source function $c_{1C}(s)$ is defined as

$$c_{1C}(s) = \frac{s}{\eta_{1CD}} - \frac{k_m/k_{1C}}{2x_{fCD}} \sqrt{\frac{s}{\eta_{mD}}} \left\{ \tanh \left[(x_{fBD} - y_{eOCD}) \sqrt{\frac{s}{\eta_{mD}}} \right] + \tanh \left[(x_{fBD} - y_{eICD}) \sqrt{\frac{s}{\eta_{mD}}} \right] \right\} \quad (3.83)$$

The analytical solution to Equation 3.82 is given by:

$$\bar{p}_{1CD} = \frac{(\bar{p}_{fCD})_{x_D=w_{CD}/2} \cosh \left[(x_D - x_{eCD}) \sqrt{c_{1C}(s)} \right]}{\cosh \left[(w_{CD}/2 - x_{eCD}) \sqrt{c_{1C}(s)} \right] - s_{fB} \sqrt{c_{1C}(s)} \sinh \left[(w_{CD}/2 - x_{eCD}) \sqrt{c_{1C}(s)} \right]} \quad (3.84)$$

where s_{fC} is the fracture skin damage of well C. Derivative of Equation 3.84 with respect to x_D , evaluated at $x_D = w_{CD}/2$, yields the flux-source function describing

mass conservation across the SRV/fracture interface:

$$\left(\frac{d\bar{p}_{fCD}}{dx_D} \right)_{x_D=w_{CD}/2} = \frac{(k_{1C}/k_{fC})(\bar{p}_{fCD})_{x_D=w_{CD}/2} \sqrt{c_{1C}(s)}}{\coth \left[(w_{CD}/2 - x_{eCD}) \sqrt{c_{1C}(s)} \right] - s_{fC} \sqrt{c_{1C}(s)}} \quad (3.85)$$

3.5.6.4 Fracture (Region fC)

The derivation of the 1-D governing equation for fluid-flow in the fracture of well C is accomplished by replacing Equation 3.85 into 3.29 under the assumption that that $(\bar{p}_{fCD}) \neq f(x_D)$. This results in

$$\frac{d^2 \bar{p}_{fCD}}{dy_{CD}^2} - c_{2C}(s) \bar{p}_{fCD} = 0 \quad (3.86)$$

The flux-source function c_{2C} is defined in Laplace domain as:

$$c_{2C}(s) = \frac{s}{\eta_{fCD}} - \frac{2x_{fCD} \sqrt{c_{1C}(s)} / (F'_{CD})_C}{\coth \left[(w_{CD}/2 - x_{eCD}) \sqrt{c_{1C}(s)} \right] - s_{fC} \sqrt{c_{1C}(s)}} \quad (3.87)$$

There are two boundary conditions associated with the fracture. One condition is a no-flow boundary located at the outer fracture tip ($y_{CD} = -x_{fCD}$). The other one must allow pressure communication between wells A and wells C, due to frac hits at $y_{CD} = x_{fCD}$ (see Figure 3.6). The derivation of this "leaky" boundary conditions is detailed in Section 3.6. Similar to well B, we define a "dummy" flux boundary condition for the inner fracture tip. The resulting boundary conditions are given as:

$$\left(\frac{d\bar{p}_{fBD}}{dy_{BD}} \right)_{y_D=x_{fCD}} = C_{fA}(s) \quad (3.88)$$

$$\left(\frac{d\bar{p}_{fBD}}{dy_{BD}} \right)_{y_D=-x_{fCD}} = 0 \quad (3.89)$$

The analytical solution to Equation 3.60 evaluated at the wellbore ($y_D = 0$), based on the dummy flux boundary conditions, is found to be:

$$(\bar{p}_{fCD})_{y_{CD}=0} = \frac{\pi q'_{CD}}{(F'_{CD})_C} \frac{\coth(x_{fCD} \sqrt{c_{2C}(s)})}{s \sqrt{c_{2C}(s)}} + \frac{1}{2} C_{fA}(s) \frac{\operatorname{csch}(x_{fCD} \sqrt{c_{2C}(s)})}{\sqrt{c_{2C}(s)}} \quad (3.90)$$

Similar to wells A and B, $C_{fA}(s) \neq 0$ indicates pressure communication between wells A and B due to frac hits. Conversely, $C_{fA}(s) = 0$ indicates that production from well B is not being influenced by well A.

3.6. Mathematical Model—Part II: The Frac Hits Boundary Condition

3.6.1 Frac Hits between Wells A and B

3.6.1.1 Per-fracture Flow from/into Well A due to Frac Hits with Well B

The maximum influx, or leakage, rate into, or from, well A due to pressure connectivity with well B through primary fractures is defined as:

$$q_{LAB}(t) = -\varepsilon_{AB} \frac{C_{fA} h}{2\pi \times 141.2 \mu B} n_{fA} \left(\frac{\partial \Delta p_{fA}}{\partial y} \right)_{y=x_{fA}} \quad (3.91)$$

where $C_{fA} = k_{fA} w_A$ is the fracture conductivity of well A and ε_{AB} is given by:

$$\varepsilon_{AB} = \begin{cases} 1 & \text{if } (q_{\text{well}})_A > (q_{\text{well}})_B \quad (\text{leakage}) \\ -1 & \text{if } (q_{\text{well}})_A < (q_{\text{well}})_B \quad (\text{influx}) \end{cases} \quad (3.92)$$

Recognize that q'_{LAB} is actually time-dependent, therefore $q'_{LAB} \equiv q'_{LAB}(t)$. In light of the result in Equation 3.91, we find the equivalent maximum per-fracture influx/leakage rate of well A:

$$(q'_{LAB})_{\max} \equiv \frac{q_{LAB}(t)}{n_{fA}} = -\varepsilon_{AB} \frac{C_{fA} h}{2\pi \times 141.2 \mu B} \left(\frac{\partial \Delta p_{fA}}{\partial y} \right)_{y=x_{fA}} \quad (3.93)$$

It is likely, however, that not all but only several fractures are interacting with their counterparts from well B. Thus, a more accurate way to express the actual per-fracture

influx/leakage rate q'_L would be:

$$q'_{LAB}(t) = \frac{(q'_{LAB})_{\max}}{\delta_{wAB}} = -\varepsilon_{AB} \frac{C_{fA}h}{2\pi \times 141.2\delta_{wAB}\mu B} \left(\frac{\partial \Delta p_{fA}}{\partial y} \right)_{y=x_{fA}} \quad (3.94)$$

where δ_{wAB} is the frac hits coefficient, defined as the ratio of frac hits between wells A and B ($n_{fh,AB} = n_{fh,BA}$) to the total number of primary fractures in well A (n_{fA}). Thence,

$$\delta_{wAB} = \frac{n_{fh,AB}}{n_{fA}} \quad (0 \leq \delta_{wAB} \leq 1) \quad (3.95)$$

We can further normalize Equation 3.94 using Equation A.4 and A.11, so that:

$$\left(\frac{\partial p_{fAD}}{\partial y_D} \right)_{y_D=1} = -\varepsilon_{AB} \frac{2\pi\delta_{wAB}}{(F'_{CD})_A} \left(\frac{q'_{LAB}(t)}{q'_i} \right) = -\varepsilon_{AB} \frac{2\pi\delta_{wAB}}{(F'_{CD})_A} q'_{LABD}(t) \quad (3.96)$$

In Laplace domain,

$$\left(\frac{d\bar{p}_{fAD}}{dy_D} \right)_{y_D=1} = -\varepsilon_{AB} \frac{2\pi\delta_{wAB}}{(F'_{CD})_A} \mathcal{L}\{q'_{LABD}(t)\} \quad (3.97)$$

For convenience, we define the dimensionless group $B_w(s)$ as follows:

$$B_w(s) = \frac{2\pi\delta_{wAB}}{(F'_{CD})_A} \mathcal{L}\{q'_{LABD}(t)\} \quad (3.98)$$

Consequently,

$$\left(\frac{d\bar{p}_{fAD}}{dy_D} \right)_{y_D=1} = -\varepsilon_{AB} B_w(s) \quad (3.99)$$

$B_w(s)$ is the dimensionless ratio, in Laplace domain, of actual per-fracture influx/leakage rate to combined (total) production of wells A and B. Comparison of Equation 3.99 and Equation 3.62 shows that

$$F_{AB}(s) = -\varepsilon_{AB} B_w(s) \quad (3.100)$$

3.6.1.2 Per-fracture Flow Rate into/from Well B

Similar to the derivation of per-fracture influx/leakage rate for well A due to frac hits with well B, discussed in the previous section, we derive the per-fracture influx/leakage rate into/from well B due to frac hits, which results in

$$q'_{LAB}(t) = \frac{C_{fB}h}{2\pi \times 141.2\delta_{wBA}\mu B} \left(\frac{\partial \Delta p_{fB}}{\partial y_B} \right)_{y_B=-x_{fB}} \quad (3.101)$$

where $C_{fB} = k_{fB}w_B$ is the fracture conductivity of well B and δ_{wBA} is given by

$$\delta_{wBA} = \frac{n_{fh,AB}}{n_{fB}} \quad (0 \leq \delta_{wBA} \leq 1) \quad (3.102)$$

Because flux across wells must be conserved, then it must be true that Equation 3.94 and 3.101 are equal once pressure had reached equilibrium across the frac hits. Therefore,

$$-\varepsilon_{AB} \frac{C_{fA}}{\delta_{wAB}} \left(\frac{\partial \Delta p_{fA}}{\partial y} \right)_{y=x_{fA}} = \frac{C_{fB}}{\delta_{wBA}} \left(\frac{\partial \Delta p_{fB}}{\partial y_B} \right)_{y_B=-x_{fB}} \quad (3.103)$$

In the subsequent derivations, we assume that storativity effects are negligible hence Equation 3.103 is valid at all times.

From Equation 3.95 and 3.102) we get $\delta_{wBA}/\delta_{wAB} = n_{fA}/n_{fB}$. Further normalization of Equation 3.103, and subsequent transformation into Laplace domain, yields

$$\left(\frac{d\bar{p}_{fBD}}{dy_{BD}} \right)_{y_{BD}=-x_{fBD}} = -\varepsilon_{AB} \frac{n_{fA}(F'_{CD})_A}{n_{fB}(F'_{CD})_B} B_w(s) \quad (3.104)$$

As a result,

$$F_{BA}(s) = -\varepsilon_{AB} \frac{n_{fA}(F'_{CD})_A}{n_{fB}(F'_{CD})_B} B_w(s) \quad (3.105)$$

3.6.1.3 Coupling Boundary Condition

In short, modeling frac hits between wells A and B implies the development of a boundary condition that enables coupling these wells via influx/leakage occurring through primary fractures. There are, however, two assumptions that are necessary for developing such a boundary condition. Firstly, we assume that the equivalent fracture conductivity along the intersecting primary fractures is large enough such that inter-fracture storativity is negligible. This is a reasonable assumption, moreover, given that frac hits would not appear at early time when storativity effects may influence pressure-transient response.

The second assumption is flux across intersecting primary fractures is controlled by the difference in bottomhole pressure of each well. That is, flux along frac hits is governed by steady-state Darcy's law, expressed as:

$$q'_{LAB}(t) = \frac{\overline{C}_f h}{2\pi \times 141.2 \mu B L_{AB}} \varepsilon_{AB} [(\Delta p_{fA})_{y=0} - (\Delta p_{fB})_{y_B=0}] \quad (3.106)$$

where \overline{C}_f is the equivalent fracture conductivity between wells A and B. Recognize that, if we utilize the assumption of negligible transience along the frac hits then \overline{C}_f can be estimated as the equivalent fracture conductivity of three regions in series, as shown in Figure 3.7. As a result, we obtain:

$$\overline{C}_f = \frac{L_{AB}}{\frac{x_{fA}}{C_{fA}} + \frac{L_{AB} - (x_{fA} + x_{fB})}{C_{fA}} + \frac{x_{fB}}{C_{fB}}} \quad (3.107)$$

Dividing through the expression above by $k_{1A} L_{AB}$, gives:

$$\frac{\overline{C}_f}{k_{1A} L_{AB}} = \frac{1}{\frac{k_{1A} x_{fA}}{C_{fA}} + \frac{k_{1A} [L_{AB} - (x_{fA} + x_{fB})]}{C_{fA}} + \frac{k_{1A} x_{fB}}{C_{fB}}} \quad (3.108)$$

Now, let us define the equivalent dimensionless fracture conductivity \overline{F}_{CD} as:

$$\overline{F}_{CD} \equiv \frac{\overline{C}_f}{k_{1A} L_{AB}} \quad (3.109)$$

Furthermore, Equation 3.106 can be normalized as follows:

$$q'_{LABD}(t) = \frac{\overline{F_{CD}}}{2\pi} \varepsilon_{AB} [(p_{fAD})_{y_D=0} - (p_{fBD})_{y_{BD}=0}] \quad (3.110)$$

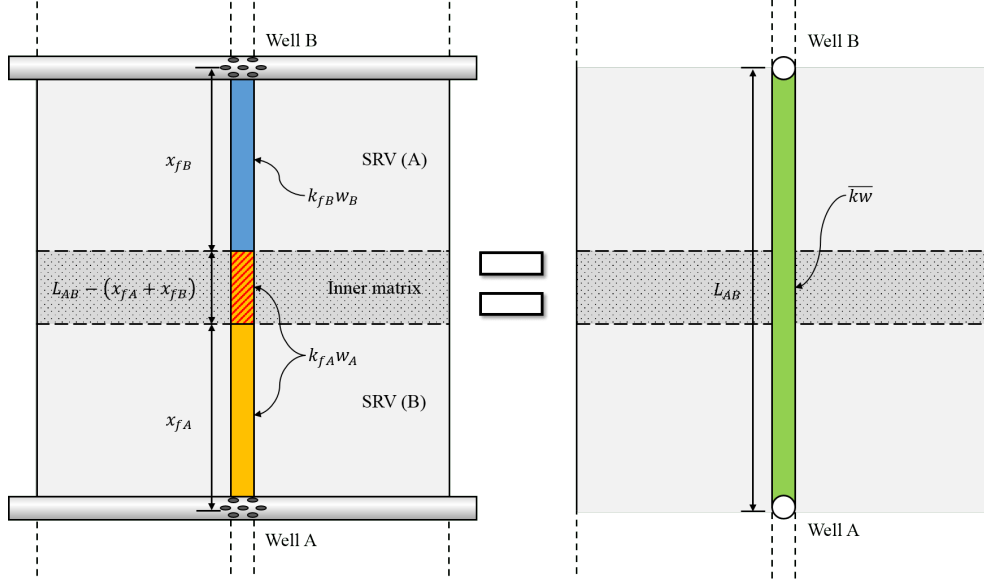


Figure 3.7: Definition of equivalent fracture conductivity $\overline{C_f}$ to model fluid-flow between wells A and B through primary fractures and the frac hit.

Transformation of Equation 3.110 into Laplace domain yields

$$\mathcal{L}\{q'_{LABD}(t)\} = \frac{\overline{F_{CD}}}{2\pi} \varepsilon_{AB} [(\bar{p}_{fAD})_{y_D=0} - (\bar{p}_{fBD})_{y_{BD}=0}] \quad (3.111)$$

From Equation 3.98, we find that

$$\mathcal{L}\{q'_{LABD}(t)\} = \frac{(F'_{CD})_A}{2\pi\delta_{wAB}} B_w(s) \quad (3.112)$$

Substituting Equation 3.112 into 3.111 gives:

$$\varepsilon_{AB} B_w(s) = \frac{\overline{F_{CD}}}{(F'_{CD})_A} \delta_{wAB} [(p_{fAD})_{y_D=0} - (p_{fBD})_{y_{BD}=0}] \quad (3.113)$$

Moreover, let us assume that $\overline{F_{CD}}$ is proportional to $(F_{CD})_A \equiv (F'_{CD})_A$, such that:

$$\overline{F_{CD}} = \alpha_{wAB} (F_{CD})_A \quad (3.114)$$

where α_{wAB} is the proportionality constant. Substitution of Equation 3.114 into 3.113, and further transformation into Laplace domain leads to:

$$\varepsilon_{AB} B_w(s) = \alpha_{wAB} \delta_{wAB} [(\bar{p}_{fAD})_{y_D=0} - (\bar{p}_{fBD})_{y_{BD}=0}] \quad (3.115)$$

By definition, $\overline{F_{CD}} = \frac{\bar{C}_f}{k_{1A} L_{AB}}$ and $\alpha_{wAB} = \overline{F_{CD}} / (F_{CD})_A$. Therefore, Equation 3.108 can be recast as follows:

$$\alpha_{wAB} = \frac{1}{1 + \frac{L_{AB} - (x_{fA} + x_{fB})}{x_{fA}} + x_{fBD} \frac{(F'_{CD})_A}{(F'_{CD})_B}} \quad (3.116)$$

Substitution of Equation 3.116 into 3.115 yields

$$\varepsilon_{AB} B_w(s) = \frac{\delta_{wAB}}{1 + \frac{D_{AB}}{x_{fA}} + x_{fBD} \frac{(F'_{CD})_A}{(F'_{CD})_B}} [(\bar{p}_{fAD})_{y_D=0} - (\bar{p}_{fBD})_{y_{BD}=0}] \quad (3.117)$$

Furthermore, let us define the frac hits skin factor between wells A and B as follows:

$$s_{fAB} = \frac{1}{\delta_{wAB}} \left[1 + \frac{L_{AB} - (x_{fA} + x_{fB})}{x_{fA}} + x_{fBD} \frac{(F'_{CD})_A}{(F'_{CD})_B} \right] \quad (3.118)$$

To prove that Equation 3.118 corresponds to a skin factor, consider two extreme cases. On the one hand, assume that there are no frac hits in the system therefore $\delta_{wAB} = 0$. This assumption leads to $s_{fAB} \rightarrow \infty$. On the other hand, if primary fractures are fully interfering then $\delta_{wAB} = 1$ and s_{fAB} reaches a minimum value, given by

$$(s_{fAB})_{\min} = 1 + \frac{L_{AB} - (x_{fA} + x_{fB})}{x_{fA}} + x_{fBD} \frac{(F'_{CD})_A}{(F'_{CD})_B} \quad (3.119)$$

As a result, we get $(s_{fAB})_{\min} \leq s_{fAB} < \infty$, which proves that Equation 3.118 is indeed the definition of a skin factor.

Finally, the coupling boundary condition between wells A and B is derived after substituting Equation 3.98 and 3.118 into Equation 3.117:

$$\varepsilon_{AB} s_{fAB} B_w(s) = (\bar{p}_{fAD})_{y_D=0} - (\bar{p}_{fBD})_{y_{BD}=0} \quad (3.120)$$

3.6.2 Frac Hits between Wells A and C

3.6.2.1 Per-fracture Flow from/into Well A due to Frac Hits with Well C

The derivation of the frac hits boundary condition between wells A and C is analogous to the derivation detailed in Section 3.6.1. As such, the influx/leakage rate into/from well A due to frac hits with well C is given by:

$$\left(\frac{d\bar{p}_{fAD}}{dy_D} \right)_{y_D=-1} = \varepsilon_{AC} C_w(s) \quad (3.121)$$

The boundary condition above is equivalent to:

$$F_{AC}(s) = \varepsilon_{AC} C_w(s) \quad (3.122)$$

where the conditional parameter ε_{AC} is defined as:

$$\varepsilon_{AC} = \begin{cases} 1 & \text{if } (q_{\text{well}})_A > (q_{\text{well}})_C & \text{(leakage)} \\ -1 & \text{if } (q_{\text{well}})_A < (q_{\text{well}})_C & \text{(influx)} \end{cases} \quad (3.123)$$

Similar to Equation 3.98, $C_w(s)$ refers to the dimensionless ratio of actual per-fracture influx/leakage rate to combined (total) production of wells A and B, given in Laplace domain as:

$$C_w(s) = \frac{2\pi\delta_{wAC}}{(F'_{CD})_A} \mathcal{L} \left\{ \frac{q'_{LAC}(t)}{q'_t} \right\} = \frac{2\pi\delta_{wAC}}{(F'_{CD})_A} \mathcal{L} \{ q'_{LACD}(t) \} \quad (3.124)$$

In addition, δ_{wAC} is defined as the ratio of the number of frac hits between wells A and C to the total number of primary fractures in well A:

$$\delta_{wAC} = \frac{n_{h,AC}}{n_{fA}} \quad (3.125)$$

3.6.2.2 Per-fracture Flow Rate into/from Well C

Similar to the derivation discussed in the previous section, we find the per-fracture influx/leakage rate into/from well C due to frac hits with well A to be:

$$q'_{LAC}(t) = \varepsilon_{AC} \frac{C_{fC}h}{2\pi \times 141.2\delta_{wCA}\mu B} \left(\frac{\partial \Delta p_{fC}}{\partial y_C} \right)_{y_C=x_{fC}} \quad (3.126)$$

where $C_{fC} = k_{fC}w_f$ is the fracture conductivity of well C and δ_{wCA} is the fraction of frac hits between wells A and C, defined as:

$$\delta_{wCA} = \frac{n_{fh,AC}}{n_{fC}} \quad (0 \leq \delta_{wBA} \leq 1) \quad (3.127)$$

Note that $n_{h,AC} = n_{h,CA}$ (i.e. number of frac hits is the same in both wells). Flux across wells A and C must be conserved, therefore

$$\varepsilon_{AC} \frac{C_{fA}}{\delta_{wAC}} \left(\frac{\partial \Delta p_{fA}}{\partial y} \right)_{y=-x_{fA}} = \frac{C_{fC}}{\delta_{wCA}} \left(\frac{\partial \Delta p_{fC}}{\partial y_C} \right)_{y=x_{fC}} \quad (3.128)$$

Notice that, by definition, $\delta_{wCA}/\delta_{wAC} = n_{fA}/n_{fC}$. Normalization of Equation 3.128 and further transformation into Laplace domain yields

$$\left(\frac{d\bar{p}_{fCD}}{dy_{CD}} \right)_{y_{CD}=x_{fCD}} = \varepsilon_{AC} \frac{n_{fA}(F'_{CD})_A}{n_{fC}(F'_{CD})_C} C_w(s) \quad (3.129)$$

Consequently,

$$C_{fA}(s) = \varepsilon_{AC} \frac{n_{fA}(F'_{CD})_A}{n_{fC}(F'_{CD})_C} C_w(s) \quad (3.130)$$

3.6.2.3 Coupling Boundary Condition

We derive the frac hits boundary condition in Laplace domain, for interference between wells A and C while considering the following assumptions: (1) flux across interconnected primary fractures between wells A and C is controlled by the difference in bottomhole pressure of each well, and (2) negligible transience effects within the interconnected primary fractures. This leads to

$$\varepsilon_{AC} C_w(s) = \alpha_{wAC} \delta_{wAC} [(\bar{p}_{fAD})_{y_D=0} - (\bar{p}_{fCD})_{y_{CD}=0}] \quad (3.131)$$

As discussed in the previous section, α_{wAC} is the proportionality constant between the dimensionless fracture conductivity of well A and the equivalent dimensionless fracture conductivity of the frac hits between wells A and C.

Following an analogous derivation to that presented in Section 3.6.1.3, we arrive at the frac hits boundary condition for wells A and C:

$$\varepsilon_{AC} C_w(s) = \frac{\delta_{wAC}}{1 + \frac{D_{AC}}{x_{fA}} + x_{fCD} \frac{(F'_{CD})_A}{(F'_{CD})_C}} [(\bar{p}_{fAD})_{y_D=0} - (\bar{p}_{fCD})_{y_{CD}=0}] \quad (3.132)$$

Alike, we define the frac hits skin factor between wells A and C as

$$s_{fAC} = \frac{1}{\delta_{wAC}} \left[1 + \frac{L_{AC} - (x_{fA} + x_{fC})}{x_{fA}} + x_{fCD} \frac{(F'_{CD})_A}{(F'_{CD})_C} \right] \quad (3.133)$$

Because $0 \leq \delta_{wAC} \leq 1$ then $(s_{fAC})_{\min} \leq s_{fAC} < \infty$, where

$$(s_{fAC})_{\min} = 1 + \frac{L_{AC} - (x_{fA} + x_{fC})}{x_{fA}} + x_{fCD} \frac{(F'_{CD})_A}{(F'_{CD})_C} \quad (3.134)$$

Finally, the coupling boundary condition for wells A and C is recast as

$$\varepsilon_{AC} s_{fAC} C_w(s) = (\bar{p}_{fAD})_{y_D=0} - (\bar{p}_{fCD})_{y_{CD}=0} \quad (3.135)$$

3.6.3 Determination of $B_w(s)$ and $C_w(s)$

We combine the analytical solution to normalized pressure-drawdowns (Equation 3.64, 3.77 and 3.90) with their respective coupling boundary condition (Equation 3.120 and 3.135). We consider the following three cases of well interference due to frachits:

Case I. Interference between wells A and B only. Frac hits allow pressure communication between wells A and B but not well C, thus $C_w(s) = 0$ as $s_{fAC} \rightarrow \infty$. In this case, $B_w(s)$ is given as:

$$B_w(s) = \varepsilon_{AB} \frac{\frac{\pi q'_{AD}}{(F'_{CD})_A} \frac{\coth \sqrt{c_{2A}(s)}}{s \sqrt{c_{2A}(s)}} - \frac{\pi q'_{BD}}{(F'_{CD})_B} \frac{\coth(x_{fBD} \sqrt{c_{2B}(s)})}{s \sqrt{c_{2B}(s)}}}{s_{fAB} + \frac{1}{2} \left[\frac{\operatorname{csch} \sqrt{c_{2A}(s)}}{\sqrt{c_{2A}(s)}} + \frac{n_{fA}(F'_{CD})_A}{n_{fB}(F'_{CD})_B} \frac{\operatorname{csch}(x_{fBD}) \sqrt{c_{2B}(s)}}{\sqrt{c_{2B}(s)}} \right]} \quad (3.136)$$

Case II. Interference between wells A and C only. Frac hits allow pressure communication between wells A and C but not well B, hence $B_w(s) = 0$ because $s_{fAB} \rightarrow \infty$. In this case, $C_w(s)$ is given as:

$$C_w(s) = \varepsilon_{AC} \frac{\frac{\pi q'_{AD}}{(F'_{CD})_A} \frac{\coth \sqrt{c_{2A}(s)}}{s \sqrt{c_{2A}(s)}} - \frac{\pi q'_{CD}}{(F'_{CD})_C} \frac{\coth(x_{fCD} \sqrt{c_{2C}(s)})}{s \sqrt{c_{2C}(s)}}}{s_{fAC} + \frac{1}{2} \left[\frac{\operatorname{csch} \sqrt{c_{2A}(s)}}{\sqrt{c_{2A}(s)}} + \frac{n_{fA}(F'_{CD})_A}{n_{fC}(F'_{CD})_C} \frac{\operatorname{csch}(x_{fCD}) \sqrt{c_{2C}(s)}}{\sqrt{c_{2C}(s)}} \right]} \quad (3.137)$$

Case III. Interference between wells A, B and C. This is the worst-case scenario because frac hits are affecting all wells in the pad (Figure 3.5). In this case, $B_w(s) \neq 0$ and $C_w(s) \neq 0$. In this case, $C_w(s)$ and $B_w(s)$ are given as:

$$B_w(s) = \varepsilon_{AB} \frac{A_1(s)A_2(s) - A_3(s)}{A_4(s)A_2(s) - A_5(s)} \quad (3.138)$$

$$C_w(s) = \varepsilon_{AC} \frac{\frac{\pi q'_{AD}}{(F'_{CD})_A} \frac{\coth \sqrt{c_{2A}(s)}}{s \sqrt{c_{2A}(s)}} - \frac{\pi q'_{CD}}{(F'_{CD})_C} \frac{\coth(x_{fCD} \sqrt{c_{2C}(s)})}{s \sqrt{c_{2C}(s)}} - \frac{1}{2} B_w(s) \frac{\operatorname{csch} \sqrt{c_{2A}(s)}}{\sqrt{c_{2A}(s)}}}{s_{fAC} + \frac{1}{2} \left[\frac{\operatorname{csch} \sqrt{c_{2A}(s)}}{\sqrt{c_{2A}(s)}} + \frac{n_{fA}(F'_{CD})_A}{n_{fC}(F'_{CD})_C} \frac{\operatorname{csch}(x_{fCD}) \sqrt{c_{2C}(s)}}{\sqrt{c_{2C}(s)}} \right]} \quad (3.139)$$

The auxiliary functions $A_1(s)$ – $A_5(s)$ in Equation 3.138 are defined as follows:

$$A_1(s) = \frac{\pi q'_{AD}}{(F'_{CD})_A} \frac{\coth \sqrt{c_{2A}(s)}}{s \sqrt{c_{2A}(s)}} - \frac{\pi q'_{BD}}{(F'_{CD})_B} \frac{\coth(x_{fBD} \sqrt{c_{2B}(s)})}{s \sqrt{c_{2B}(s)}} \quad (3.140)$$

$$A_2(s) = s_{fAC} + \frac{1}{2} \left[\frac{\operatorname{csch} \sqrt{c_{2A}(s)}}{\sqrt{c_{2A}(s)}} + \frac{n_{fA}(F'_{CD})_A}{n_{fC}(F'_{CD})_C} \frac{\operatorname{csch}(x_{fCD} \sqrt{c_{2C}(s)})}{\sqrt{c_{2C}(s)}} \right] \quad (3.141)$$

$$A_3(s) = \frac{1}{2} \frac{\operatorname{csch} \sqrt{c_{2A}(s)}}{\sqrt{c_{2A}(s)}} \left[\frac{\pi q'_{AD}}{(F'_{CD})_A} \frac{\coth \sqrt{c_{2A}(s)}}{s \sqrt{c_{2A}(s)}} - \frac{\pi q'_{CD}}{(F'_{CD})_C} \frac{\coth(x_{fCD} \sqrt{c_{2C}(s)})}{s \sqrt{c_{2C}(s)}} \right] \quad (3.142)$$

$$A_4(s) = s_{fAB} + \frac{1}{2} \left[\frac{\operatorname{csch} \sqrt{c_{2A}(s)}}{\sqrt{c_{2A}(s)}} + \frac{n_{fA}(F'_{CD})_A}{n_{fB}(F'_{CD})_B} \frac{\operatorname{csch}(x_{fBD} \sqrt{c_{2B}(s)})}{\sqrt{c_{2B}(s)}} \right] \quad (3.143)$$

$$A_5(s) = \frac{1}{4} \frac{(\operatorname{csch} \sqrt{c_{2A}(s)})^2}{c_{2A}(s)} \quad (3.144)$$

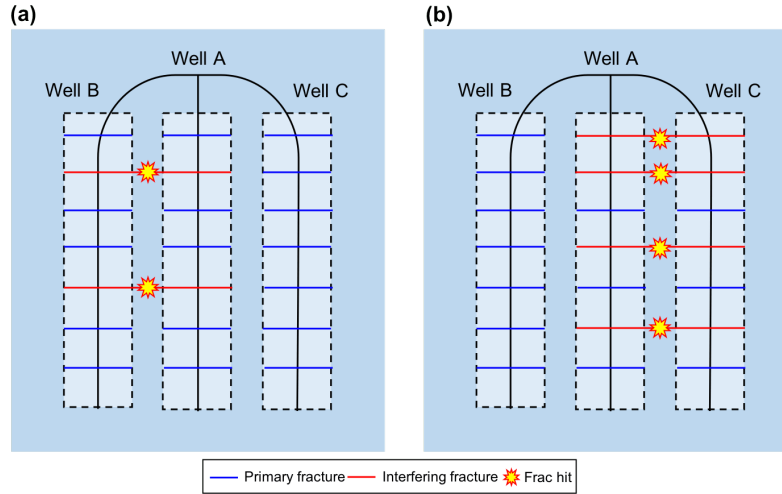


Figure 3.8: Case I (wells A and B) and Case II (wells A and B).

3.7. Analytical Solution

3.7.1 Transient BHP Solution for Well A

Normalized pressure-drawdown of well A is given, in Laplace domain, as:

$$\bar{p}_{wAD} = \frac{\pi q'_{AD}}{(F'_{CD})_A} \frac{\coth \sqrt{c_{2A}(s)}}{s \sqrt{c_{2A}(s)}} - \frac{1}{2} [\varepsilon_{AB} B_w(s) + \varepsilon_{AC} C_w(s)] \frac{\operatorname{csch} \sqrt{c_{2A}(s)}}{\sqrt{c_{2A}(s)}} + \frac{q'_{AD} s_{cA}}{s} \quad (3.145)$$

where s_{cA} is the choking skin of well A (see Equation 2.101). The definition of both $B_w(s)$ and $C_w(s)$ depend on the interference case under study. Laplace inversion of Equation 3.145 gives:

$$\begin{aligned} \Delta p_{wA}(t) = & \frac{141.2 q'_t \mu B}{k_{1A} h} \mathcal{L}^{-1} \left\{ \frac{\pi q'_{AD}}{(F'_{CD})_A} \frac{\coth \sqrt{c_{2A}(s)}}{s \sqrt{c_{2A}(s)}} - \frac{1}{2} [\varepsilon_{AB} B_w(s) + \varepsilon_{AC} C_w(s)] \frac{\operatorname{csch} \sqrt{c_{2A}(s)}}{\sqrt{c_{2A}(s)}} \right\} \\ & + \frac{141.2 q'_A \mu B}{C_{fA}} \left[\ln \left(\frac{h}{2 r_{wA}} \right) - \frac{\pi}{2} \right] \end{aligned} \quad (3.146)$$

$\Delta p_{wA} = p_i - \text{BHP}_A(t)$ and r_{wA} are the pressure-drawdown and wellbore radius of well A, respectively. Wellbore storage (WBS) can be incorporated into the analytical model via:

$$\Delta p_{wA}(t) = \frac{141.2 q'_t \mu B}{k_{1A} h} \mathcal{L}^{-1} \left\{ \frac{\bar{p}_{wAD}(s)}{1 + C_{AD} s^2 \bar{p}_{wAD}(s)} \right\} \quad (3.147)$$

where C_{AD} is the dimensionless wellbore storage coefficient of well A by (Equation 2.107). This approach also applies for wells B and C.

3.7.2 Transient BHP Solution for Well B

Normalized pressure-drawdown of well B is given, in Laplace domain, as:

$$\bar{p}_{wBD} = \frac{\pi q'_{BD}}{(F'_{CD})_B} \frac{\coth(x_{fBD} \sqrt{c_{2B}(s)})}{s \sqrt{c_{2B}(s)}} + \frac{1}{2} \varepsilon_{AB} \frac{n_{fA} (F'_{CD})_A}{n_{fB} (F'_{CD})_B} B_w(s) \frac{\operatorname{csch}(x_{fBD} \sqrt{c_{2B}(s)})}{\sqrt{c_{2B}(s)}} + \frac{q'_{BD} s_{cB}}{s} \quad (3.148)$$

where s_{cB} is the convergence or choking skin (Equation 2.101). The definition of $B_w(s)$ depends on the interference case under study. Inversion of Equation 3.148 into time domain, yields:

$$\Delta p_{wB}(t) = \frac{141.2q'_i\mu B}{k_{1A}h} \mathcal{L}^{-1} \left\{ \frac{\pi q'_{BD}}{(F'_{CD})_B} \frac{\coth(x_{fBD}\sqrt{c_{2B}(s)})}{s\sqrt{c_{2B}(s)}} + \frac{1}{2}\varepsilon_{AB} \frac{n_{fA}(F'_{CD})_A}{n_{fB}(F'_{CD})_B} B_w(s) \frac{\operatorname{csch}(x_{fBD}\sqrt{c_{2B}(s)})}{\sqrt{c_{2B}(s)}} \right\} \\ + \frac{141.2q'_B\mu B}{C_{fB}} \left[\ln\left(\frac{h}{2r_{wB}}\right) - \frac{\pi}{2} \right] \quad (3.149)$$

3.7.3 Transient BHP Solution for Well C

Normalized pressure-drawdown of well C is given, in Laplace domain, as:

$$\bar{p}_{wCD} = \frac{\pi q'_{CD}}{(F'_{CD})_C} \frac{\coth(x_{fCD}\sqrt{c_{2C}(s)})}{s\sqrt{c_{2C}(s)}} + \frac{1}{2}\varepsilon_{AC} \frac{n_{fA}(F'_{CD})_A}{n_{fC}(F'_{CD})_C} C_w(s) \frac{\operatorname{csch}(x_{fCD}\sqrt{c_{2C}(s)})}{\sqrt{c_{2C}(s)}} + \frac{q'_{CD}s_{cC}}{s} \quad (3.150)$$

Once again, the functional form of both $B_w(s)$ and $C_w(s)$ is given by the interference case under study. Inversion of Equation 3.150 into time domain, yields:

$$\Delta p_{wC}(t) = \frac{141.2q'_i\mu B}{k_{1A}h} \mathcal{L}^{-1} \left\{ \frac{\pi q'_{CD}}{(F'_{CD})_C} \frac{\coth(x_{fCD}\sqrt{c_{2C}(s)})}{s\sqrt{c_{2C}(s)}} + \frac{1}{2}\varepsilon_{AC} \frac{n_{fA}(F'_{CD})_A}{n_{fC}(F'_{CD})_C} C_w(s) \frac{\operatorname{csch}(x_{fCD}\sqrt{c_{2C}(s)})}{\sqrt{c_{2C}(s)}} \right\} \\ + \frac{141.2q'_C\mu B}{C_{fC}} \left[\ln\left(\frac{h}{2r_{wC}}\right) - \frac{\pi}{2} \right] \quad (3.151)$$

3.8. Analytical Functions for Pressure-Transient Analysis of Frac Hits

The analytical expressions used for pressure-transient analysis in rate-normalized form $\text{RNP}_{Aj}(t)$ (Equation 3.3) and $\text{RNP}'_{Aj}(t)$ (Equation 3.4) are the following:

$$\Delta p_{wAB}(t) = \frac{141.2q'_i\mu B}{k_{1A}h} \varepsilon_{AB} \mathcal{L}^{-1} \{ \bar{p}_{wAD}(s) - \bar{p}_{wBD}(s) \} \quad (3.152)$$

$$\Delta p_{wAC}(t) = \frac{141.2q'_i\mu B}{k_{1A}h} \varepsilon_{AC} \mathcal{L}^{-1} \{ \bar{p}_{wAD}(s) - \bar{p}_{wCD}(s) \} \quad (3.153)$$

3.9. Validation Cases

Four simulation case studies are explored in this section. Case Study 1 is the scenario with no frac hits in the pad. Our interest here is to determine whether the analytical solution is able to capture interference through the matrix. Case Study 2 through 4 examine various degrees of interference due to frac hits. Wells are producing at constant rate. Frac hits are artificially imposed onto the simulation model by interconnecting one or more hydraulic fractures between wells A, B and C. Further, we consider frac hits to have equal conductivity of primary fractures from well A. The multi-well pad is initially at constant pressure throughout. Fractured stages have equal dimensions and properties in all MFHWs.

Frac hits are randomly placed in the multi-well pad. Molina and Zeidouni (2017b) found that, for equal values of δ_{wAB} , location of the frac hits will not influence expected pressure response. For example, consider two MFHWs with 5 fractured stages. Frac hits across stages 2, 3 and 5 ($[-][\times][\times][-][\times]$) will produce the same transient response when frac hits are located across stages 1, 3, and 4 ($[\times][-][\times][\times][-]$) because $\delta_{wAB} = 3/10 = 0.3$ in both cases. This eliminates the need for running simulations for all possible scenarios for a given δ_{wAB} .

Reservoir and fluid properties are taken from Table 2.1. Initial pressure as well as total compressibility ($c_t = 10^{-6} \text{ psi}^{-1}$) and completion properties, summarized in Table 3.1, are assumed equal in all MFHWs.

Table 3.1: Completion and multi-well pad properties.

Hydraulic fractures properties	
Fracture conductivity, $C_{fA} = C_{fB} = C_{fC}$ [md-ft]	500
Proppant pack porosity, ϕ_f [-]	0.35
Distance between fractured stages, $2x_{eA} = 2x_{eB} = 2x_{eC}$ [ft]	500
Fracture half-length, $x_{fA} = x_{fB} = x_{fC}$ [ft]	200
Multi-well pad configuration	
Fractured stages (all MFHWs)	10
Distance between wells A and B, L_{AB} [ft]	600
Distance between wells A and C, L_{AC} [ft]	600
Flow rate of well A, $(q_{\text{well}})_A$ [STB/D]	200
Flow rate of well B, $(q_{\text{well}})_B$ [STB/D]	100
Flow rate of well C, $(q_{\text{well}})_C$ [STB/D]	80

3.9.1 Validation Case Study 1: No Frac Hits.

In this case, we consider no frac hits between offset wells (B and C) and infill well (A) thus $d_{wAB}^* = d_{wAC}^* = 0$. Figure 3.9 shows a snapshot of pressure distribution in the multi-well pad after 67 days of constant-rate withdrawal. Notice that, in the absence of frac hits, pressure behaves symmetrically across fractured stages.

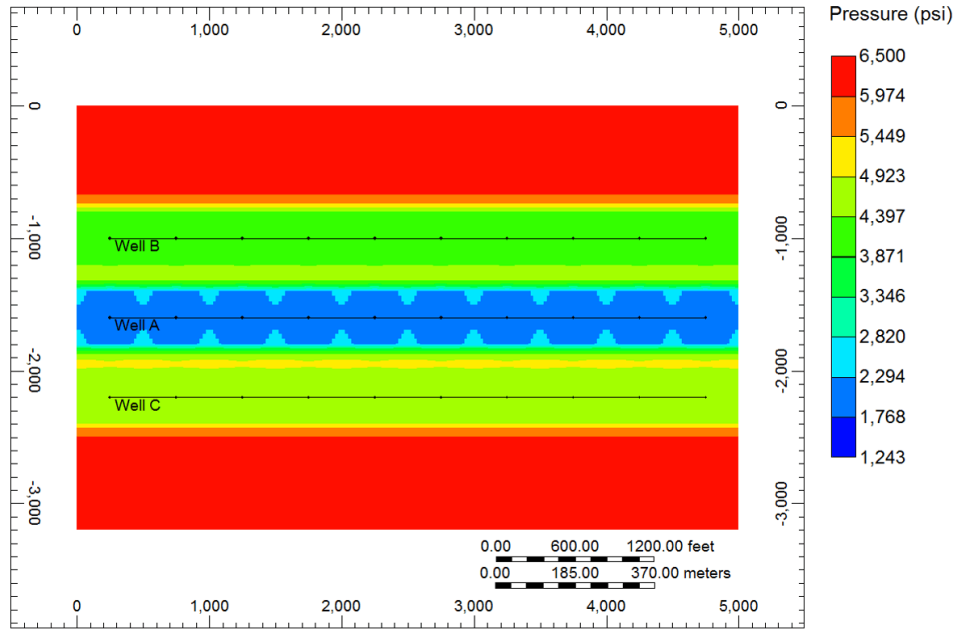


Figure 3.9: Pressure distribution after 67 days (no frac hits) ($d_{wAB}^* = d_{wAC}^* = 0$).

Figure 3.10 shows that analytical and numerical BHP data are in good agreement for the case $\delta_{wAB} = \delta_{wAC} = 0$. Figure 3.11 shows that analytical RNP_{Aj} and RNP'_{Aj} ($j = B, C$) match with numerical early-time data. Yet, even though there are no frac hits in the multi-well pad, analytical rate-normalized parameters depart from numerical rate-normalized data after 30 days. One plausible explanation for the mismatch observed during mid to late times is that pressure interference would take place through the matrix after 30 days. We obtained better history-matching results, both at early and late times, by assigning $\delta_{wAB} = \delta_{wAC} = 8.9 \times 10^{-4}$. Figure 3.12 shows analytical and numerical BHP data. In particular, note that the late-time mismatch from Figure 3.10 was fixed by setting $\delta_{wAB} = \delta_{wAC} = 8.9 \times 10^{-4}$. Similarly, Figure 3.13 shows that analytical and numerical data are in good agreement. Thus, the analytical model can handle interference through the matrix in the form of a small frac hit that would result in the same degree of interference.

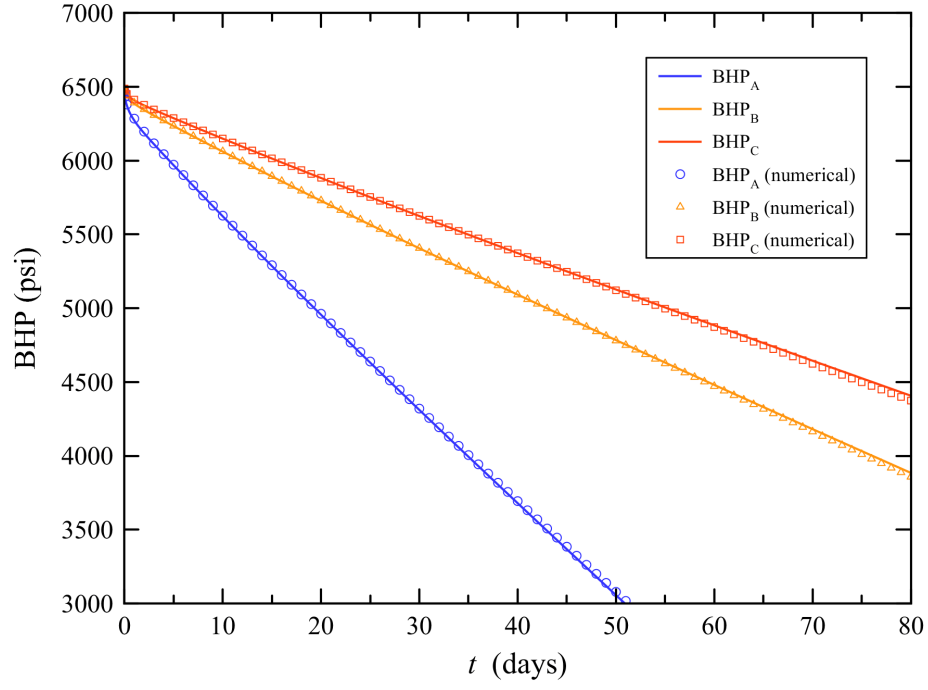


Figure 3.10: Analytical and numerical BHP data for $\delta_{wAB} = \delta_{wAC} = 0$.

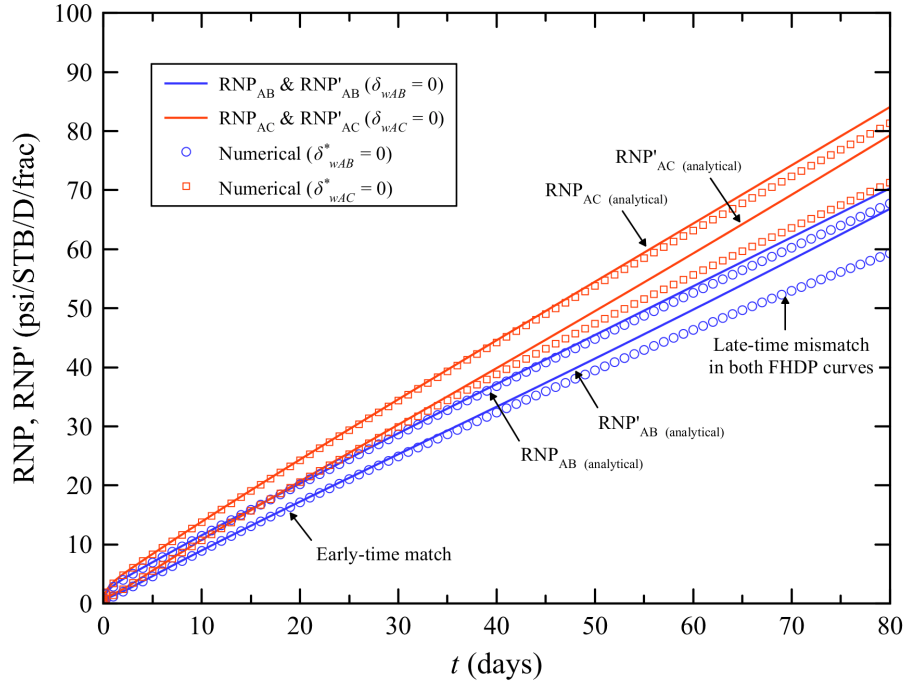


Figure 3.11: Rate-normalized plot for $\delta_{wAB} = \delta_{wAC} = 0$.

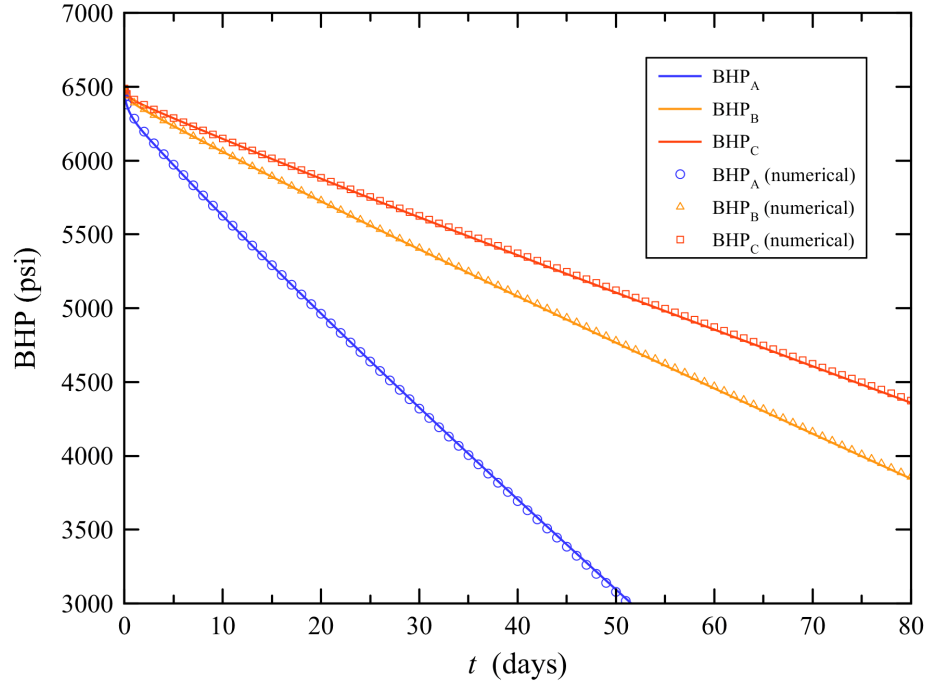


Figure 3.12: Analytical and numerical BHP data for $\delta_{wAB} = \delta_{wAC} = 8.9 \times 10^{-4}$.

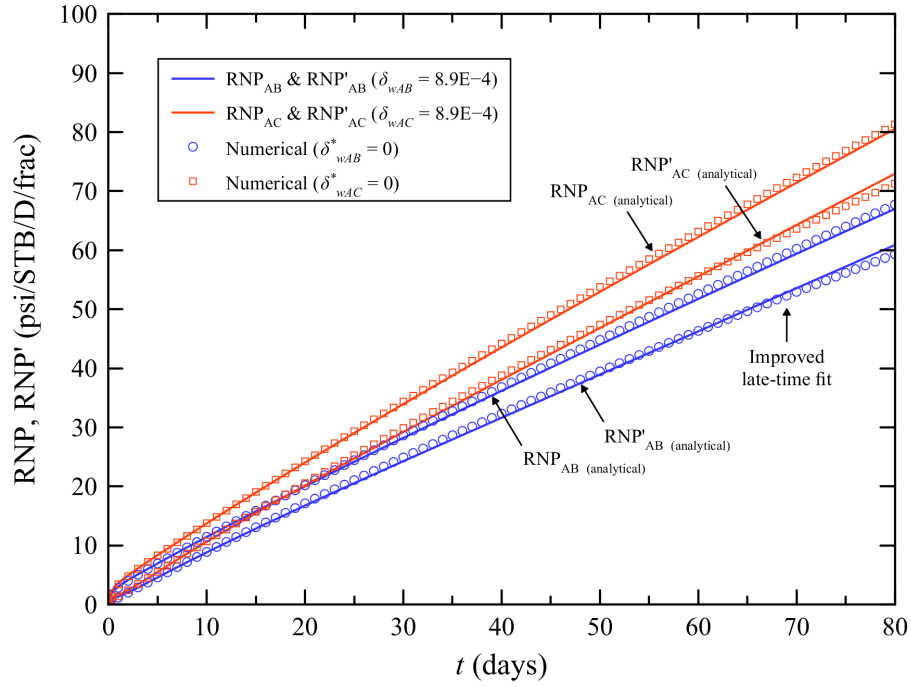


Figure 3.13: Rate-normalized plot for $\delta_{wAB} = \delta_{wAC} = 8.9 \times 10^{-4}$ ($\delta_{wAB}^* = \delta_{wAC}^* = 0$).

3.9.2 Validation Case Study 2

In this case, we impose three frac hits between wells A and B and two frac hits between wells A and C. This gives $\delta_{wAB}^* = 3/10 = 0.3$ and $\delta_{wAC}^* = 2/10 = 0.2$. Figure 3.14 illustrates pressure distribution in the multi-well pad after 68 days of production. Location of frac hits are indicated in this figure. Furthermore, recognize from the pressure distribution snapshot that fluid-flow around the frac hits is presumably two-dimensional. This may be a source of error for the estimation of δ_{wAB} and δ_{wAC} . Yet, pressure distribution remains fairly symmetric across other regions in the pad.

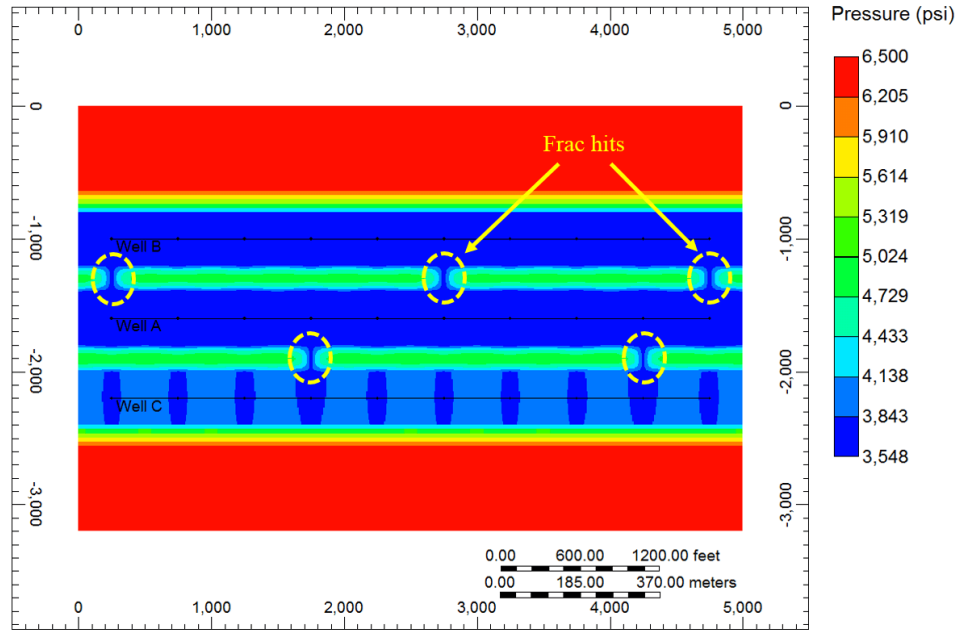


Figure 3.14: Pressure distribution after after 68 days for $\delta_{wAB}^* = 0.3$ and $\delta_{wAC}^* = 0.2$.

A good match between analytical and numerical data is obtained for $\delta_{wAB} = 0.28$ and $\delta_{wAC} = 0.18$. Compared to the actual fraction of frac hits, we see that the estimation of frac hits given by the analytical model is fairly accurate, with only 2% absolute error with respect to the actual fraction of frac hits.

Figure 3.15 compares analytical and numerical BHP data. An excellent match between models is observed. Likewise, the corresponding rate-normalized plot, shown by Figure 3.16, confirms the excellent match between analytical and numerical data when $\delta_{wAB} = 0.28$ and $\delta_{wAC} = 0.18$. RNP_{Aj} and RNP'_{Aj} exhibit a trend toward stabilization which confirms the pressure equilibration hypothesis initially proposed.

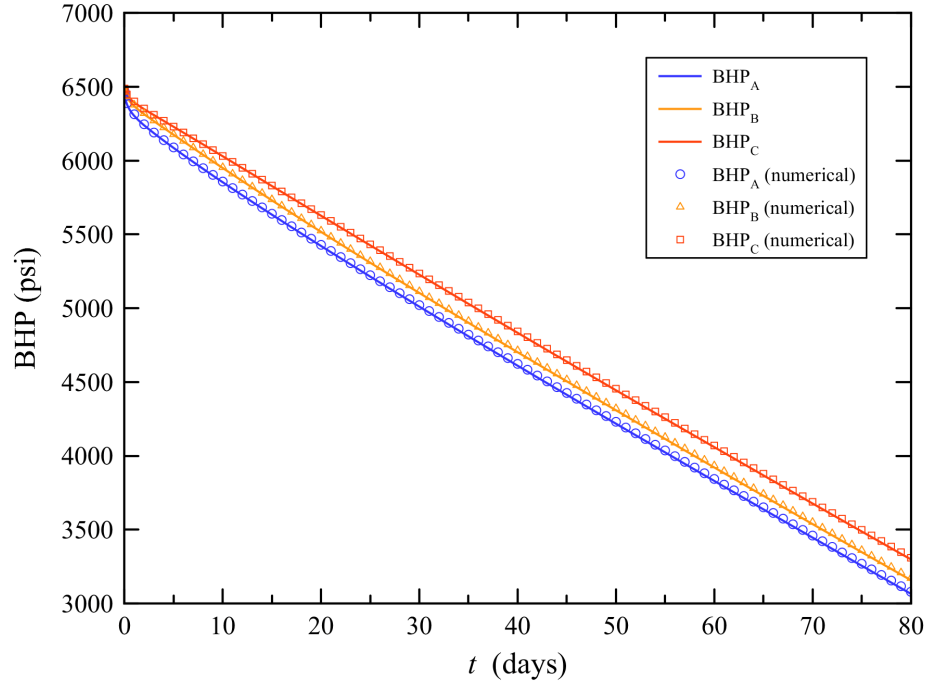


Figure 3.15: Analytical and numerical BHP data for $\delta_{wAB} = 0.28$ and $\delta_{wAC} = 0.18$.

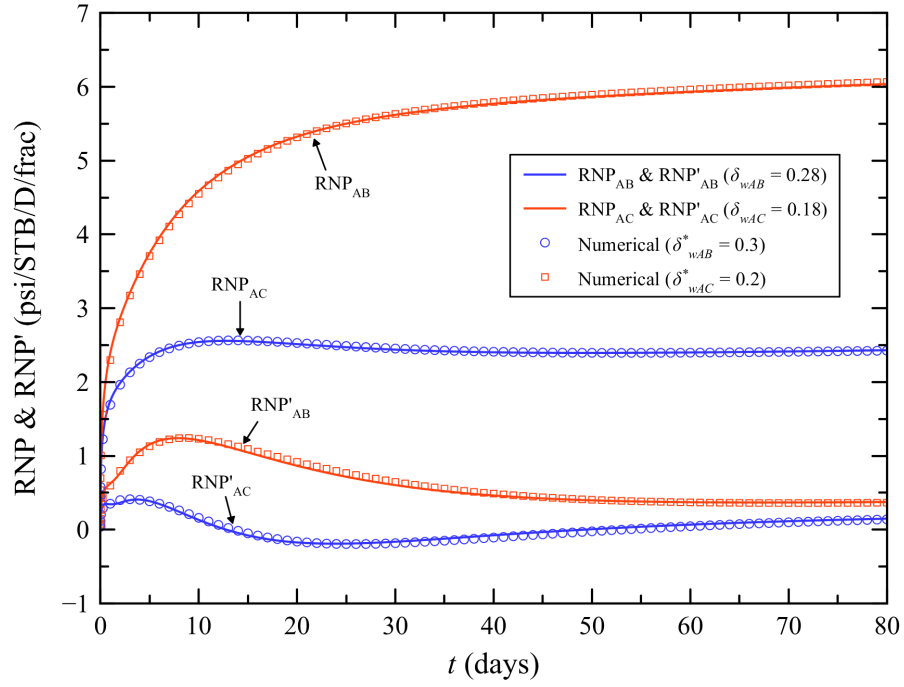


Figure 3.16: Rate-normalized plot for $\delta_{wAB}^* = 0.3$ and $\delta_{wAC}^* = 0.2$.

3.9.3 Validation Case Study 3

We impose two frac hits between wells A and B and four frac hits between wells A and C hence $\delta_{wAB}^* = 2/10 = 0.2$ and $\delta_{wAC}^* = 4/10 = 0.4$. Figure 3.17 illustrates the numerical estimation of pressure distribution in the pad after 70 days. Notice that, in addition to the 2-D flow occurring near the frac hits, and compared to the overall pressure behavior across fractured stages, pressure behaves asymmetrically in the stages of well B located near the frac hits and approximately half-way between frac hits in well C. This may be a source of error in the estimation of δ_{wAj} given that the analytical model was derived on the ground of symmetry pressure conditions and communication between frac hits and matrix.

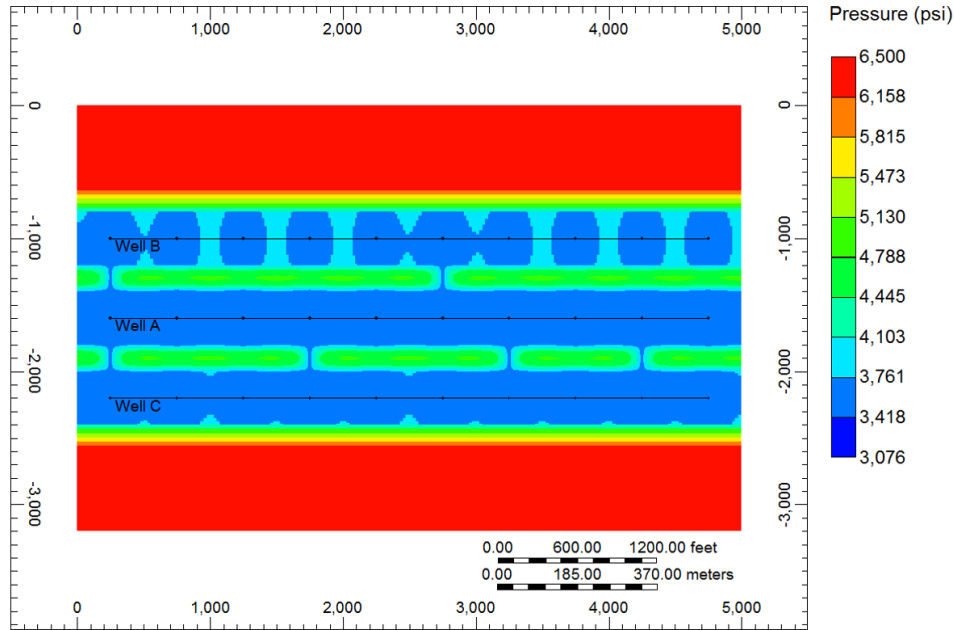


Figure 3.17: Pressure distribution after 70 days for the case $\delta_{wAB}^* = 0.2$ and $\delta_{wAC}^* = 0.4$.

An excellent match between analytical solution and numerical data is obtained when $\delta_{wAB} = 0.176$ and $\delta_{wAC} = 0.36$. Figure 3.18 presents the benchmark between analytical and numerical BHP data while Figure 3.19 shows the resulting rate-normalized plot. An excellent match between analytical and numerical data is observed in both figures. Similar to the previous case study, both RNP_{Aj} and RNP'_{Aj} show a marked trend toward stabilization; however, this plateau-type response is attained earlier than the previous case (i.e. compare Figure 3.16 and Figure 3.19).

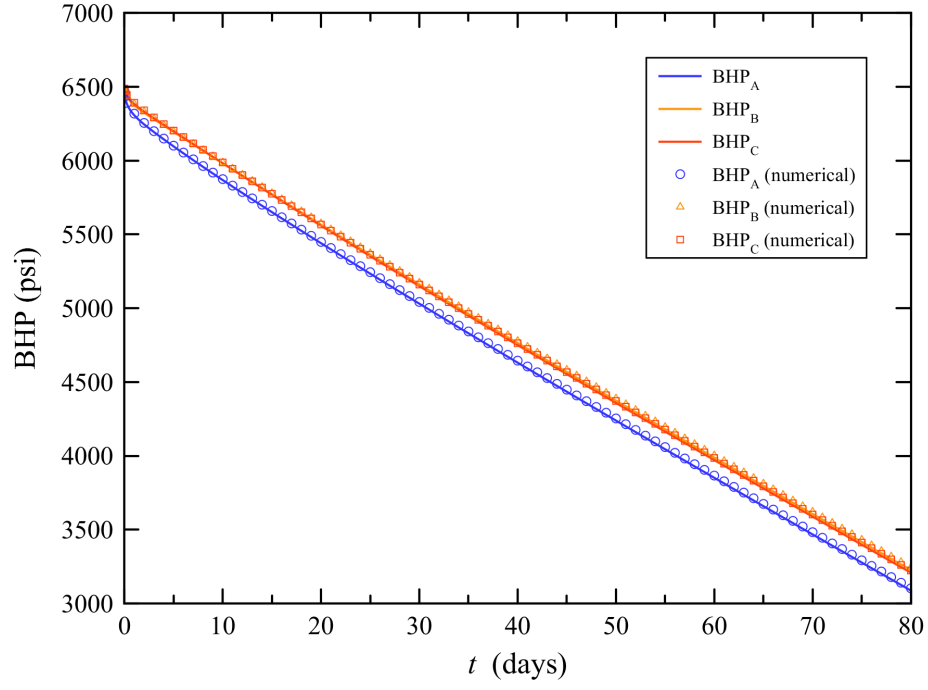


Figure 3.18: Analytical and numerical BHP data for $\delta_{wAB} = 0.176$ and $\delta_{wAC} = 0.36$.

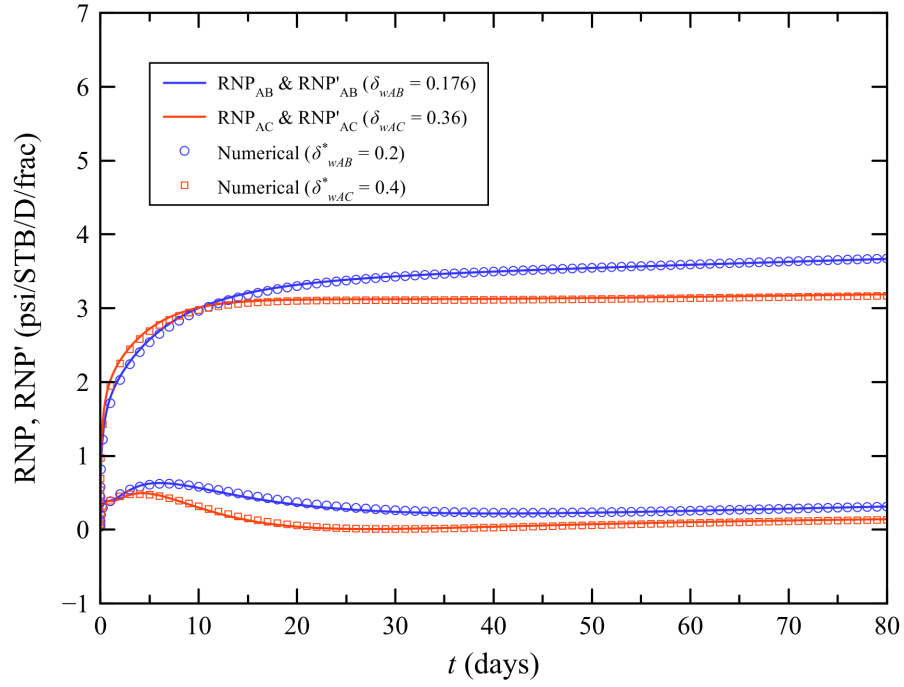


Figure 3.19: Rate-normalized plot for $\delta_{wAB} = 0.176$ and $\delta_{wAC} = 0.36$.

3.9.4 Validation Case Study 4

In this case study, we create one frac hit between wells A and B, and eight frac hits between wells A and C, resulting in $\delta_{wAB}^* = 0.1$ and $\delta_{wAC}^* = 0.8$. Given the highly contrasted degree of interference, we would expect RNP_{AC} and RNP'_{AC} to attain equilibrium quicker than RNP_{AB} and RNP'_{AB} . Figure 3.20 illustrates the location of the frac hits and the current pressure distribution in the multi-well pad at $t = 70$ days. Similar to previous case studies, 2-D fluid-flow seems to appear near the frac hits at late time, thus potentially leading to some degree of error in the estimation of δ_{wAj} .

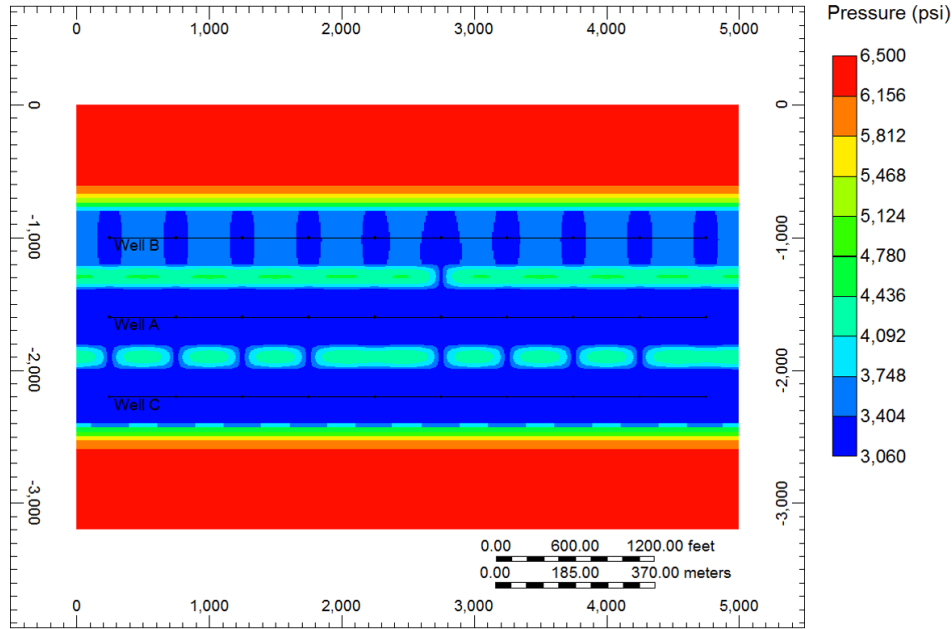


Figure 3.20: Pressure distribution after 70 days for the scenario $\delta_{wAB}^* = 0.1$ and $\delta_{wAC}^* = 0.8$.

Figure 3.21 shows the history-matching between analytical and numerical BHP data for $d_{wAB} = 0.089$ and $d_{wAC} = 0.76$, resulting in 1.1% and 4% absolute error, respectively. Notice the slight mismatch in the analytical estimation of BHP of well A. Nonetheless, we conclude that the overall history-match of numerical pressure-transient data is excellent. The agreement between analytical and numerical data is further confirmed by the rate-normalized plot in Figure 3.22. Recognize that RNP_{AC} and RNP'_{AC} reach stabilization faster than RNP_{AB} and RNP'_{AB} , as expected. Also, be aware that RNP_{AC} and RNP'_{AC} exhibit a slightly better match with numerical data than RNP_{AB} and RNP'_{AB} .

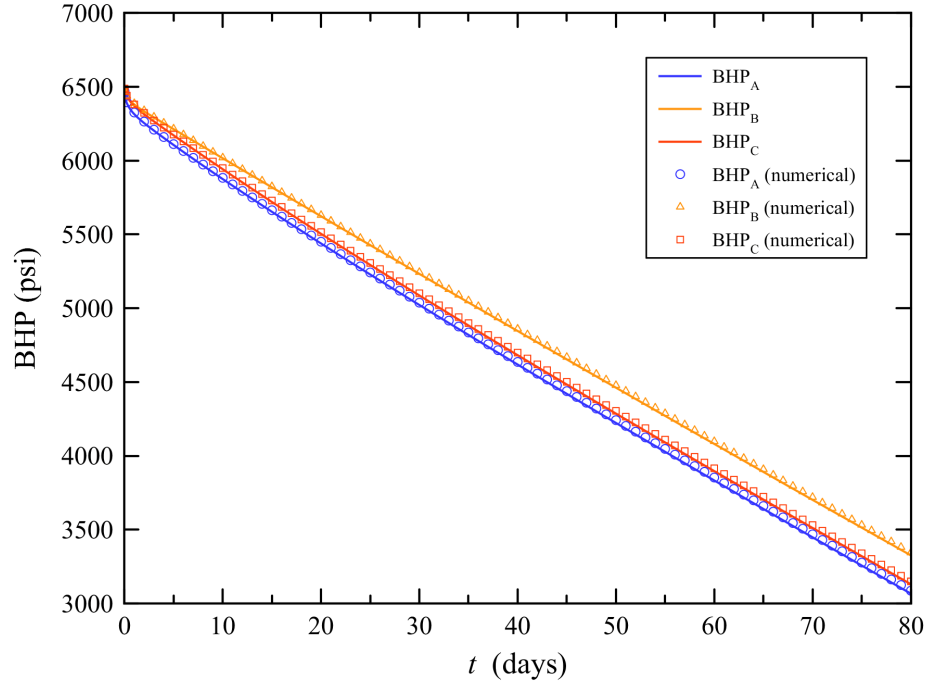


Figure 3.21: Comparison of analytical and numerical BHP data for $\delta_{wAB} = 0.089$ and $\delta_{wAC} = 0.76$.

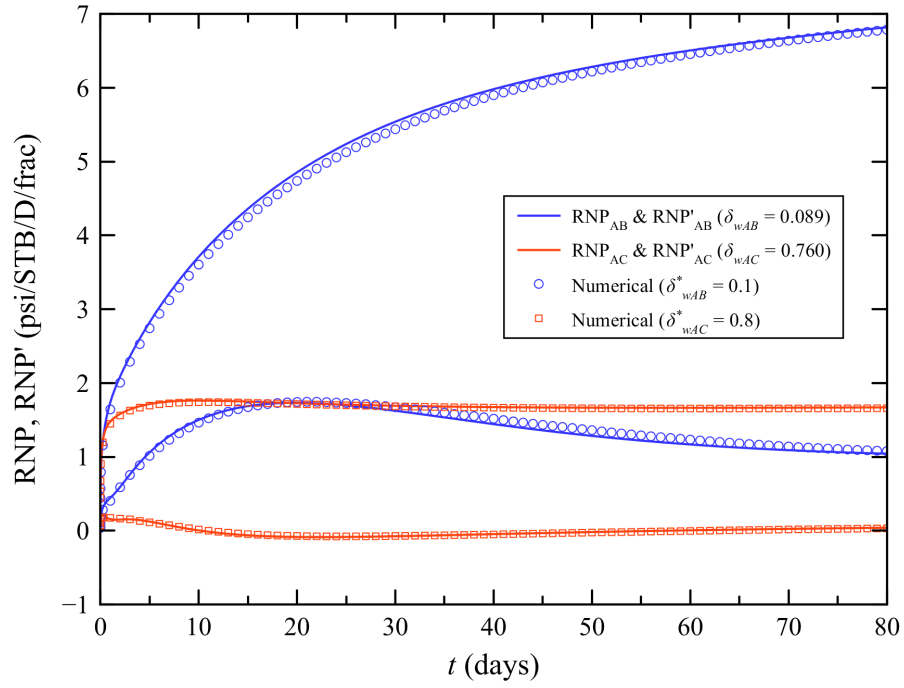


Figure 3.22: Rate-normalized plot for $\delta_{wAB} = 0.089$ and $\delta_{wAC} = 0.76$.

3.10. Sensitivity Analysis

In this section, we design several flow scenarios to test the sensitivity of the estimation of δ_{wAj}^* to several parameters, such as distance between MFHWs (L_{Aj}), fracture half-length (x_{fj}), fracture conductivity ($C_{fj} = k_{fj}w_j$), SRV permeability (k_{1j}) and distance between fractured stages ($2x_{ej}$) for $j = B, C$. Here, we consider the baseline case $L_{Aj} = 600$ ft, $x_{fj} = 200$ ft, $k_{1j} = 0.1$ md, $C_{fj} = 500$ md-ft and $2x_{ej} = 500$ ft. The main objective of this study is to history-match analytical and numerical RNP_{AB} and RNP'_{AB} data, rather than individual BHPs, to estimate δ_{wAB}^* using type-curves.

We assume that frac hits only occur between wells A and B; however, pressure communication through the matrix between wells A and C is still possible. We assign well C the same properties from well A for all cases. Figure 3.23 illustrates the schematic of the well pad used in this section. Fractures are assumed planar and perpendicular to their host MFHW. Each MFHW has 10 hydraulic fractures, equally spaced with respect to their counterparts (i.e. $x_{eA} = x_{eB} = x_{eC}$). Moreover, all fractured stages are assume to have equal properties per well. Reservoir and fluid properties are taken from Table 3.1.

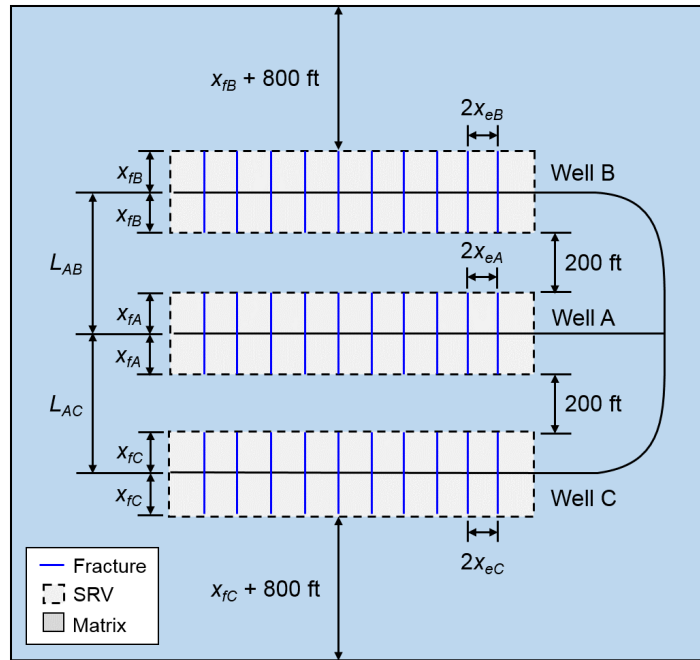


Figure 3.23: Three-MFHW pad model used for sensitivity analyses.

For pressure-transient analysis purposes, we consider that well A is flowing at constant rate while wells B and C are shut-in, this way modeling the more realistic well interfer-

ence test setup (Awada et al., 2016). Furthermore, we define $(q_{\text{well}})_B = (q_{\text{well}})_C = 10^{-4}$ STB/D in the numerical simulator to ensure that fracture stages of wells B and C are active/open even though wells are shut-in.

We carry out numerical simulations for $0 \leq \delta_{wAB} \leq 1$ with a step of 0.1 for each case study. Results are tabulated in the form of δ_{wAB}^* versus δ_{wAB} correlations. Correlation results will be presented graphically. Lastly, we introduce the history-matched rate-normalized type-curves corresponding to each sensitivity study. BHP data will not be discussed in this section.

3.10.1 Impact of Distance between Wells

MFHW properties are the same for all wells ($x_f = 200$ ft, $k_1 = 0.1$ md and $C_f = 500$ md-ft). In this case study, $500 \leq L_{AB} \leq 1000$ ft while $L_{AC} = 600$ ft is assumed fixed. Table 3.2 summarizes the correlation between δ_{wAB}^* and δ_{wAB} as a function of L_{AB} . Additionally, we found that $\delta_{wAC} \neq 0$ indicating that pressure communication between wells A and C took place through the inner matrix region.

Table 3.2: Correlation between δ_{wAB}^* and δ_{wAB} as a function of L_{AB} .

δ_{wAB}^*	δ_{wAB} vs. L_{AB} [ft]					
	500	600*	700	800	900	1000
0.1	0.088	0.087	0.087	0.088	0.09	0.091
0.2	0.172	0.175	0.18	0.18	0.18	0.184
0.3	0.269	0.268	0.27	0.275	0.278	0.28
0.4	0.366	0.365	0.365	0.367	0.372	0.375
0.5	0.465	0.46	0.47	0.47	0.475	0.478
0.6	0.562	0.56	0.57	0.57	0.575	0.578
0.7	0.672	0.67	0.678	0.68	0.682	0.686
0.8	0.781	0.78	0.785	0.785	0.79	0.794
0.9	0.91	0.9	0.9	0.9	0.9	0.9
1.0	1.02	1.015	1.02	1.02	1.02	1.02
δ_{wAC}	7×10^{-4}	6×10^{-4}	6×10^{-4}	8×10^{-4}	7×10^{-4}	6×10^{-4}

* = baseline scenario.

The case $L_{AB} = L_{AC} = 600$ ft will be the baseline scenario for the subsequent sensitivity analyses. The results for this case are shown under the 600* column in Ta-

ble 3.2. It is important to emphasize that values for δ_{wAB} and δ_{wAC} were obtained by history-matching analytical and numerical RNP_{AB} and RNP'_{AB} data not individual BHPs. Type-curves matching for RNP_{AB} and RNP'_{AB} will be discussed later in this section.

Figure 3.24 illustrates the numerical pressure distribution of the multi-well pad under analysis for the case $L_{AB} = 1000$ ft and $\delta_{wAB}^* = 0.4$ at $t = 80$ days. The most salient feature from this figure is the occurrence of 2-D flow in the inner matrix region between wells A and B. As such, pressure may equilibrate at a slower rate than that predicted by the analytical solution because of the pressure support due to frac-hit-matrix communication.

Furthermore, note that pressure communication between wells A and C is apparently weak. Nonetheless, we found that $\delta_{wAC} = 6 \times 10^{-4}$ in this scenario. It is noteworthy to mention that neglecting pressure communication between wells A and C through the matrix may lead to erroneous results or make it challenging when estimating the fraction of frac hits between wells A and B via history-matching δ_{wAB} .

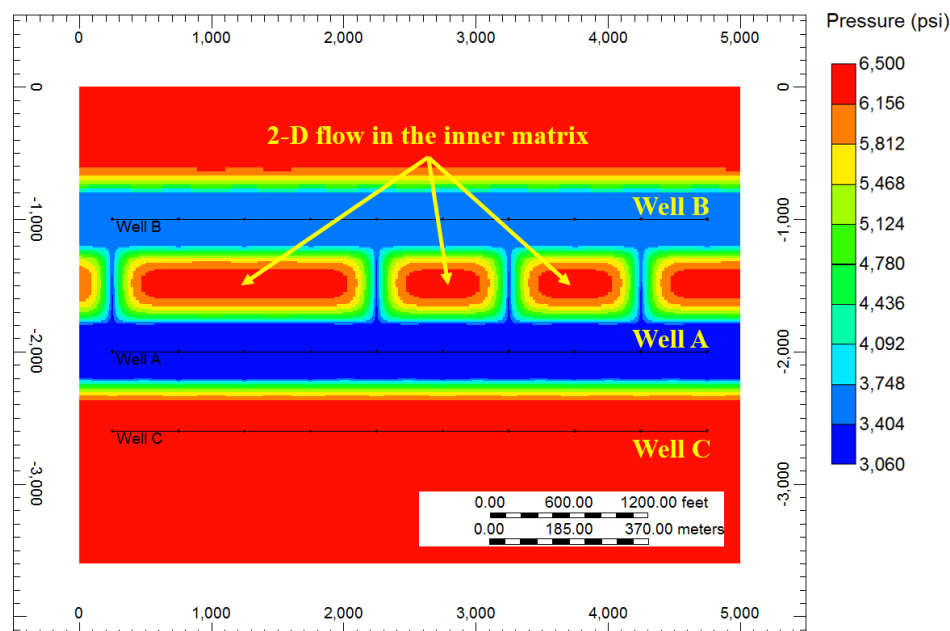


Figure 3.24: Pressure distribution in the multi-well pad under study for the case $L_{AB} = 1000$ ft and $\delta_{wAB}^* = 0.4$.

Figure 3.25 compares the history-matched values of δ_{wAB} and δ_{wAB}^* to the ideal correlation $\delta_{wAB} = \delta_{wAB}^*$ (i.e. identity line with a unit slope crossing by the origin). Variations

in L_{AB} do not have a significant impact on the analytical estimation of the fraction of frac hits. Notice that values of δ_{wAB} lie close to the identity line, thus confirming the goodness of the analytical estimation of δ_{wAB}^* .

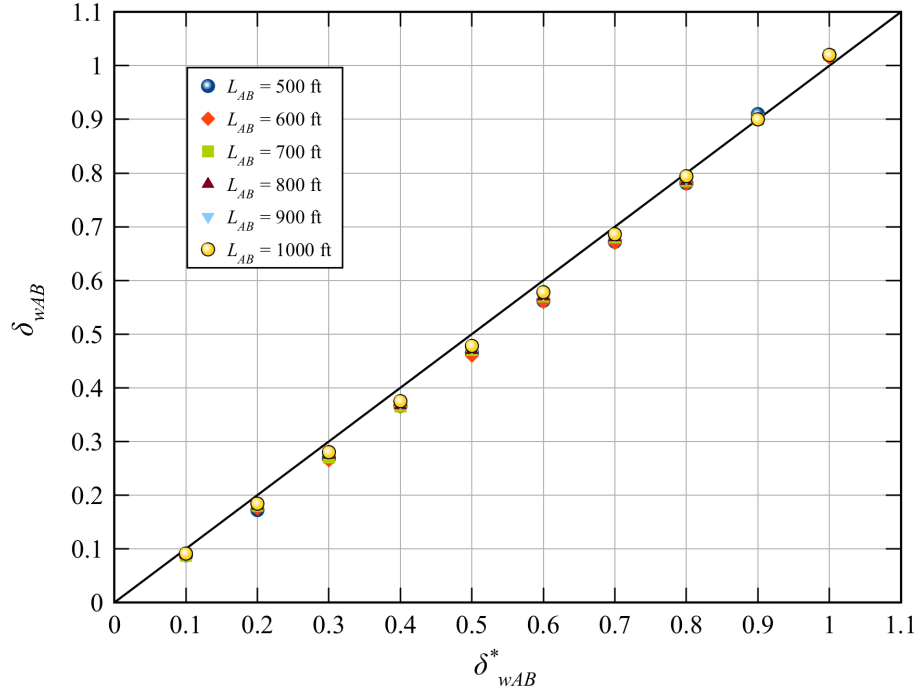


Figure 3.25: Graphical correlation between δ_{wAB}^* and δ_{wAB} for $500 \leq L_{AB} \leq 1000$ ft and $L_{AC} = 600$ ft.

History-matching results show that the accuracy of the analytical estimation of BHP decreases with increasing L_{AB} particularly at late times when 2-D flow becomes dominant near the frac hits. To illustrate this point, let us consider two cases for which $\delta_{wAB}^* = 0.4$. Figure 3.26 and Figure 3.27 show the history-matched BHP for $L_{AB} = 600$ and 1000 ft, respectively. While BHP forecast is accurate for the former case, late-time mismatch is observed for the latter case. Therefore, we recommend using the proposed analytical model for well performance forecast only when $L_{AB} < 800$ ft.

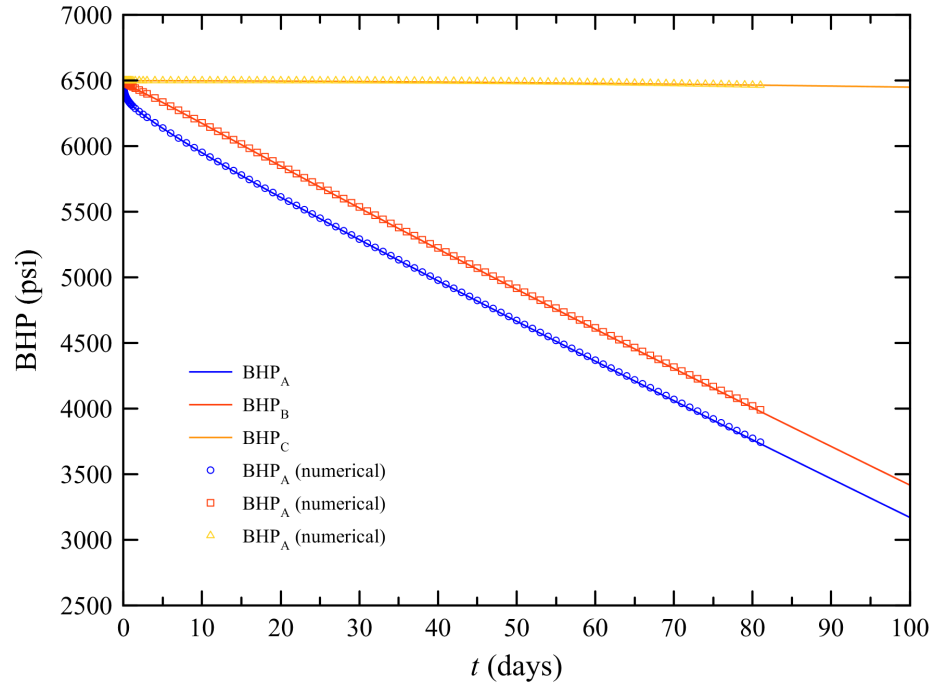


Figure 3.26: History-matching of BHP for $L_{AB} = 600$ ft and $\delta_{wAB}^* = 0.4$.

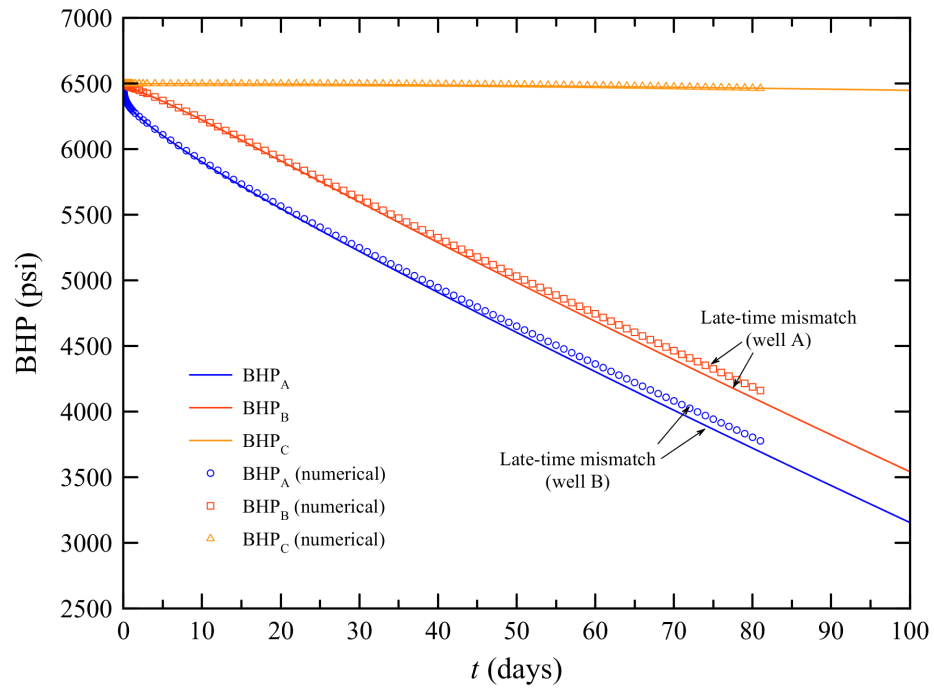


Figure 3.27: History-matching of BHP for $L_{AB} = 1000$ ft and $\delta_{wAB}^* = 0.4$.

Figure 3.28 through Figure 3.33 show the history-matched type-curves, based on RNP_{AB} and RNP'_{AB} , for the present sensitivity case study. There are a number of relevant facts worth highlighting hereby.

To begin with, note that, in the absence of well interference effects, RNP_{AB} and RNP'_{AB} curves exhibit the behavior of SRV-matrix flow, characterized by the 1/2-slope (SRV linear-flow regime) and ~ 1 -slope ("boundary-dominated" flow regime) lines resulting from $\delta_{wAB}^* = 0$. However, transient pressure response starts deviating from the ideal SRV-matrix response as δ_{wAB}^* increases.

Second, RNP_{AB} curves exhibit a clear trend toward stabilization. The higher δ_{wAB}^* the faster the stabilization and the smaller the variation in RNP_{AB} over time. Numerical data can be easily history-matched against RNP_{AB} type-curves regardless of the time (early or late-time data).

Conversely, RNP'_{AB} curves exhibit a skin-factor-like bump at mid-times, followed by a rebound towards their final stabilized value. Unlike RNP_{AB} , numerical data can only be history-matched with RNP'_{AB} type-curves up to a certain time, which depends on δ_{wAB}^* , beyond which data departs from the type-curves. This time window is approximately given by the dashed line on each type-curve plot.

The fact that numerical RNP'_{AB} data continue to decline without the late rebound trend exhibited by the analytical solution may indicate the onset of pressure equilibration within the inner matrix region, which is not accounted for the analytical model. In other words, while numerical data suggest equilibration would take place across the entire pad, the analytical model only allows for equilibration to occur through frac hits hence extending the time to reach final equilibrium across interfering wells.

Third, recognize that frac hits can be detected at early times and its characterization can be achieved via history-matching of RNP_{AB} and/or RNP'_{AB} (up to the time window limit). According to data from the type-curves in discussion, one would need 10 days or less worth of pressure-transient data to detect and estimate the fraction of frac hits between wells A and B. Notably, even a 24-hour well test should suffice for that matter.

Finally, the fact that RNP_{AB} and RNP'_{AB} match numerical data regardless of δ_{wAB}^* may be explained as follows. Suppose that $(\Delta p_{wj})_{\text{true}} = (\Delta p_{wj})_{\text{analytical}} + \epsilon_{wj}(t)$ where $\epsilon_{wj}(t)$ is the error due to late-time 2-D flow in the pad. Assuming that $\epsilon_{wA}(t) \approx \epsilon_{wB}(t)$, then $(\Delta p_{wAB})_{\text{true}} = (\Delta p_{wA})_{\text{analytical}} + \epsilon_{wA}(t) - (\Delta p_{wB})_{\text{analytical}} - \epsilon_{wB}(t) \approx (\Delta p_{wAB})_{\text{analytical}}$.

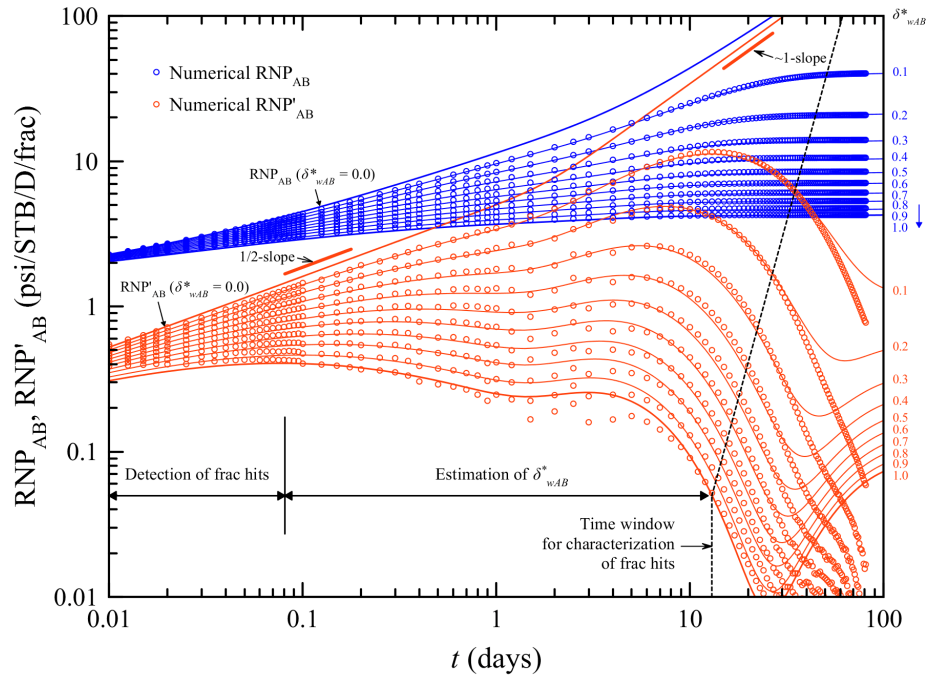


Figure 3.28: Frac-hits type-curves for $L_{AB} = 500$ ft.

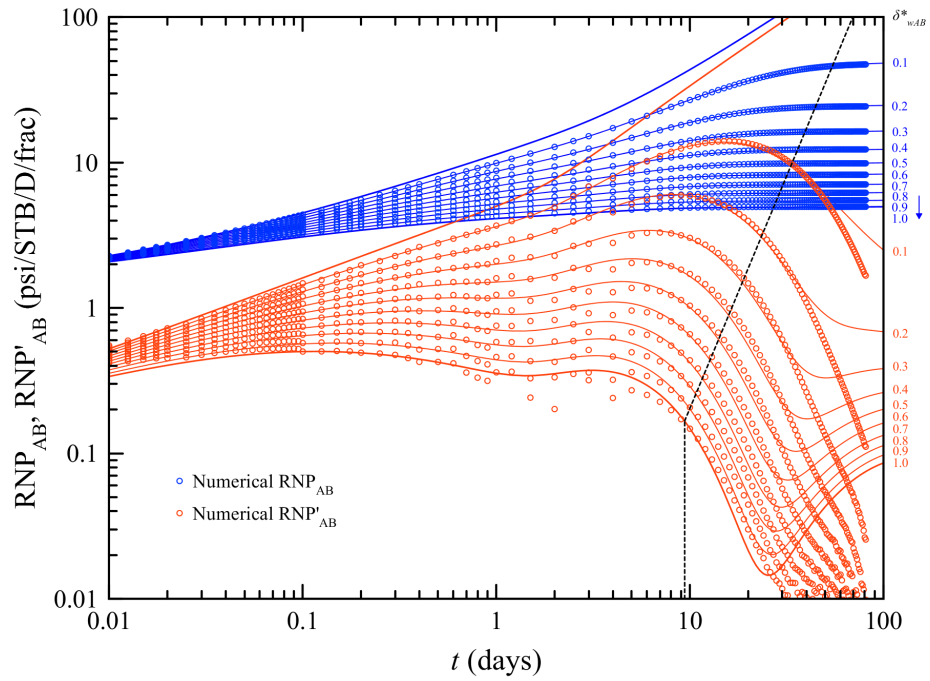


Figure 3.29: Frac-hits type-curves for $L_{AB} = 600$ ft (base case).

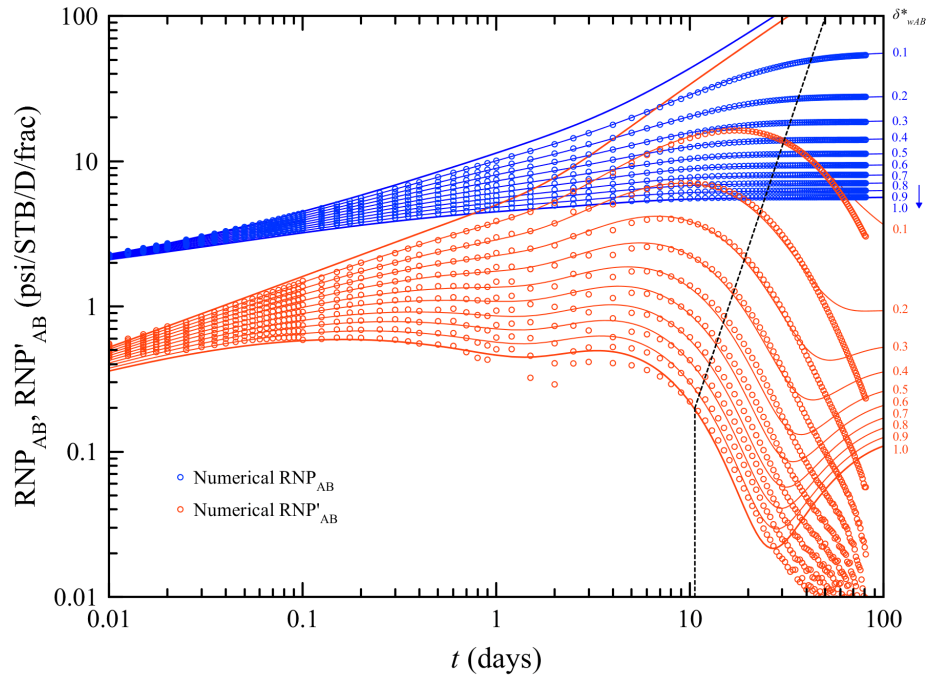


Figure 3.30: Frac-hits type-curves for $L_{AB} = 700$ ft.

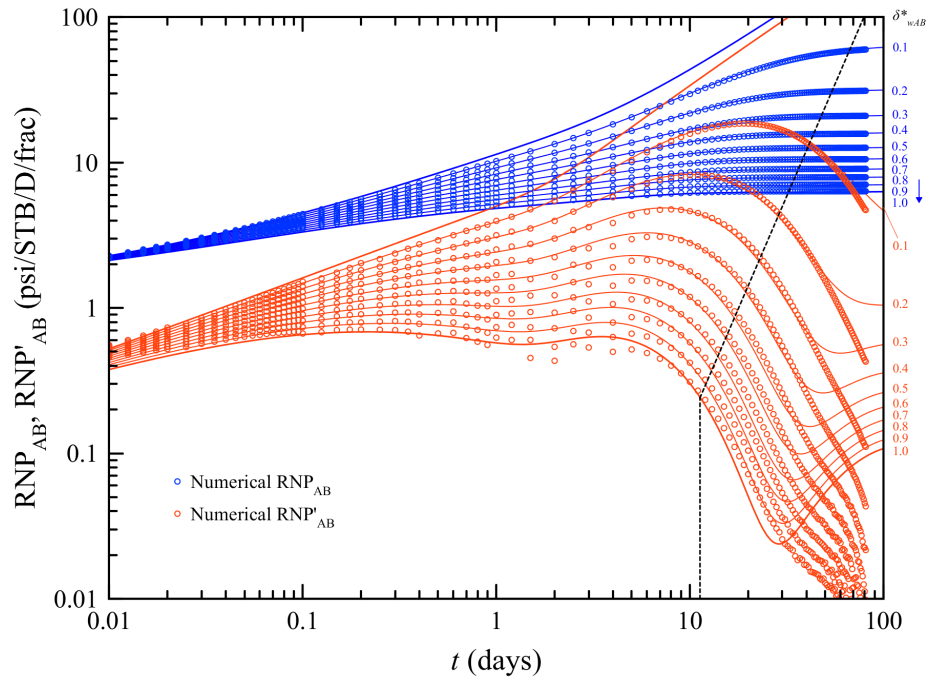


Figure 3.31: Frac-hits type-curves for $L_{AB} = 800$ ft.

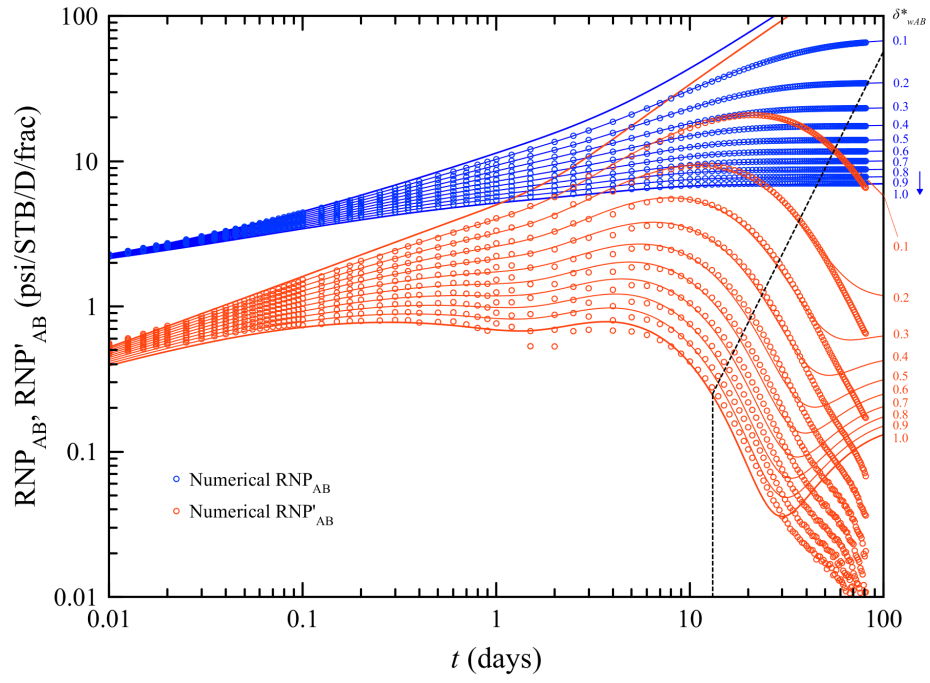


Figure 3.32: Frac-hits type-curves for $L_{AB} = 900$ ft.

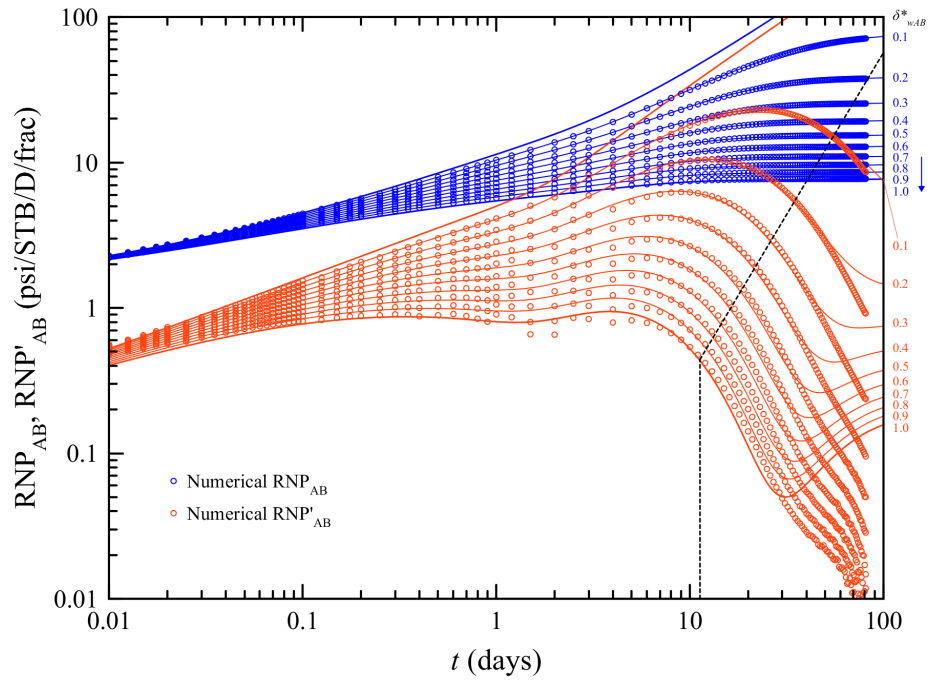


Figure 3.33: Frac-hits type-curves for $L_{AB} = 1000$ ft.

3.10.2 Impact of Fracture Half-length

3.10.2.1 Equal Fracture Half-length for all Wells

The scenario under evaluation relates to the case of equal completion design for all stages in the pad. The objective is to examine the influence of producing equally longer fractures in the pad on detecting frac hits. Thus, we assign equal fracture half-length to all fractures in the model, so that $x_{fA} = x_{fB} = x_{fC}$ and evaluate $200 \leq x_f \leq 600$ ft. We calculate the distance between wells and to external boundaries (wells B and C) using the relationships described in Figure 3.23, $L_{AB} = L_{AC} = 2x_f + 200$ [ft], $y_{eOB} = y_{eOC} = x_f + 800$ [ft]. The numerical simulation model was systematically adjusted with these relationships. In addition, SRV permeability ($k_1 = 0.1$ md) and fracture conductivity ($C_f = 500$ md-ft) is assumed equal for all wells.

Table 3.3 summarizes the resulting correlation between δ_{wAB}^* , δ_{wAB} and δ_{wAC} . Similar to the previous case study, $\delta_{wAC} \neq 0$ as an indication of pressure communication between wells A and C through the inner matrix region. In general, the analytical estimation of the fraction of frac hits is in good agreement with the actual degree of interference. The baseline scenario is shown in the column for $x_f = 200$ ft.

Table 3.3: Correlation between δ_{wAB}^* , δ_{wAB} and δ_{wAC} for $200 \leq x_f \leq 600$ ft.

δ_{wAB}^*	δ_{wAB} vs. x_f [ft]				
	200*	300	400	500	600
0.1	0.087	0.092	0.096	0.1	0.103
0.2	0.175	0.185	0.194	0.203	0.21
0.3	0.268	0.28	0.29	0.3	0.306
0.4	0.365	0.378	0.39	0.407	0.412
0.5	0.46	0.477	0.49	0.5	0.51
0.6	0.56	0.58	0.6	0.605	0.61
0.7	0.67	0.688	0.71	0.71	0.72
0.8	0.78	0.795	0.83	0.83	0.84
0.9	0.9	0.905	0.93	0.94	0.95
1.0	1.015	1.02	1.04	1.05	1.06
δ_{wAC}	9×10^{-4}				

* = baseline scenario.

Figure 3.34 illustrates the graphical correlation between δ_{wAB} and δ_{wAB}^* obtained for $200 \leq x_f \leq 600$ ft compared to the ideal correlation $\delta_{wAB} = \delta_{wAB}^*$. Alike the previous sensitivity case study, variations in x_f do not have a significant impact on the analytical estimation of the fraction of frac hits when x_f is equal in all MFHWs in the pad. This is confirmed graphically as all the history-matched values of δ_{wAB} are lying close to the identity line.

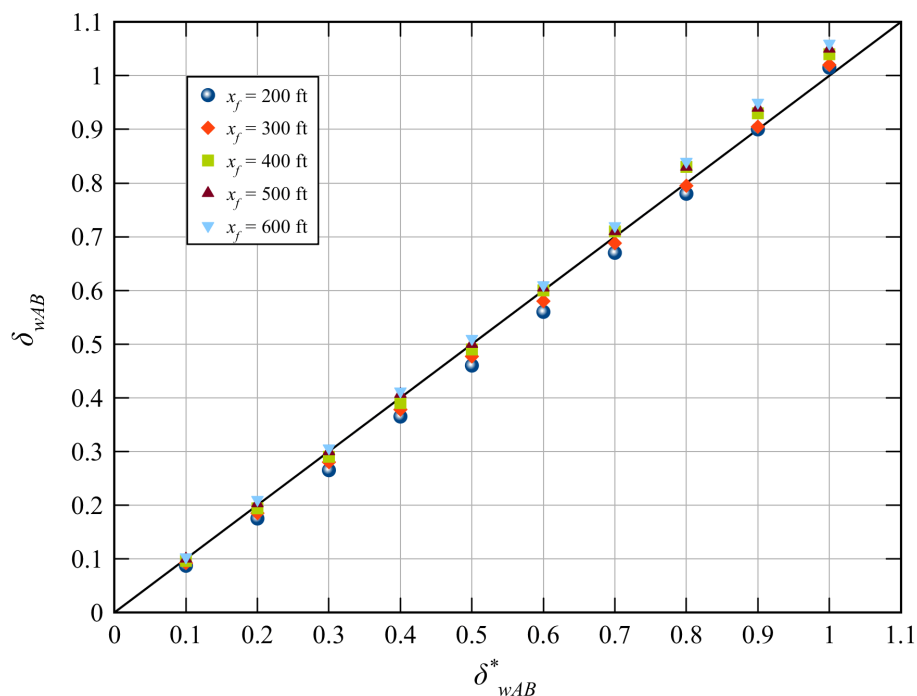


Figure 3.34: Graphical correlation between δ_{wAB}^* and δ_{wAB} for $200 \leq x_f \leq 600$ ft.

The resulting history-matching of BHPs is in good agreement with numerical data for all the evaluated values of x_f . Nevertheless, BHP matching is slightly better for larger values of x_f , the reason being that larger fracture half-lengths would ensue and sustain linear flow for longer. Figure 3.35 illustrates the resulting history-match of BHP for $x_f = 300$ ft while Figure 3.36 for $x_f = 600$ ft. $\delta_{wAB}^* = 0.5$ for both cases. As mentioned earlier, notice that BHP match is slightly better for the case $x_f = 600$ ft. In general, we conclude that the accuracy of the analytical frac hits model would not be affected if $200 \leq x_f \leq 600$ ft.

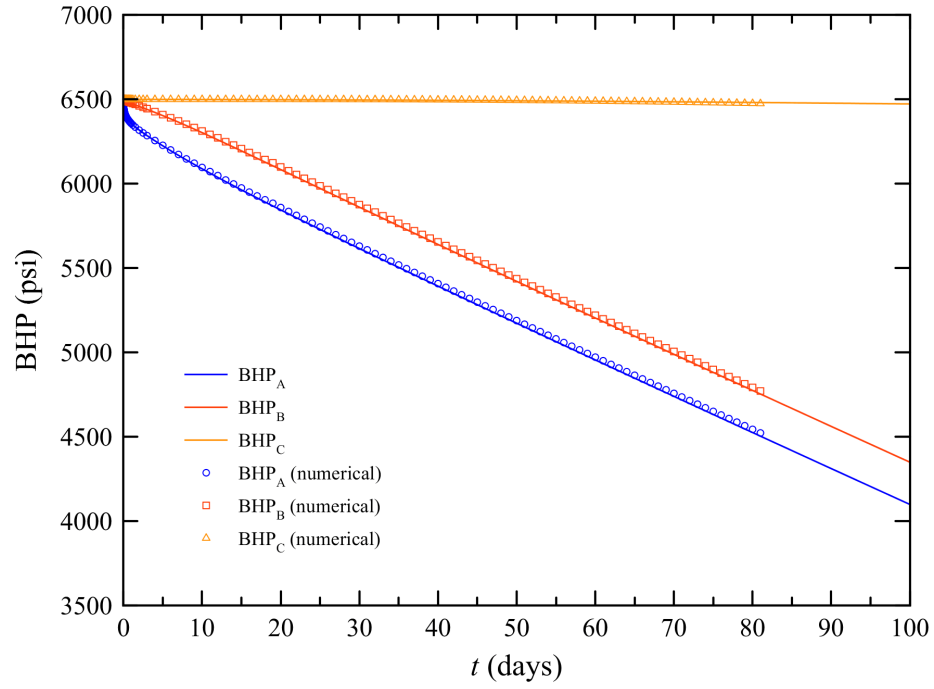


Figure 3.35: History-matching of BHP for $x_f = 300$ ft and $\delta_{wAB}^* = 0.5$.

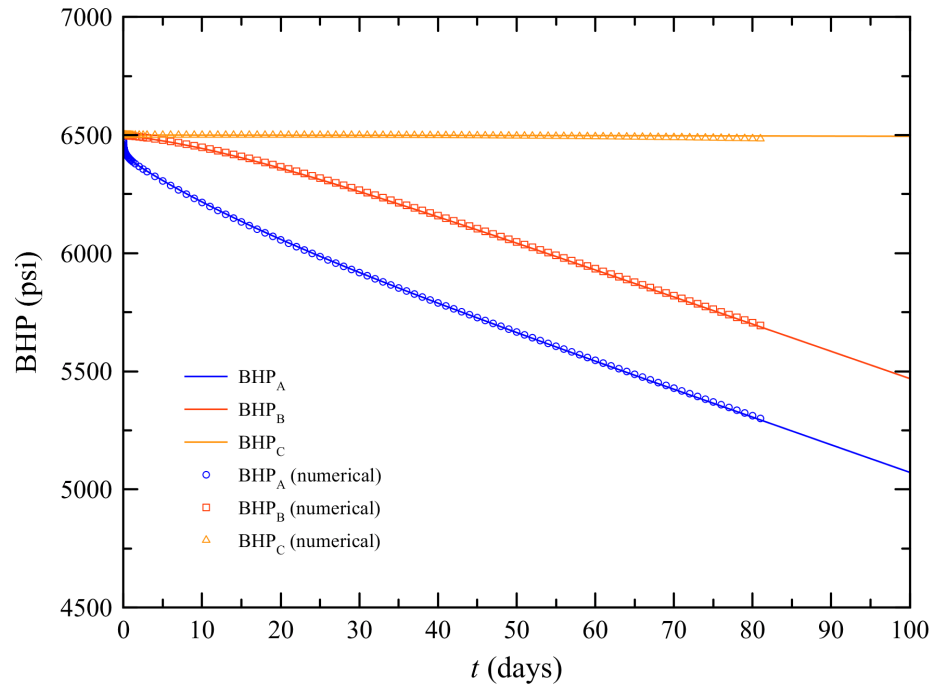


Figure 3.36: History-matching of BHP for $x_f = 600$ ft and $\delta_{wAB}^* = 0.5$.

Type-curves for this case study are shown in Figure 3.37 through Figure 3.40. Similar to the previous case study, $\delta_{wAB}^* = 0$ will result in the RNP_{AB} and RNP'_{AB} corresponding to the case of SRV-matrix flow. However, this behavior changes when $\delta_{wAB}^* > 0$.

Transient RNP_{AB} data exhibits a marked trend towards stabilization that increases with increasing δ_{wAB}^* . Both analytical and numerical data are in excellent agreement, regardless of time and/or degree of interference. This means that δ_{wAB}^* can be characterized using either early or late-time data, regardless of the degree of interference.

Numerical RNP'_{AB} data, on the other hand, only matches analytical type-curves up to a point where pressure support from the inner matrix region is seen by both wells. The approximate limiting time margin up to which RNP'_{AB} can be history-matched is shown in dashed lines on each type-curves plot. In this case, frac hits can be detected and characterized using early to mid-time data only (<10 day), the minimum time window for the estimation of fraction of frac hits being $0 < t \leq 3$ days.

Finally, recognize that the range of RNP_{AB} and RNP'_{AB} for $0 \leq \delta_{wAB}^* \leq 1$ shrinks with increasing x_f when $x_{fA} = x_{fB}$. Although this does not represent any restriction for using the analytical mode, this is worth mentioning given that these type-curves could double as diagnostic plots.

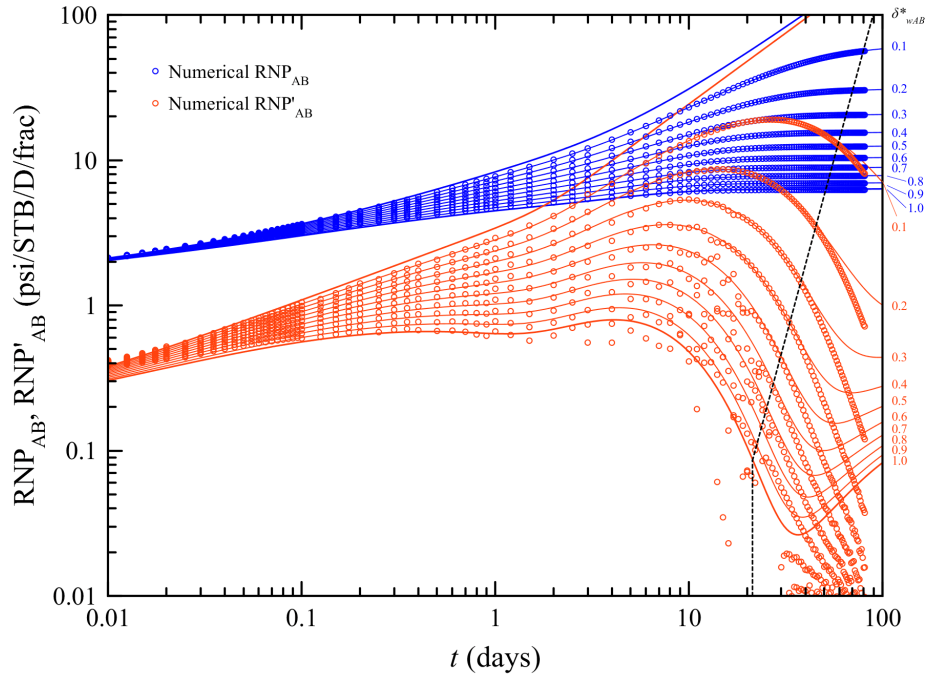


Figure 3.37: Frac-hits type-curves for $x_{fA} = x_{fB} = 300$ ft.

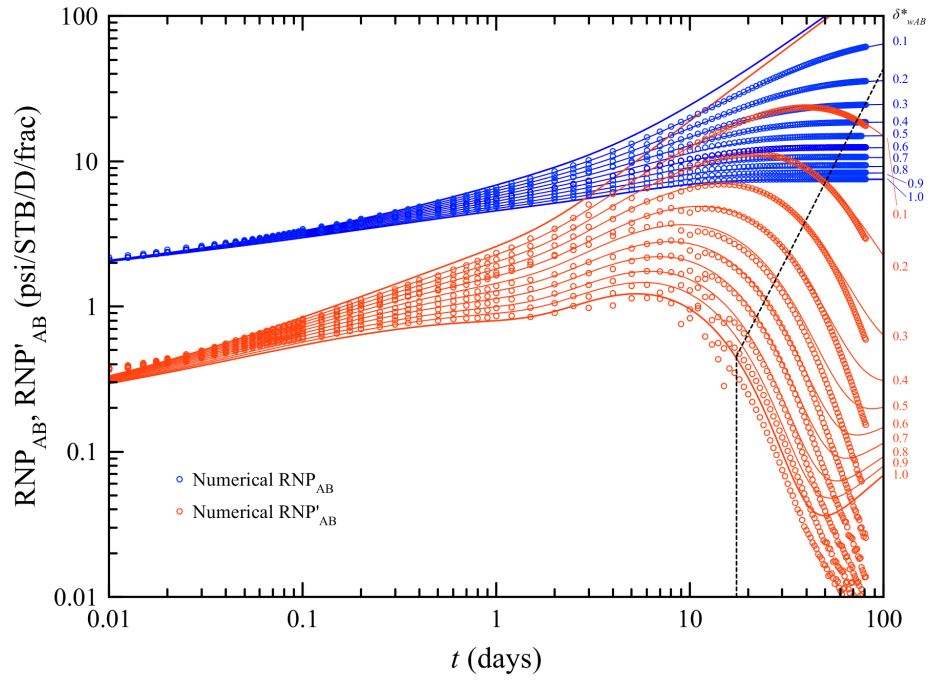


Figure 3.38: Frac-hits type-curves for $x_{fA} = x_{fB} = 400$ ft.

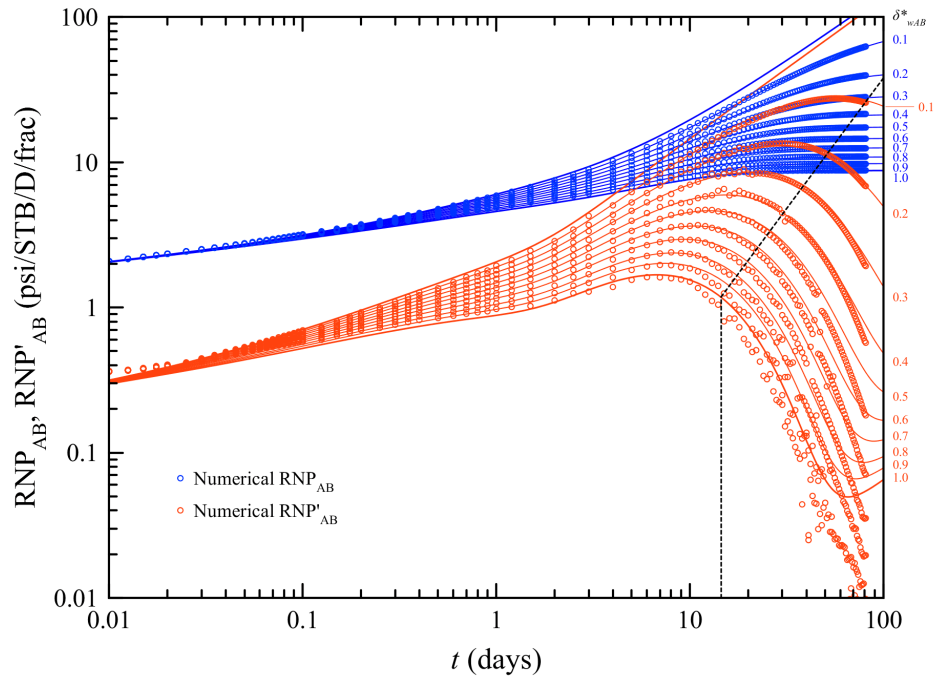


Figure 3.39: Frac-hits type-curves for $x_{fA} = x_{fB} = 500$ ft.

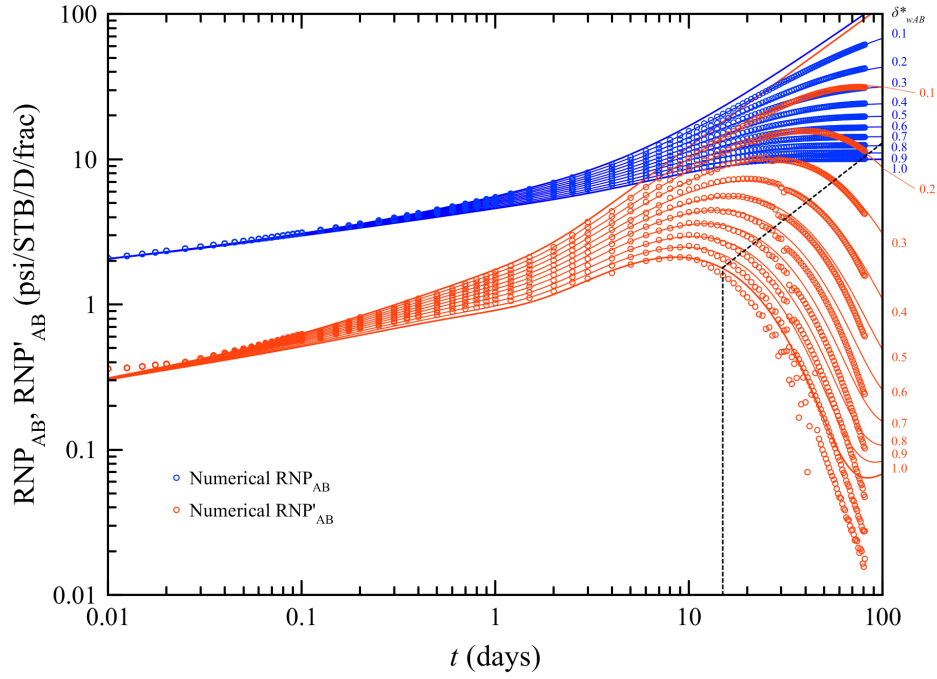


Figure 3.40: Frac-hits type-curves for $x_{fA} = x_{fB} = 600$ ft.

3.10.2.2 Different Fracture Half-length

This case is related to different fracturing job sizes in a multi-well pad. We assume equal fracture half-length for wells A and C ($x_{fA} = x_{fC} = 200$ ft) while $200 \leq x_{fB} \leq 600$ ft. SRV permeability ($k_1 = 0.1$ md) and fracture conductivity ($C_f = 500$ md-ft) are equal for all wells. Distance between wells A and C ($L_{AC} = 600$ ft) and distance from well C to the reservoir boundary ($y_{eOC} = 1000$ ft) are fixed.

This case study may be considered a special case study of variability in F_{CD} for which $(F_{CD})_A = 25$ and $16.67 \geq (F_{CD})_B \geq 8.34$. Because x_{fB} is variable, distance from well B to the reservoir boundary was updated in both analytical and numerical models via $y_{eOB} = x_{fB} + 800$ [ft].

Table 3.4 summarizes the history-matching results for δ_{wAB} and δ_{wAC} . In contrast with the previous case, variability in x_{fB} alone leads to an overestimation of δ_{wAB}^* when history-matching the analytical type-curves. This phenomenon is particularly outstanding when $\delta_{wAB}^* > 0.5$. In addition, δ_{wAC}^* is relatively small for this case because $x_{fB} > x_{fA}$ inhibits a stronger interference between wells A and B.

In general, highly-contrasting values of x_{fA} and x_{fB} would result in the overestimation of δ_{wAB}^* , which can be as high as 22% for the case under study.

Table 3.4: Correlation between δ_{wAB}^* , δ_{wAB} , δ_{wAC} and x_{fB} for $x_{fA} = 200$ ft.

δ_{wAB}^*	δ_{wAB} vs. x_{fB} [ft]				
	200*	300	400	500	600
0.1	0.087	0.092	0.096	0.1	0.104
0.2	0.175	0.183	0.19	0.2	0.202
0.3	0.268	0.278	0.29	0.3	0.31
0.4	0.365	0.375	0.395	0.403	0.415
0.5	0.46	0.49	0.505	0.52	0.53
0.6	0.56	0.6	0.615	0.64	0.65
0.7	0.67	0.71	0.725	0.76	0.77
0.8	0.78	0.82	0.85	0.89	0.9
0.9	0.9	0.95	0.99	1.03	1.05
1.0	1.015	1.07	1.15	1.17	1.2
δ_{wAC}	6×10^{-4}				

* = baseline scenario.

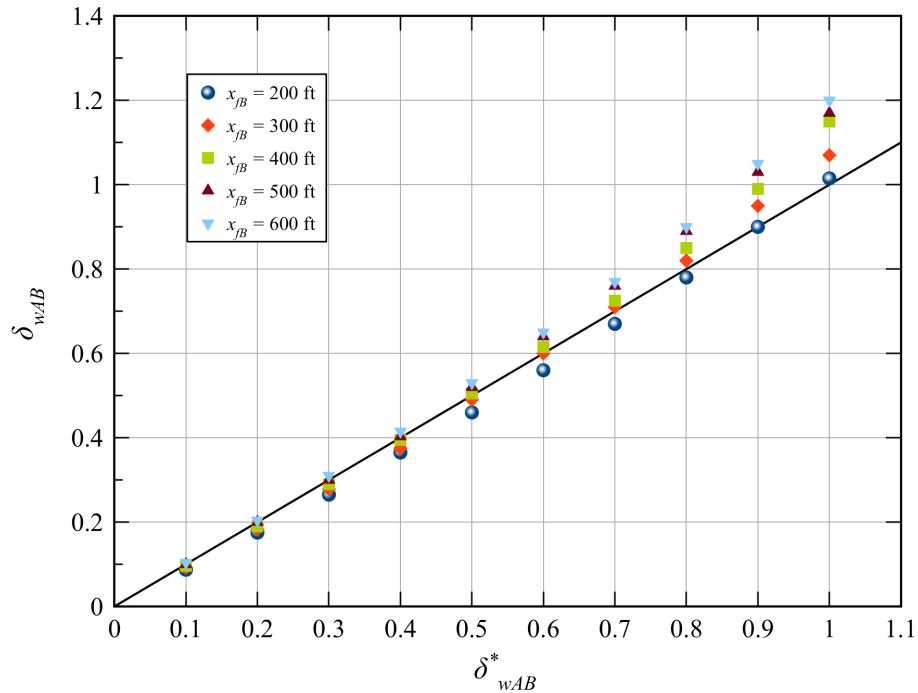


Figure 3.41: Graphical correlation between δ_{wAB}^* , δ_{wAB} and x_{fB} for $x_{fA} = 200$ ft.

Similar to the case for equal but increasing fracture half-length, history-matching of BHP seems to be in good agreement with numerical data for all x_{fB} . Figure 3.42 shows the history-matched BHP for all wells when $x_{fB} = 400$ ft and Figure 3.43 for $x_{fB} = 600$ ft. $\delta_{wAB}^* = 0.6$ in both scenarios. However, note that there is a slight mismatch with numerical BHP data in both figures at late times. But overall, the accuracy of the estimation of fraction of frac hits would not be compromised when $x_{fB} > x_{fA}$ and the analytical model may be used for well pad performance forecast.

History-matched type-curves for the present sensitivity analysis are presented in Figure 3.44 through Figure 3.47. Transient RNP_{AB} data can be history-matched with analytical type-curves during all time periods (early, mid and late time). RNP'_{AB} , however, can only be history-matched up to a certain time upon which 2-D flow becomes increasingly dominant in the multi-well pad due to simultaneous inner-matrix-to-frac hit and inner-matrix-to-SRV flow.

Notice that numerical data exhibit a rapid trend towards stabilization after surpassing the skin-like hump in RNP'_{AB} , which likely indicates additional pressure support from the inner matrix region. In general, analytical and numerical data can be history-matched up to 12 days for the worst-case scenario of $\delta_{AB}^* = 1$ (full frac hits).

The time window within which frac hits can be characterized using pressure-derivative data is delineated with dashed lines on each type-curves plot. Similar to the previous cases, frac hits can be detected and characterized within a relative short period of time, regardless of x_{fB} and/or δ_{AB}^* . In all cases, a one-day interference test would be sufficient to produce an accurate estimation of δ_{wAB}^* based on type-curves matching.

Additionally, note that the type-curves for this case exhibit a different response than those for the case of equal fracture half-length in all wells. The most significant of such differences is the steeper downward trend, followed by a rapid upward trend with increasing x_{fB} and δ_{wAB}^* in the analytical RNP'_{AB} . This feature is made evident when comparing Figure 3.44 and Figure 3.47.

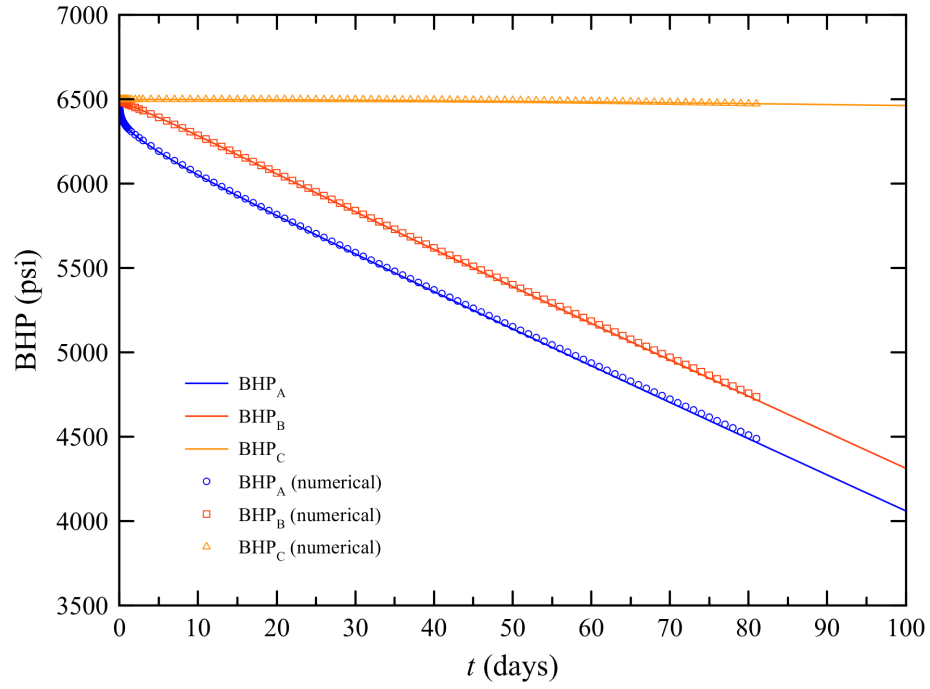


Figure 3.42: History-matching of BHP for $x_{fB} = 400$ ft and $\delta_{wAB}^* = 0.6$.

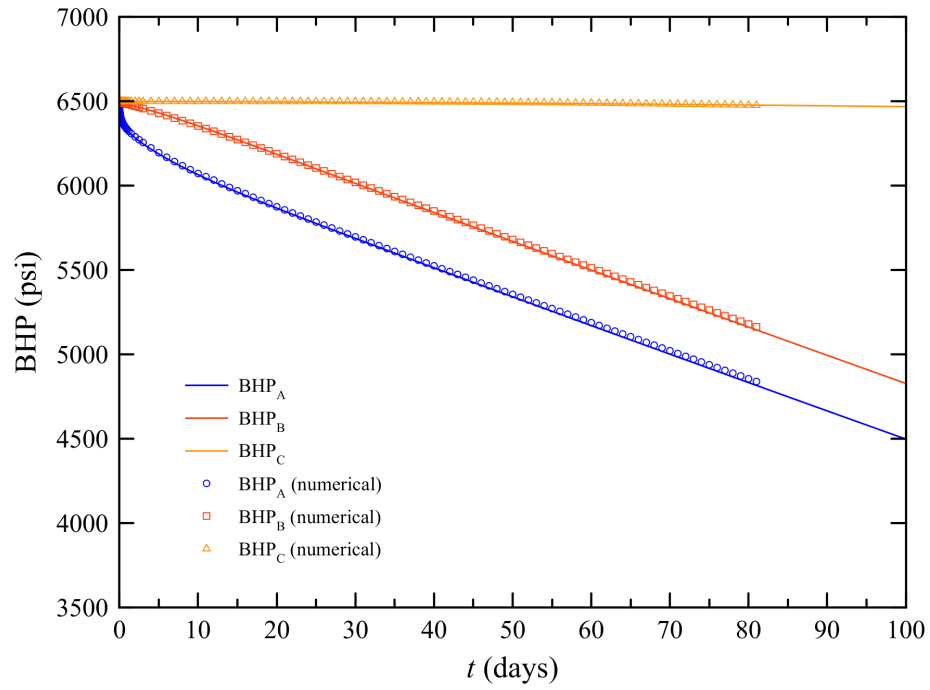


Figure 3.43: History-matching of BHP for $x_{fB} = 600$ ft and $\delta_{wAB}^* = 0.6$.

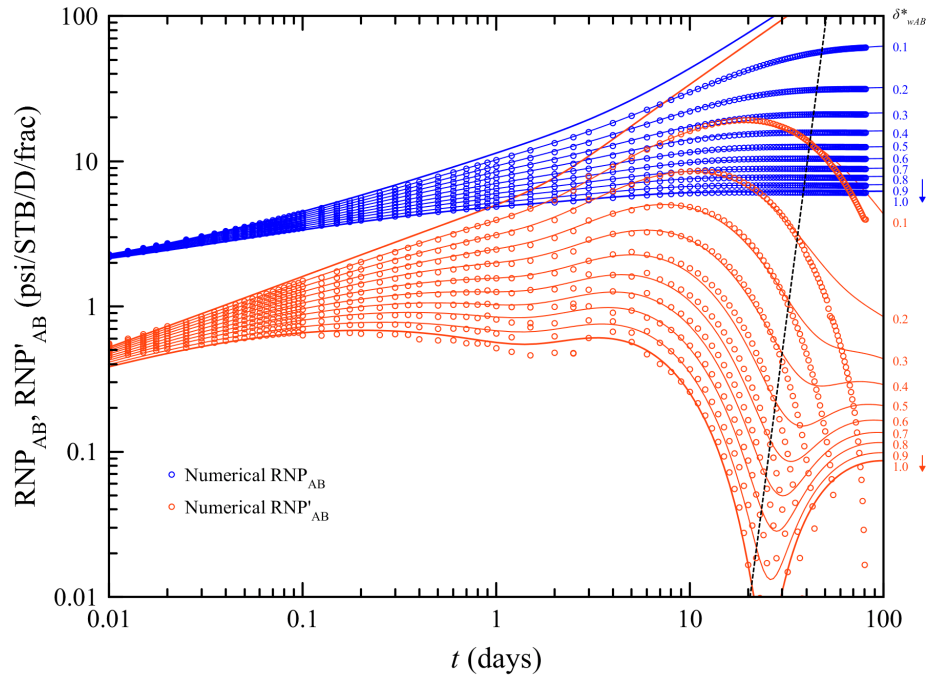


Figure 3.44: Frac-hits type-curves for $x_{fB} = 300$ ft.

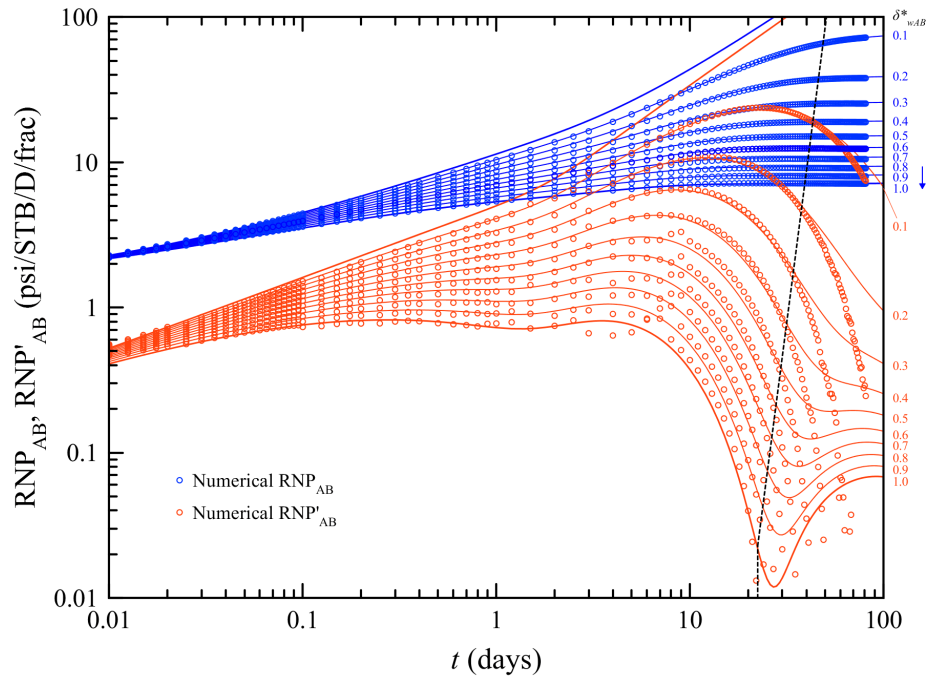


Figure 3.45: Frac-hits type-curves for $x_{fB} = 400$ ft.

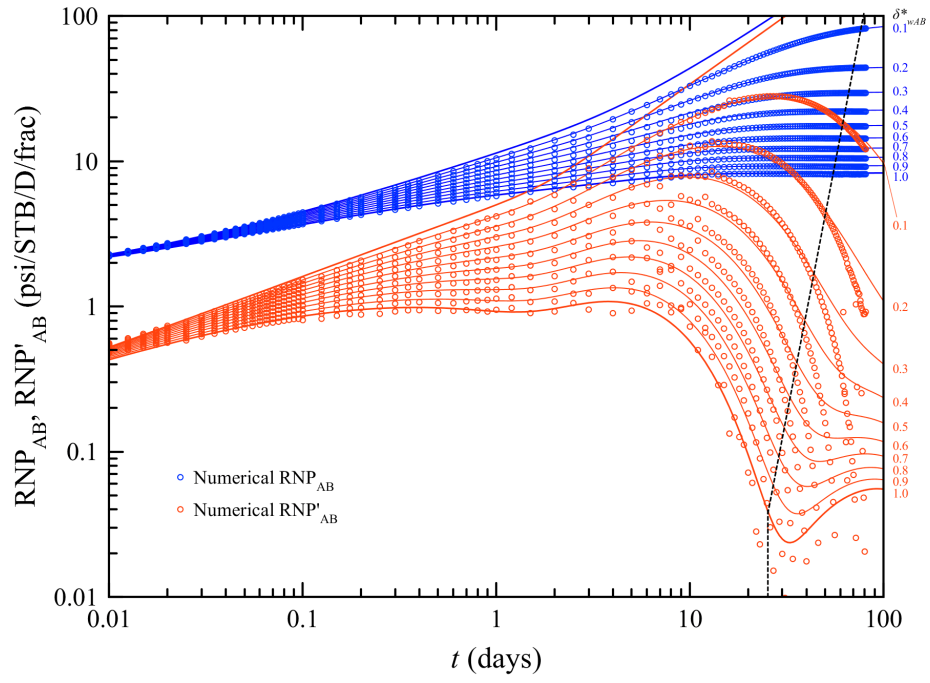


Figure 3.46: Frac-hits type-curves for $x_{fB} = 500$ ft.

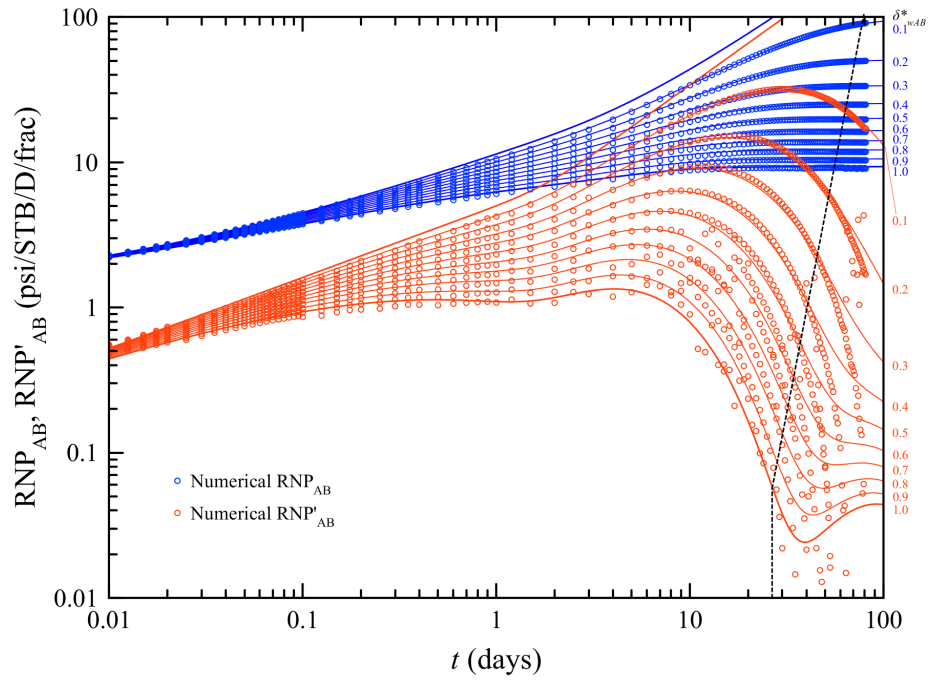


Figure 3.47: Frac-hits type-curves for $x_{fB} = 600$ ft.

3.10.3 Impact of Fracture Conductivity

3.10.3.1 Equal Fracture Conductivity for all Wells

This scenario relates to the case of using equal hydraulic fracture design for all stages in the pad. Here, we consider equal fracture conductivity for all MFHWs with $50 \leq C_f \leq 2500$ md-ft. SRV permeability ($k_1 = 0.1$ md) and fracture half-length ($x_f = 200$ ft) is assumed equal. This sensitivity analysis may be considered as special case of F_{CD} sensitivity with $2.5 \leq F_{CD} \leq 125$. Distance from wells B and C to well A is 600 ft.

The resulting correlation between δ_{wAB}^* , δ_{wAB} and δ_{wAC} is summarized in Table 3.5. The estimated degree of interference is fairly close to the actual fraction of frac hits except when fracture conductivity is relatively small (i.e. $C_f \leq 50$ md-ft). The maximum absolute error in the estimation of δ_{wAB}^* is +17% (overestimation).

Figure 3.48 shows the graphic correlation between δ_{wAB}^* and δ_{wAB} . It is evident from this figure that δ_{wAC} rapidly deviates upward off the identity line when $\delta_{wAB}^* > 0.4$. Aside from this result, we observe that the analytical estimation of the fraction of frac hits delivers fairly accurate results that would not get sensibly affected by an increasing fracture conductivity if $C_{fA} = C_{fB}$.

Table 3.5: Correlation between δ_{wAB}^* , δ_{wAB} and δ_{wAC} for $C_{fA} = C_{fB}$.

δ_{wAB}^*	δ_{wAB} vs. C_f [md-ft]				
	50	250	500*	1000	2500
0.1	0.105	0.09	0.087	0.085	0.084
0.2	0.21	0.18	0.175	0.172	0.17
0.3	0.31	0.275	0.268	0.26	0.258
0.4	0.415	0.37	0.365	0.355	0.35
0.5	0.53	0.47	0.46	0.45	0.445
0.6	0.645	0.57	0.56	0.55	0.545
0.7	0.77	0.68	0.67	0.66	0.65
0.8	0.89	0.79	0.78	0.77	0.76
0.9	1.03	0.92	0.9	0.88	0.87
1.0	1.17	1.03	1.015	1	0.99
δ_{wAC}	5×10^{-3}	1×10^{-3}	6×10^{-4}	5×10^{-4}	3×10^{-4}

* = baseline scenario.

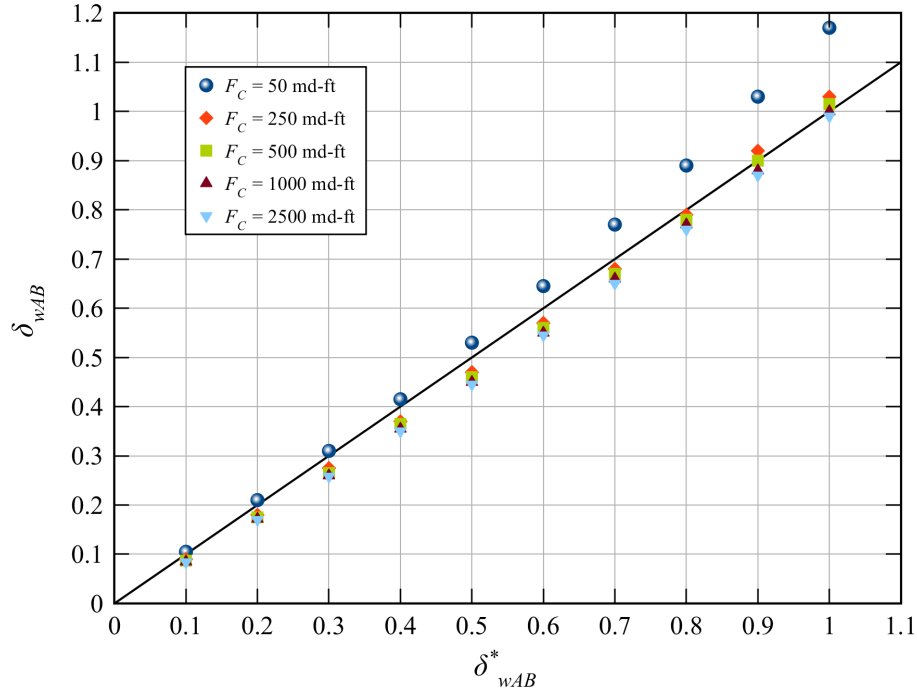


Figure 3.48: Graphical correlation between δ_{wAB}^* and δ_{wAB} for $C_{fA} = C_{fB}$.

Analytical and numerical BHP responses are in good agreement for all wells and values of fracture conductivity. Nonetheless, there is a slight misfit at late times when $C_f = 50$ md-ft. Be aware that $C_f = 50$ md-ft is equivalent to $F_{CD} = 2.5$ md-ft in this scenario, arguably a low dimensionless fracture conductivity, which may introduce some error into the analytical estimation of BHP.

Figure 3.49 illustrates the resulting history-match of BHP for $C_f = 50$ md-ft and Figure 3.50 for $C_f = 1000$ md-ft; $\delta_{wAB}^* = 0.5$ for both cases. Notice the negligible late-time mismatch in the latter figure. Also, realize that in despite $\delta_{wAB}^* = 0.5$ for both scenarios, BHP from wells A and B seem closer to each other for $C_f = 1000$ md-ft. This observation is physically tied to higher fracture conductivity enabling better pressure communication through frac hits between wells A and B.

In general, the analytical frac hits model gives a fairly accurate estimation of the degree of interference when $C_f > 50$ md-ft and all MFHWs have equal fracture conductivity. Given that late-time estimation of BHP is in good agreement with numerical data for all wells in the pad, we conclude that the analytical frac hits model may be implemented to forecast well performance if $C_f > 50$ md-ft.

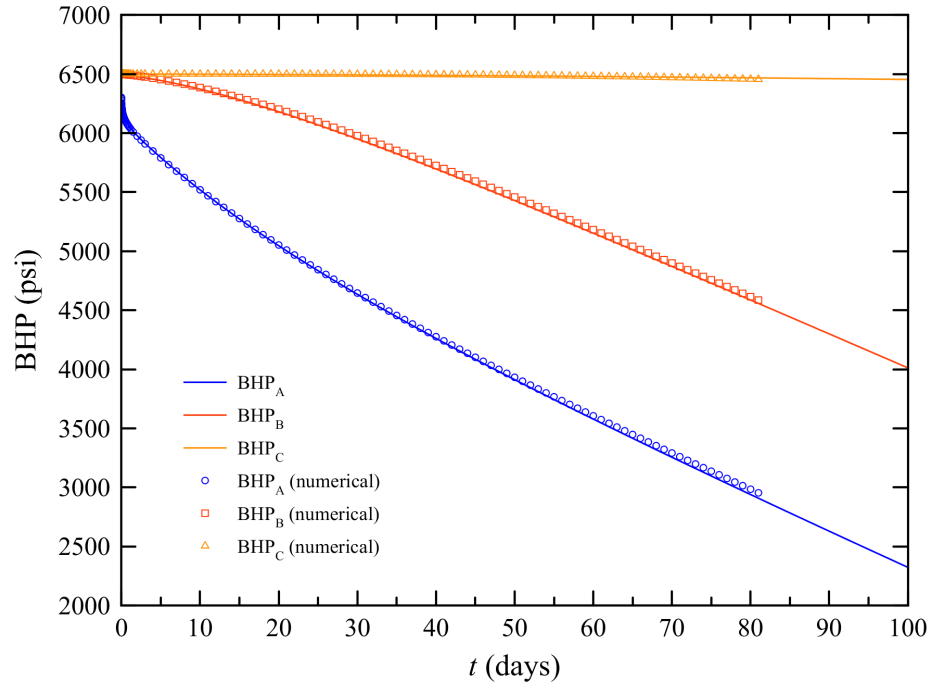


Figure 3.49: History-matching of BHP for $C_f = 50$ md-ft and $\delta_{wAB}^* = 0.5$.

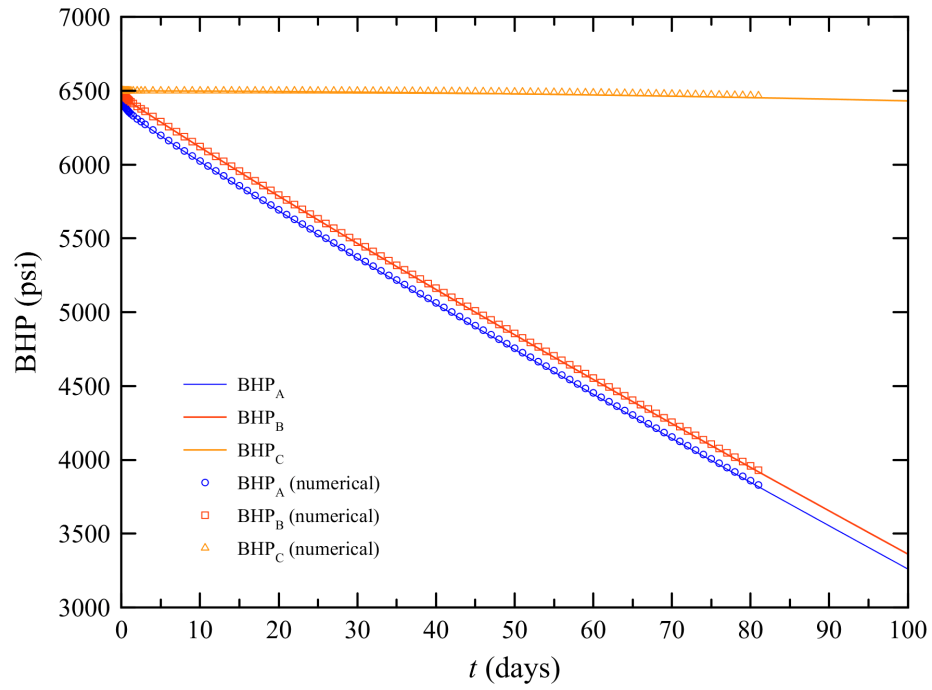


Figure 3.50: History-matching of BHP for $C_f = 1000$ md-ft and $\delta_{wAB}^* = 0.5$.

History-matched type-curves for the present case study are presented in Figure 3.51 through Figure 3.54. Numerical RNP_{AB} is smooth for all values of fracture conductivity; yet, numerical RNP'_{AB} data becomes considerably noisy for $C_f > 1000$ md-ft once it overcomes the skin-like hump in the type-curves.

This effect may be attributable to numerical issues due to a sudden appearance of 2-D. The reason is that a higher fracture conductivity would favor linear flow from the SRV into the fractures and, at the same time, enhancing flux from the inner matrix region into the frac hits. Implementation of smaller time steps for $t > 10$ days should improve the convergence of the numerical solution. Nonetheless, type-curves matching suggests pressure-transient data for $t \leq 10$ days would be sufficient to extract and interpret the required information about frac hits.

Figure 3.51 portrays an interesting case in which the range of both RNP_{AB} and RNP'_{AB} becomes narrow for $t < 0.1$ days (~ 2.5 hours). In fact, it may be challenging to detect frac hits within this period of time if fracture conductivity is sensibly low. In such case, frac hits can only be detected and assessed within 1 and 10 days. This temporal restriction should be taken into consideration when designing an interference test for low fracture conductivity multi-well pads.

On the contrary, relatively large and equal fracture conductivity in all wells would allow for early detection and estimation of the fraction of frac hits between wells A and B. Resulting type-curves for $C_f > 250$ md-ft suggest that frac hits characterization could be accomplished within 0.4 days (~ 10 hours), which further enables the design and implement short interference tests. The recommended time window for frac hits characterization based on RNP'_{AB} as a function of δ_{wAB}^* is delimited on each type-curves plot using dashed lines.

Lastly, observe that RNP'_{AB} type-curves do not exhibit the rapid downward-upward behavior, occurring after the skin-like hump, when $C_f = 50$ md-ft (Figure 3.51). Yet, this behavior heightens with increasing fracture conductivity. This effect is particularly noticeable for $C_f = 2500$ md-ft given that RNP'_{AB} becomes negative for $\delta_{wAB}^* > 0.8$ (Figure 3.54).

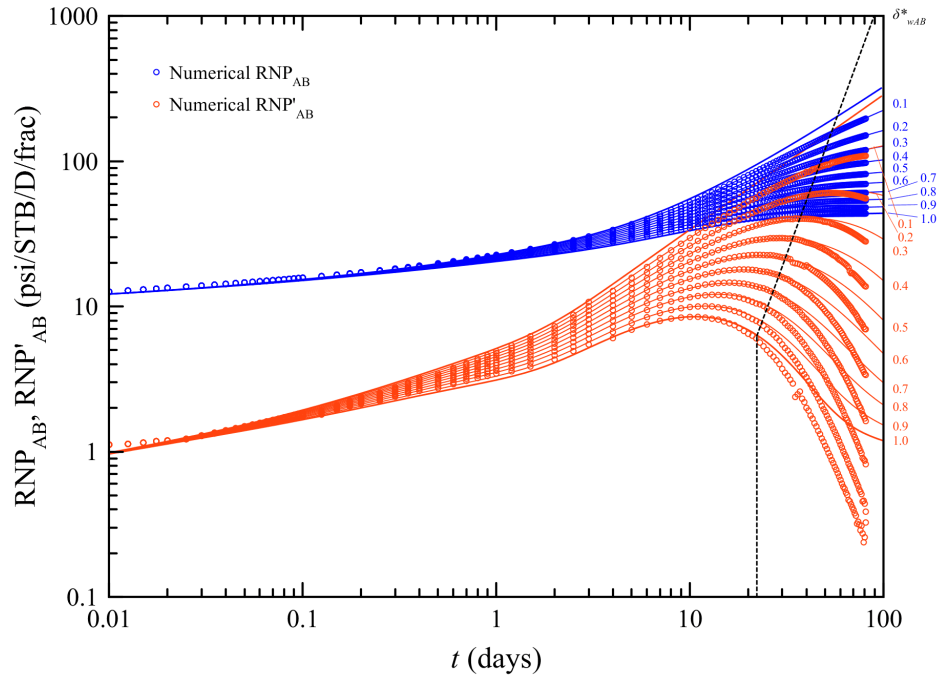


Figure 3.51: Frac-hits type-curves for $C_{fA} = C_{fB} = 50$ md-ft.

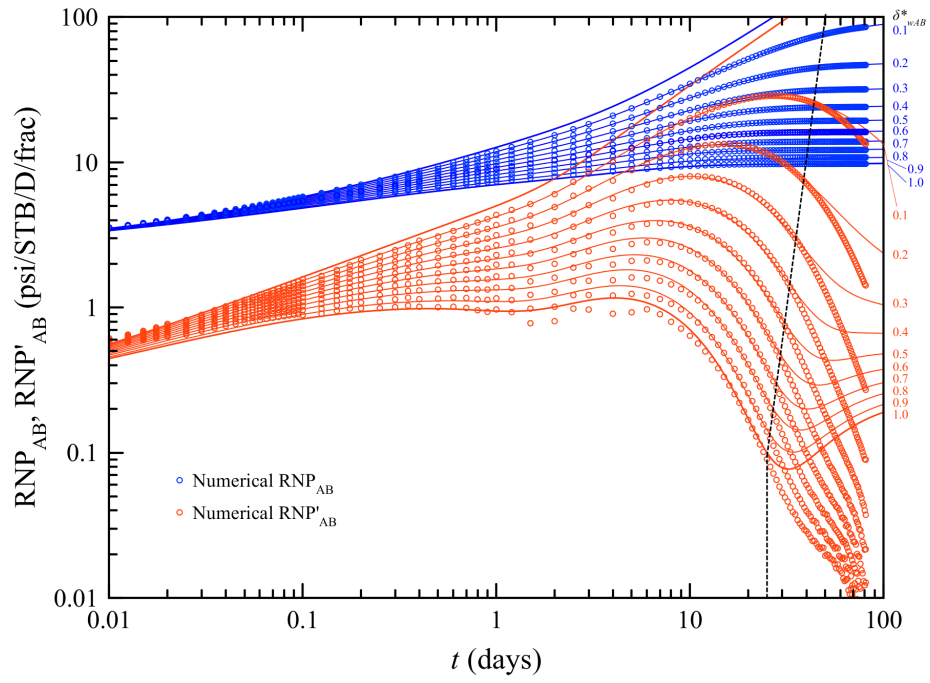


Figure 3.52: Frac-hits type-curves for $C_{fA} = C_{fB} = 250$ md-ft.

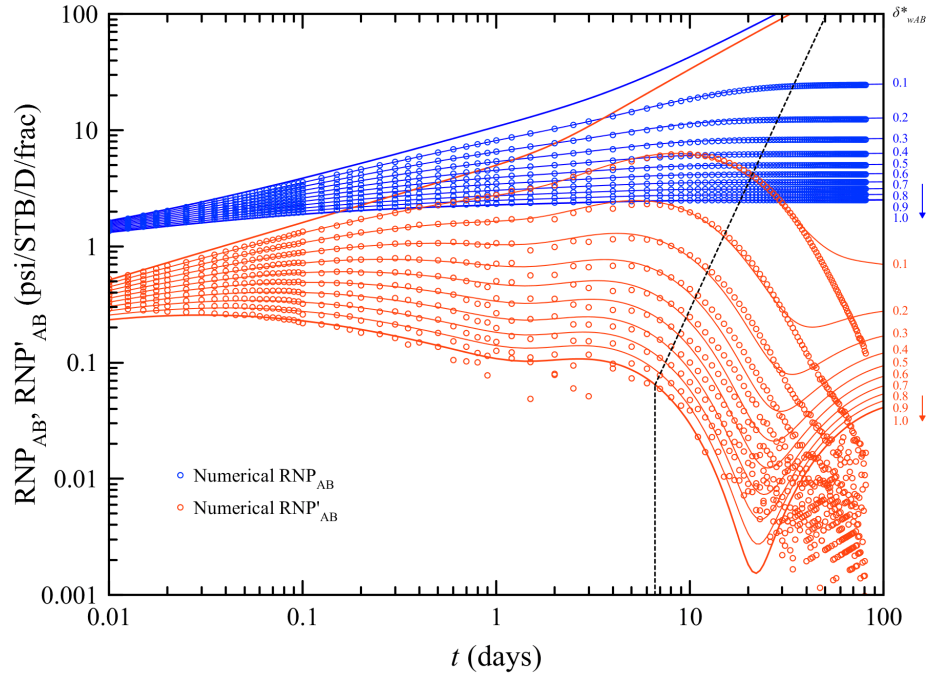


Figure 3.53: Frac-hits type-curves for $C_{fA} = C_{fB} = 1000$ md-ft.

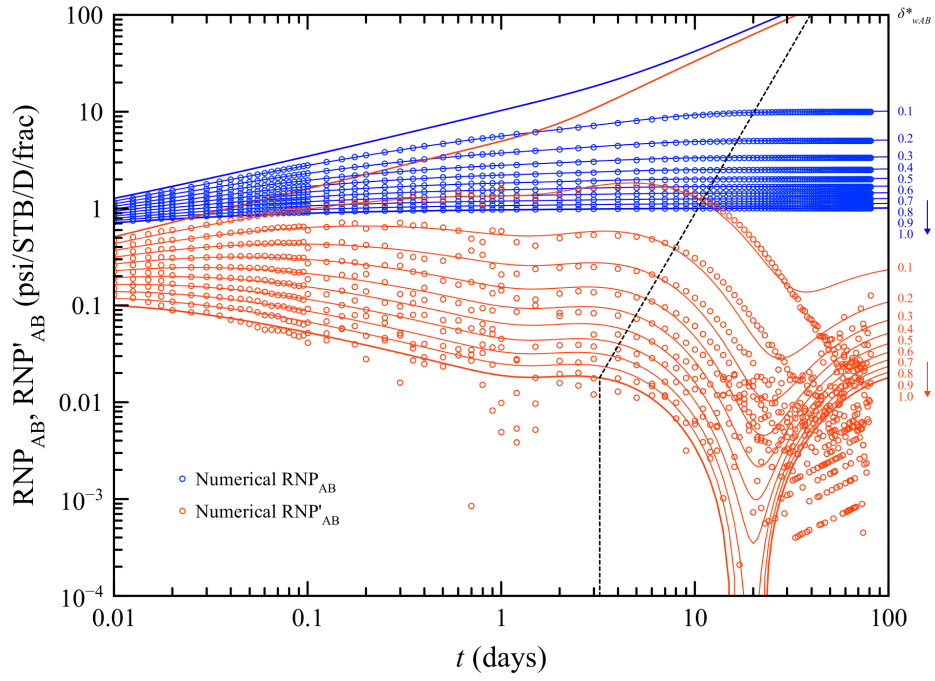


Figure 3.54: Frac-hits type-curves for $C_{fA} = C_{fB} = 2500$ md-ft.

3.10.3.2 Different Fracture Conductivity

This case study considers equal fracture design for all wells in the pad; however, proppant type and concentration may be different between wells. Here, fracture conductivity of wells A and C is equal while that of well B is subject to variations. Hence, $C_{fA} = 500$ md-ft and $50 \leq C_{fB} \leq 2500$ md-ft. SRV permeability ($k_1 = 0.1$ md) and fracture half-length ($x_f = 200$ ft) are assumed equal in all MFHWs. We may consider this case a sensitivity testing of F_{CD} for which $(F_{CD})_A = 25$ and $2.5 \leq (F_{CD})_B \leq 125$.

Table 3.6 summarizes the values of δ_{wAB}^* , δ_{wAB} and δ_{wAC} . The analytical estimation of the fraction of frac hits is fairly accurate for medium-to-high fracture conductivity in well B (i.e. $C_{fB} > 250$ md-ft). Note that values of δ_{wAB} for $C_{fB} = 25$ md-ft result in a considerable overestimation of δ_{wAB}^* , yielding up to 57% absolute error for the scenario of full frac hits.

Figure 3.55 shows that history-matched values of δ_{wAB} for $C_{fB} = 25$ md-ft deviate from the identity line as soon as $\delta_{wAB}^* > 0.2$. Aside from that scenario, we see that δ_{wAB} is a fairly accurate estimator of δ_{wAB}^* when $C_{fB} \geq 250$ md-ft in the multi-well pad under analysis.

Table 3.6: Correlation between δ_{wAB}^* , δ_{wAB} , δ_{wAC} and C_{fB} for $C_{fA} = 500$ md-ft.

δ_{wAB}^*	δ_{wAB} vs. C_{fB} [md-ft]				
	50	250	500*	1000	2500
0.1	0.105	0.088	0.087	0.087	0.088
0.2	0.225	0.178	0.175	0.174	0.175
0.3	0.32	0.273	0.268	0.267	0.267
0.4	0.45	0.37	0.365	0.362	0.355
0.5	0.59	0.48	0.46	0.45	0.445
0.6	0.74	0.585	0.56	0.545	0.54
0.7	0.91	0.71	0.67	0.64	0.63
0.8	1.1	0.835	0.78	0.75	0.72
0.9	1.33	0.965	0.9	0.85	0.81
1.0	1.57	1.1	1.015	0.96	0.91
δ_{wAC}	6×10^{-4}				

* = baseline scenario.

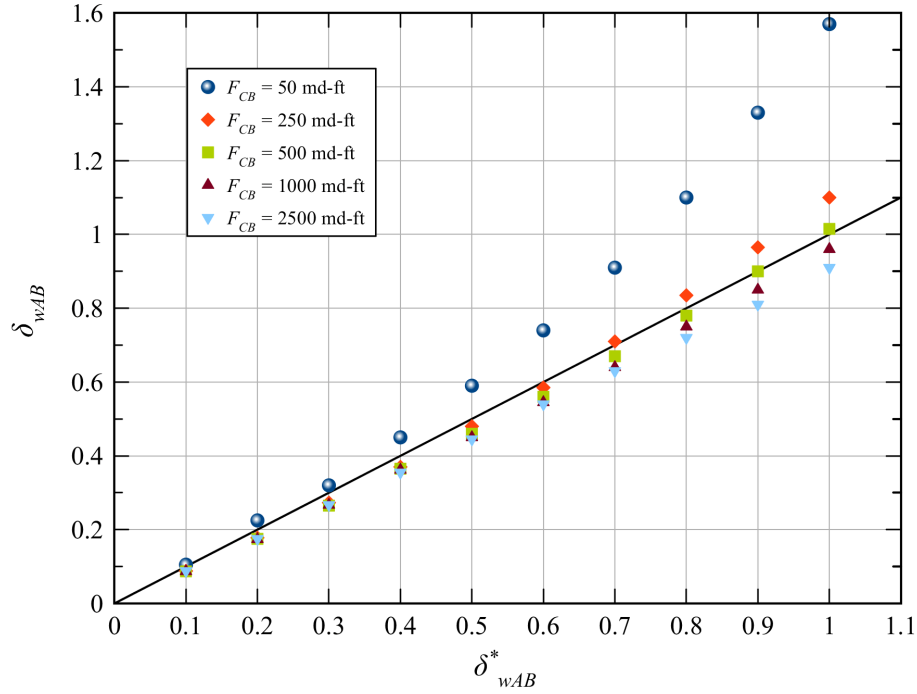


Figure 3.55: Graphical correlation between δ_{wAB}^* , δ_{wAB} and C_{fB} for $C_{fA} = 500$ md-ft.

With respect to individual bottomhole pressure matching, the analytical solution seems in excellent agreement with numerical data. A slight late-time mismatch is observed for all cases, nonetheless negligible. Hence, we conclude that the frac hits model can be used for well performance forecasting when fracture conductivity of wells A and B are different in the scenario under discussion.

Figure 3.56 shows the history-matched values of BHP for $C_{fB} = 50$ md-ft and Figure 3.57 for $C_{fB} = 2500$ md-ft. In both cases $\delta_{wAB}^* = 0.8$. Notice that, in despite difference in fracture conductivity can be highly contrasting (i.e. $C_{fB} = 50$ and 2500 md-ft versus $C_{fA} = 250$ md-ft), the analytical model is able capture transient BHP behavior for all wells accurately.

Alike the scenario in which fracture conductivity is equal for all MFHWs, BHP of wells A and B seem closer to each other when $C_{fB} = 1000$ md-ft. The reason is that, although $C_{fA} < C_{fB}$, fracture conductivity of interfering wells is sufficiently high to enable sufficient pressure communication thus allowing pressure to equilibrate faster across wells A and B.

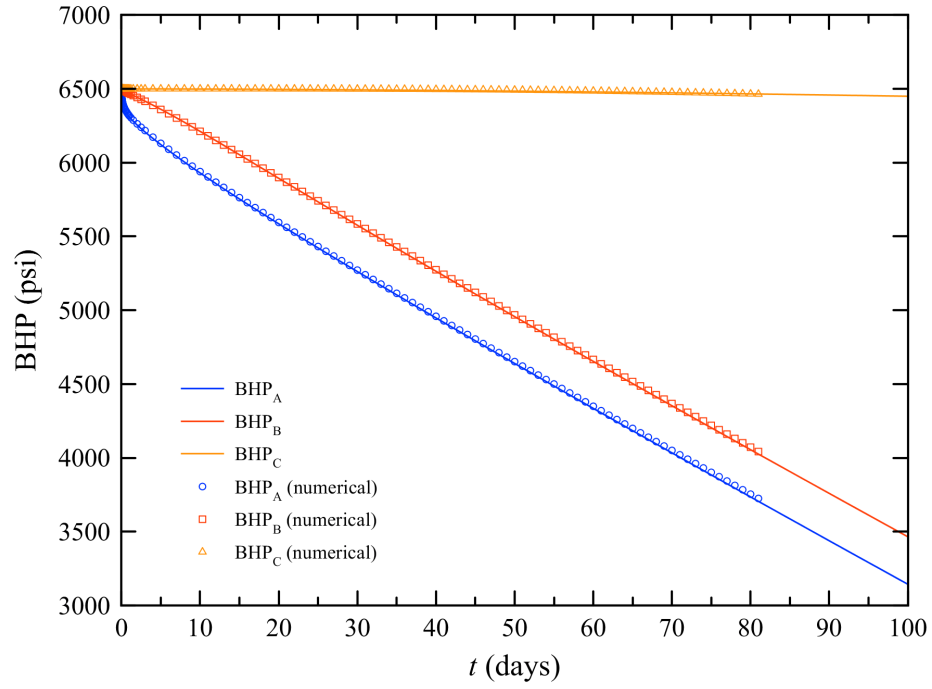


Figure 3.56: History-matching of BHP for $C_{fB} = 50$ md-ft and $\delta_{wAB}^* = 0.8$.

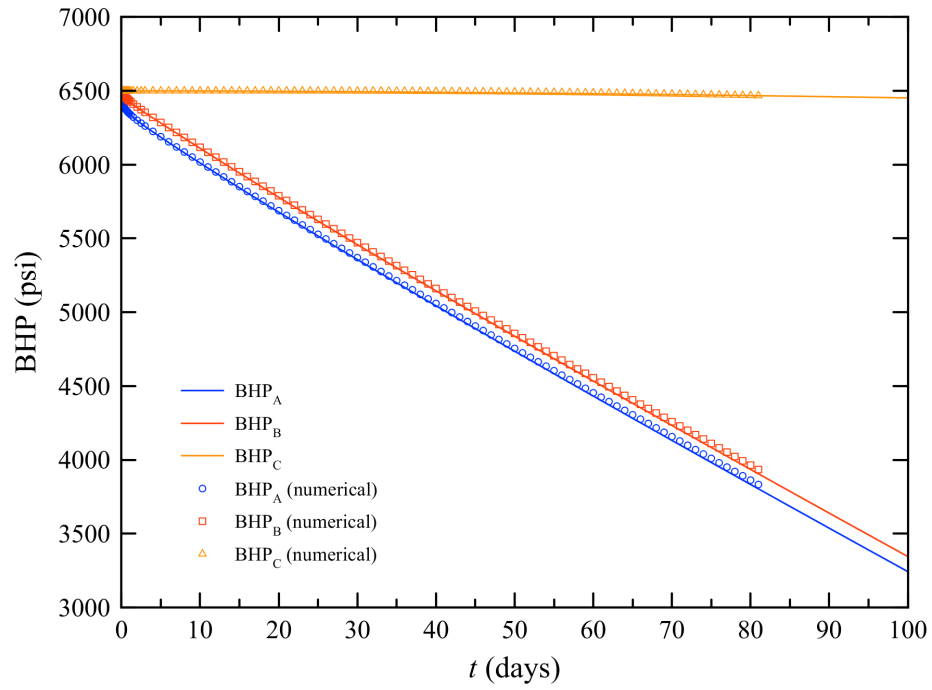


Figure 3.57: History-matching of BHP for $C_{fB} = 1000$ md-ft and $\delta_{wAB}^* = 0.8$.

History-matched type-curves for this case study are shown in Figure 3.58 to Figure 3.61. Analytical and numerical RNP_{AB} and RNP'_{AB} data are in good agreement. Analytical RNP_{AB} matches numerical data for all values C_{fB} and δ_{wAB}^* . Note that RNP_{AB} do not vary largely for $C_{fB} \geq 250$ md-ft. Yet, RNP'_{AB} can only be history-matched up to the time window for frac hits characterization, shown in dashed lines on each plot.

Based on Figure 3.58, we conclude that the range of RNP_{AB} is quite small for $t < 0.1$ days; however, it expands after 12 hours, enabling the use of early-time RNP_{AB} data for frac hits characterization. Furthermore, RNP'_{AB} data can be used for frac hits characterization as early as 0.1 days (~ 2.5 hours). Realize that the minimum time required for frac hits characterization is 9 days for RNP_{AB} and 3 days for RNP'_{AB} when $C_{fA} = C_{fB} = 25$ md-ft (see Figure 3.51).

In general, detection and assessment of frac hits can be accomplished within 12 hours of pressure-transient test via RNP'_{AB} , regardless of the difference in fracture conductivity. Therefore, we can design and implement short interference tests for frac hits detection and characterization for the scenario under study.

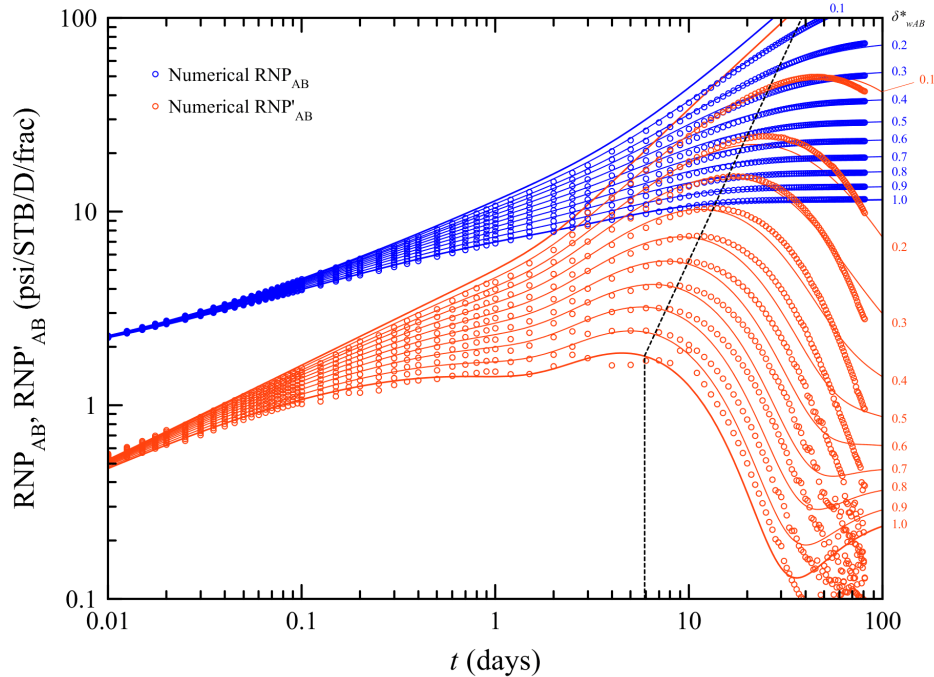


Figure 3.58: Frac-hits type-curves for $C_{fB} = 50$ md-ft.

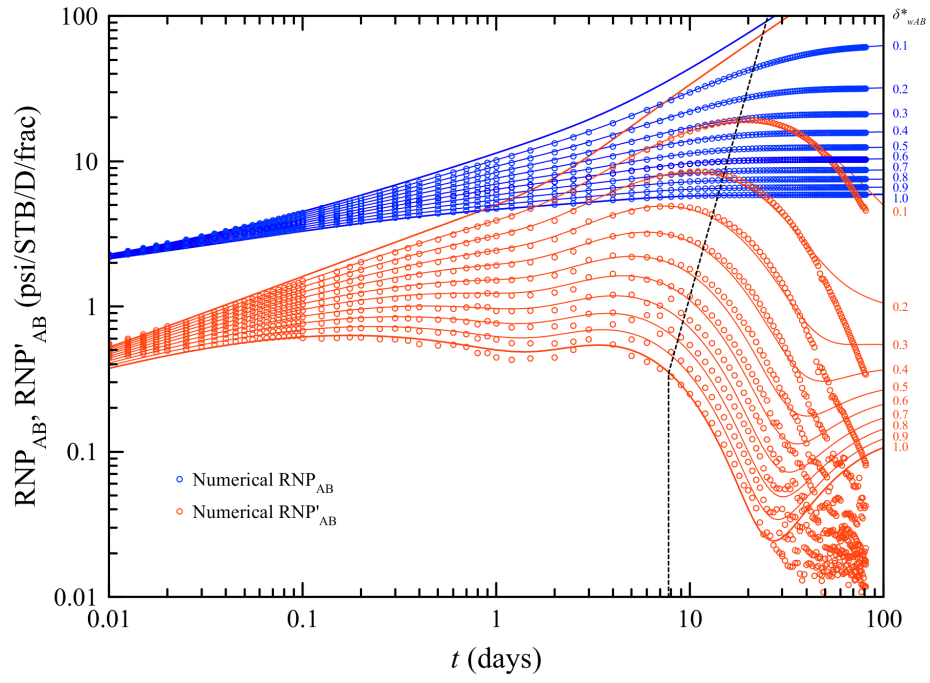


Figure 3.59: Frac-hits type-curves for $C_{fB} = 250$ md-ft.

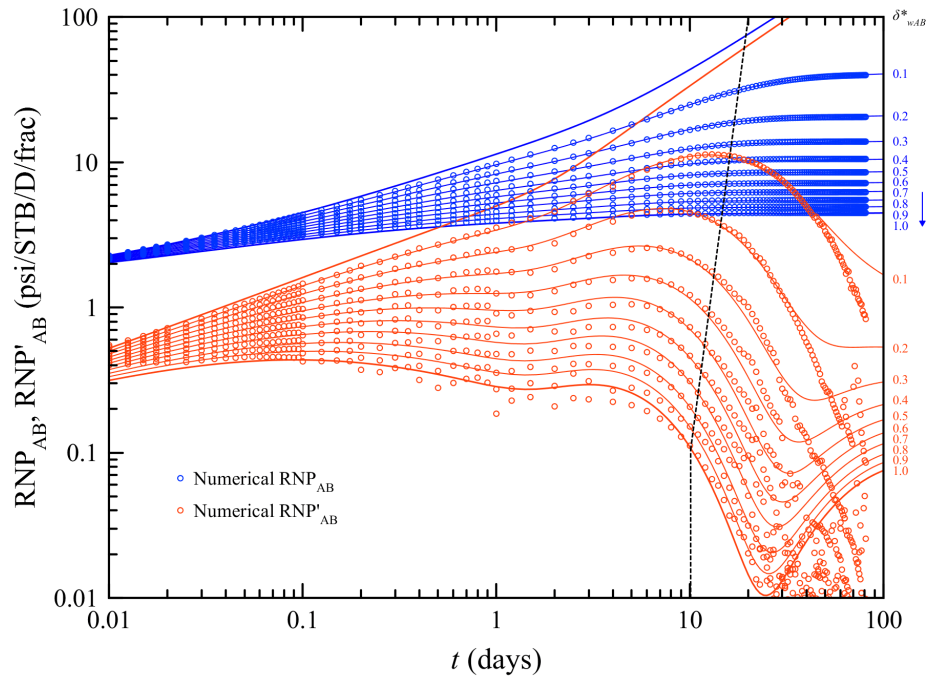


Figure 3.60: Frac-hits type-curves for $C_{fB} = 1000$ md-ft.

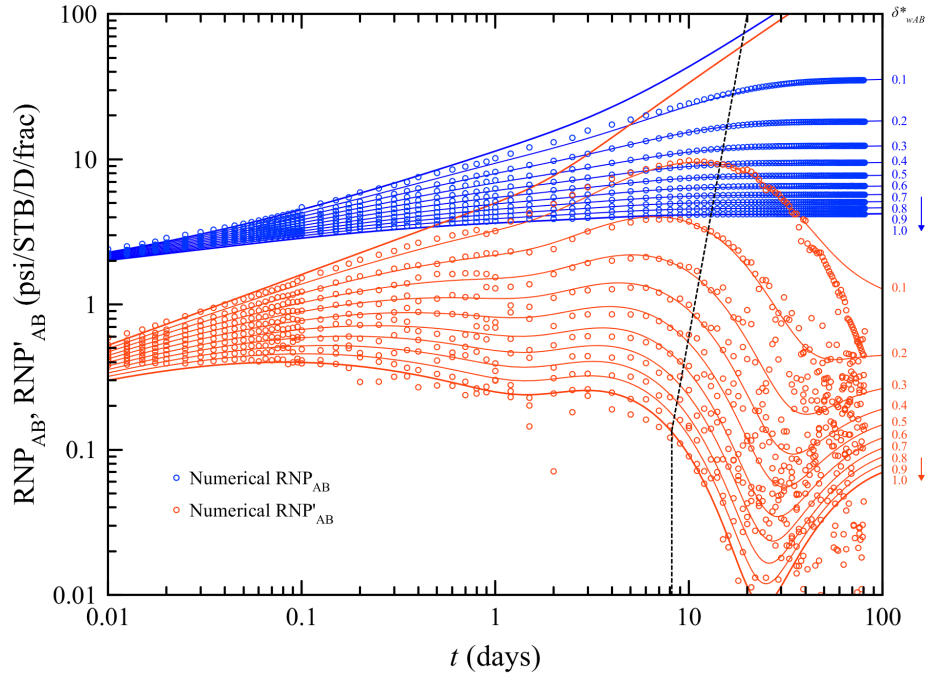


Figure 3.61: Frac-hits type-curves for $C_{fB} = 2500$ md-ft.

3.10.4 Impact of SRV Permeability

3.10.4.1 Equal SRV Permeability for all MFHWs

This case study relates to the quality of the stimulation job in the reservoir rock near the well, assuming that the same job is executed on each stage of the multi-well pad. In this case study, $k_{1A} = k_{1B} = k_1$ with $0.001 \leq k_1 \leq 1$ md. Fracture conductivity and half-length are both assumed equal in all MFHWs. The present sensitivity analysis can be deemed as a sensitivity test of F_{CD} for which $2500 \geq F_{CD} \geq 2.5$.

Table 3.7 summarizes the correlation between δ^*_{wAB} , δ_{wAB} and δ_{wAC} . In general, the analytical estimation of fraction of frac hits is in close agreement with the actual values. The least accurate estimation of δ^*_{wAB} is obtained for the case $k_1 = 1$ md, which yields a maximum absolute error of +16% (overestimation). Also, $\delta_{wAC} \neq 0$ indicates pressure interference between wells A and C taking place through the matrix.

Figure 3.62 shows the history-matching results for this case. A good correlation between estimated and actual fraction of frac hits is observed. Though the scenario $k_1 = 1$ md appears to be the least accurate, it still gives a fair estimation of δ^*_{wAB} .

Table 3.7: Correlation between δ_{wAB}^* , δ_{wAB} and δ_{wAC} for $k_{1A} = k_{1B}$.

δ_{wAB}^*	δ_{wAB} vs. k_1 [md]			
	0.001	0.01	0.1*	1
0.1	0.082	0.084	0.087	0.102
0.2	0.168	0.172	0.175	0.203
0.3	0.257	0.262	0.268	0.31
0.4	0.35	0.358	0.365	0.415
0.5	0.45	0.455	0.46	0.53
0.6	0.54	0.55	0.56	0.65
0.7	0.64	0.655	0.67	0.77
0.8	0.75	0.765	0.78	0.89
0.9	0.86	0.88	0.9	1.02
1.0	0.97	1	1.015	1.16
δ_{wAC}	2×10^{-5}	2×10^{-4}	6×10^{-4}	8×10^{-4}

* = baseline scenario.

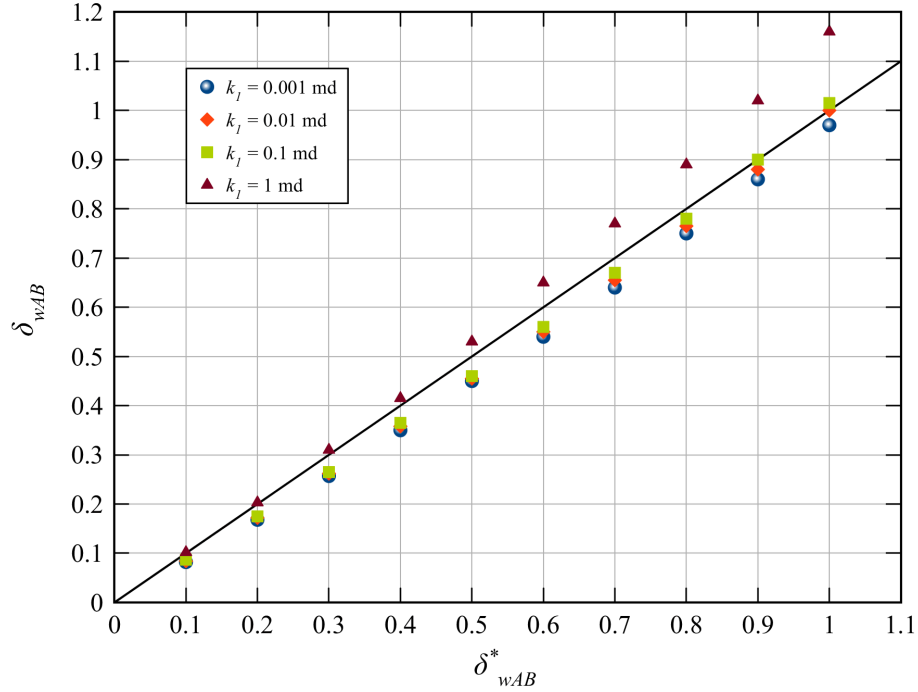


Figure 3.62: Graphical correlation between δ_{wAB}^* and δ_{wAB} for $k_{1A} = k_{1B}$.

In general, we found that analytical and numerical data are in good agreement when SRV permeability is orders-of-magnitude higher than matrix permeability. For instance, consider the BHP results shown in Figure 3.63 for $k_1 = 0.001$ md and $\delta_{wAB}^* = 0.7$. Realize that, in this case, $k_1 = 1 \mu\text{d}$ and $k_m = 0.73 \mu\text{d}$. This means that both permeabilities are comparable in magnitude. As such, we should expect 2-D flow to prevail over linear flow thus leading to an erroneous prediction of BHP for this case.

However, $(\Delta p_{wAB})_{\text{analytical}} \approx (\Delta p_{wAB})_{\text{data}}$, as explained in Section 3.10.1. Henceforth, we expect that $(\text{RNP}_{AB})_{\text{analytical}} \approx (\text{RNP}_{AB})_{\text{data}}$ and $(\text{RNP}'_{AB})_{\text{analytical}} \approx (\text{RNP}'_{AB})_{\text{data}}$, as shown in Figure 3.65. Type-curves will be discussed next.

Conversely, analytical and numerical BHP data seems to be in good agreement for $k_1 = 1$ md and $\delta_{wAB}^* = 0.3$, as depicted on Figure 3.63. In this case, $k_1 \gg k_m$ therefore combined linear fracture/SRV/matrix flow regimes are likely to occur in the well pad. This explains the excellent forecast of BHP response given by the analytical model. Overall, the analytical frac hits model may be used for well performance forecast when SRV permeability is orders-of-magnitude higher than matrix permeability for the multi-well pad configuration in discussion.

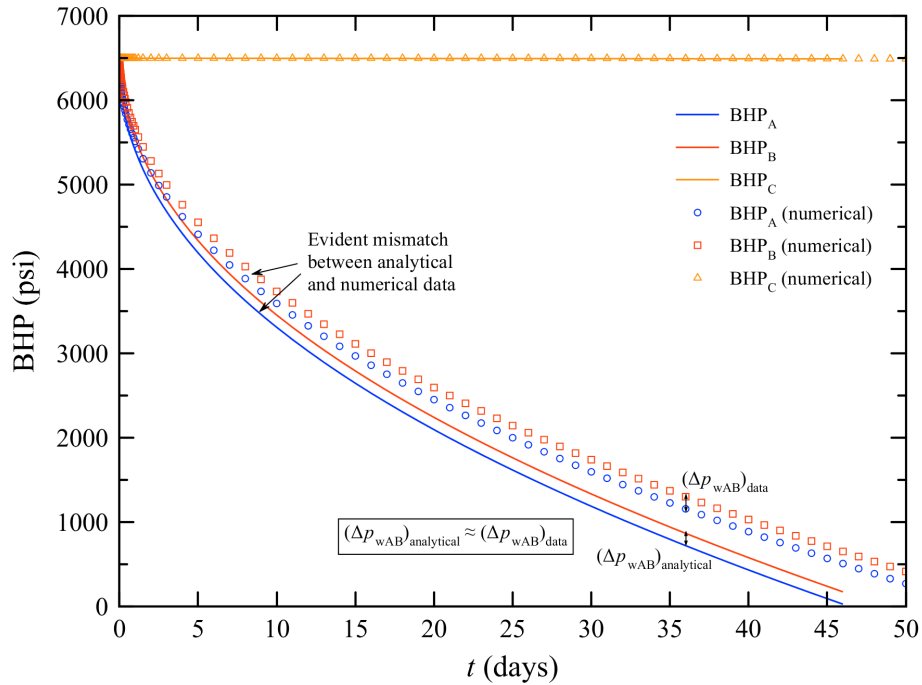


Figure 3.63: History-matching of BHP for $k_1 = 0.001$ md and $\delta_{wAB}^* = 0.7$.

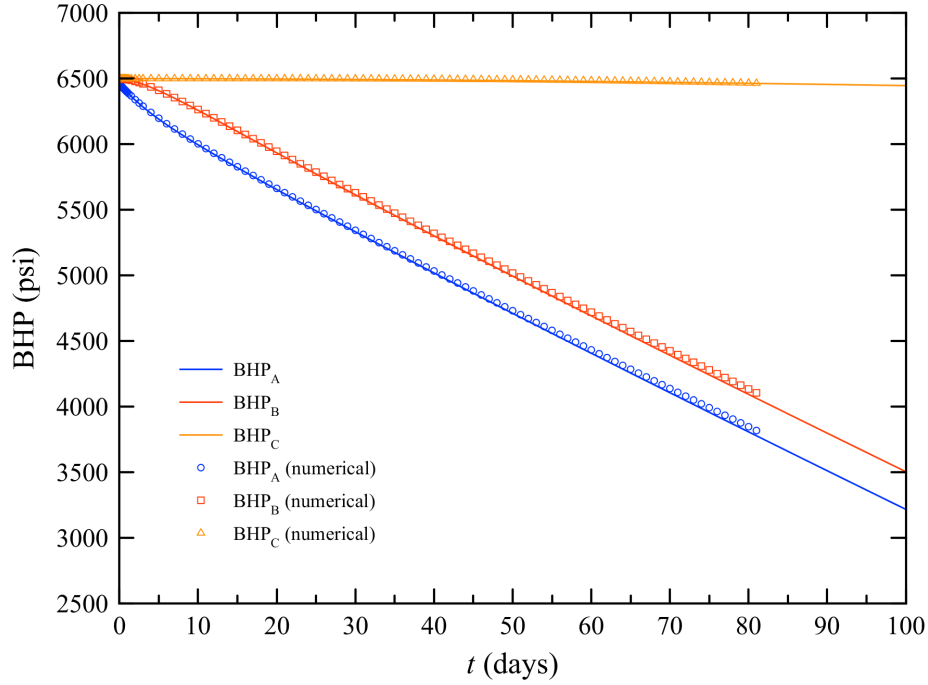


Figure 3.64: History-matching of BHP for $k_1 = 1$ md and $\delta_{wAB}^* = 0.3$.

History-matched frac-hits type-curves are shown in Figure 3.65 through Figure 3.62. The shape and range of both RNP_{AB} and RNP'_{AB} type-curves change considerably with SRV permeability.

For instance, consider the case when $k_1 = 0.001$ md (Figure 3.65). Note that frac hits can be detected and assessed using early-time data that could be as early as ~ 1 hour, because the range of the type-curves is sufficiently wide as to make an unbiased estimation of δ_{wAB}^* . Furthermore, note that RNP'_{AB} behavior is smooth and lacks of sudden changes in direction. Moreover, RNP_{AB} can be history-matched at all times henceforth allowing the use of this parameter for estimation of δ_{wAB}^* when numerical RNP'_{AB} data depart from type-curves.

In summary, the range of both RNP_{AB} and RNP'_{AB} type-curves shrinks with increasing SRV permeability. In addition, lower SRV permeability permits the use of early-time data for detection and assessment of frac hits thus allowing the implementation of short interference tests (~ 2 – 3 -hour well testing) for the well pad under study.

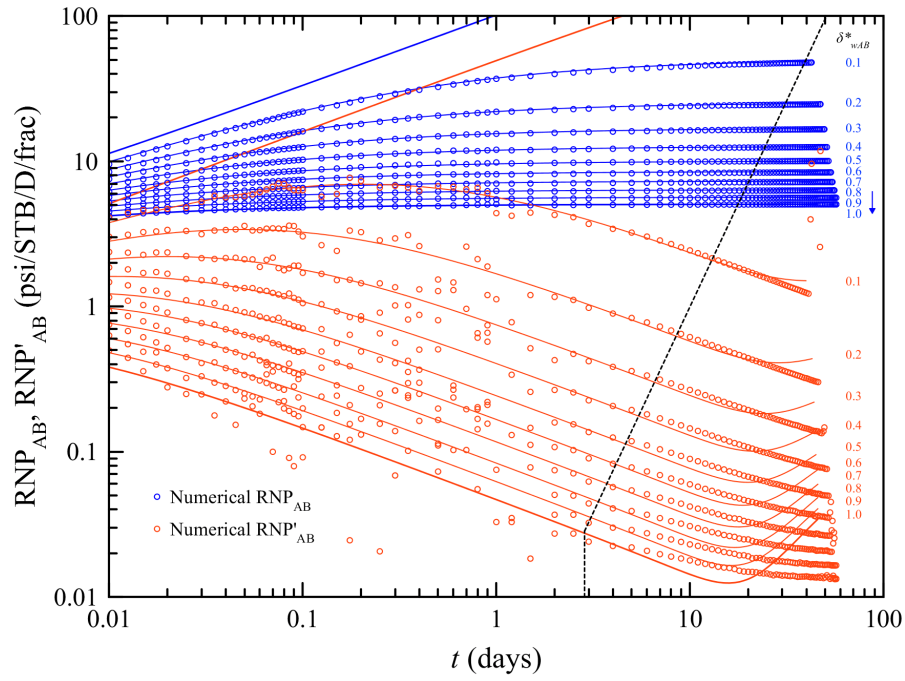


Figure 3.65: Frac-hits type-curves for $k_{1A} = k_{1B} = 0.001$ md.

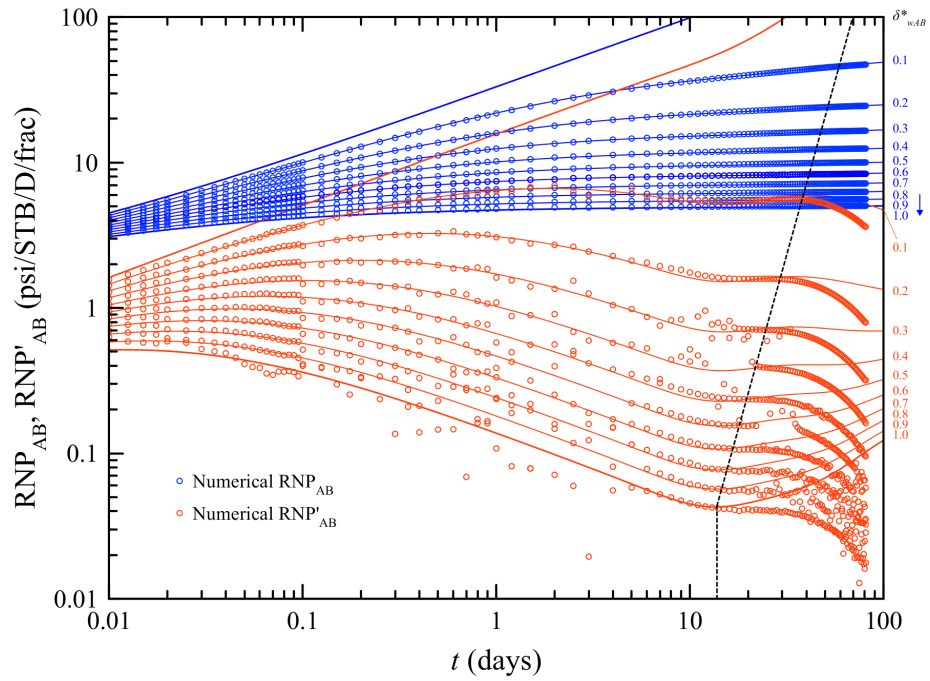


Figure 3.66: Frac-hits type-curves for $k_{1A} = k_{1B} = 0.01$ md.

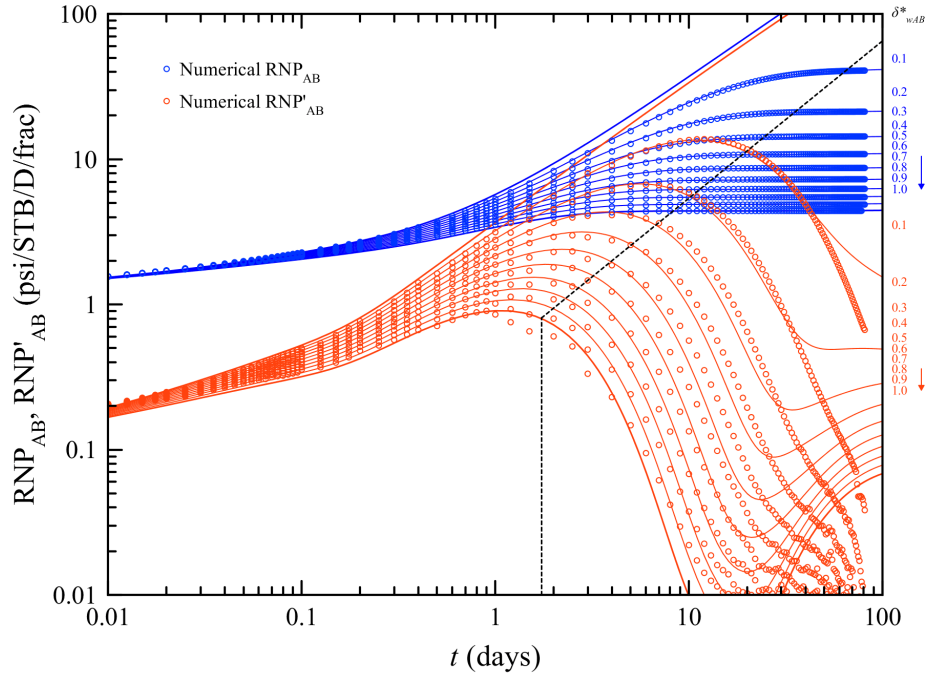


Figure 3.67: Frac-hits type-curves for $k_{1A} = k_{1B} = 1$ md.

3.10.4.2 Different SRV Permeability

This case study examines the scenario of different quality stimulation jobs in wells A and B. To assess the sensitivity of frac hits detection and assessment to k_{1B} , we consider $k_{1A} = 0.1$ md and $0.001 \leq k_{1B} \leq 1$ md. In addition, fracture conductivity ($C_f = 500$ md-ft) and fracture half-length ($x_f = 200$ ft) are assumed equal in all MFHWs. Alike previous sensitivity case studies, this analysis may be regarded as a sensitivity test of $(F_{CD})_B$ in which $(F_{CD})_A = 25$ and $2500 \geq (F_{CD})_B \geq 2.5$.

A summary of history-matched values for δ_{wAB} and δ_{wAC} is shown in Table 3.8. Overall, the analytical estimation of fraction of frac hits is fairly accurate for $k_{1B} \geq 0.01$ md, $k_{1B} \geq 0.001$ md being the least accurate case, yielding a maximum absolute error of -45% (underestimation).

Figure 3.68 shows the graphic correlation between δ_{wAB}^* and δ_{wAB} . It is evident from this plot that δ_{wAB} for $k_{1B} = 0.001$ md delivers a sensibly inaccurate estimation of the actual fraction of frac hits. Apart from this case, the analytical model delivers a close estimation of δ_{wAB}^* when $k_{1B} \geq 0.01$ md.

Table 3.8: Correlation between δ_{wAB}^* , δ_{wAB} , δ_{wAC} and k_{1B} for $k_{1A} = 0.1$ md.

δ_{wAB}^*	δ_{wAB} vs. k_{1B} [md]			
	0.001	0.01	0.1*	1
0.1	0.083	0.085	0.087	0.093
0.2	0.155	0.172	0.175	0.187
0.3	0.21	0.265	0.268	0.283
0.4	0.265	0.36	0.365	0.38
0.5	0.31	0.45	0.46	0.485
0.6	0.36	0.545	0.56	0.59
0.7	0.41	0.645	0.67	0.705
0.8	0.46	0.74	0.78	0.82
0.9	0.51	0.83	0.9	0.94
1.0	0.55	0.92	1.015	1.07
δ_{wAC}	5×10^{-4}	6×10^{-4}	6×10^{-4}	7×10^{-4}

* = baseline scenario.

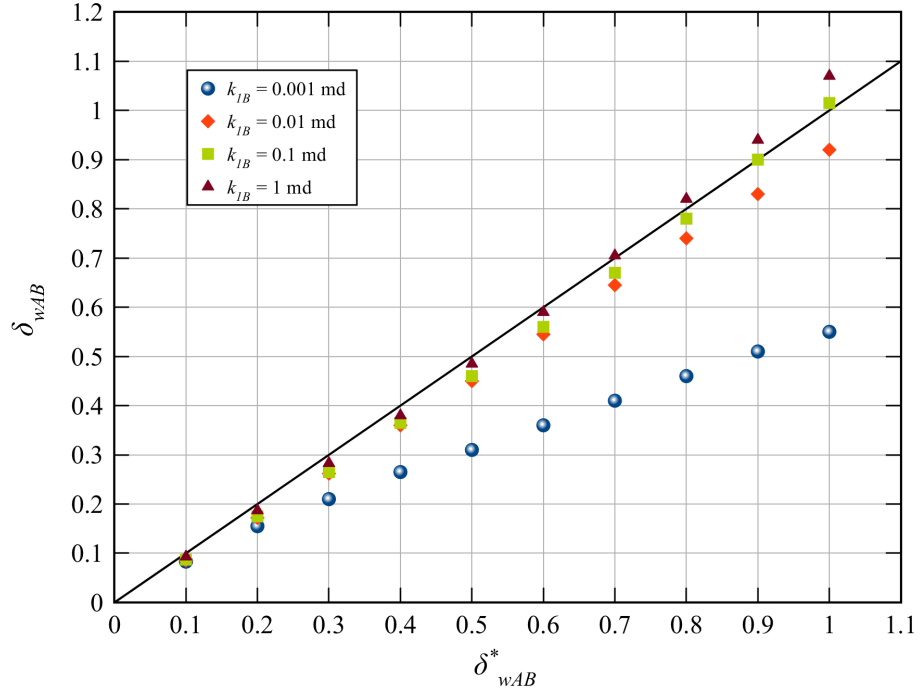


Figure 3.68: Graphical correlation between δ_{wAB}^* , δ_{wAB} and k_{1B} for $k_{1A} = 0.1$ md.

Figure 3.69 shows the resulting analytical BHP estimation resulting from history-matching $\delta_{wAB}^* = 0.7$ for the case $k_{1B} = 0.001$ md. It can be seen from this plot that analytical and numerical BHP data are in good agreement, compared to the case $k_{1A} = k_{1B} = 0.001$ md (Figure 3.63). Though the late-time mismatch may be noticeable, we consider that the analytical model still delivers a fairly accurate estimation of BHP responses for this case study. Moreover, acknowledging that $k_{1B} \approx k_m$, then we may attribute the late-time mismatch, observed for the predicted BHP responses, to the influence of 2-D flow effects on pressure-transient response of well B.

Similarly, Figure 3.70 compares BHP data for the case $k_{1B} = 1$ md and $\delta_{wAB}^* = 0.7$, where analytical and numerical pressure-transient data seem to be in good agreement. The late-time misfit in this case is negligible hence the analytical model may be used for well performance forecasting.

History-matched type-curves for this case study are presented in Figure 3.71 to Figure 3.73. Contrary to previous sensitivity studies in this section, the shape of the analytical RNP_{AB} and RNP'_{AB} type-curves is substantially influenced by k_{1B} . Figure 3.71 suggests that frac hits may be detected and assessed using transient RNP_{AB} data up to 9 days; however, the recommended time window for frac hits characterization is narrow for higher degrees of interference (e.g. $\delta_{wAB}^* > 0.5$). Moreover, recognize that RNP_{AB} type-curves can no longer be history-matched with late-time data. In light of this analysis, we consider that the estimation of the fraction of frac hits should be carried out based on early-to-mid-time RNP_{AB} data for this case study.

Type-curves from Figure 3.72 display a similar transient response to those corresponding to the baseline case (Figure 3.29). Numerical simulation data, however, suggest that frac hits characterization can be achieved by matching late-time RNP_{AB} ; contrariwise, $t > 2.5$ hours before using RNP'_{AB} for characterization purposes. Unlike the previous scenario, type-curves allow assessing the full range of fraction of frac hits ($0 \leq \delta_{wAB}^* \leq 1$) using both RNP_{AB} and RNP'_{AB} . The recommended interference testing time for this case would be up to 3 days.

Lastly, history-matched type-curves for the case $k_{1B} = 1$ md are presented in Figure 3.72. Notice that the skin-like hump in the type-curves vanishes in favor of a steepest descent of RNP'_{AB} as δ_{wAB}^* increases, which may be indicative of a sudden pressure support during the equilibration equilibration process. This phenomenon is clearly seen when the degree of interference is medium to high (e.g. $\delta_{wAB}^* > 0.4$).

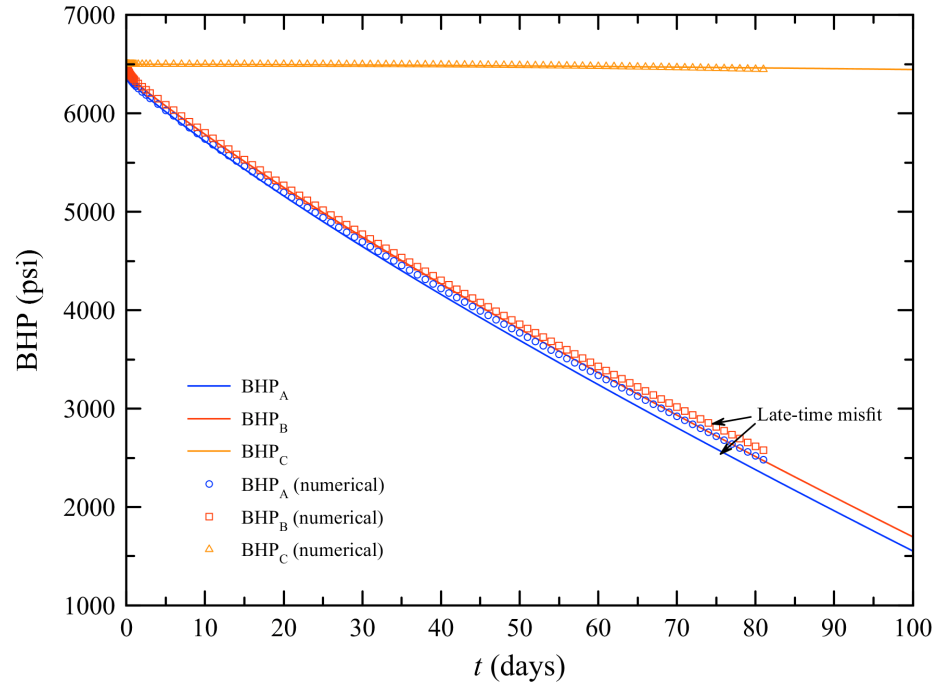


Figure 3.69: History-matching of BHP for $k_{1B} = 0.001$ md and $\delta_{wAB}^* = 0.7$.

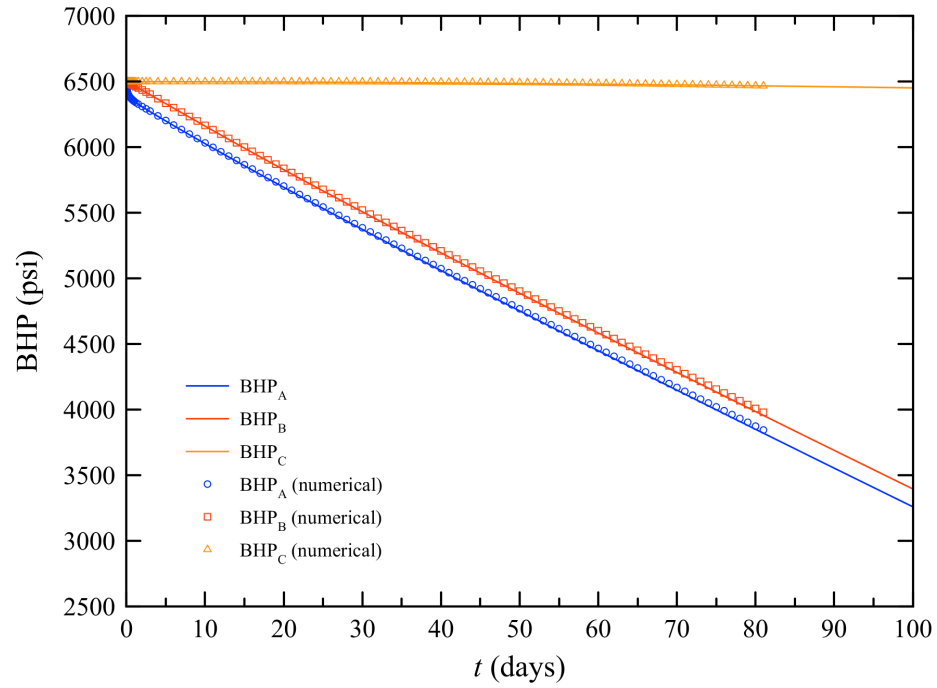


Figure 3.70: History-matching of BHP for $k_{1B} = 1$ md and $\delta_{wAB}^* = 0.7$.

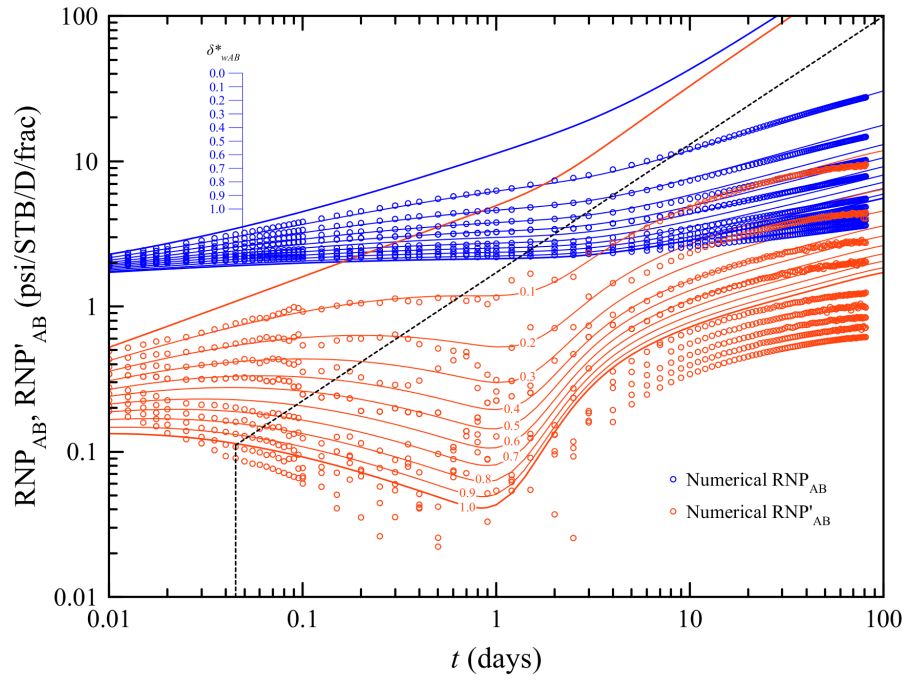


Figure 3.71: Frac-hits type-curves for $k_{1A} = 0.1$ md, $k_{1B} = 0.001$ md.

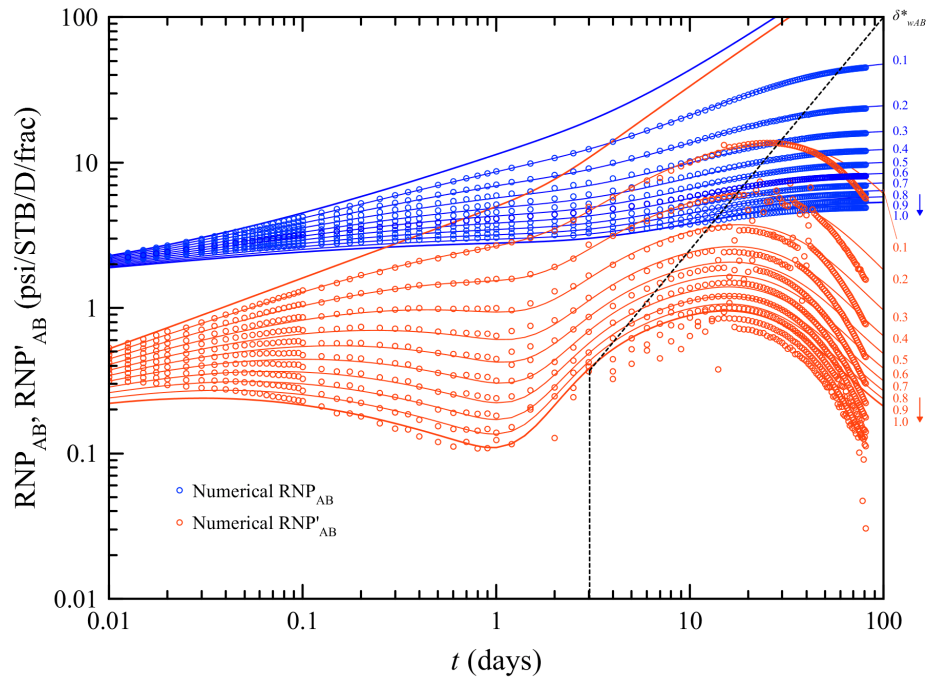


Figure 3.72: Frac-hits type-curves for $k_{1A} = 0.1$ md, $k_{1B} = 0.01$ md.

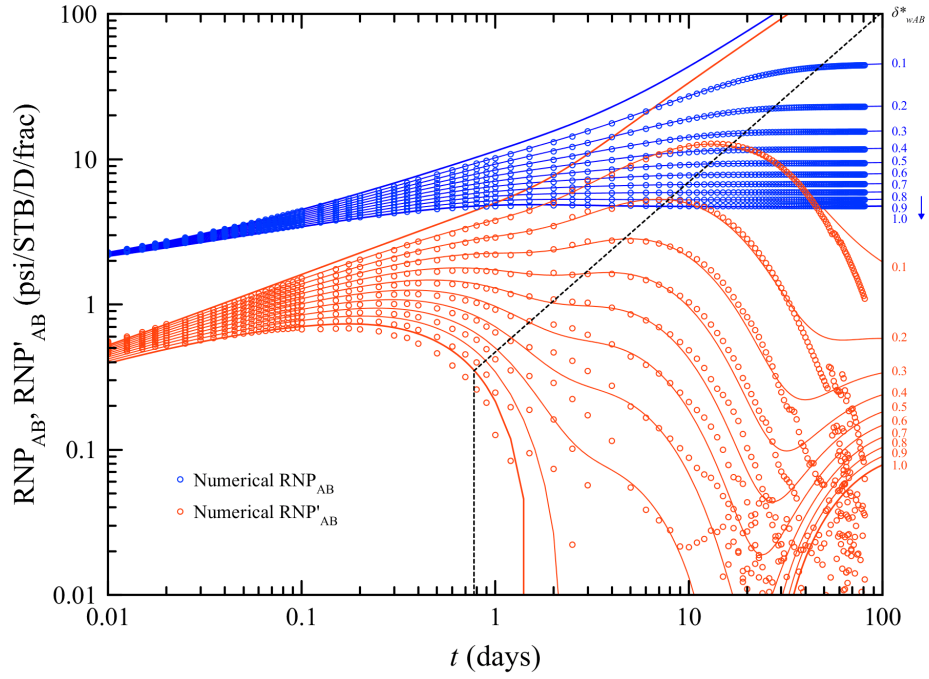


Figure 3.73: Frac-hits type-curves for $k_{1A} = 0.1$ md, $k_{1B} = 1$ md.

3.10.5 Impact of Distance between Fractured Stages

The advent of multi-stage completion technologies, such like ball-activated and coiled-tubing-activated frac sleeves, has made it possible to increase the number of fractured stages per lateral length (e.g. Stegent et al., 2011; Algadi et al., 2014). In light of this, the present case study studies the impact of average distance between fractured stages on the assessment of frac hits.

We assume equal spacing between stages for all wells, thus $2x_{eA} = 2x_{eB} = 2x_e$ (see Figure 3.23) and evaluate $25 \leq 2x_e \leq 500$ ft. Completion design is identical for all stages, with SRV permeability $k_1 = 0.1$ md, fracture conductivity $C_f = 500$ md-ft and fracture half-length $x_f = 200$ ft. Also, we assume one fracture per stage. Flow rate of well A is adjusted per case using $(q_{\text{well}})_A = 200 \times (2x_e/500)$ [STB/D].

Table 3.9 summarizes the history-matched values of δ_{wAB} and δ_{wAC} versus δ_{wAB}^* . The estimated and actual fraction of frac hits are in excellent agreement; the highest absolute error is -4% . The accuracy of the estimation is evident from Figure 3.74, because all estimated values of δ_{wAB} lie close to the identity line.

Table 3.9: Correlation between δ_{wAB}^* , δ_{wAB} and δ_{wAC} for $25 \leq 2x_e \leq 500$ ft.

δ_{wAB}^*	δ_{wAB} vs. $2x_e$ [ft]					
	25	50	75	100	250	500*
0.1	0.094	0.09	0.089	0.089	0.088	0.087
0.2	0.182	0.177	0.175	0.176	0.176	0.175
0.3	0.273	0.268	0.266	0.266	0.267	0.268
0.4	0.365	0.363	0.36	0.36	0.362	0.365
0.5	0.465	0.458	0.456	0.457	0.46	0.46
0.6	0.565	0.558	0.557	0.558	0.56	0.56
0.7	0.67	0.665	0.664	0.666	0.668	0.67
0.8	0.78	0.77	0.77	0.772	0.776	0.78
0.9	0.89	0.886	0.885	0.887	0.895	0.9
1.0	0.995	0.992	0.994	0.996	1.01	1.015
q_A [STB/D]	10	20	30	40	100	200
δ_{wAC}	1×10^{-5}	1×10^{-4}	1×10^{-4}	1×10^{-4}	2×10^{-4}	6×10^{-4}

* = baseline scenario.

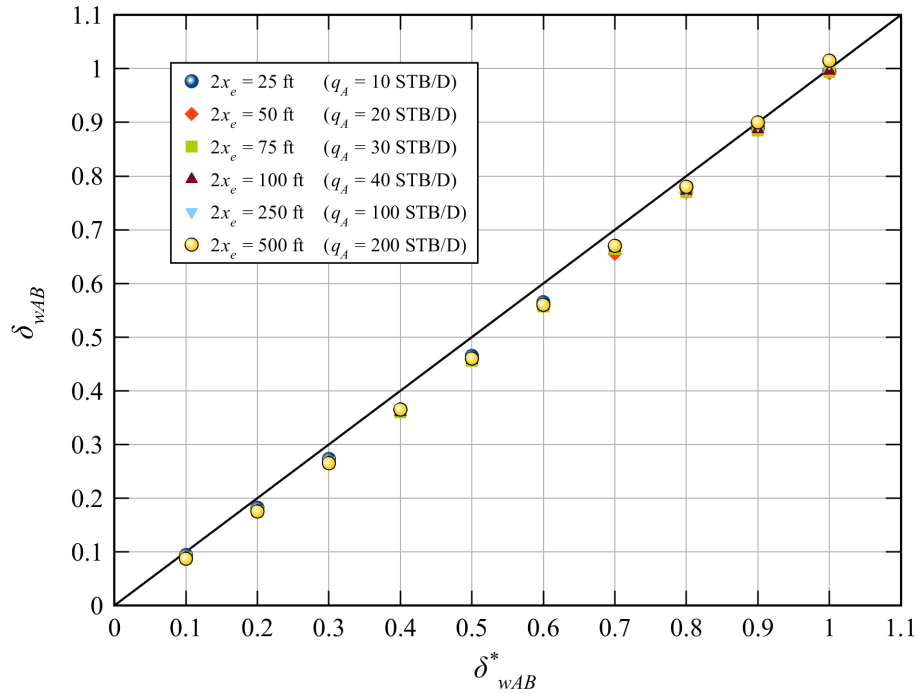


Figure 3.74: Graphical correlation between δ_{wAB}^* and δ_{wAB} as a function of $2x_e$.

We observe from history-matching results that relatively low spacing between stages lead to inaccurate estimation of BHP. In particular, we see that analytical and numerical BHP data are in good agreement when $2x_e \geq 200$ ft.

To illustrate this point, we show analytical and numerical BHP data for the case $2x_e = 25$ ft and $\delta_{wAB}^* = 0.4$ in Figure 3.75. The mismatch between approaches is evident in this plot; however, we were still able to history-match RNP_{AB} and RNP'_{AB} data using type-curves. The reason is that, even so the analytical model is unable to capture the actual fluid-flow behavior when x_e is small, $(\Delta p_{wAB})_{\text{analytical}} \approx (\Delta p_{wAB})_{\text{data}}$, as explained in Section 3.10.1. Therefore, $(\text{RNP}_{AB})_{\text{analytical}} \approx (\text{RNP}_{AB})_{\text{data}}$ hence $(\text{RNP}'_{AB})_{\text{analytical}} \approx (\text{RNP}'_{AB})_{\text{data}}$.

Figure 3.76 illustrates a comparison of BHP given by analytical and numerical data for the case $2x_e = 100$ ft and $\delta_{wAB}^* = 0.4$. Notice that the misfit between approaches is lesser compared to the former case. The mismatch between analytical and numerical BHP vanishes with increasing $2x_e$. We recommend using the analytical for well performance forecasting for wide spacing between fractured stages (e.g. $2x_e \geq 200$).

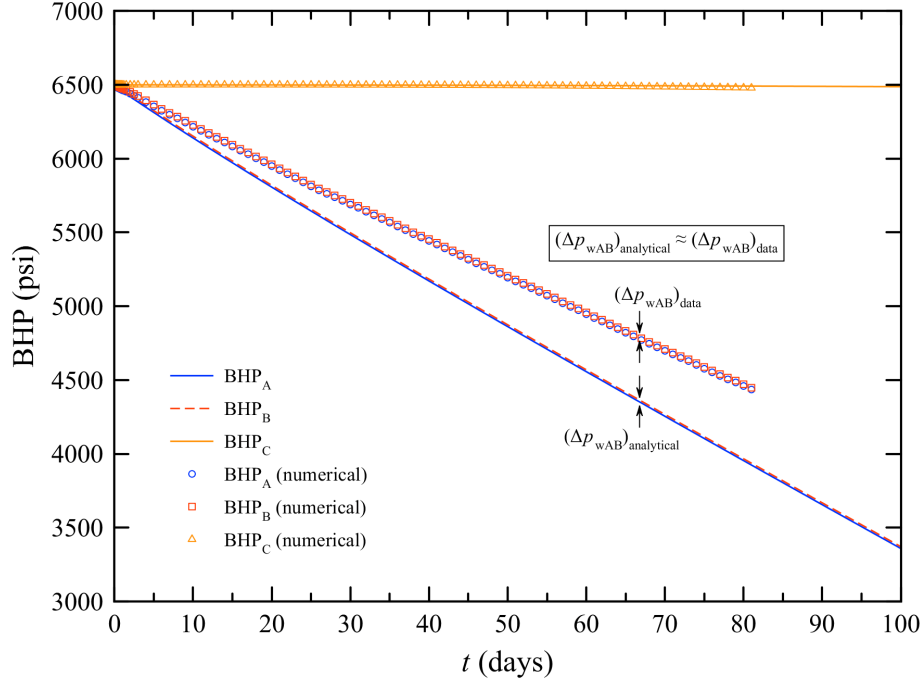


Figure 3.75: History-matching of BHP for $2x_e = 25$ ft and $\delta_{wAB}^* = 0.4$.

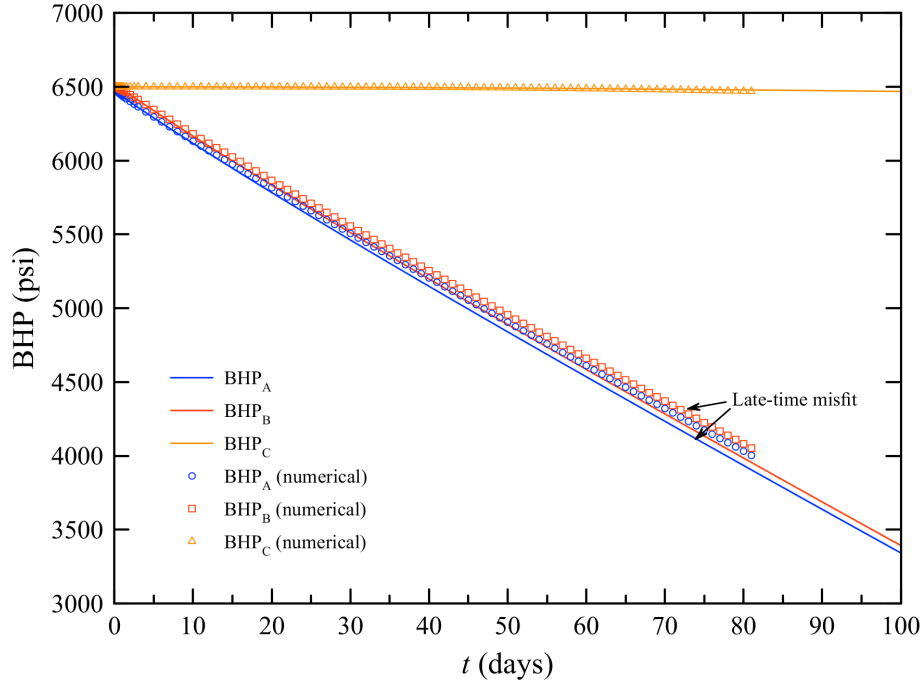


Figure 3.76: History-matching of BHP for $2x_e = 100$ ft and $\delta_{wAB}^* = 0.4$.

History-matched type-curves for this case study are presented in Figure 3.77 through Figure 3.81. As it can be seen in these plots, frac hits can be detected and characterized within ~ 2.5 hours for $2x_e = 25$ ft and ~ 1 day for $2x_e > 50$ ft.

Realize that numerical RNP'_{AB} data become noisy after passing over the skin-like hump in the type-curves. However, RNP_{AB} would still give an unbiased estimation of the fraction of frac hits irrespective of time. In fact, notice that RNP_{AB} seems to attain equilibrium across wells faster with decreasing spacing between fractured stages. Also, note that the downward-upward trend on the RNP'_{AB} type-curves is more severe, and last for longer, when spacing between stages is narrower.

Based on the analysis of results for the present sensitivity study, we conclude that the analytical frac hits model may be used for frac hits detection and assessment regardless of the spacing between fractured stages; however, it may not be used for well performance forecast purposes if stages are tightly spaced.

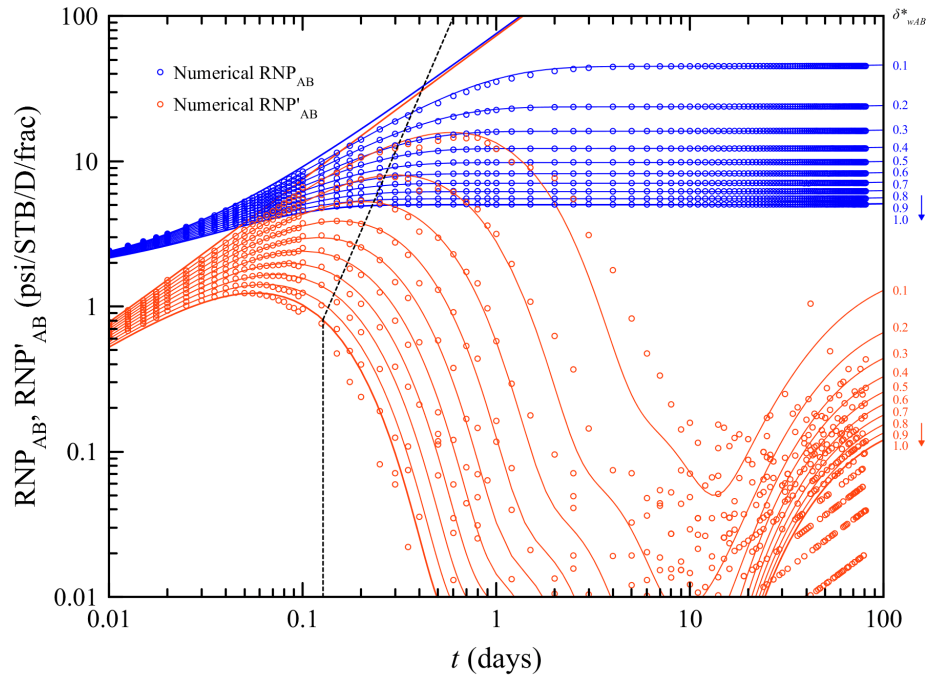


Figure 3.77: Frac-hits type-curves for $2x_{eA} = 2x_{eB} = 25$ ft.

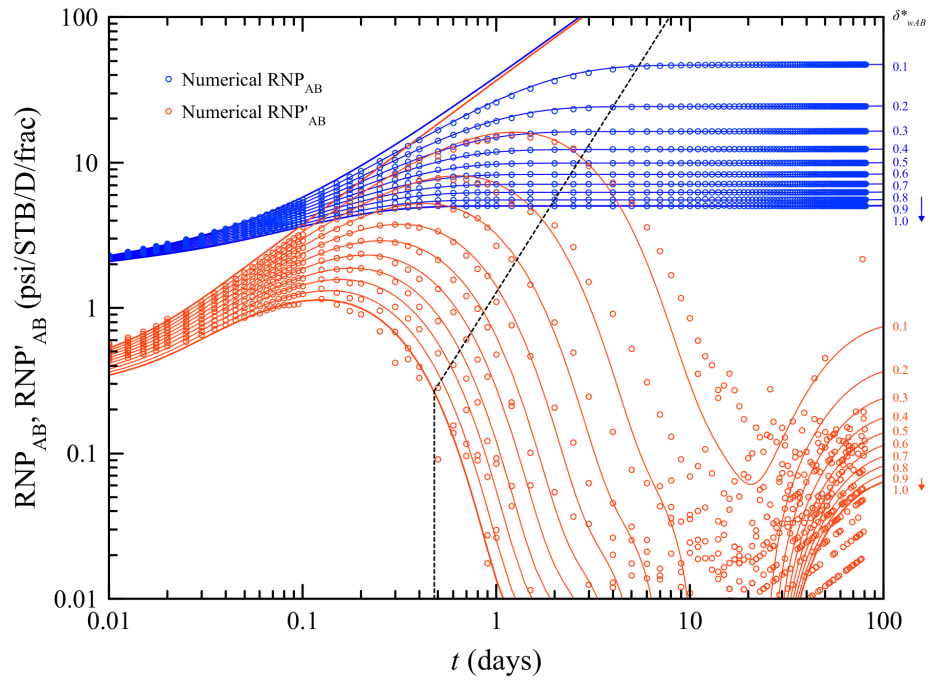


Figure 3.78: Frac-hits type-curves for $2x_{eA} = 2x_{eB} = 50$ ft.

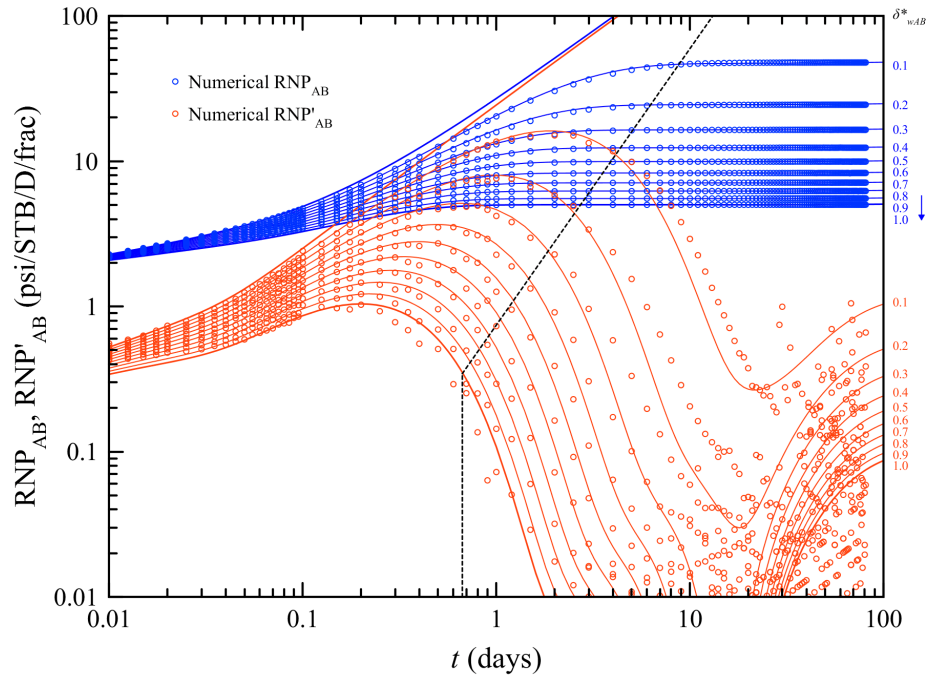


Figure 3.79: Frac-hits type-curves for $2x_{eA} = 2x_{eB} = 75$ ft.

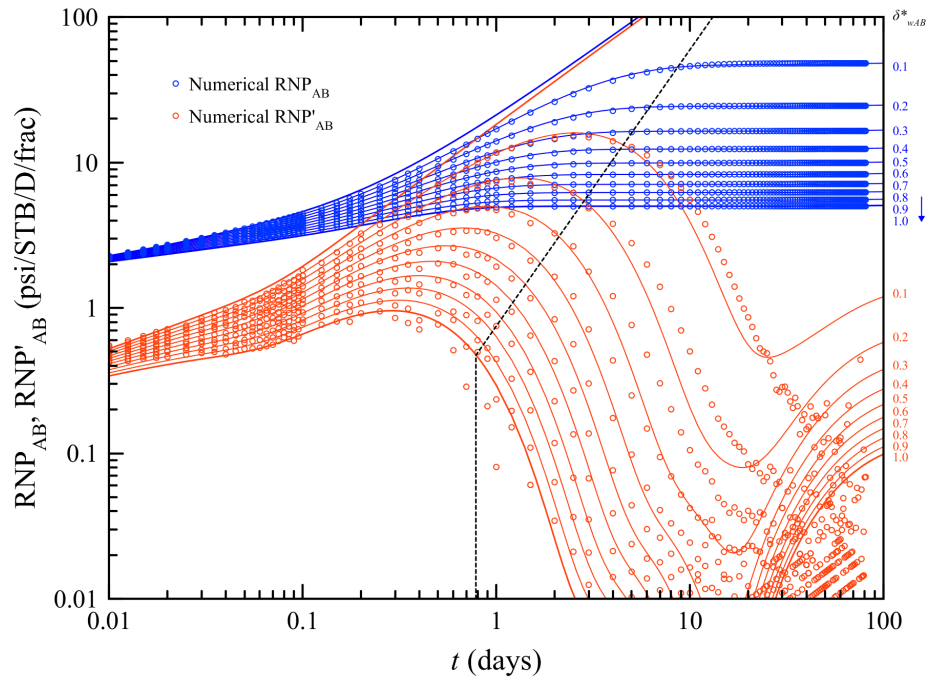


Figure 3.80: Frac-hits type-curves for $2x_{eA} = 2x_{eB} = 100$ ft.

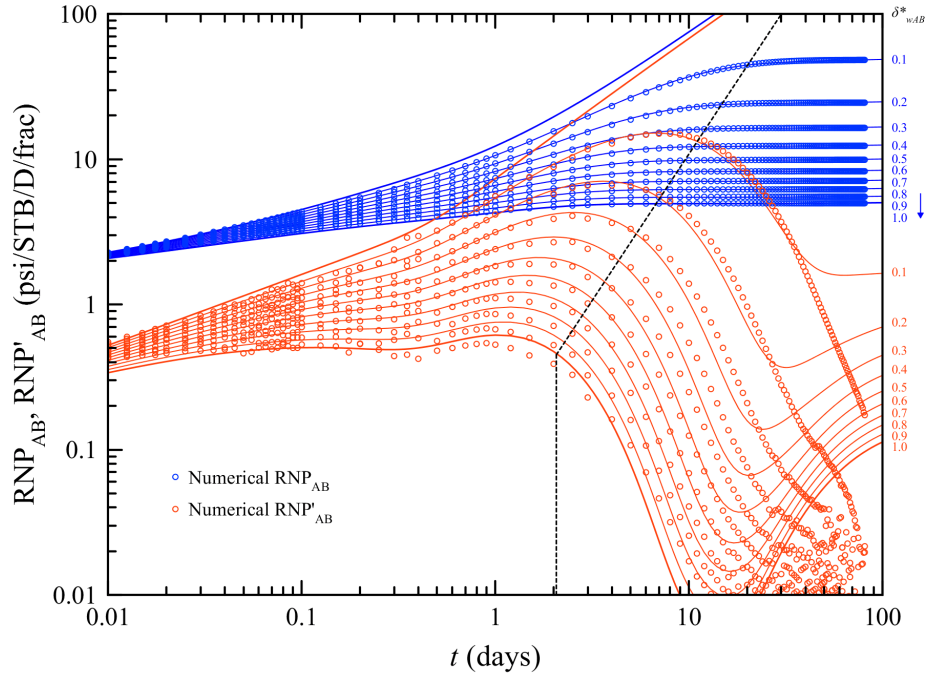


Figure 3.81: Frac-hits type-curves for $2x_{eA} = 2x_{eB} = 250$ ft.

3.11. Type-Curves Analysis

The objective of this section is use the analytical solutions derived in the previous section to generate type-curves that would allow to assess the degree of interference, due to frac hits, between two MFHWs. In this analysis, we will assume that frac hits only exist between wells A and B such that $C_w(s) = 0$. In addition, well A is flowing at constant rate while wells B and C are shut-in, thus $q'_{AD} = 1$ and $q'_{BD} = q'_{CD} = 0$. The matrix region is not considered in this study hence the application of the subsequent type-curves matching method is limited to early to mid-time pressure-transient data. The following assumptions are also made herein:

- Equal SRV permeability: $k_{1A} = k_{1B} \equiv k_1$
- Equal fracture half-length: $x_{fA} = x_{fB} \equiv x_f$
- Equal dimensionless fracture conductivity: $(F_{CD})_A = (F_{CD})_B \equiv F_{CD}$

Because properties of both wells are assumed equal then $c_{2A}(s) = c_{2B}(s) \equiv c(s)$. The dimensionless pressure differential between wells A and B is defined as:

$$\Delta p_{wAD} = \mathcal{L}^{-1} \{ \bar{p}_{wAD} - \bar{p}_{wBD} \} \quad (3.154)$$

Replacing Equation 3.145 and 3.148 into Equation 3.154, while incorporating all of the assumptions initially made, leads to:

$$\Delta p'_{wAD} = \mathcal{L}^{-1} \left\{ \frac{\pi}{F_{CD}} \frac{\coth \sqrt{c(s)}}{s \sqrt{c(s)}} - B_w(s) \frac{\operatorname{csch} \sqrt{c(s)}}{\sqrt{c(s)}} \right\} \quad (3.155)$$

$$B_w(s) = \left(\frac{\pi}{s F_{CD}} \right) \frac{\coth \sqrt{c(s)}}{s_{fAB} \sqrt{c(s)} + \operatorname{csch} \sqrt{c(s)}} \quad (3.156)$$

For convenience, we have made the definition $\Delta p'_{wAD} = \Delta p_{wAD} - s_c$. Combining the two equations above yields:

$$\Delta p_{wAD} = \frac{\pi}{F_{CD}} \mathcal{L}^{-1} \left\{ \frac{\coth \sqrt{c(s)}}{s \left[\sqrt{c(s)} + s_{fAB}^{-1} \operatorname{csch} \sqrt{c(s)} \right]} \right\} \quad (3.157)$$

Now that $\Delta \bar{p}_{wAD}$ is defined for the scenario under study, let us analyze the flux-source function $c(s)$. If matrix is ignored in the model, $c(s)$ becomes:

$$c(s) = \frac{2}{\eta_{fD}} + \frac{2\sqrt{s}}{F_{CD}} \tanh(x_{eD} \sqrt{s}) \quad (3.158)$$

For the present analysis, the dimensionless fracture diffusivity coefficient is defined as $\eta_{fD} = k_f \phi_1 / k_1 \phi_f$. Since fracture permeability is orders-of-magnitude larger than SRV permeability (i.e. $k_f \gg k_1$) then we can safely assume that $s / \eta_{fD} \approx 0$. As a result,

$$\Delta \bar{p}_{wAD} = \frac{\pi}{F_{CD}} \mathcal{L}^{-1} \left\{ \frac{\coth \sqrt{\frac{2}{F_{CD}} \sqrt{s} \tanh(x_{eD} \sqrt{s})}}{s \left[\sqrt{\frac{2}{F_{CD}} \sqrt{s} \tanh(x_{eD} \sqrt{s})} + s_{fAB}^{-1} \operatorname{csch} \sqrt{\frac{2}{F_{CD}} \sqrt{s} \tanh(x_{eD} \sqrt{s})} \right]} \right\} \quad (3.159)$$

Given that frac hits can be characterized using mid-to-late time transient data, we apply

the initial value theorem in Laplace domain to derive the following late-time asymptotic approximations for the hyperbolic functions in Equation 3.159:

$$\lim_{s \rightarrow 0} s \coth \sqrt{\frac{2}{F_{CD}} \sqrt{s} \tanh(x_{eD} \sqrt{s})} \approx s \sqrt{\frac{F_{CD}}{2}} \coth \sqrt{\sqrt{s} \tanh(x_{eD} \sqrt{s})} \quad (3.160)$$

$$\lim_{s \rightarrow 0} s \operatorname{csch} \sqrt{\frac{2}{F_{CD}} \sqrt{s} \tanh(x_{eD} \sqrt{s})} \approx s \sqrt{\frac{F_{CD}}{2}} \operatorname{csch} \sqrt{\sqrt{s} \tanh(x_{eD} \sqrt{s})} \quad (3.161)$$

Therefore, Equation 3.159 becomes

$$\Delta p'_{wAD} = \frac{\pi}{F_{CD}} \mathcal{L}^{-1} \left\{ \frac{\coth \sqrt{\sqrt{s} \tanh(x_{eD} \sqrt{s})}}{s \left[s^{1/4} \sqrt{\tanh(x_{eD} \sqrt{s})} + \frac{F_{CD}}{2s_{fAB}} \operatorname{csch} \sqrt{\sqrt{s} \tanh(x_{eD} \sqrt{s})} \right]} \right\} \quad (3.162)$$

Further application of the initial value theorem in Laplace domain for late-time response of Equation 3.162, yields:

$$\lim_{s \rightarrow 0} s \sqrt{\tanh(x_{eD} \sqrt{s})} \approx \frac{s}{\sqrt{x_{eD}}} \sqrt{\tanh \sqrt{s}} \quad (3.163)$$

$$\lim_{s \rightarrow 0} s \operatorname{csch} \sqrt{s^{1/2} \tanh(x_{eD} \sqrt{s})} \approx s \sqrt{x_{eD}} \operatorname{csch} \sqrt{s^{1/2} \tanh \sqrt{s}} \quad (3.164)$$

$$\lim_{s \rightarrow 0} s \coth \sqrt{s^{1/2} \tanh(x_{eD} \sqrt{s})} \approx s \sqrt{x_{eD}} \coth \sqrt{s^{1/2} \tanh \sqrt{s}} \quad (3.165)$$

Replacing these approximations into Equation 3.162, while simplifying the resulting expression, leads to:

$$\frac{\Delta p'_{wAD}}{x_{eD}} = \frac{\pi}{2} \mathcal{L}^{-1} \left\{ \frac{\coth \sqrt{s^{1/2} \tanh \sqrt{s}}}{s \left[s^{1/4} \sqrt{\tanh \sqrt{s}} + \frac{F_{CD} x_{eD}}{2s_{fAB}} \operatorname{csch} \sqrt{s^{1/2} \tanh \sqrt{s}} \right]} \right\} \quad (3.166)$$

For the case of identical MFHWs, the definition of s_{fAB} (Equation 3.118) reduces to:

$$s_{fAB} = \frac{L_{AB}}{x_f \delta_{wAB}} \quad (3.167)$$

where L_{AB} and δ_{wAB} are the distance and fraction of frac hits between MFHWs, respectively. Furthermore, let us use Equation 3.167 to define the lumped frac-hits skin factor S_F as:

$$S_F = \frac{2L_{AB}}{F_{CD} x_{eD} x_f \delta_{wAB}} \quad (3.168)$$

Finally, we arrive at the dimensionless pressure differential between wells A and B and its logarithmic derivative:

$$\frac{\Delta p_{wAD}}{x_{eD}} = \frac{\pi}{2} \mathcal{L}^{-1} \left\{ \frac{\coth \sqrt{\sqrt{s} \tanh \sqrt{s}}}{s \left[s^{1/4} \sqrt{\tanh \sqrt{s}} + \frac{1}{s_F} \operatorname{csch} \sqrt{\sqrt{s} \tanh \sqrt{s}} \right]} \right\} + \frac{s_c}{x_{eD}} \quad (3.169)$$

$$\frac{d}{d \ln t_D} \left(\frac{\Delta p_{wAD}}{x_{eD}} \right) = \frac{\pi t_D}{2} \mathcal{L}^{-1} \left\{ \frac{\coth \sqrt{\sqrt{s} \tanh \sqrt{s}}}{s^{1/4} \sqrt{\tanh \sqrt{s}} + \frac{1}{s_F} \operatorname{csch} \sqrt{\sqrt{s} \tanh \sqrt{s}}} \right\} \quad (3.170)$$

At very early times, pressure-transient response in well A is dominated by the choking skin and fracture properties. Additionally, the choking skin does not affect transient response of the log-derivative. Therefore, we can drop the second term in the denominator of Equation 3.169 to plot type-curves at early times using

$$\frac{\Delta p_{wAD}}{x_{eD}} = \frac{\pi}{2} \mathcal{L}^{-1} \left\{ \frac{\coth \sqrt{\sqrt{s} \tanh \sqrt{s}}}{s^{5/4} \sqrt{\tanh \sqrt{s}}} \right\} + \frac{s_c}{x_{eD}} \quad (3.171)$$

Using Equation 3.169, 3.170 and 3.171, we generate the following type-curves chart:

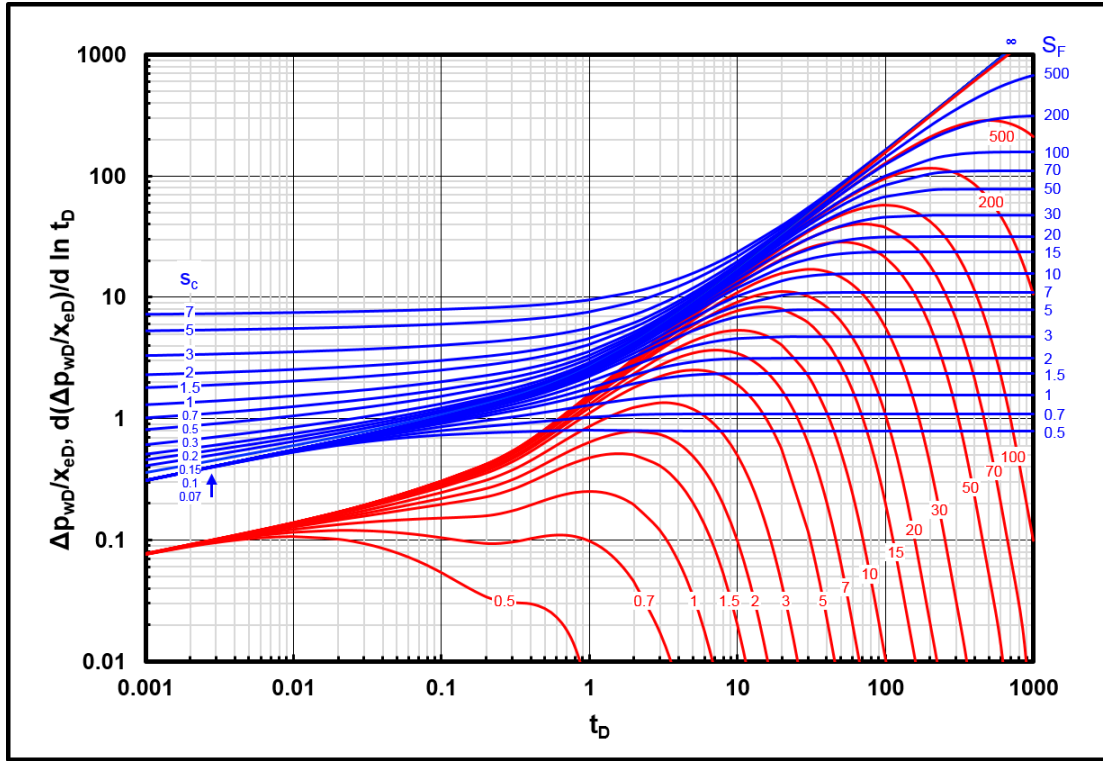


Figure 3.82: Dimensionless frac-hits type-curves as a function of the lumped frac-hits skin factor S_F .

3.11.1 Interference Diagnostics Workflow

The workflow of the interference diagnostics test described next is intended to be a post-treatment assessment of well interference caused by frac hits between the infill well and an offset well.

► Prior to starting the interference test:

1. Select the infill/offset pair to be analyzed.
2. Shut-in and repressurize offset well.
3. Install downhole pressure gauges in the target wells.

► During the well test:

4. Start flowing the infill well.
5. Record pressure from both wells.

6. Hold production at constant rate once only oil is flowing from the MFHW. High rates will shorten the required duration of the test; however, minimum BHP at the end of the test should be above the bubble-point pressure.

► After the well test:

8. Perform production data quality control check.
9. Estimate RNP_{AB} from well-test data (Equation 3.3). Filter noisy data, if necessary.
10. Estimate RNP'_{AB} using data from previous step. Filter noisy data, if necessary.

► Type-curves matching and estimation of average parameters:

11. Plot pressure-transient data from Steps 9 and 10 in a log-log plot with equal log-cycles as in Figure 3.82.
12. If interference effects are detected (i.e. deviation of RNP'_{AB} from $S_F = \infty$), find the best matching-curves and read the values of choking skin s_c and lumped frac-hits skin S_F .
13. Choose a matching point. We recommend reading the values of $(t_D)_{MP}$ and $(\Delta p_{wD})_{MP}$ corresponding to $t_{MP} = 1$ and $(RNP_{AB})_{MP} = 1$ (both in actual dimensions) from well-test data.
14. If the storativity of the SRV $(\phi c_t)_1$ is uncertain but its probable range can be deduced from neighboring wells in the same formation, use P_{10} , P_{50} and P_{90} values of $(\phi c_t)_1$ to perform the calculations required in Step 15.
15. Estimate average well properties and fraction of frac hits using both Interpretation Method 1 (Section 3.11.2) and Interpretation Methods 2 (Section 3.11.3). Note: estimations made with both methods should be comparable.

► Conclusion

16. Give P_{10} , P_{50} and P_{90} values for the estimated fraction of frac hits δ_{wAB} .

3.11.2 Interpretation Method # 1

This interpretation method considers $x_{eD} \approx 1$ in Equation 3.163 through 3.165. As a result, $\Delta p_{wAD}/x_{eD} \approx \Delta p_{wAD}$ and $s_c/x_{eD} \approx s_c$. This method uses matching-point data and best-matched parameters from the type-curves, more specifically choking skin s_c (early-time data) and lumped frac-hits skin factor S_F (mid-time data). The estimation of average parameters between wells A and B is carried out as follows:

1. Use $(\Delta p_{wAD})_{MP}$ and $(RNP_{AB})_{MP}$ [psi/STB/D/fracture] to estimate average SRV permeability (k_1 [md]):

$$k_1 = \frac{141.2\mu B}{h} \left(\frac{\Delta p_{wAD}}{RNP_{AB}} \right)_{MP} \quad (3.172)$$

2. Use k_1 [md] to estimate the average fracture half-length (x_f [ft]) using $(t_D)_{MP}$ and t_{MP} [days]:

$$x_f = 0.07956 \sqrt{\frac{k_1}{\mu(\phi c_t)_1} \left(\frac{t}{t_D} \right)_{MP}} \quad (3.173)$$

3. Estimate average dimensionless fracture conductivity (F_{CD}) using the best-matched value of choking skin (s_c) and x_f [ft] from the previous step:

$$F_{CD} = \frac{h}{x_f s_c} \left[\ln \left(\frac{h}{2r_{wA}} \right) - \frac{\pi}{2} \right] \quad (3.174)$$

4. Estimate the fraction of frac hits between wells δ_{wAB} using the best-matched value of lumped frac-hits skin (S_F), distance between wells (L_{AB} [ft]) and F_{CD} calculated in the previous step:

$$\delta_{wAB} = \frac{2L_{AB}}{x_f F_{CD} S_F} \quad (3.175)$$

3.11.3 Interpretation Method # 2

In this method, $x_{eD} \neq 1$. In consequence, $(\Delta p_{wAD}/x_{eD}) \neq \Delta p_{wAD}$. Similar to Interpretation Method 1, this methods uses matching-point data and best-matched values of choking skin s_c (early-time data) and lumped frac-hits skin factor S_F (mid-time data) to estimate of average parameters between wells A and B as follows:

1. Use $(\Delta p_{wAD})_{MP}$, $(RNP_{AB})_{MP}$ [psi/STB/D/fracture], $(t_D)_{MP}$ and t_{MP} [days] to estimate the dimensionless average half-distance between fractures (x_{eD} [ft]):

$$x_{eD} = 1.038 \left[\frac{(\phi c_t)_1 x_e^2 h}{B} \left(\frac{t_D}{t} \right)_{MP} \left(\frac{RNP_{AB}}{\Delta p_{wAD}/x_{eD}} \right)_{MP} \right]^{1/3} \quad (3.176)$$

2. Use the estimated value of x_{eD} to estimate the average SRV permeability:

$$k_1 = \frac{141.2 \mu B x_{eD}}{h} \left(\frac{\Delta p_{wAD}/x_{eD}}{RNP_{AB}} \right)_{MP} \quad (3.177)$$

3. Estimate average fracture half-length (x_f [ft]) using k_1 [md] from the previous step:

$$x_f = 0.07956 \sqrt{\frac{k_1}{\mu (\phi c_t)_1} \left(\frac{t}{t_D} \right)_{MP}} \quad (3.178)$$

4. Estimate average dimensionless fracture conductivity (F_{CD}) using the best-matched value of choking skin (s_c) and x_f [ft] from the previous step:

$$F_{CD} = \frac{h x_{eD}}{x_f s_c} \left[\ln \left(\frac{h}{2 r_{wA}} \right) - \frac{\pi}{2} \right] \quad (3.179)$$

5. Estimate the fraction of frac hits between wells δ_{wAB} using the best-matched value of S_F :

$$\delta_{wAB} = \frac{2 L_{AB}}{F_{CD} x_{eD} x_f S_F} \quad (3.180)$$

3.11.4 Application Example 1

Pressure-transient data for a dual-MFHW system with 10 fractures per well is generated using numerical simulations. Fracture half-length is not uniform and varies from stage to stage between 180 and 350 ft. Fracture conductivity varies between 275 and 575 md-ft. Average distance between fractured stages is 250 ft. Distance between wells is 900 ft. Storativity of the SRV is assumed equal to 10^{-7} psi^{-1} . Pay thickness and wellbore radius are 100 and 0.25 ft, respectively. Reservoir fluid properties correspond to lower Eagle Ford oil (see Table 2.1).

The offset well (B) was shut-in and repressurized to initial reservoir pressure (6,500 psi) while the infill well (A) was completed. Fracking fluid is flowed back until single-phase oil is produced at 10 STB/D/fracture for 80 days, after which BHP of wells A and B are 5,022 and 6,201 psi, respectively. BHP of well B is lower than initial pressure, suggesting the existence of pressure communication. Pressure was recorded using downhole gauges. Pressure-transient data is reported as $\text{RNP}_{AB}(t)$ and $\text{RNP}'_{AB}(t)$ [psi/STB/D]. Figure 3.83 shows the resulting rate-normalized diagnostic plot. The hump-like behavior of $\text{RNP}'_{AB}(t)$ may indicate frac hits between wells A and B.

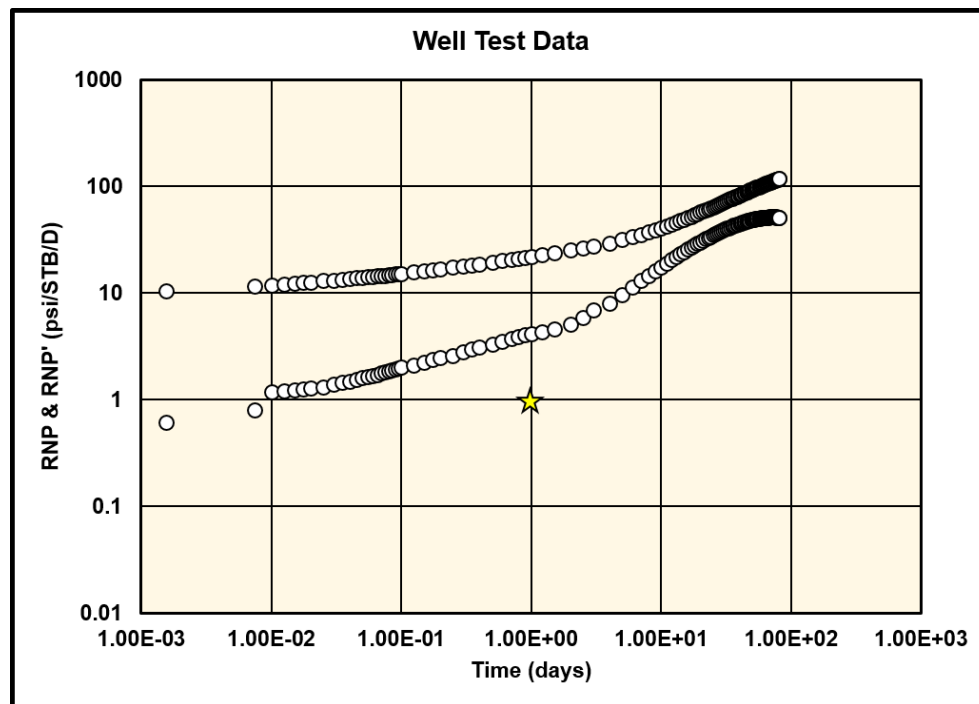


Figure 3.83: Resulting $\text{RNP}_{AB}(t)$ and $\text{RNP}'_{AB}(t)$ for Example 1.

The rate-normalized diagnostic plot of actual pressure-transient data is matched with frac hits type-curves, as shown in Figure 3.84. We chose $t_{MP} = 1$ day and $(RNP_{AB})_{MP} = 1$ psi/STB/D. The best matching parameters are:

- $(t_D)_{MP} = 0.1$
- $(\Delta p_{wAD}/x_{eD})_{MP} = 0.06$
- $s_c = 0.5$
- $S_F = 7$

We setup a spreadsheet containing the equations required to estimate average properties from the dual-MFHW system using Interpretation Methods # 1 and # 2. Table 3.10 summarizes the calculation results. Actual properties of the simulation model are summarized in Table 3.11.

Table 3.10: Estimated average properties for wells A and B in Example 1.

	Method # 1	Method # 2
Dimensionless half-distance, x_{eD}	0.928	0.9514
SRV permeability, k_1	0.0665 md	0.0633 md
Fracture half-length, x_f	269.39 ft	262.76 ft
Dimensionless fracture conductivity, F_{CD}	2.767	2.699
Fracture conductivity, $C_f = F_{CD}k_1x_f$	48.82 md-ft	44.89 md-ft
Fraction of frac hits, δ_{wAB}	0.345	0.381

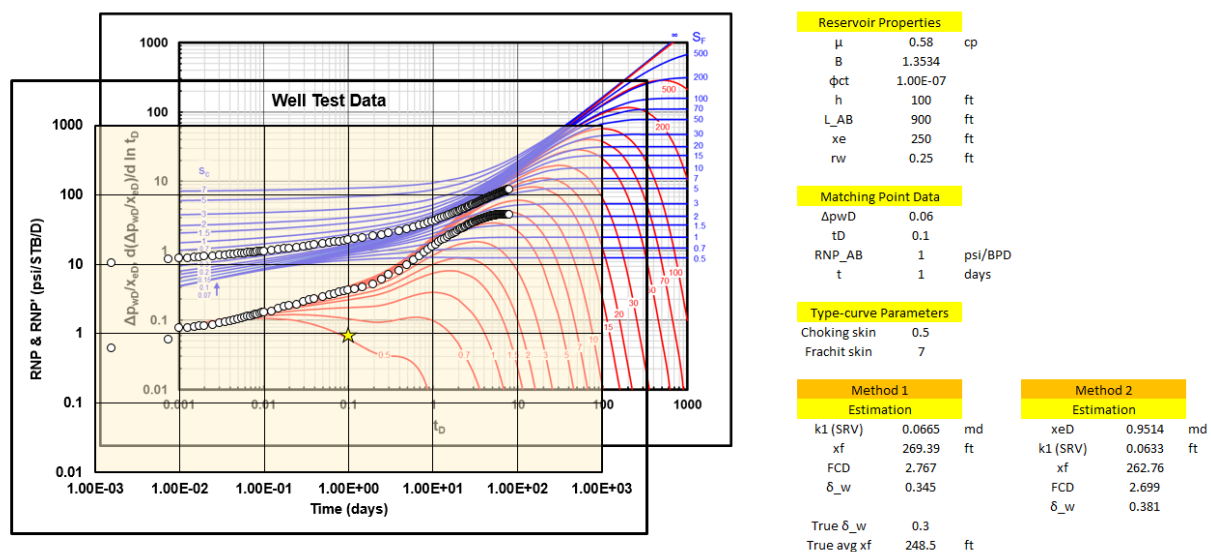


Figure 3.84: Resulting type-curves matching for assessment of frac hits in Example 1.

Table 3.11: Actual MFHW properties used in Example 1.

SRV permeability (per stage), k_1	0.1 md
Fracture half-length, x_f	180 ft (Well A: stages # 2, 9–Well B: stages # 1, 10) 200 ft (Well A: stages # 1, 5, 7, 10–Well B: stages # 2, 5, 9) 250 ft (Well A: stage # 8–Well B: stages # 7, 8) 350 ft (Wells A & B: stages # 3, 4, 6–frac hits)
True average fracture half-length	248.5 ft
Fracture conductivity, C_f	Varies between 275 and 575 md-ft
Fraction of frac hits, δ_{wAB}^*	0.3

Based on type-curves matching results, we conclude that frac hits are the cause of pressure interference between wells A and B, initially detected as a drop in BHP of well B during the test. Under current interference conditions, each well is expected to perform as a MFHW with the average properties listed in Table 3.10. Note that both methods give $x_{eD} < 1$, which means that, on average, fracture half-length is larger than distance between fractured stages. However, when compared to actual values, Method # 1 gives a more accurate estimation of MFHW parameters, including the fraction of frac hits. Yet, note that estimation given by both methods is comparable, which serves as a consistency check for the type-curves analysis.

3.11.5 Application Example 2

This scenario deals with the pressure-transient testing of an individual MFHW with 20 fractures. The completion job was engineered to generate fractures of approximately equal half-length. Yet, actual average fracture half-length is unknown. Distance between fractured stages is 250 ft. Storativity of the SRV is assumed equal to 10^{-7} psi⁻¹. Pay thickness and wellbore radius are 100 and 0.25 ft, respectively. Oil properties are summarized in Table 2.1.

Once oil begins to flow, the MFHW is held at a constant rate of 400 STB/D (20 STB/D per fracture) during 20 days, after which pressure had dropped from 6,500 to 6,208 psi. Pressure was recorded using downhole gauges. Figure 3.85 shows the rate-normalized pressure-transient data resulting from this well test. We chose $t_{MP} = 1$ day and $(RNP_{AB})_{MP} = 1$ psi/STB/D.

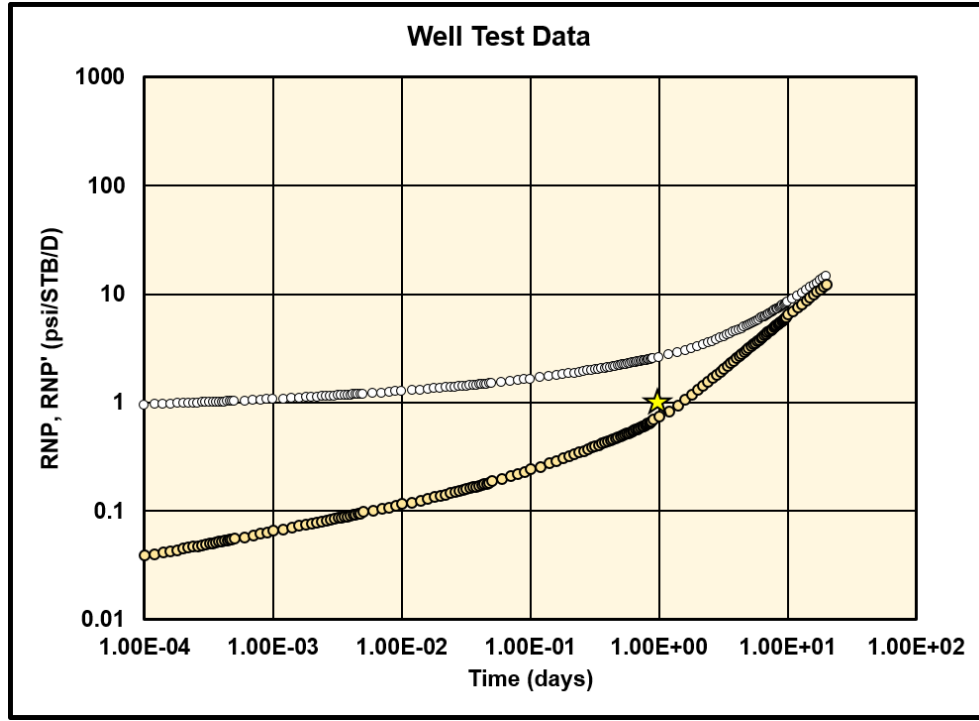


Figure 3.85: Resulting $RNP_{AB}(t)$ and $RNP'_{AB}(t)$ for Example 2.

The best matching parameters for this case are:

- $(t_D)_{MP} = 0.4$
- $(\Delta p_{wAD}/x_{eD})_{MP} = 0.9$
- $s_c = 0.7$
- $S_F = \infty$

Table 3.12 enlists the MFHW parameters estimated with Methods # 1 and # 2. Actual properties of the simulation model are summarized in Table 3.13.

Table 3.12: Estimated average properties for MFHW in Example 2.

	Method # 1	Method # 2
Dimensionless half-distance, x_{eD}	1.154	1.01
SRV permeability, k_1	0.9975 md	1.0974 md
Fracture half-length, x_f	216.62 ft	227.20 ft
Dimensionless fracture conductivity, F_{CD}	2.458	2.578
Fracture conductivity, $C_f = F_{CD}k_1x_f$	531.12 md-ft	642.77 md-ft
Fraction of frac hits, δ_{wAB}	0	0

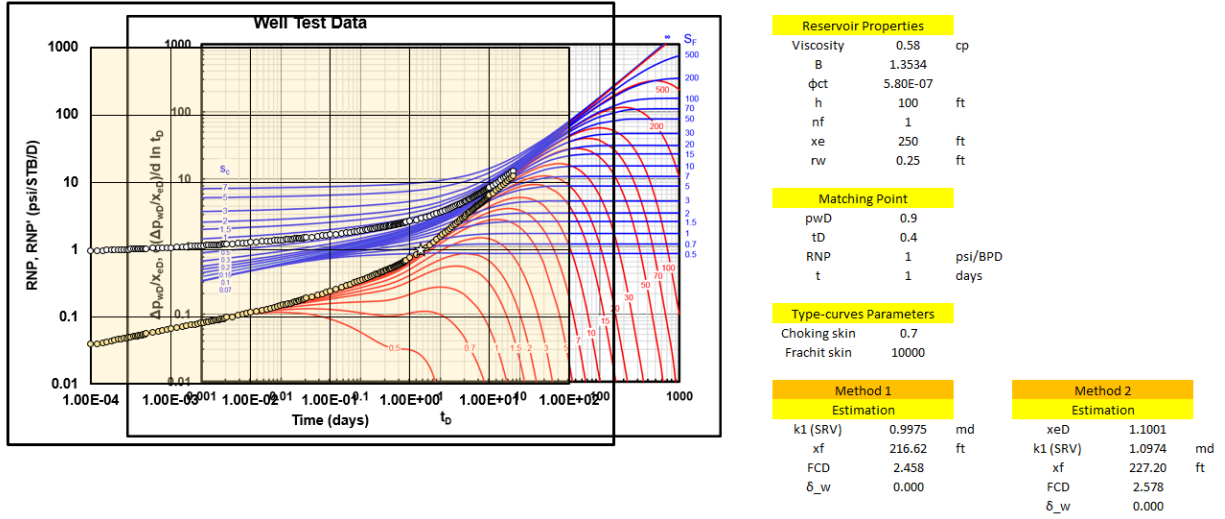


Figure 3.86: Result in type-curves matching for Example 2.

Table 3.13: Actual MFHW properties used in Example 2.

SRV permeability (per stage), k_1	1 md
Fracture half-length, x_f	200 ft
Fracture conductivity, C_f	500 md-ft
Fraction of frac hits, δ_{wAB}^*	0

Analysis of results allows to conclude that the proposed type-curves matching method gives reliable estimation of average MFHW properties. As observed in the previous example case, Method # 1 is more accurate than Method # 2; however, estimations made with both methods are comparable.

3.12. Discussion

This chapter focuses on the development of an analytical model capable of detecting well interference effects due to frac hits in a multi-well pad using diagnostic plots and type-curves. Instead of analyzing transient data for each MFHW in the pad individually, we define the pressure differential parameter $\Delta p_{wAB} = |\Delta p_{wA} - \Delta p_{wB}|$, where A is the infill well and B is the offset well. The initial hypothesis that energy tends to attain late-time equilibrium across interfering wells is tested and confirmed by numerical simulation data showing that Δp_{wAB} reaches a late-time plateau when frac hits exist between wells A and B. The correlation between the degree of interference and

the observed pressure equilibration behavior is simple: the higher the number of frac hits the faster the plateau is reached.

Based on the equilibration hypothesis as an indicator of frac hits, we develop the fluid-flow model for a three-MFHW pad. Frac hits are modeled as a boundary condition that enables pressure communication between MFHWs through the fractures. We validate the analytical solution against numerical validations for four different scenarios where all MFHWs are flowing at constant rate. To the best of our knowledge, no previous study have been able to detect and estimate the number (or fraction) of frac hits without the need for any shut-in (Awada et al., 2016).

As mentioned earlier, the present analytical model considers three MFHW in the pad. Nonetheless, the proposed approach can be extended for as many wells as required. However, the history-matching process may become challenging when dealing with transient data for more than 3 wells. The script used to run the analytical frac hits model takes around 30 seconds to generate the required analytical pressure-transient data, hence making the three-MFHW model convenient for field application during the flowback period (i.e. single-phase fluid-flow). Notice that the rate-normalized approach should also work for variable rate during the interference test; however, changes in rate must be smooth and small compared to total flow rate.

Given the vast number of possible combinations of fracture properties, pad dimensions and distance between infill and offset wells in a multi-well pad, we design several sensitivity studies to narrow those down and try to cover realistic field configurations as to understand how these would impact the detection and assessment of frac hits, based on the analytical solution. In total, 330 simulations were carried out and history-matched with the analytical model. These results are presented in the form of PTA type-curves of rate-normalized data RNP_{AB} and RNP'_{AB} . We observe that, in the absence of frac hits, transient RNP_{AB} and RNP'_{AB} response corresponds to that of an isolated MFHW. However, new type-curves develop as the number of frac hits increases. A total of 33 frac-hits type-curves are presented and discussed in this chapter.

In addition, we developed dimensionless type-curves for well characterization and assessment of frac hits between two MFHWs (wells A and B). We assume that performance of wells in communication through frac hits is analogous to that of two identical wells with certain average properties. Furthermore, we set well A to flow at constant rate while well B is shut-in. The analytical solution to the forward problem is reduced

to a more convenient dimensionless solution for pressure changes in well A, which allows to generate type-curves for varying degrees of well interference. We discussed two examples that demonstrate the applicability and usefulness of the proposed type-curves.

Although the analytical frac hits model can history-match any of the scenarios discussed herein, accuracy of the prediction of individual BHP in the pad depends on the geometric configuration of each MFHW as well as other properties, such as SRV permeability. Another shortcoming of the analytical frac hits model is that it performs best before the onset of 2-D flow between the inner matrix region and interfering wells. A 2-D semi-analytical approach to this model may solve this issue; however, the practical applicability of the such semi-analytical model may be overshadowed by its computational requirement.

Lastly, estimation of ultimate recovery as well as mass balance over individual well's productivity are the starting point for future work regarding the application of the proposed frac hits model.

3.13. Conclusions

We introduce an analytical model for the detection of frac hits in a multi-well pad. The well is represented as a source-line in the governing equation of each MFHW such that two boundary conditions are available for modeling fluid-flow in the hydraulic fractures. Therefore, we develop the frac hits boundary condition which connects two or three MFHW through the hydraulic fracture interfaces.

Furthermore, we introduce the quad-linear flow model (QLF) to account for asymmetric distribution of wells in the pad. The analytical solution for individual BHP is derived in Laplace domain and are inverted into time domain numerically. The proposed analytical PTA approach was validated against four numerical simulation cases in which all wells were flowing at constant rate. Frac hits were successfully detected and characterized in these cases. Moreover, even though interference effects through the matrix was not considered in the analytical model, we observed that matrix interference can actually be accounted for in the form of a small fraction of frac hits, commonly smaller than 0.001 (equivalent to 1 frac hit out of 1000 fractured stages). Pressure interference effects through the matrix were detected at late times, as expected.

We proved that individual BHP does not provide as much information about frac hits as the combined pressure differential between wells, as the latter tends to attain equilibrium in the presence of pressure interference effects; the higher the fraction of frac hits the faster the equilibrium plateau is attained in both pressure differential and pressure-differential derivative.

The use of typical rate-normalized PTA type-curves allows the estimation of the fraction of frac hits across wells in the three-MFHW used as the basis for the analysis. Type-curves for various well configurations, associated with realistic field completion scenarios, were generated and history-matched against numerical simulation data. Dimensionless type-curves for frac hits characterization were generated and two application examples were discussed, showing the potential benefit of the application of the proposed type-curves.

4. Effect of Anisotropic Fault Permeability Enhancement on Pressure-Transient Behavior

4.1. Background

Faulted reservoirs feature a segmenting fault acting as the primary barrier to leakage of hydrocarbons into neighboring permeable strata (Knipe et al., 1998; Jolley et al., 2010). Yet, an initially sealing fault can abruptly become partially conductive in response to changes in local stresses induced by rapid variations in pore pressure. Such rapid alteration of fault permeability is often connected with (aseismic or seismic) fault slip (Cappa and Rutqvist, 2011; Guglielmi et al., 2015; Jeanne et al., 2018). In general, variation in fault permeability upon fault reactivation is a very complicated process that depends on the hydro-mechanical interaction between pore pressure, in-situ stress orientation and magnitudes, and fault properties (e.g. mineralogy, roughness, and rock fabric). Yet, observations from coupled hydromechanical modeling (Cappa and Rutqvist, 2011; Rutqvist et al., 2013) and field experiments of induced fault slip (Jeanne et al., 2018) suggest that fault permeability gets suddenly enhanced upon fault slip. Besides, the enhanced fault permeability resulting from fault reactivation is anisotropic, pressure-dependent and may even be self-healing with time.

Hydrocarbon production operations may potentially lead to fault reactivation and related fault permeability enhancement when 1) cumulative volumes of produced fluids are large enough to prompt a fast decline in reservoir pressure, 2) the fault is favorably oriented with respect to current in-situ stresses, and 3) subsidence rates near producing wells are substantially higher than geologic subsidence rates (Buijze et al., 2017; Chan and Zoback, 2007; Morton and Purcell, 2001). Visund field offshore Norway (Wiprut and Zoback, 2000) and South Marsh Island 36 field in the Gulf of Mexico (Davies et al., 2003) are examples of initially sealing faults becoming conductive due to fast, differential pressure depletion across the fault. In a similar fashion, subsurface fluids injection may induce fault reactivation due to differential pressure build-up across fault blocks (Bourouis and Bernard, 2007; Jha and Juanes, 2014; Rutqvist et al., 2013).

Subsurface fluid injection is primarily utilized in oil and gas fields for disposal of produced and wastewater, natural gas storage, CO₂ storage and enhanced oil/gas recovery. Research efforts made in recent years suggest the existence of a relationship

between induced seismicity and injection of fluids in the subsurface (Ellsworth, 2013; Keranen et al., 2013; Rubinstein et al., 2014; McGarr et al., 2015). For example, Keranen et al. (2014) pointed out that fluid migration from the injection zone is potentially responsible for the increase in seismic activity in Oklahoma since 2008.

Although it is commonly believed that induced seismicity can only occur near the injection point, field observations suggest that seismic events may actually be triggered far away from the injection well (Healy et al., 1968; Hsieh and Bredehoeft, 1981; Rubinstein and Mahani, 2015). Because man-made seismic activity is associated with fault slip, caused by pressure changes in the subsurface, fluid leakage from the injection zone is correlated with fault reactivation (Sibson, 1985; Wiprut and Zoback, 2000). Thus, prior information about permeability of potentially conductive faults in the target formation is key for assessing the suitability of a certain permeable formation for storage and long-term containment of fluids.

There may be undetected non-conductive and/or slightly conductive faults in the underground that could be reactivated thus becoming conduits for fluid leakage. Wiprut and Zoback (2000) argue that gas leakage resulted from the reactivation of a previously dormant fault in the Visund oil and gas field in Norway. Likewise, Davies et al. (2003) reported that an initially sealing fault in the South Marsh Island 36 field in the US Gulf of Mexico became conductive after the across-fault pressure differential, caused by differential gas production, reached 3000 psi. Henceforth, the need for studying the evolution of fault properties must be primordial for reservoir management purposes.

The potential risks associated with leakage of injected and/or native fluids, such as contamination of ground water resources and induced seismicity, as well as other reservoir management issues associated with oil and gas production operations, can be mitigated if the evolution of fault characteristics is monitored properly. For such cases, pressure-transient analysis would be a low-cost alternative to the more expensive permanent active/passive seismic monitoring techniques.

4.2. Statement of the Problem

Several analytical models for faulted reservoirs have been developed over the years for pressure transient analysis (PTA) purposes. In despite that reservoir pressure changes over time during fluid withdrawal or injection, all of the analytical models assume that fault properties remain constant.

The earliest of such models is the method of image wells, developed for an isotropic and homogeneous reservoir containing a sealing linear boundary (Horner, 1951). Diagnostic pressure-transient plots derived from this model are often used to detect and estimate the distance from the well to sealing boundaries. Figure 4.2a illustrates pressure-drawdown distribution in Region 1, $\Delta p_1(x, y, t \leq t_s)$, given by the image wells solution while pressure-drawdown in Region 2, $\Delta p_2(x, y, t \leq t_s)$, is null due to the absence of pressure communication. Bixel et al. (1963) introduced the analytical solution for fluid-flow in a composite reservoir in which the fault is represented as a linear discontinuity between formations; however, the fault itself has zero skin. Later, (Yaxley, 1987) introduced the partially-communicating or linear leaky fault model for an infinite reservoir to overcome the zero fault-skin limitation from Bixel et al. (1963) by assuming that fault leakage rate is controlled by pressure differential across the fault. Figure 4.2b depicts the evolution of pressure-drawdown occurring in Region 1 and 2 simultaneously as the fault is partially communicating. Along the same lines, Ambastha et al. (1989) derived pressure-transient solutions for a partially-communicating fault in a composite striped reservoir. Nonetheless, (Yaxley, 1987) and Ambastha et al. (1989) considered across-fault leakage only.

Abbaszadeh and Cinco-Ley (1995) introduced the linear-lateral leaky fault model with finite skin and conductivity that accounts for flow transience within the fault as well as simultaneous along-across-fault leakage. However, the mathematical complexity of the proposed solution forfeited its applicability. Rahman et al. (2003) presented a more practical version of the former model by modeling across-fault leakage simply as a flux-source term, characterized by fault skin s_f , while accounting for transience effects along the fault where fluid-flow is controlled by the dimensionless fault conductivity F_{CD} (Figure 4.2c). Additionally, fault blocks may have different diffusivity η_j and transmissibility T_j .

Due to its ease of implementation, Rahman et al. (2003) leaky fault model is the most widely used leaky fault model. There exists, however, another possible scenario in which the leaky fault exists in a bounded reservoir (Figure 4.2d). Although more realistic, analytical expressions for $\Delta p_1(x, y, t \leq t_s)$ and $\Delta p_2(x, y, t \leq t_s)$ may be difficult to obtain for such scenario. Furthermore, information about reservoir limits, fault properties, and reservoir size should be known a priori. Therefore, characterization of fault properties is typically achieved during transient flow conditions when boundaries are unseen by the pressure disturbance.

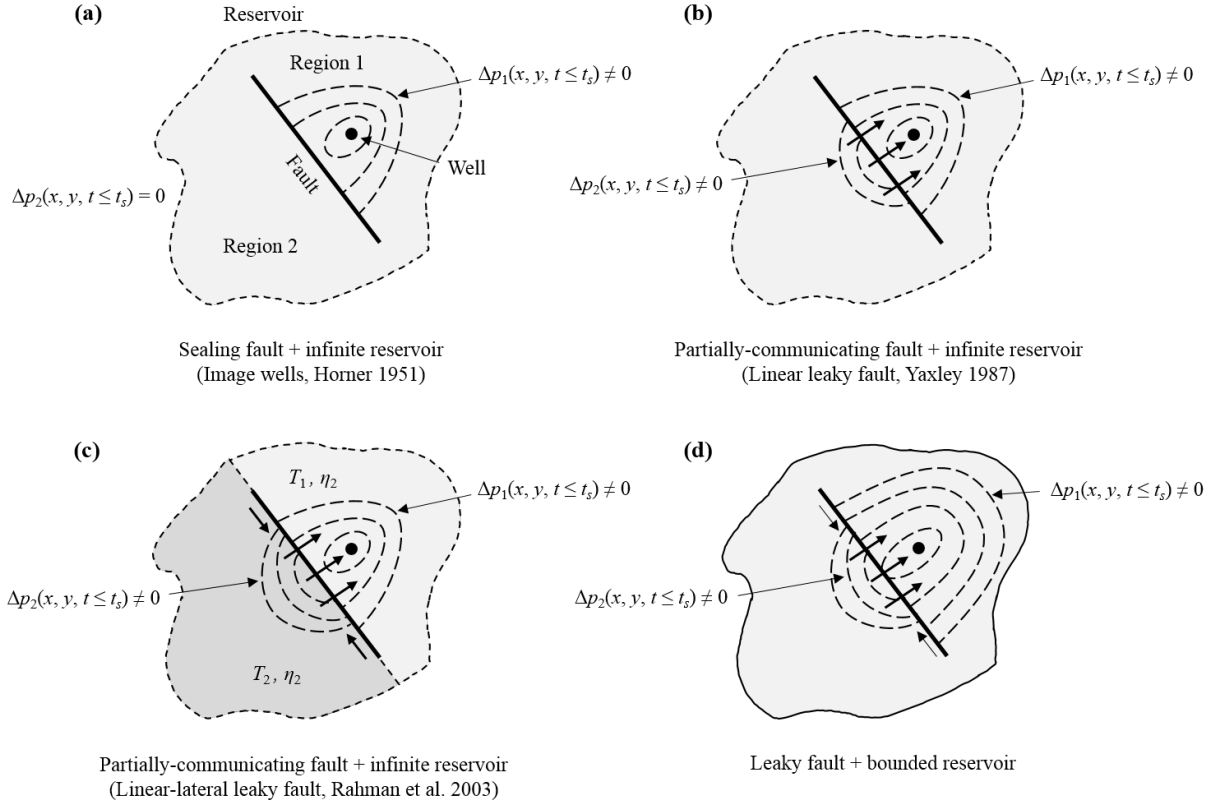


Figure 4.1: Different types of pressure-drawdown distribution in a compartmentalized reservoir before the onset of fault reactivation.

4.3. Proposed Methodology

In departure from previous models, the analytical model presented in this work goes beyond the assumption of constant fault properties by allowing fault permeability to behave in a more geologically realistic manner, in this case step-wise, after the onset of fault slip has been reached. We consider a faulted reservoir scenario in which the fault is originally sealing during $0 \leq t \leq t_s$, where t_s is the onset of fault reactivation. The pressure distribution in Region 1 at $t = t_s$ is given by the image wells solution. Subsequently, we model fault reactivation at $t = t_s$ as a sudden change in anisotropic fault permeability so that the initially sealing fault becomes partially conductive, both perpendicular and laterally (Figure 4.2a), consistent with the typical structure of the fault zone of a conductive fault (Caine et al., 1996). Since the fault is leaky for $t > t_s$, Rahman et al. (2003) model applies thereon. Therefore, given that pressure-drawdown in Region 1 is non-null, we setup the leaky fault model for non-null initial pressure distribution in Region 1, designated as $\Delta p_1^0(x, y, t' = 0)$ where $t' = t - t_s$ is the elapsed time after the onset of fault reactivation.

We solve the governing equations for Region 1 using the Laplace-Fourier transformation and use the analytical solution at the wellbore to extract the signature transient response to fault reactivation. We introduce type curves for various dimensionless onset times (t_{sD}), s_f and F_{CD} . Moreover, we discuss fault permeability characterization using late-time pressure response and benchmark the proposed model against numerical simulations.

The primary application of our model is the interpretation of well-test data for extracting valuable information about the fault and reservoir after fault reactivation had occurred. More specifically, the purpose of the analytical workflow hereby introduced is threefold:

1. To identify pressure and pressure- derivative responses to a sudden enhancement of fault permeability as an indicator of fault seal breakdown,
2. to estimate the onset time of fault slip from diagnostic plots, and
3. to characterize fault properties before and after fault reactivation.

4.4. Mathematical Modeling

We examine the scenario of a sealing fault before the onset of fault reactivation ($t = t_s$) and subsequent simultaneous linear-lateral leakage after fault reactivation. The slightly compressible fluid flow assumption is followed herein. Fluid is the same in both formations. Formation layers are isotropic and homogeneous with respect to porosity and permeability and are semi-infinite in extension with constant thickness. As mentioned earlier, fault blocks can have distinct transmissibility ($T_j = k_j h_j$) and diffusivity ($\eta_j = k_j / \mu(\phi c_t)_j$). Fault is assumed initially sealing thus fault skin is infinite ($s_f \rightarrow \infty$) thus the effect of F_{CD} on pressure-transient response becomes negligible.

We propose a fault permeability enhancement scenario based on a composite reservoir segmented by a planar fault represented as a linear interface between fault blocks located at $x = 0$, as shown in Figure 4.2b. The interface is infinite along the y -axis. The target reservoir is represented as Region 1 ($x \geq 0$) while the adjacent fault block is referred to as Region 2 ($x \leq 0$). The constant-rate well in Region 1 is modeled as a line-source located at a distance b away from the fault. Simultaneous across-along-fault flow is modeled following the approach by Rahman et al. (2003).

Enhancement of anisotropic (directional) fault permeability is mathematically repre-

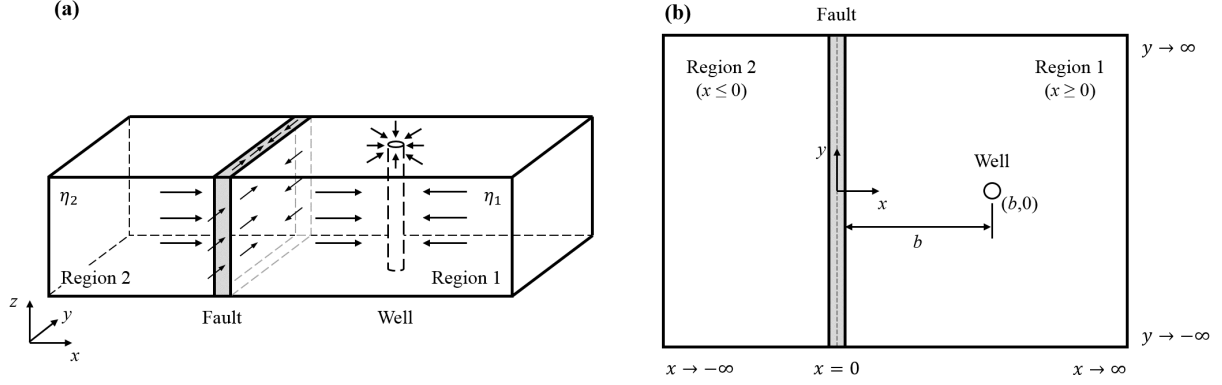


Figure 4.2: Idealization of a segmenting fault as a linear interface in a composite reservoir (Ambastha et al., 1989). Flow direction in a typical fault zone, and idealization of a compartmentalized reservoir in which the fault is modeled as a linear interface between fault blocks.

sented as a sudden change from null fault permeability into finite directional fault permeability occurring at $t = t_s$ or $t_D = t_{sD}$ (see Equation B.7). In this view, across and along-fault permeability changes are incorporated into the system as sudden changes in s_f (Equation B.11) and F_{CD} (Equation B.12), respectively. In this study, we examine pressure-drawdown and pressure- derivative responses to $0 \leq s_f < \infty$ and $F_{CD} > 0$ at various onset times. It is worthwhile to mention that, unlike other models, the definition of s_f proposed herein is based on the dimensionless fault transmissibility α proposed by Yaxley (1987) such that $\alpha = s_f^{-1}$ (Equation B.11). This definition enables the use of s_f for fault characterization purposes.

4.4.1 Governing Equations

The governing equation for Regions 1 and 2 (Ambastha et al., 1989) and fault (Rahman et al., 2003) are, respectively, given as

$$\frac{\partial^2 \Delta p_1}{\partial x^2} + \frac{\partial^2 \Delta p_1}{\partial y^2} + \frac{q\mu B}{k_1 h_1} \delta(x-b)\delta(y) = \frac{1}{\eta_1} \frac{\partial \Delta p_1}{\partial (t-t_s)} \quad (4.1)$$

$$\frac{\partial^2 \Delta p_2}{\partial x^2} + \frac{\partial^2 \Delta p_2}{\partial y^2} = \frac{1}{\eta_2} \frac{\partial \Delta p_2}{\partial (t-t_s)} \quad (4.2)$$

$$\frac{\partial^2 \Delta p_f}{\partial y^2} + \frac{k_1}{k_{f1} w_f} \left[\left(\frac{\partial \Delta p_1}{\partial x} \right)_{x=0} - T_D \left(\frac{\partial \Delta p_2}{\partial x} \right)_{x=0} \right] = \frac{1}{\eta_f} \frac{\partial \Delta p_f}{\partial (t-t_s)} \quad (4.3)$$

The term $\frac{q\mu B}{k_1 h_1} \delta(x-b)\delta(y)$ in Equation 4.1 is the line-source representation of the constant-rate well located at $x = b$ and $y = 0$. Also, we assume that pressure is initially constant throughout the reservoir so that $\Delta p_j(x, y, t = 0) = 0$.

Normalization of the governing equations is accomplished by using the corresponding dimensionless parameters for Δp_j (Equation B.1), x and y (Equation B.2— B.3), $t - t_s$ (Equation B.6) and η_j (Equation B.9 and B.10). Replacing these normalized parameters into the governing equations Equation 4.1—4.3 leads to:

$$\frac{\partial^2 p_{1D}}{\partial x_D^2} + \frac{\partial^2 p_{1D}}{\partial y_D^2} + 2\pi\delta(x_D - 1)\delta(y_D) = \frac{\partial p_{1D}}{\partial t'_D} \quad (4.4)$$

$$\frac{\partial^2 p_{2D}}{\partial x_D^2} + \frac{\partial^2 p_{2D}}{\partial y_D^2} = \frac{1}{\eta_D} \frac{\partial p_{2D}}{\partial t'_D} \quad (4.5)$$

$$\frac{\partial^2 p_{fD}}{\partial y_D^2} + \frac{1}{F_{CD}} \left[\left(\frac{\partial p_{1D}}{\partial x_D} \right)_{x_D=0} - T_D \left(\frac{\partial p_{2D}}{\partial x_D} \right)_{x_D=0} \right] = \frac{1}{\eta_{fD}} \frac{\partial p_{fD}}{\partial t'_D} \quad (4.6)$$

Next, we introduce a sudden change in fault permeability at $t'_D = 0$ so that the initially-sealing fault becomes leaky some time after fluid withdrawal (or injection, if q is negative) had started. This means that pressure had been depleting (or building up) in the reservoir during the period $0 \leq t_D \leq t_{sD}$. On the one hand, the dimensionless pressure distribution in Region 1 before fault reactivation, defined as $p_{1D}^0(x_D, y_D, 0 \leq t_D \leq t_{sD})$, is given by the analytical solution to Equation 4.4 for $t'_D = t_D$ and $0 \leq t_D \leq t_{sD}$. On the other hand, given that the fault is assumed initially sealing, $p_{2D}^0(x_D, y_D, 0 \leq t_D \leq t_{sD}) = p_{fD}^0(x_D, y_D, 0 \leq t_D \leq t_{sD}) = 0$.

Nonetheless, if the fault was initially conductive, $p_{2D}^0(x_D, y_D, 0 \leq t_D \leq t_{sD}) \neq 0$ and $p_{fD}^0(x_D, y_D, 0 \leq t_D \leq t_{sD}) \neq 0$. In that case, initial dimensionless pressure in these regions are given by the analytical solution to Equation 4.5 and 4.6, respectively, for $t'_D = t_D$ and $0 \leq t_D \leq t_{sD}$.

4.4.2 Laplace-Fourier Transform

To simplify the analytical solution process for the governing equations of the fault reactivation model, we conveniently apply Laplace transform over time and Fourier transform along the y -axis because $0 < t'_D < \infty$ and $-\infty \leq y_D \leq \infty$. The simultaneous

Laplace-Fourier transform of p_{jD} is mathematically defined as

$$\mathcal{FL} \{p_{jD}\} \equiv \bar{\bar{p}}_{jD}(x_D, \omega, s) = \int_0^\infty \int_{-\infty}^\infty e^{-st'_D - i\omega y_D} p_{jD}(x_D, y_D, t'_D) dy_D dt'_D \quad (4.7)$$

The inverse transform pair of Equation 4.7 is given by

$$p_{jD}(x_D, y_D, t'_D) = \mathcal{F}^{-1} \mathcal{L}^{-1} \{\bar{\bar{p}}_{jD}\} = \frac{1}{2\pi} \int_{-\infty}^\infty e^{-i\omega y_D} \mathcal{L}^{-1} \{\bar{\bar{p}}_{jD}(x_D, \omega, s)\} dy_D \quad (4.8)$$

Since p_{jD} is symmetric with respect to the y -axis, Equation 4.8 may be rewritten as

$$p_{jD}(x_D, y_D, t'_D) = \frac{1}{\pi} \int_0^\infty \cos(\omega y_D) \mathcal{L}^{-1} \{\bar{\bar{p}}_{jD}(x_D, \omega, s)\} dy_D \quad (4.9)$$

For the case when $p_{jD}^0(x_D, y_D, 0 \leq t_D \leq t_{sD}) \neq 0$,

$$\mathcal{FL} \left\{ \frac{\partial p_{jD}}{\partial t'_D} \right\} = s \bar{\bar{p}}_{jD} - \mathcal{F} \left\{ p_{jD}^0(x_D, y_D, t'_D = 0) \right\} \quad (4.10)$$

Be reminded that $p_{jD}^0(x_D, y_D, t'_D = 0)$ is the current dimensionless pressure distribution in Region j at the onset of fault reactivation ($t'_D = 0$ or $t_D = t_{sD}$). For simplicity, we will refer to this initial condition as $p_{jD}^0(x_D, y_D)$.

4.4.3 Canonical Solutions in Laplace-Fourier Domain

Replacement of Equation 4.7 and 4.10 into Equation 4.4 to 4.5 yields the following set of ordinary differential equations for Regions 1 and 2, respectively, in the Laplace-Fourier domain:

$$\frac{d^2 \bar{\bar{p}}_{1D}}{dx_D^2} - (s + \omega^2) \bar{\bar{p}}_{1D} = -\frac{2\pi}{s} \delta(x_D - 1) - \mathcal{F} \left\{ p_{1D}^0(x_D, y_D) \right\} \quad (4.11)$$

$$\frac{d^2 \bar{p}_{2D}}{dx_D^2} - \left(\frac{s}{\eta_D} + \omega^2 \right) \bar{p}_{2D} = -\mathcal{F} \left\{ p_{2D}^0(x_D, y_D) \right\} \quad (4.12)$$

In a similar fashion, we obtain the transformed governing equation for the fault region:

$$\left(\frac{s}{\eta_{fD}} + \omega^2 \right) \bar{p}_{fD} = \frac{1}{F_{CD}} \left[\left(\frac{d\bar{p}_{1D}}{dx_D} \right)_{x_D=0} - T_D \left(\frac{d\bar{p}_{1D}}{dx_D} \right)_{x_D=0} \right] + \mathcal{F} \left\{ p_{fD}^0(y_D) \right\} \quad (4.13)$$

Notice that Equation 4.13 is the actual solution to the governing equation Equation 4.6 in the Laplace-Fourier domain. To simplify the expressions above, let us define $\sigma^2 = s + \omega^2$, $\sigma_2^2 = \frac{s}{\eta_{2D}} + \omega^2$ and $\sigma_f = \frac{s}{\eta_{fD}} + \omega^2$.

Utilization of the method of variation of parameters, along with the infinite-acting-reservoir boundary conditions for Regions 1 and 2, i.e. $\bar{p}_{1D}(x_D, \omega, s) = 0$ as $x_D \rightarrow \infty$ and $\bar{p}_{2D}(x_D, \omega, s) = 0$ as $x_D \rightarrow -\infty$, leads to the solution to Equation 4.11 and 4.12:

$$\begin{aligned} \bar{p}_{1D} = & \frac{\pi e^{-\sigma|x_D-1|}}{s\sigma} + B e^{-\sigma x_D} + \frac{1}{2\sigma} \int_0^{x_D} e^{-\sigma(x_D-\xi)} \mathcal{F} \left\{ p_{1D}^0(x_D, y_D) \right\} d\xi \\ & + \frac{1}{2\sigma} \int_{x_D}^{\infty} e^{-\sigma(\xi-x_D)} \mathcal{F} \left\{ p_{1D}^0(x_D, y_D) \right\} d\xi \end{aligned} \quad (4.14)$$

$$\begin{aligned} \bar{p}_{2D} = & A e^{-\sigma|x_D|} + \frac{1}{2\sigma_2} \int_0^{|x_D|} e^{-\sigma_2(|x_D|-\xi)} \mathcal{F} \left\{ p_{2D}^0(x_D, y_D) \right\} d\xi \\ & + \frac{1}{2\sigma_2} \int_{|x_D|}^{\infty} e^{-\sigma_2(\xi-|x_D|)} \mathcal{F} \left\{ p_{2D}^0(x_D, y_D) \right\} d\xi \end{aligned} \quad (4.15)$$

We use the following inversion pairs (Bateman, 1954) to invert Equation 4.38 and 4.39 into dimensionless time-space domain:

$$\mathcal{L}^{-1} \left\{ \frac{e^{-a\sqrt{s}}}{\sqrt{s}} \right\} = \frac{e^{-\frac{a^2}{4t}}}{\sqrt{\pi t}} \quad (4.16)$$

$$\mathcal{F}^{-1} \mathcal{L}^{-1} \left\{ \frac{f(s + \omega^2)}{s} \right\} = \frac{1}{2\sqrt{\pi}} \int_0^t \frac{e^{-\frac{y^2}{4\tau}}}{\sqrt{\tau}} \mathcal{L}^{-1} \{f(s)\} d\tau \quad (4.17)$$

$$\mathcal{F}^{-1} \{f(\omega)g(\omega)\} = \int_{-\infty}^{\infty} f(v)g(y - v) dv \quad (4.18)$$

Equation 4.18 is the Fourier convolution theorem. This transform pair is particularly important to handle the inversion process when $p_{jD}^0(x_D, y_D) \neq 0$.

Inversion of Equation 4.15 is not discussed herein because the focus of this chapter is to analyze transient pressure response at the well, located in Region 1. Yet, the procedure that will be explained next also applies to Region 2.

4.5. Analytical Solution to the Fault Reactivation Model

In developing the analytical solution to the governing equations to along-across-fault flow upon fault reactivation (Equation 4.11 to 4.13), we consider the general case in which dimensionless pressure distribution in Regions 1 and 2 are not specific to any of the fluid-flow cases discussed in Section 4.2 (Figure 4.2). Instead, we simply assume that $p_{jD}^0(x_D, y_D) \neq 0$. This section is divided into two subsections. First, we find the solution to the general problem of fault reactivation after the onset of fault slip ($t_D > t_{sD}$ or $t'_D > 0$). Additionally, we derive the late-time asymptotic pressure behavior of Region 1 based on the work of Molina and Zeidouni (2018). Second, we derive the analytical solution to the initially-sealing fault problem using the general solution. We present and discuss the analytical model using typical PTA diagnostic plots and type-curves for a variety of fluid-flow scenarios. Finally, the proposed analytical solution is validated against numerical simulations.

4.5.1 Analytical Solution after Fault Reactivation ($t > t_s$)

Figure 4.3 illustrates the material balance of across and along fault flux after the enhancement of anisotropic fault permeability occurring at $t = t_s$. Pressure across the

fault is discontinuous; however, total flux across and along the fault must be conserved. Equation 4.13 is used to couple Regions 1 and 2 at the interface ($x = 0$).

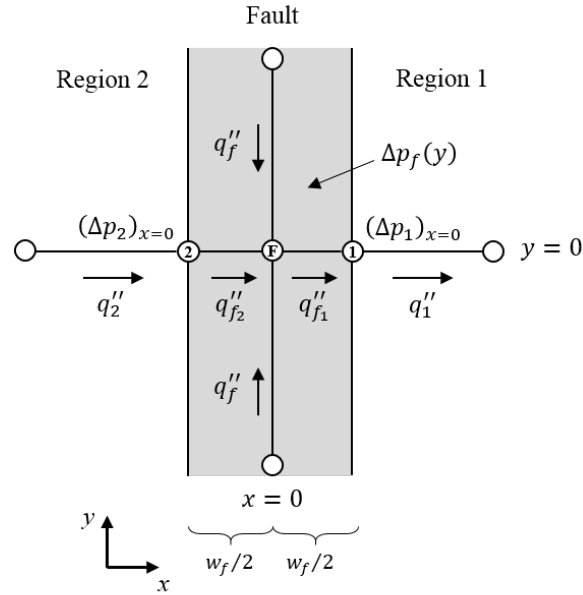


Figure 4.3: Material balance in the fault: steady-state flux across the fault and transient flux along the fault.

Fluxes across the fault interfaces are defined as follows:

$$q''_1 = \frac{k_1 h_1}{\mu B} \left(\frac{\partial \Delta p_1}{\partial x} \right)_{x=0} \quad (4.19)$$

$$q''_2 = \frac{k_2 h_2}{\mu B} \left(\frac{\partial \Delta p_2}{\partial x} \right)_{x=0} \quad (4.20)$$

$$q''_{f1} = \frac{k_f h_1}{\mu B (w_f/2)} (\Delta p_1 - \Delta p_f)_{x=0} \quad (4.21)$$

$$q''_{f2} = \frac{k_f h_1}{\mu B (w_f/2)} (\Delta p_f - \Delta p_2)_{x=0} \quad (4.22)$$

Fluxes across the fault are defined in reference to the thickness of the reservoir (Region 1). Note that both Equation 4.19 and 4.20 assume that across-fault flux occurs in steady-state and is controlled by the pressure differential across the fault interface. According to Figure 4.3, the mass balance at Node 2 gives $q''_2 = q''_{f2}$ henceforth

$$\frac{k_2 h_2}{\mu B} \left(\frac{\partial \Delta p_2}{\partial x} \right)_{x=0} = \frac{k_f h_1}{\mu B (w_f/2)} (\Delta p_f - \Delta p_2)_{x=0} \quad (4.23)$$

Normalization of Equation 4.23 and subsequent transformation into Laplace-Fourier domain leads to:

$$T_D \left(\frac{d\bar{\bar{p}}_{2D}}{dx_D} \right)_{x_D=0} = \frac{2}{s_f} (\bar{\bar{p}}_{fD} - \bar{\bar{p}}_{2D})_{x_D=0} \quad (4.24)$$

Likewise, the mass balance at Node 1 yields

$$\left(\frac{d\bar{\bar{p}}_{1D}}{dx_D} \right)_{x_D=0} = \frac{2}{s_f} (\bar{\bar{p}}_{1D} - \bar{\bar{p}}_{fD})_{x_D=0} \quad (4.25)$$

Summation of Equation 4.24 and 4.25 gives

$$\left(\frac{d\bar{\bar{p}}_{1D}}{dx_D} \right)_{x_D=0} + T_D \left(\frac{d\bar{\bar{p}}_{2D}}{dx_D} \right)_{x_D=0} = \frac{2}{s_f} (\bar{\bar{p}}_{1D} - \bar{\bar{p}}_{2D})_{x_D=0} \quad (4.26)$$

We can further use this result to eliminate $\bar{\bar{p}}_{fD}$ from Equation 4.6. After some mathematical manipulation, we obtain

$$\begin{aligned} \frac{1}{\sigma_f^2 F_{CD}} \left[\left(\frac{d\bar{\bar{p}}_{1D}}{dx_D} \right)_{x_D=0} - T_D \left(\frac{d\bar{\bar{p}}_{2D}}{dx_D} \right)_{x_D=0} \right] + \mathcal{F} \left\{ p_{fD}^0(y_D) \right\} = \\ (\bar{\bar{p}}_{1D})_{x_D=0} - \frac{s_f}{2} \left(\frac{d\bar{\bar{p}}_{1D}}{dx_D} \right)_{x_D=0} \end{aligned} \quad (4.27)$$

Using Equation 4.14 and 4.15, we obtain the following relationships:

$$(\bar{\bar{p}}_{1D})_{x_D=0} = \frac{\pi e^{-\sigma}}{s\sigma} + B + \frac{\mathcal{L}_1}{2\sigma} \quad (4.28)$$

$$(\bar{\bar{p}}_{2D})_{x_D=0} = A + \frac{\mathcal{L}_2}{2\sigma_2} \quad (4.29)$$

$$\left(\frac{d\bar{p}_{1D}}{dx_D}\right)_{x_D=0} = \frac{\pi e^{-\sigma}}{s} - \sigma B + \frac{\mathcal{L}_1}{2} \quad (4.30)$$

$$\left(\frac{d\bar{p}_{2D}}{dx_D}\right)_{x_D=0} = \sigma_2 A - \frac{\mathcal{L}_2}{2} \quad (4.31)$$

where

$$\mathcal{L}_1 = \int_0^\infty e^{-\xi\sigma} \mathcal{F}\{p_{1D}^0(\xi, y_D)\} d\xi \quad (4.32)$$

$$\mathcal{L}_2 = \int_0^\infty e^{-\xi\sigma_2} \mathcal{F}\{p_{2D}^0(\xi, y_D)\} d\xi \quad (4.33)$$

Combining Equation 4.28—4.31 with Equation 4.26 and 4.27 yields the following system of linear equations with the integration constants A and B as the unknowns:

$$\frac{\pi e^{-\sigma}}{s} - \sigma B + \frac{\mathcal{L}_1}{2} + T_D \left(\sigma_2 A - \frac{\mathcal{L}_2}{2} \right) = \frac{2}{s_f} \left(\frac{\pi e^{-\sigma}}{s\sigma} + B + \frac{\mathcal{L}_1}{2\sigma} - A - \frac{\mathcal{L}_2}{2\sigma_2} \right) \quad (4.34)$$

$$\begin{aligned} \frac{\pi e^{-\sigma}}{s} - \sigma B + \frac{\mathcal{L}_1}{2} + T_D \left(\sigma_2 A - \frac{\mathcal{L}_2}{2} \right) + \mathcal{F}\{p_{fD}^0(y_D)\} = \\ F_{CD}\sigma_f^2 \left[\frac{\pi e^{-\sigma}}{s\sigma} + B + \frac{\mathcal{L}_1}{2\sigma} - \frac{s_f}{2} \left(\frac{\pi e^{-\sigma}}{s} - \sigma B + \frac{\mathcal{L}_1}{2} \right) \right] \end{aligned} \quad (4.35)$$

There are two important facts to take into account before solving the system of equations for A and B . First, recognize that $\mathcal{L}_2 = 0$ in Region 1 in the same way that $\mathcal{L}_1 = 0$ in Region 2. Second, $p_{fD}^0(y_D) = 0$ in both Regions 1 and 2 as fault flow only occurs at the interface $x_D = 0$. Keeping these conditions in hand, we obtain the solution to the system of equations:

$$A = \frac{e^{-\sigma}}{s} \frac{8\pi\alpha}{4\alpha[\alpha\sigma + T_D\sigma_2(\sigma + \alpha)] + F_{CD}\sigma_f^2(\sigma + 2\alpha)(T_D\sigma_2 + 2\alpha)}$$

$$+ \frac{1}{2} \int_0^\infty \frac{e^{-\xi\sigma_2}}{\sigma_2} \frac{4\alpha[-\alpha\sigma + T_D\sigma_2(\sigma + \alpha)] + F_{CD}\sigma_f^2(\sigma + 2\alpha)(T_D\sigma_2 - 2\alpha)}{4\alpha[\alpha\sigma + T_D\sigma_2(\sigma + \alpha)] + F_{CD}\sigma_f^2(\sigma + 2\alpha)(T_D\sigma_2 + 2\alpha)} \mathcal{F}\{p_{2D}^0\} d\xi \quad (4.36)$$

$$B = \frac{\pi e^{-\sigma}}{s\sigma} \frac{4\alpha[\alpha\sigma + T_D\sigma_2(\sigma - \alpha)] + F_{CD}\sigma_f^2(\sigma - 2\alpha)(T_D\sigma_2 + 2\alpha)}{4\alpha[\alpha\sigma + T_D\sigma_2(\sigma + \alpha)] + F_{CD}\sigma_f^2(\sigma + 2\alpha)(T_D\sigma_2 + 2\alpha)} \\ + \frac{1}{2} \int_0^\infty \frac{e^{-\xi\sigma}}{\sigma} \frac{4\alpha[\alpha\sigma + T_D\sigma_2(\sigma - \alpha)] + F_{CD}\sigma_f^2(\sigma - 2\alpha)(T_D\sigma_2 + 2\alpha)}{4\alpha[\alpha\sigma + T_D\sigma_2(\sigma + \alpha)] + F_{CD}\sigma_f^2(\sigma + 2\alpha)(T_D\sigma_2 + 2\alpha)} \mathcal{F}\{p_{1D}^0\} d\xi \quad (4.37)$$

$\alpha = s_f^{-1}$ is the dimensionless fault transmissibility (Equation B.11). $p_{1D}^0 \equiv p_{1D}^0(\xi, y_D)$ and $p_{2D}^0 \equiv p_{2D}^0(\xi, y_D)$. Replacing Equation 4.36 and 4.37 into 4.38 and 4.39, yields:

$$\bar{p}_{1D} = \frac{\pi e^{-|x_D-1|\sqrt{s+\omega^2}}}{s\sqrt{s+\omega^2}} + \frac{\pi e^{-(x_D+1)\sqrt{s+\omega^2}}}{s\sqrt{s+\omega^2}} \frac{T_DR_1(s, \omega) + \sqrt{\eta_D} [1 + F_{CD}W_1(s, \omega)]}{T_DR_0(s, \omega) + \sqrt{\eta_D} [1 + F_{CD}W_0(s, \omega)]} \\ + \frac{1}{2} \int_0^\infty \frac{e^{-(x_D+\xi)\sqrt{s+\omega^2}}}{\sqrt{s+\omega^2}} \frac{T_DR_1(s, \omega) + \sqrt{\eta_D} [1 + F_{CD}W_1(s, \omega)]}{T_DR_0(s, \omega) + \sqrt{\eta_D} [1 + F_{CD}W_0(s, \omega)]} \mathcal{F}\{p_{1D}^0(\xi, y_D)\} d\xi \\ + \frac{1}{2} \int_0^{x_D} \frac{e^{-(x_D-\xi)\sqrt{s+\omega^2}}}{\sqrt{s+\omega^2}} \mathcal{F}\{p_{1D}^0(\xi, y_D)\} d\xi \\ + \frac{1}{2} \int_{x_D}^\infty \frac{e^{-(\xi-x_D)\sqrt{s+\omega^2}}}{\sqrt{s+\omega^2}} \mathcal{F}\{p_{1D}^0(\xi, y_D)\} d\xi \quad (4.38)$$

$$\bar{p}_{2D} = \frac{e^{-\sqrt{s+\omega^2}} e^{-|x_D|\sqrt{\frac{s}{\eta_D} + \omega^2}}}{s} \frac{2\pi\alpha}{T_DR_0(s, \omega) + \sqrt{\eta_D} [1 + F_{CD}W_0(s, \omega)]} \\ + \frac{1}{2} \int_0^\infty \frac{e^{-(|x_D|+\xi)\sqrt{\frac{s}{\eta_D} + \omega^2}}}{\sqrt{\frac{s}{\eta_D} + \omega^2}} \frac{T_DR_0(s, \omega) - \sqrt{\eta_D} [1 - F_{CD}W_2(s, \omega)]}{T_DR_0(s, \omega) + \sqrt{\eta_D} [1 + F_{CD}W_2(s, \omega)]} \mathcal{F}\{p_{2D}^0(\xi, y_D)\} d\xi \\ + \frac{1}{2} \int_0^{|x_D|} \frac{e^{-(|x_D|-\xi)\sqrt{\frac{s}{\eta_D} + \omega^2}}}{\sqrt{\frac{s}{\eta_D} + \omega^2}} \mathcal{F}\{p_{2D}^0(\xi, y_D)\} d\xi \\ + \frac{1}{2} \int_{|x_D|}^\infty \frac{e^{-(\xi-|x_D|)\sqrt{\frac{s}{\eta_D} + \omega^2}}}{\sqrt{\frac{s}{\eta_D} + \omega^2}} \mathcal{F}\{p_{2D}^0(\xi, y_D)\} d\xi \quad (4.39)$$

where $R(s, \omega)$ and $W(s, \omega)$ are auxiliary functions in Laplace-Fourier domain, defined as follows:

$$R_0(s, \omega) = \left(s + \frac{1}{\sqrt{s + \omega^2}} \right) \sqrt{s + \eta_D \omega^2} \quad (4.40)$$

$$R_1(s, \omega) = \left(s - \frac{1}{\sqrt{s + \omega^2}} \right) \sqrt{s + \eta_D \omega^2} \quad (4.41)$$

$$W_0(s, \omega) = \frac{1}{4} \left(\frac{s}{\eta_{fD}} + \omega^2 \right) \left(s_f + \frac{2}{\sqrt{s + \omega^2}} \right) \left(s_f T_D \sqrt{\frac{s}{\eta_D} + \omega^2} + 2 \right) \quad (4.42)$$

$$W_1(s, \omega) = \frac{1}{4} \left(\frac{s}{\eta_{fD}} + \omega^2 \right) \left(s_f - \frac{2}{\sqrt{s + \omega^2}} \right) \left(s_f T_D \sqrt{\frac{s}{\eta_D} + \omega^2} + 2 \right) \quad (4.43)$$

$$W_2(s, \omega) = \frac{1}{4} \left(\frac{s}{\eta_{fD}} + \omega^2 \right) \left(s_f + \frac{2}{\sqrt{s + \omega^2}} \right) \left(s_f T_D \sqrt{\frac{s}{\eta_D} + \omega^2} - 2 \right) \quad (4.44)$$

Laplace-Fourier inversion of Equation 4.38 yields:

$$\begin{aligned} p_{1D} = & \pi \mathcal{F}^{-1} \mathcal{L}^{-1} \left\{ \frac{e^{-|x_D-1|\sqrt{s+\omega^2}}}{s\sqrt{s+\omega^2}} \right\} \\ & + \pi \mathcal{F}^{-1} \mathcal{L}^{-1} \left\{ \frac{e^{-(x_D+1)\sqrt{s+\omega^2}}}{s\sqrt{s+\omega^2}} \frac{T_D R_1(s, \omega) + \sqrt{\eta_D} [1 + F_{CD} W_1(s, \omega)]}{T_D R_0(s, \omega) + \sqrt{\eta_D} [1 + F_{CD} W_0(s, \omega)]} \right\} \\ & + \frac{1}{2\pi} \mathcal{F}^{-1} \mathcal{L}^{-1} \left\{ \int_0^\infty \frac{\pi e^{-(x_D+\xi)\sqrt{s+\omega^2}}}{\sqrt{s+\omega^2}} \frac{T_D R_1(s, \omega) + \sqrt{\eta_D} [1 + F_{CD} W_1(s, \omega)]}{T_D R_0(s, \omega) + \sqrt{\eta_D} [1 + F_{CD} W_0(s, \omega)]} \mathcal{F}\{p_{1D}^0(\xi, y_D)\} d\xi \right\} \\ & + \frac{1}{2} \mathcal{F}^{-1} \mathcal{L}^{-1} \left\{ \int_0^{x_D} \frac{e^{-(x_D-\xi)\sqrt{s+\omega^2}}}{\sqrt{s+\omega^2}} \mathcal{F}\{p_{1D}^0(\xi, y_D)\} d\xi \right\} \\ & + \frac{1}{2} \mathcal{F}^{-1} \mathcal{L}^{-1} \left\{ \int_{x_D}^\infty \frac{e^{-(\xi-x_D)\sqrt{s+\omega^2}}}{\sqrt{s+\omega^2}} \mathcal{F}\{p_{1D}^0(\xi, y_D)\} d\xi \right\} \end{aligned} \quad (4.45)$$

Moreover,

$$\begin{aligned}
& \mathcal{F}^{-1} \mathcal{L}^{-1} \left\{ \int_0^\infty \frac{\pi e^{-(x_D + \xi)\sqrt{s+\omega^2}}}{\sqrt{s+\omega^2}} \frac{T_D R_1(s, \omega) + \sqrt{\eta_D} [1 + F_{CD} W_1(s, \omega)]}{T_D R_0(s, \omega) + \sqrt{\eta_D} [1 + F_{CD} W_0(s, \omega)]} \mathcal{F}\{p_{1D}^0(\xi, y_D)\} d\xi \right\} = \\
& \int_0^\infty \int_{-\infty}^\infty \mathcal{F}^{-1} \mathcal{L}^{-1} \left\{ \int_0^\infty \frac{\pi e^{-(x_D + \xi)\sqrt{s+\omega^2}}}{\sqrt{s+\omega^2}} \frac{T_D R_1(s, \omega) + \sqrt{\eta_D} [1 + F_{CD} W_1(s, \omega)]}{T_D R_0(s, \omega) + \sqrt{\eta_D} [1 + F_{CD} W_0(s, \omega)]} \right\}_\nu p_{1D}^0(\xi, y_D - \nu) d\nu d\xi
\end{aligned} \tag{4.46}$$

$$\begin{aligned}
& \frac{1}{2} \mathcal{F}^{-1} \mathcal{L}^{-1} \left\{ \int_0^{x_D} \frac{e^{-(x_D - \xi)\sqrt{s+\omega^2}}}{\sqrt{s+\omega^2}} \mathcal{F}\{p_{1D}^0(\xi, y_D)\} d\xi + \int_{x_D}^\infty \frac{e^{-(\xi - x_D)\sqrt{s+\omega^2}}}{\sqrt{s+\omega^2}} \mathcal{F}\{p_{1D}^0(\xi, y_D)\} d\xi \right\} = \\
& \frac{1}{4\pi t'_D} \int_0^\infty \int_{-\infty}^\infty e^{-\frac{(x_D - \xi)^2 + (y_D - \nu)^2}{4t'_D}} p_{1D}^0(\xi, \nu) d\nu d\xi \tag{4.47}
\end{aligned}$$

Additionally, we make use of the following Laplace-Fourier inverse transform pair (Molina and Zeidouni, 2018):

$$\pi \mathcal{F}^{-1} \mathcal{L}^{-1} \left\{ \frac{e^{-|x_D - 1|\sqrt{s+\omega^2}}}{s\sqrt{s+\omega^2}} \right\} = -\frac{1}{2} \text{Ei} \left(-\frac{(x_D - 1)^2 + y_D^2}{4t'_D} \right) \tag{4.48}$$

Replacing Equation 4.47 and 4.48 into 4.45 while applying the inverse Laplace-Fourier transform identity from Equation 4.9, gives

$$\begin{aligned}
p_{1D} &= -\frac{1}{2} \text{Ei} \left(-\frac{(x_D - 1)^2 + y_D^2}{4t'_D} \right) \\
&+ \int_0^\infty \cos(\omega y_D) \mathcal{L}^{-1} \left\{ \frac{e^{-(x_D + 1)\sqrt{s+\omega^2}}}{s\sqrt{s+\omega^2}} \frac{T_D R_1(s, \omega) + \sqrt{\eta_D} [1 + F_{CD} W_1(s, \omega)]}{T_D R_0(s, \omega) + \sqrt{\eta_D} [1 + F_{CD} W_0(s, \omega)]} \right\} d\omega \\
&+ \frac{1}{2\pi} \int_0^\infty \int_0^\infty \int_{-\infty}^\infty \cos(\omega \nu) \mathcal{L}^{-1} \left\{ \frac{e^{-(x_D + 1)\sqrt{s+\omega^2}}}{s\sqrt{s+\omega^2}} \frac{T_D R_1(s, \omega) + \sqrt{\eta_D} [1 + F_{CD} W_1(s, \omega)]}{T_D R_0(s, \omega) + \sqrt{\eta_D} [1 + F_{CD} W_0(s, \omega)]} \right\}_\nu \\
&\times p_{1D}^0(\xi, y_D - \nu) d\nu d\xi d\omega + \frac{1}{4\pi t'_D} \int_0^\infty \int_{-\infty}^\infty e^{-\frac{(x_D - \xi)^2 + (y_D - \nu)^2}{4t'_D}} p_{1D}^0(\xi, \nu) d\nu d\xi
\end{aligned} \tag{4.49}$$

The first term in the right-hand side of Equation 4.49 corresponds to the infinite-acting

reservoir solution. The second term represents the additional pressure gain (or loss, if the well is an injector) due to the presence of a leaky fault. The multi-dimensional indefinite integrals arising during the inversion process are referred to as *convolution integrals*. These integrals are estimated using a combination of the Stehfest algorithm (Stehfest, 1970) for the inverse Laplace transform and a robust numerical integration strategy built in Mathematica®. Nonetheless, recognize that the Laplace inversion algorithm generates N summation terms, which will produce $N - 1$ additional indefinite integrals, making the estimation of p_{1D} computationally expensive, especially when $t'_D \approx 0$.

Equation 4.49 shows that fluid transport capacity of the fault upon fault reactivation is simultaneously controlled by s_f and F_{CD} , which would individually set the amount of flux flowing across and along the fault and finally into the reservoir. Note that the across-fault flux solution for a composite reservoir is yielded from Equation 4.49 if along-fault permeability enhancement is neglected (i.e. $F_{CD} = 0$).

In this regard, Molina and Zeidouni (2018) proved that, for an initially-sealing fault in an infinite reservoir with $M = h_D = \eta_D = 1$ and $F_{CD} = 0$, Equation 4.49 reduces to

$$\begin{aligned}
p_{1D} = & -\frac{1}{2} \text{Ei} \left(-\frac{(x_D - 1)^2 + y_D^2}{4t'_D} \right) - \frac{1}{2} \text{Ei} \left(-\frac{(x_D + 1)^2 + y_D^2}{4t'_D} \right) \\
& - \sqrt{\pi} \alpha e^{2\alpha(x_D+1)} \int_0^{t'_D} e^{4\alpha^2 - \frac{y_D^2}{4\tau}} \text{erfc} \left(\frac{x_D + 1}{2\sqrt{\tau}} + 2\alpha\sqrt{\tau} \right) \frac{d\tau}{\sqrt{\tau}} \\
& + \frac{1}{4\pi t'_D} \int_0^\infty \int_{-\infty}^\infty \left(e^{-\frac{(x_D - \xi)^2 + (y_D - \nu)^2}{4t'_D}} + e^{-\frac{(x_D + \xi)^2 + (y_D - \nu)^2}{4t'_D}} \right) \left\{ -\frac{1}{2} \text{Ei} \left(-\frac{(\xi - 1)^2 + \nu^2}{4t_{sD}} \right) \right. \\
& - \frac{1}{2} \text{Ei} \left(-\frac{(\xi + 1)^2 + \nu^2}{4t_{sD}} \right) \left. \right\} d\nu d\xi - \frac{\alpha e^{4\alpha^2 t'_D}}{2\sqrt{\pi t'_D}} \int_0^\infty \int_{-\infty}^\infty e^{2\alpha(x_D + \xi) - \frac{(y_D - \nu)^2}{4t'_D}} \text{erfc} \left(\frac{x_D + \xi}{2\sqrt{t'_D}} + 2\alpha\sqrt{t'_D} \right) \\
& \times \left\{ -\frac{1}{2} \text{Ei} \left(-\frac{(\xi - 1)^2 + \nu^2}{4t_{sD}} \right) - \frac{1}{2} \text{Ei} \left(-\frac{(\xi + 1)^2 + \nu^2}{4t_{sD}} \right) \right\} d\nu d\xi
\end{aligned} \tag{4.50}$$

In general, $p_{1D}^0(x_D, y_D)$ in Equation 4.49 refers to any kind of dimensionless pressure distribution present in Region 1 at the onset of fault reactivation, as discussed in Section 4.2 (see Figure 4.2). This enables the use of other production scenarios before fault

reactivation with the analytical model so long as pressure distributions for Regions 1 and 2 are explicitly given at $t_D = t_{sD}$.

4.5.2 Late-time Asymptotic Pressure Behavior in Region 1

Molina and Zeidouni (2018) used their infinite-acting compartmentalized reservoir model to prove that, while convolution integrals strongly influence pressure behavior shortly after the onset of fault reactivation, their effect on late-time behavior (i.e., $t'_D \approx t_D$) is negligible. Based on this observation, we may infer that the dominance of the convolution integrals in Equation 4.49 will alike vanish as $t_D \gg t_{sD}$, so that late-time behavior will be exclusively dominated by the first two terms on the right-hand side of Equation 4.49. This observation allows us to conclude that:

$$p_{1D} \sim -\frac{1}{2} \text{Ei} \left(-\frac{(x_D - 1)^2 + y_D^2}{4t_D} \right) + \int_0^\infty \cos(\omega y_D) \mathcal{L}^{-1} \left\{ \frac{e^{-(x_D+1)\sqrt{s+\omega^2}} T_D R_1(s, \omega) + \sqrt{\eta_D} [1 + F_{CD} W_1(s, \omega)]}{s \sqrt{s + \omega^2} T_D R_0(s, \omega) + \sqrt{\eta_D} [1 + F_{CD} W_0(s, \omega)]} \right\} d\omega \quad (4.51)$$

The expression above is the same analytical solution given by Rahman et al. (2003) to the problem of an initially across-along leaky fault. This result indicates that the fault will reach a late-time equilibrium state with the response of an initially along-lateral leaky fault. Therefore, we can use Equation 4.51 to history-match late time data.

4.5.3 Analytical Solution Before Fault Reactivation ($0 \leq t \leq t_s$)

There are two possible scenarios for fluid flow near the fault before fault reactivation: (1) fault is initially sealing and (2) fault is initially across-along leaky.

On the one hand, the fault acts as a barrier to flow since the beginning of production until the onset of fault permeability enhancement ($0 \leq t_D \leq t_{sD}$) when it is initially sealing. During this period, the image wells solution applies (cf. Stewart, 2011; Spivey and Lee, 2013). Because the fault is impermeable, $\alpha = 0$ or $s_f \rightarrow \infty$, thus p_{1D}^0 is given by

$$p_{1D}(x_D, y_D) = -\frac{1}{2} \text{Ei} \left(-\frac{(x_D - 1)^2 + y_D^2}{4t'_D} \right) - \frac{1}{2} \text{Ei} \left(-\frac{(x_D + 1)^2 + y_D^2}{4t'_D} \right) \quad (4.52)$$

for $0 \leq t_D \leq t_{sD}$. At the onset of fault slip $t_D = t_{sD}$, the current dimensionless pressure distribution in Region 1 is given by

$$p_{1D}^0(x_D, y_D) = -\frac{1}{2} \text{Ei} \left(-\frac{(x_D - 1)^2 + y_D^2}{4t_{sD}} \right) - \frac{1}{2} \text{Ei} \left(-\frac{(x_D + 1)^2 + y_D^2}{4t_{sD}} \right) \quad (4.53)$$

This result can be analytically derived from Equation 4.49 as well. Let us set $t_{sD} = 0$, $p_{1D}^0 = 0$ and $T_D = F_{CD} = 0$, equivalent to $s_f \rightarrow \infty$, so that Equation 4.49 becomes

$$p_{1D} = -\frac{1}{2} \text{Ei} \left(-\frac{(x_D - 1)^2 + y_D^2}{4t_D} \right) + \pi \mathcal{F}^{-1} \mathcal{L}^{-1} \left\{ \frac{e^{-(x_D+1)\sqrt{s+\omega^2}}}{s\sqrt{s+\omega^2}} \right\} \quad (4.54)$$

Replacing Equation 4.16 and 4.17 into the expression above yields

$$p_{1D} = -\frac{1}{2} \text{Ei} \left(-\frac{(x_D - 1)^2 + y_D^2}{4t_D} \right) + \frac{\pi}{2\sqrt{\pi}} \int_0^{t_D} \left(\frac{e^{-\frac{y_D^2}{4\tau}}}{\sqrt{\tau}} \right) \left(\frac{e^{-\frac{(x_D+1)^2}{4\tau}}}{\sqrt{\pi\tau}} \right) d\tau \quad (4.55)$$

Moreover,

$$p_{1D} = -\frac{1}{2} \text{Ei} \left(-\frac{(x_D - 1)^2 + y_D^2}{4t_D} \right) + \frac{1}{2} \int_0^{t_D} \frac{e^{-\frac{(x_D+1)^2 + y_D^2}{4\tau}}}{\tau} d\tau \quad (4.56)$$

The integral on the right-hand side is the definition of the exponential integral function (see Equation 4.48). Evaluating the resulting expression at the dimensionless onset of fault slip $t_D = t_{sD}$ yields

$$p_{1D}^0 = -\frac{1}{2} \text{Ei} \left(-\frac{(x_D - 1)^2 + y_D^2}{4t_{sD}} \right) - \frac{1}{2} \text{Ei} \left(-\frac{(x_D + 1)^2 + y_D^2}{4t_{sD}} \right) \quad (4.57)$$

which coincides with the result in Equation 4.53.

We will consider in this work that the fault is initially sealing and infinite-acting reservoir conditions are ensued before fault reactivation. Therefore, we replace Equation 4.53 into 4.49 to examine the pressure response in the reservoir to fault reactivation under the assumption that the fault was initially sealing.

On the other hand, if the fault was across-lateral leaky before fault reactivation, dimensionless pressure response in Region 1 is given by:

$$p_{1D} = -\frac{1}{2} \text{Ei} \left(-\frac{(x_D - 1)^2 + y_D^2}{4t_D} \right) + \int_0^\infty \cos(\omega y_D) \mathcal{L}^{-1} \left\{ \frac{e^{-(x_D+1)\sqrt{s+\omega^2}} T_D R_{1i}(s, \omega) + \sqrt{\eta_D} [1 + F_{CD} W_{1i}(s, \omega)]}{s \sqrt{s + \omega^2} T_D R_{0i}(s, \omega) + \sqrt{\eta_D} [1 + F_{CD} W_{0i}(s, \omega)]} \right\} d\omega \quad (4.58)$$

where the definitions of $R_i(s, \omega)$ and $W_i(s, \omega)$ are the same as $R(s, \omega)$ and $W(s, \omega)$, the difference being that the R_i and W_i use s_{fi} (initial fault skin) instead of s_f .

4.6. Pressure Transient Analysis of Fault Reactivation

Analytical solutions derived in this study are compared against analytical faulted reservoir models from the literature. The objective of this section is to observe dimensionless pressure and pressure-derivative responses to sudden changes in anisotropic fault permeability for an initially sealing fault. We investigate the transitional flow regime originating at the onset of fault reactivation and that lasts until pressure reaches the late-time equilibrium condition dictated by the pressure behavior of an initially-leaky fault. This transitional flow regime is mathematically governed by convolution integrals and its influence on transient pressure response depends on the magnitude of anisotropic fault permeability enhancement. Late-time pressure behavior is examined herein to check the validity of the proposed late-time asymptotic solutions. Results are presented as type-curves for identification of sudden fault permeability changes and associated transitional flow regime.

To examine dimensionless pressure behavior at the wellbore p_{wD} before and after fault reactivation, we substitute $x_D = x_{wD} = 1 - r_w/b$ and $y_D = 0$ into Equation 4.53 for

$0 \leq t_D \leq t_{sD}$ and Equation 4.49 for $t_D > t_{sD}$ or $t'_D \geq 0$. Wellbore radius and distance to the fault are $r_w = 0.25$ ft and $b = 500$ ft, respectively, resulting in $x_{wD} = 0.9995$. In addition, $k_1 = 10$ md, $w_f = 1$ ft, $\phi_f = \phi_1 = \phi_2$. The storativity ratio is equal in both reservoirs hence $F_s = 1$ and $\eta_D = M$ and $\eta_{fD} = 500F_{CD}$. Initial pressure is constant, isotropic and homogeneous across the entire flow domain.

Before fault reactivation, the log pressure-derivative $dp_{wD}/d \ln t_D = p'_{wD}$ is given by:

$$p'_{wD} = \frac{1}{2} \left(e^{-\frac{(x_{wD}-1)^2}{4t_D}} + e^{-\frac{(x_{wD}+1)^2}{4t_D}} \right) \quad (4.59)$$

After fault reactivation, $dp_{wD}/d \ln t_D$ must be approximated numerically using Equation 4.49 along with a finite centered difference scheme:

$$p'_{wD} \approx \frac{t_D}{2\Delta t_D} [p_{wD}(t_D - t_{sD} + \Delta t_D) - p_{wD}(t_D - t_{sD} - \Delta t_D)] \quad (4.60)$$

Δt_D is a small dimensionless timestep ($\Delta t_D \ll t_D$). Estimation of p_{wD} and $dp_{wD}/d \ln t_D$ is computationally expensive, especially when $t_D \approx t_{sD}$ or $t'_D \approx 0$. This is primarily due to the number of computations required to calculate the value of the convolution integrals. Nonetheless, late-time asymptotic solutions can be used at the end of the transitional flow between sealing and conductive fault regimes.

4.6.1 Across-Fault Leakage in an Infinite Reservoir with an Initially Sealing Fault

Figure 4.4 shows the dimensionless pressure response to a sudden enhancement in across-fault permeability in an infinite, isotropic and homogeneous reservoir ($h_D = \eta_D = F_s = M = 1$) with an initially-sealing fault and no along-fault flow capacity ($F_{CD} = 0$). Fault becomes linear leaky at $t_{sD} = 1, 10$ and 100 with $s_f = 0.1, 1, 10, 100$ and 1000 . Figure 4.6 presents the resulting type curves for this case. Transient response to an initially linear leaky fault in an infinite reservoir (Yaxley, 1987) is also shown in Figure 4.4 to 4.6.

According to Figure 4.4, it would be problematic to diagnose whether the fault was initially dormant or linear leaky if $t_{sD} \leq 1$. This is because the difference in pressure response between a sealing and linear leaky fault is virtually indiscernible if $t_{sD} \leq 1$. Be aware that $t_{sD} \leq 1$ not only relates to early-time onset of fault permeability alteration

but also to low reservoir diffusivity and/or large separation between the well and sealing boundary. Nevertheless, dimensionless pressure response clearly departs from the sealing fault solution when $t_{sD} = 10$ and $s_f \leq 10$ and $t_{sD} = 100$ and $s_f \leq 100$, exhibiting a drop in dimensionless pressure.

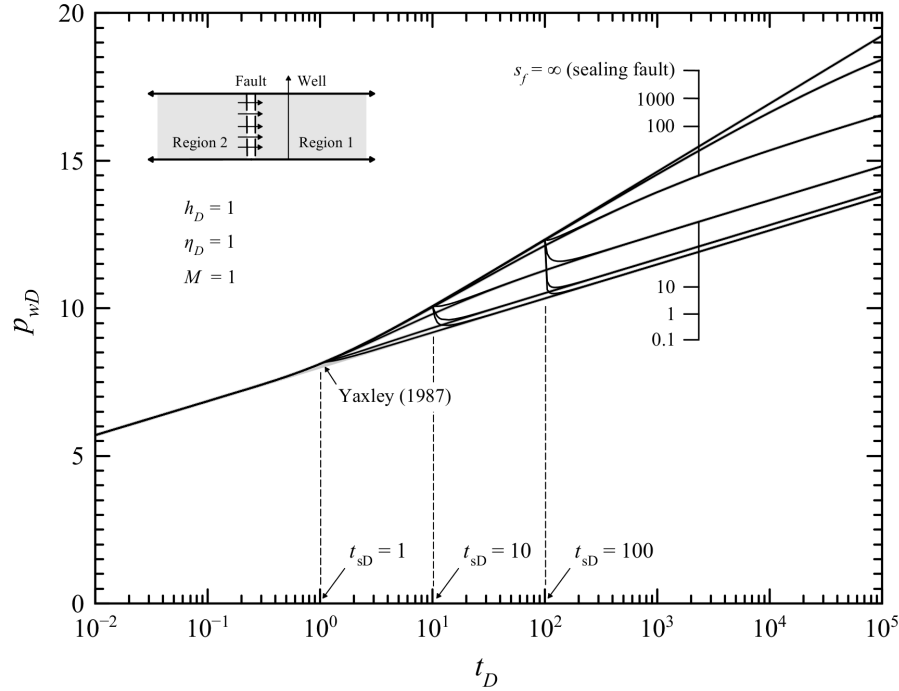
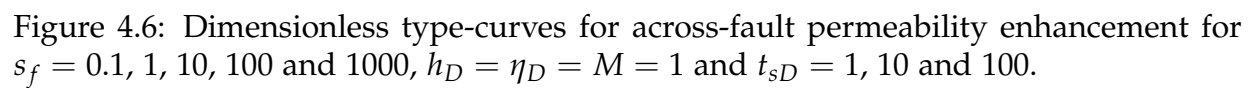
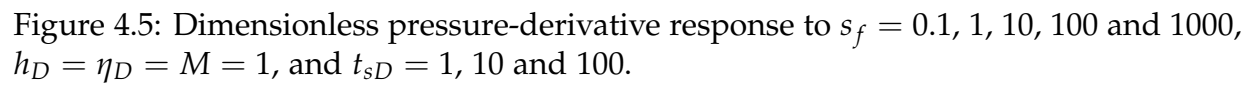


Figure 4.4: Dimensionless pressure response to a sudden change in across-fault permeability for $s_f = 0.1, 1, 10, 100$ and 1000 , $h_D = \eta_D = M = 1$, and $t_{sD} = 1, 10$ and 100 .

In contrast, Figure 4.5 suggests that pressure-derivative response is more sensitive to changes in fault permeability and its signature response depends on the magnitude of the permeability enhancement. Note that the pressure-derivative sharply drops at $t_D = t_{sD}$ becoming negative when s_f is small and $t_{sD} > 1$, then it rebounds towards the response of an initially leaky fault with finite fault skin. All pressure-derivative stems undergo such transitional flow regime which last for about one log-cycle before attaining late-time equilibrium. At late time, pressure-derivative stems reach the second infinite-acting radial flow regime ($t_D p'_{wD} = 0.5$).



In general, late-time pressure and pressure-derivative response from Figure 4.5 coincides with Figure 8 from Yaxley (1987) and Figure 6 from Ambastha et al. (1989). Pressure-derivative behavior from Figure 4.5 coincides with Figure 9 from Yaxley (1987). Type-curves for the compartmentalized reservoir configuration under discussion are presented in Figure 4.6.

4.6.2 Across-Fault Leakage in a Composite Reservoir with an Initially Sealing Fault

Dimensionless pressure response to across-fault permeability enhancement in a composite reservoir is presented in Figure 4.7. In this case, a segmenting fault separates two semi-infinite isotropic and homogeneous reservoirs with equal thickness, porosity and total compressibility ($h_D = F_s = 1$) but different permeability, so that $M = \eta_D \equiv k_2/k_1 = 0.01, 0.1, 1$ and 10 . Figure 4.7 presents the type curves corresponding to this Case Study. Transient response for a linear leaky fault in a composite reservoir with negligible fault skin (Bixel et al., 1963) is added to Figure 4.7 to 4.9.

On the one hand, alike the previous Case Study, the effect of across-fault permeability enhancement on dimensionless pressure response, represented as a sudden removal of across-fault skin ($s_f \rightarrow 0$), is trivial when $t_{sD} \leq 1$. This is because the difference in pressure response between a sealing and leaky fault is nearly equal during that period. On the contrary, pressure derivative exhibits a strong response to anisotropic fault permeability alteration for $t_{sD} \leq 1$ when $M \geq 0.01$ (Figure 4.7). Dimensionless pressure behavior, on the other hand, notably departs from the sealing fault solution when $t_{sD} \geq 10$ and $M \geq 0.01$.

According to Figure 4.8, the signature dimensionless pressure-derivative response to a sudden enhancement in across-fault permeability is unambiguous for $t_{sD} \geq 10$, regardless of the permeability contrast between reservoirs. Intriguingly, a surge in pressure-derivative response occurs when $t_{sD} = 100$ and $M \leq 0.01$, which may indicate that the pressure front "hits a wall" once it sees a low-mobility barrier after the fault, much like pressure-drawdown can no longer travel at the same speed across Region 2 due to the marked contrast in permeability.

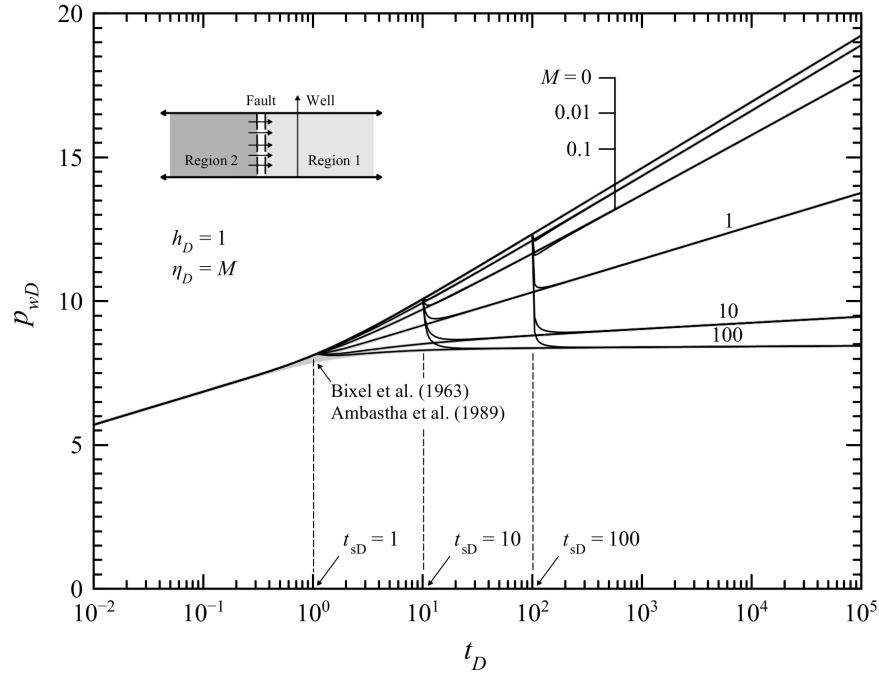


Figure 4.7: Dimensionless pressure response to $s_f = 0$ for $h_D = 1$, $M = \eta_D = 0, 0.01, 0.1, 1$ and 10 , and $t_{sD} = 1, 10$ and 100 .

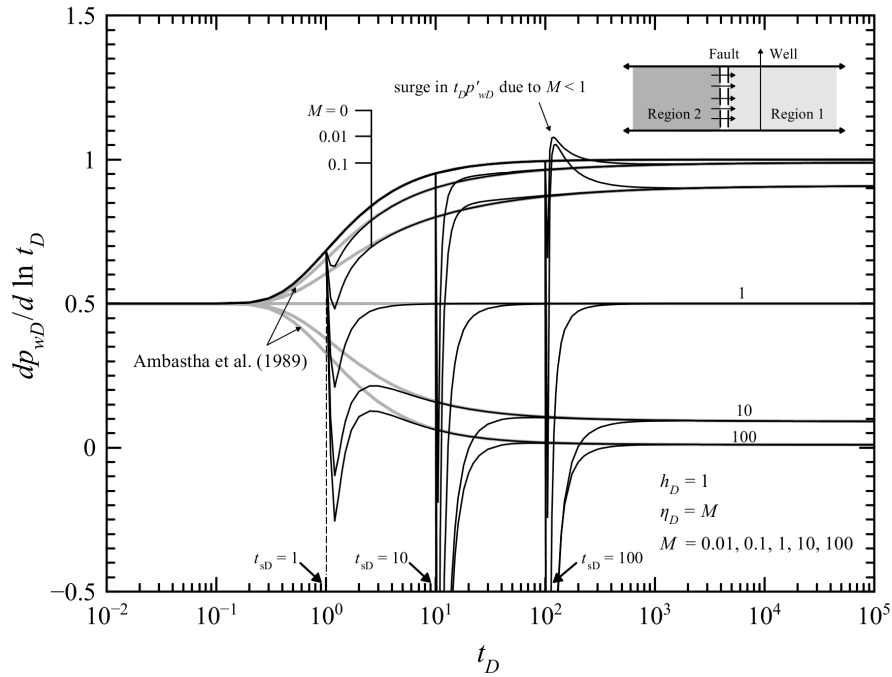


Figure 4.8: Dimensionless pressure derivative response to $M = \eta_D = 0.01, 0.1, 1, 10$ and 100 for $h_D = 1$, and $t_{sD} = 1, 10$ and 100 .

Overall, the stabilization process observed previously in Figure 4.5, i.e. transitional flow regime which begins at $t_D = t_{sD}$ and lasts for nearly one log-cycle, followed by a late-time trend to achieve equilibrium with the response of a linear leaky fault in a composite reservoir, also takes place in this Case Study. It is worthwhile to mention that pressure-derivative stems tend to attain radial flow stabilization at $1/(M + 1)$. Figure 4.8 exhibits a similar behavior to Figure 5 from Ambastha et al. (1989) and Figure 7.35 from Spivey and Lee (2013). Type-curves for this fault reactivation scenario are presented in Figure 4.9.

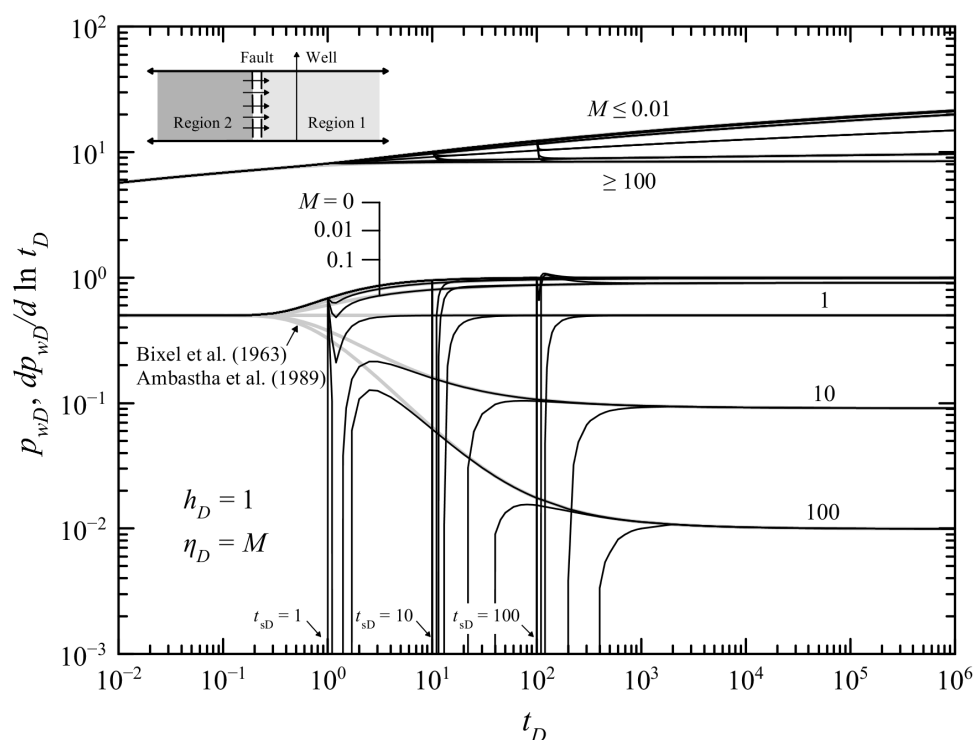


Figure 4.9: Dimensionless type-curves for across-fault permeability enhancement for $h_D = 1$, $M = \eta_D = 0.01, 0.1, 1, 10$ and 100 for $t_{sD} = 1, 10$ and 100 .

4.6.3 Simultaneous Across-Along Fault Leakage in an Infinite Reservoir with an Initially Sealing Fault

Figure 4.10 depicts the dimensionless pressure response to a sudden across-along-fault permeability enhancement in an infinite, isotropic and homogeneous reservoir with an initially dormant fault. Anisotropic fault permeability enhancement is modeled as a sudden, simultaneous change in dimensionless fault conductivity ($F_{CD} = 1, 10, 100, 1000$ and 10000) and across-fault skin, which is assumed negligible after fault

reactivation ($s_f = 0$), occurring at different dimensionless onset times ($t_{sD} = 1, 10$ and 100). Figure 4.11 presents the type curves corresponding to this flow scenario. Rahman et al. (2003) solution is included for reference in Figure 4.10 and 4.11. Type curves for this fault reactivation scenario are presented in Figure 4.12.

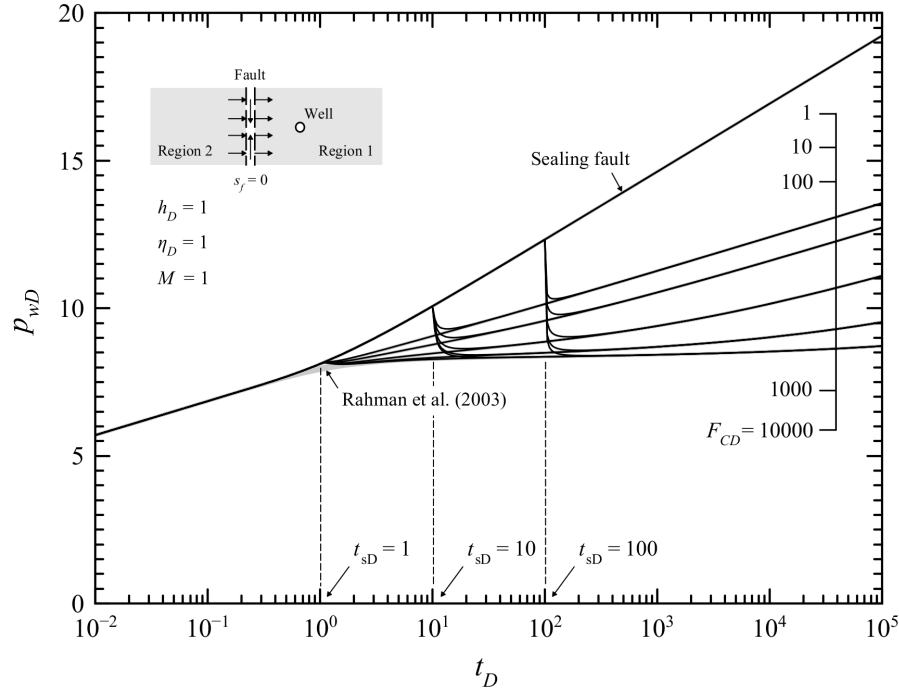


Figure 4.10: Dimensionless type curves for along-across-fault permeability enhancement for $h_D = 1$, $s_f = 0$ and $M = \eta_D = 0.01, 0.1, 1, 10$ and 100 for $t_{sD} = 1, 10$ and 100 .

Similar to previous case studies, the signature dimensionless pressure response to a step-wise change in anisotropic fault permeability would be hardly discernible if $t_{sD} \leq 1$. Again, a relatively low value of t_{sD} may be related to early-time occurrence of fault permeability alteration, low diffusivity in the reservoir and/or large separation between the well and sealing fault. Reduction in dimensionless pressure at $t_D = t_{sD}$ for $t_{sD} = 10$ and 100 is more drastic than in the previous case studies, even for a relatively low along-fault permeability enhancement ($F_{CD} = 1$), because fault permeability alteration occurs in two directions, enabling a faster pressure relief across the fault and reservoir. In fact, under certain conditions, well-test response when a sufficient large F_{CD} is present can be interpreted as pressure support (i.e. constant-pressure boundary). This is also the case for a composite reservoir with $M \geq 100$ (Spivey and Lee, 2013).

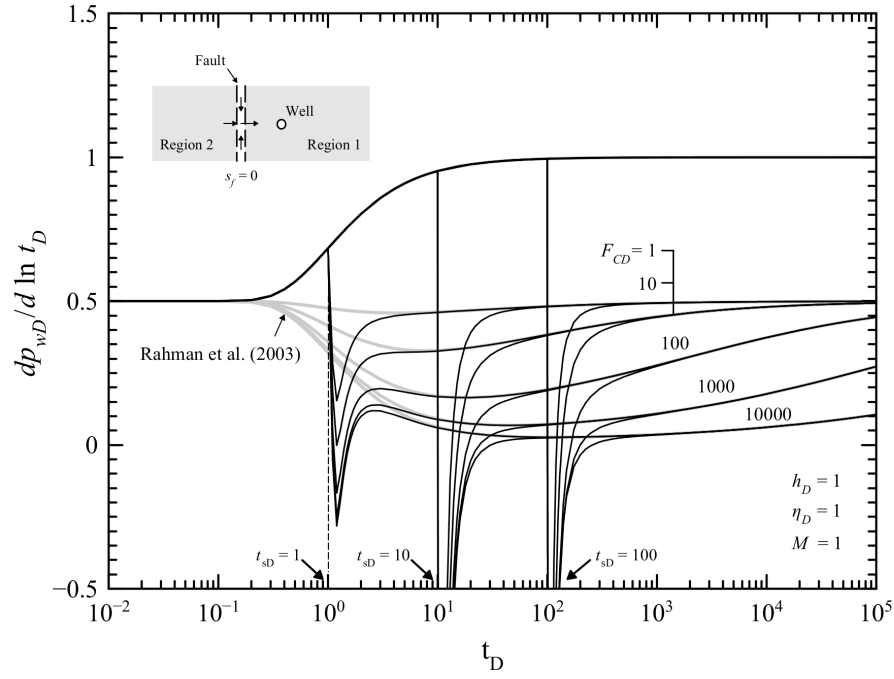


Figure 4.11: Dimensionless pressure-derivative response to along-across-fault permeability enhancement for $h_D = 1$, $s_f = 0$ and $M = \eta_D = 1$ for $t_{sD} = 1, 10$ and 100 .

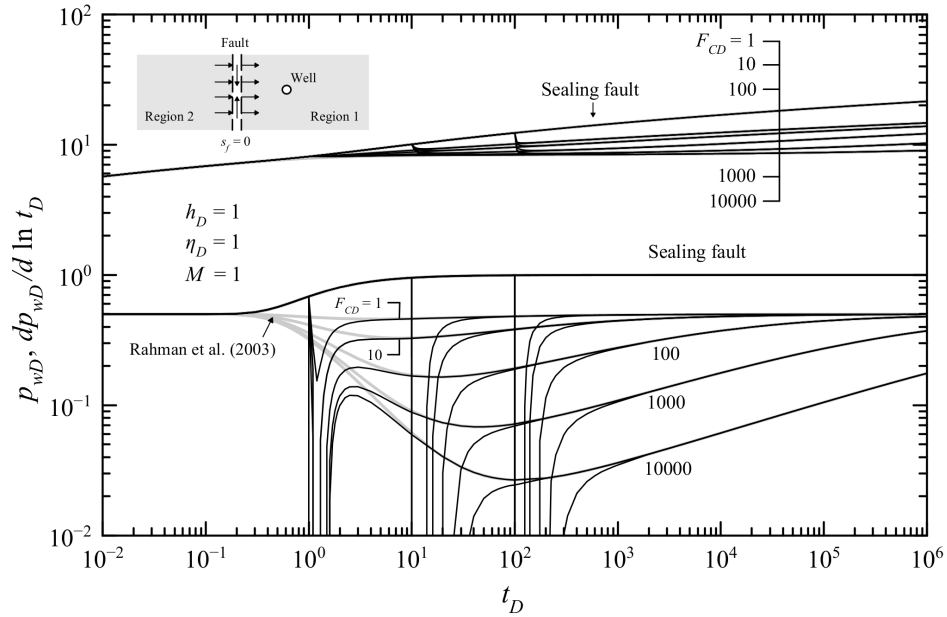


Figure 4.12: Dimensionless type curves for simultaneous along-across-fault permeability enhancement with $s_f = 0$, $h_D = 1$, $M = \eta_D = 1$ for $t_{sD} = 1, 10$ and 100 .

All pressure-derivative stems in Figure 4.11 exhibit a strong response to anisotropic fault permeability enhancement and follow the same stabilization process discussed earlier, i.e. rapid drop in pressure-derivative at $t_D = t_{sD}$ followed by a transitional flow regime that lasts for about one log-cycle until it matches the initially linear-lateral leaky fault behavior. As an important remark, Figure 4.10 and 4.11 are in excellent agreement with Figures 7 and 8 from Rahman et al. (2003).

4.7. Fault Permeability Characterization after Fault Reactivation

Figure 4.13 illustrates type curves for simultaneous effect of across and along-fault permeability alteration for $x_{wD} = 0.9995$, $y_{wD} = 0$, $k_1 = k_2 = 10$ md, $w_f = 1$ ft, $\phi_f = \phi_1 = \phi_2$ and $F_s = 1$ for various combinations of s_f and F_{CD} occurring at $t_{sD} = 10$. Type curves were generated by fixing $s_f = 1, 100$ and 10000 while varying F_{CD} from 1 to 10000. The objective of this analysis is to characterize s_f and F_{CD} for an initially-sealing fault that becomes leaky upon fault reactivation. Analytical solutions for a purely linear leaky fault with no along-fault flow ($F_{CD} = 0$ and $1 < s_f < 10000$) (dashed gray lines) and a lateral leaky fault without fault skin ($s_f = 0$ and $1 \leq F_{CD} \leq 10000$) (solid gray lines) are presented along the type-curves.

Nonetheless, notice from Figure 4.13 that there may be instances where s_f and F_{CD} cannot be uniquely determined. Realize that the lower s_f and the higher F_{CD} the more difficult to estimate s_f . Conversely, the estimation of F_{CD} is straightforward in this case.

As an example, consider the type-curves corresponding to $s_f = 1$. There, one can see that s_f cannot be uniquely determined regardless of the value of F_{CD} . On the contrary, the higher s_f and the lower F_{CD} the easier to characterize s_f however the more difficult to estimate F_{CD} . For instance, consider the type-curves for $s_f = 10000$ and realize that s_f can be uniquely estimated regardless of F_{CD} whereas F_{CD} itself cannot be determined.

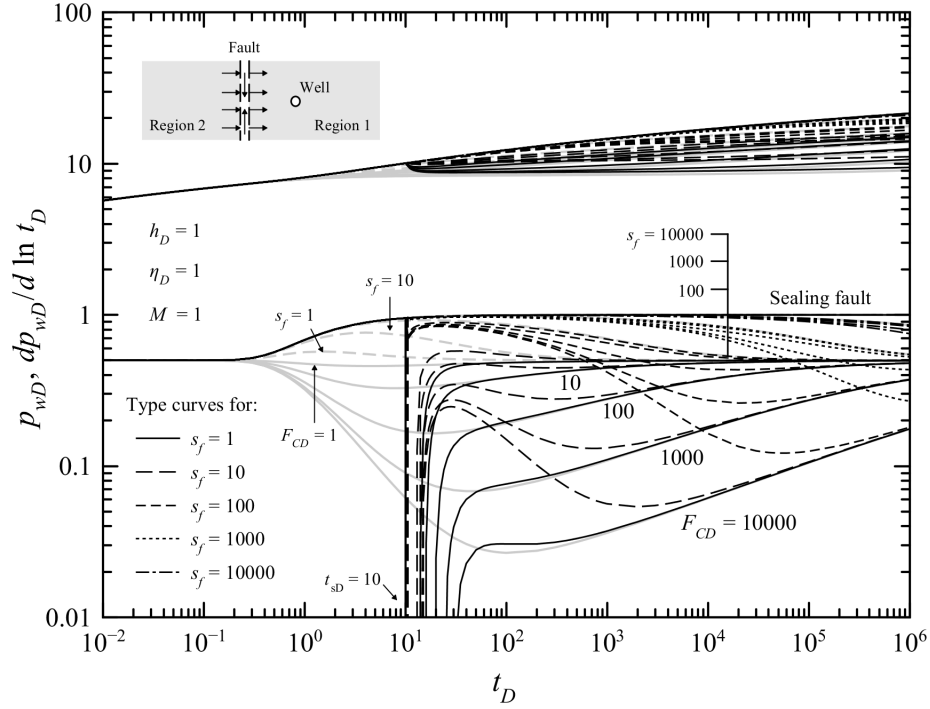


Figure 4.13: Type-curves for simultaneous across-along fault permeability enhancement. Gray dashed lines correspond to the partially-communicating fault solution for $s_f = 1, 100$ and 10000 with no along-fault flow ($F_{CD} = 0$) whereas solid gray lines correspond to along-fault flow with no fault skin for $1 \leq F_{CD} \leq 10000$.

4.8. Numerical Validation Examples

We study pressure and pressure-derivative responses to fault reactivation using a numerical model of a compartmentalized reservoir with an initially sealing fault undergoing permeability enhancement at some point after production had started ($t = t_s$). Formation layers are homogeneous and isotropic. Initial reservoir pressure is $p_i = 2000$ psia. Areal extension of the simulation domain is sufficient to sustain infinite-acting flow for approximately 150 days beyond which boundary effects would influence pressure and pressure-derivative responses. Fault width is $w_f = 1$ ft and $\phi_f = \phi_1$ and $(c_t)_f = (c_t)_1$. Reservoir fluid is slightly compressible fluid with $B = 1$ rb/STB and $\mu = 1$ cP. Well is located 500 ft away from the fault and flows at a constant rate of 100 STB/D. We examine pressure-transient behavior to $t_s = 5, 10, 30$ and 60 days. Reservoir properties are $k_1 = 10$ md, $\phi_1 = 0.1$, and $(c_t)_1 = 10^{-6} \text{ psi}^{-1}$.

For this analysis, $s_f = 0.02/k_f$, which suggests that small changes in across-fault per-

meability would lead to large changes in across-fault skin. Moreover, across-fault permeability changes from $k_f = 0$ md to 0.002 md, resulting in $s_f = 10$ at $t = t_s$ at the onset of fault reactivation. Likewise, $F_{CD} = k_{fl}/5000$. Recognize that, contrary to s_f , relatively large along-fault permeability values are necessary to obtain representative values for F_{CD} (e.g. $F_{CD} > 0.1$). Henceforth, we use k_{fl} as a sensitivity parameter ranging from 500 md to 500 D thus $F_{CD} = 0.1, 1, 10$ and 100.

4.8.1 Case Study 1: Fault Reactivation in an Infinite Reservoir

This case study relates to an infinite isotropic and homogeneous reservoir segmented by a sealing fault. Fault blocks (i.e. Regions 1 and 2) have equal porosity ($\phi_1 = \phi_2 = 0.1$), permeability ($k_1 = k_2 = 10$ md) and formation thickness ($h_1 = h_2 = 20$ ft). Thus, $M = h_D = 1$ and $F_s = 1$. Figure 4.14 and 4.15 present the rate-normalized diagnostic plots resulting from the analytical and numerical modeling. It is made evident from the diagnostic plots that both solutions are in excellent agreement. More importantly, numerical results confirm that bottomhole pressure will drop in response to a sudden change in across-along fault permeability. Boundary-dominated flow effects are detected from Figure 4.15 after 150 days. In despite of boundary effects, enhanced fault properties can still be characterized using data corresponding to the transitional flow period between the onset of fault reactivation and final equilibrium state (i.e. $t_s \leq t < 100$ days). Finally, numerical simulation results show that the transitional flow regime lasts between 1 and 1-1/2 log cycles, just as predicted by the analytical model.

4.8.2 Case Study 2: Fault Reactivation in a Composite Reservoir

In this case, $k_2 = 50$ md, $h_2 = 10$ ft while $k_1 = 10$ md and $h_1 = 20$ ft, hence $M = 5$ and $h_D = 0.5$. $\phi_1 = \phi_2 = 0.1$ thus $F_s = 1$. Figure 4.16 shows a comparison of RNP given by the analytical and numerical models. From this result, we conclude that the analytical model is in excellent agreement with numerical data. Similarly, RNP' plot in Figure 4.17 shows that the analytical and numerical models are essentially the same. Unlike the previous case study, boundary effects are less evident. Still, characterization of the fault can be accomplished by history-matching transient pressure data occurring during the transitional flow regime ($t_s \leq t < 100$ days).

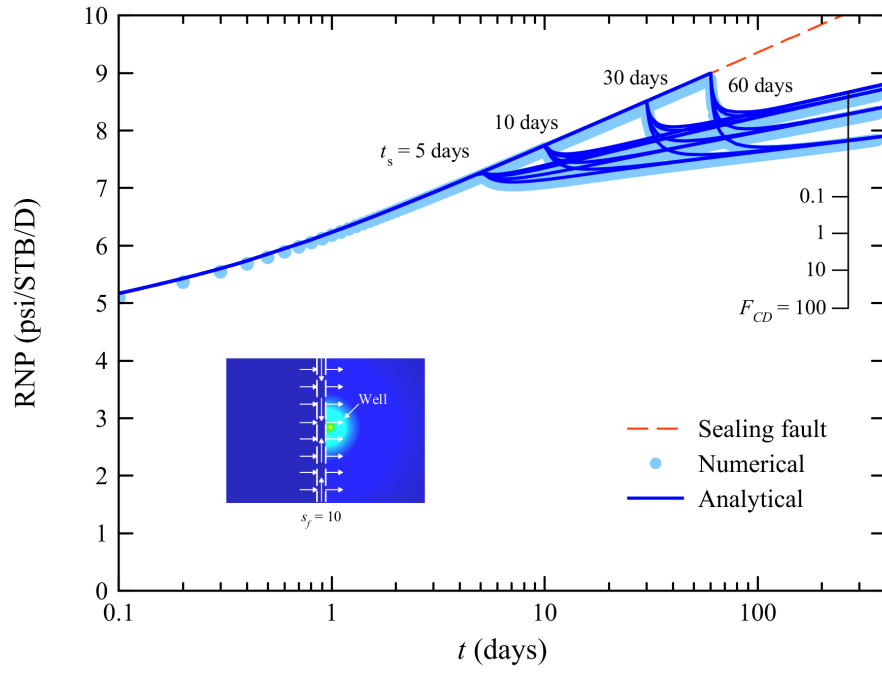


Figure 4.14: Comparison of RNP between analytical and numerical reservoir models for $M = h_D = 1$ and $s_f = 10$.

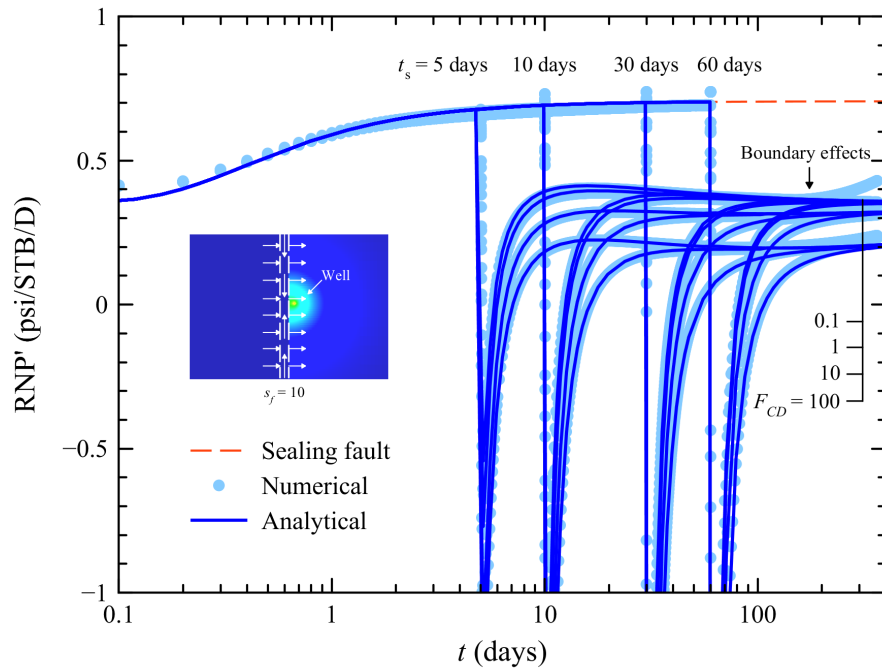


Figure 4.15: Comparison of RNP' between analytical and numerical reservoir models for $M = h_D = 1$ and $s_f = 10$. Boundary effects can be seen after 150 days.

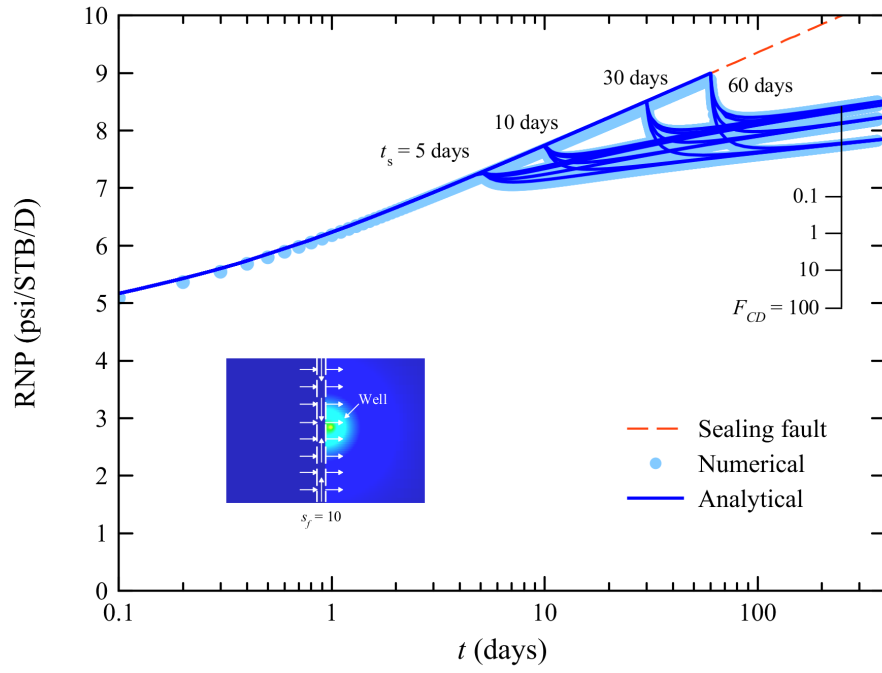


Figure 4.16: Comparison of RNP response between analytical and numerical models for $M = 5$, $h_D = 0.5$ and $s_f = 10$.

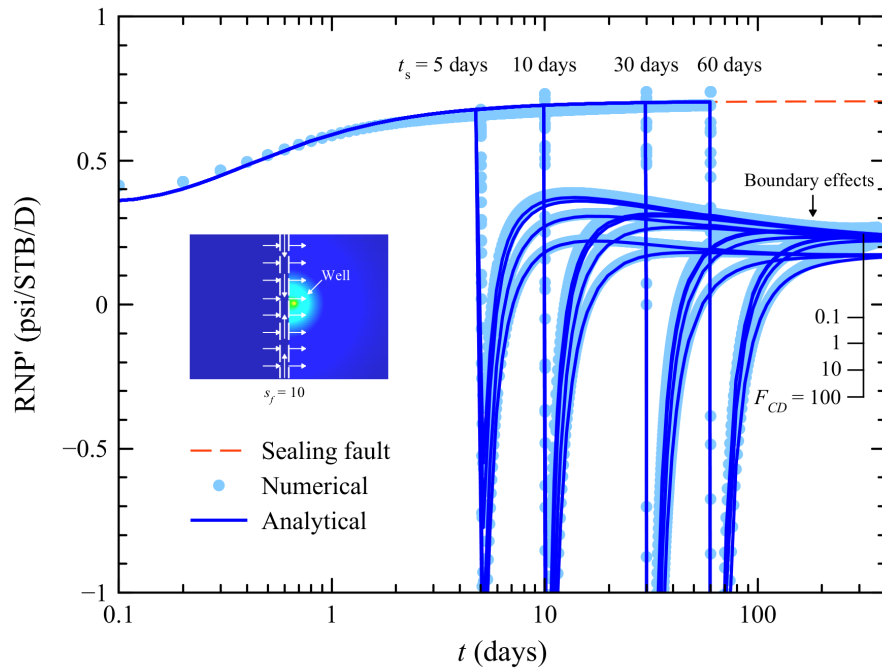


Figure 4.17: RNP' response for $M = 5$, $h_D = 0.5$ and $s_f = 10$. Influence of boundary effects on normalized drawdown-derivative response are less evident.

4.8.3 Case Study 3: Fault Reactivation in an Infinite Reservoir with Pressure-Dependent Anisotropic Fault Permeability

This synthetic scenario is based on the compartmentalized reservoir setting used for Case Study 1. The segmenting fault, however, is initially leaky with initial fault skin and dimensionless conductivity of $s_{fi} = 10$ and $F_{CDi} = 1$, respectively. Additionally, directional fault permeability is pressure-dependent. Figure 15 illustrates the permeability multipliers (i.e., fractional change in permeability) as a function of pore pressure. Notice that permeability multipliers suddenly increase by ~ 4 orders of magnitude when pore pressure is ~ 1500 psi. Pressure-dependent permeability multipliers are assigned to fault grid blocks in the numerical reservoir model.

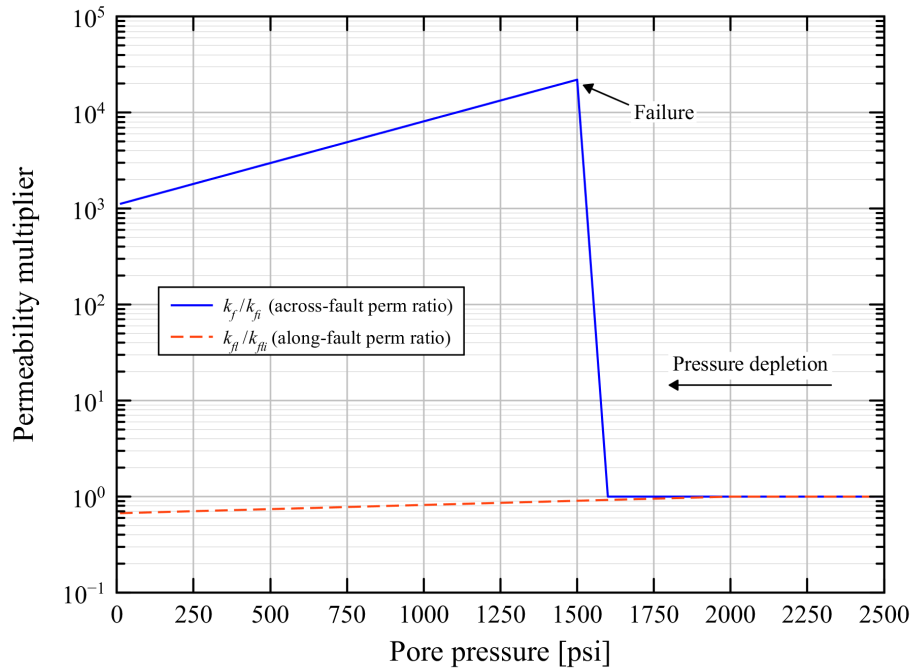


Figure 4.18: Pressure-dependent multipliers for across and along-fault permeability for Case Study 3.

Three major observations arise in this case study. First, the fault is leaky from the beginning of pressure depletion and the onset of fault reactivation is unknown beforehand. Therefore, we cannot simply adjust the analytical solution to "match" numerical data from this case. Second, unlike in the previous case studies, directional fault permeability is also a function of space because pressure would evolve across regions differently than for a constant-permeability type setting. And third, along-fault leakage is dominant over across-fault leakage as pressure depletes. Overall, this is a very complex fault

reactivation case that involves multiple processes once the onset of fault reactivation is reached.

Our strategy to tackle this case study is three-fold: (1) estimate the onset of fault reactivation, (2) study early and late-time RNP and RNP' responses, and (3) characterize the evolution of fault properties. Figure 4.19 presents the numerical results in the form of transient RNP data. Firstly, we can immediately observe the signature of fault reactivation occurring close to 220 days. Second, realize that numerical RNP data departs since early times; yet, we are able to match this data with using the early-time asymptotic solution for a linear-lateral leaky fault with $s_{fi} = 10$ and $F_{CDi} = 10$. This result indicates that, even though fault permeability is changing with pressure-drawdown, such changes are not as significant as to largely influence transient RNP response. Third, we obtain a reasonable match with numerical data at late-time using the late-time asymptotic solution for a linear-lateral leaky fault with $s_f = 16.7$ and $F_{CD} = 2200$. Realize that the history-matched values of s_f and F_{CD} are actually average values given that directional fault permeability is pressure and space-dependent.

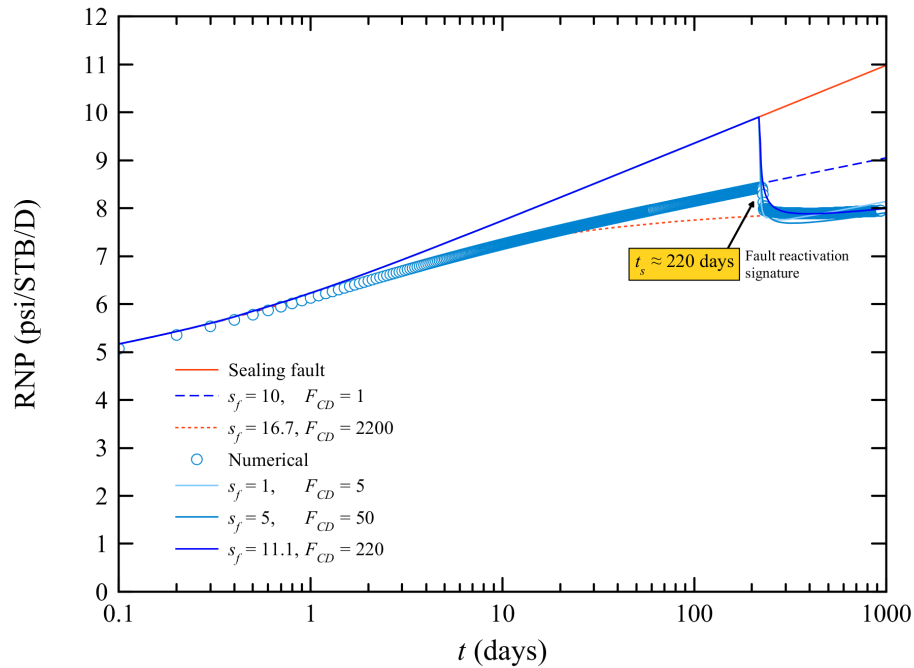


Figure 4.19: RNP response of analytical solution and numerical model for Numerical Case Study 3.

Figure 4.20 shows the RNP' diagnostic plot for the numerical simulation results as well

as early and late-time leaky fault models. In addition, we use full analytical solution for fault reactivation (Equation 5) for $t_s = 220$ days to generate RNP' responses for various values of s_f and F_{CD} . Unlike the RNP diagnostic plot, Figure 4.20 makes it straightforward to conclude that enhanced fault properties evolved from $s_f = 1$ and $F_{CD} = 5$, right after the onset of fault reactivation, to $s_f = 5$ and $F_{CD} = 50$; this change occurred between 250 and 300 days. Then, fault properties again change to $s_f = 11.1$ and $F_{CD} = 220$ and maintain these values during the period of 300 to 500 days. Finally, fault properties reach late-time behavior with $s_f = 16.7$ and $F_{CD} = 2200$. This analysis is consistent with Figure 4.19 which suggests that along-fault leakage would become dominant as pressure depletion progresses.

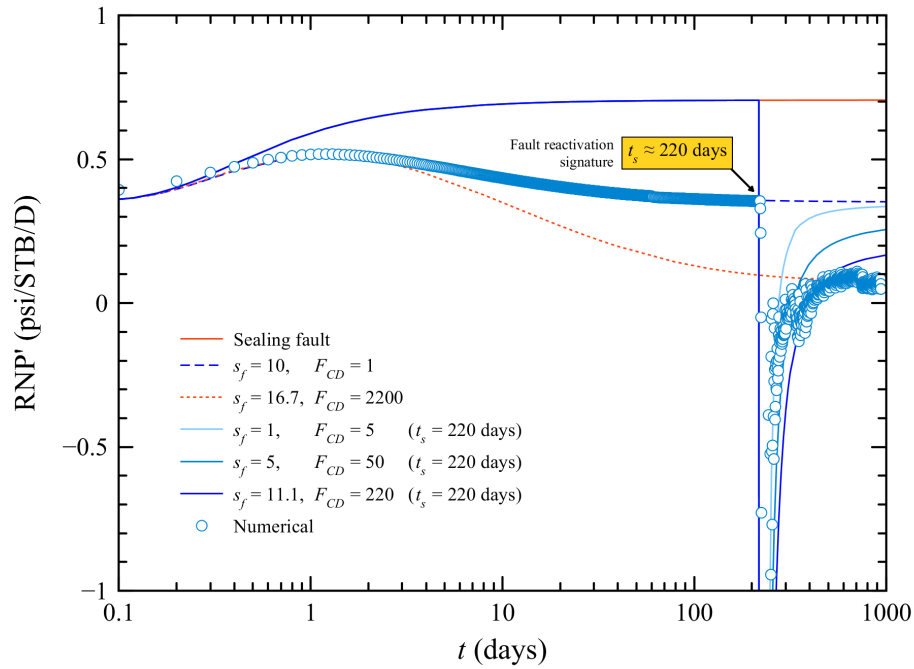


Figure 4.20: RNP' response of analytical solution and numerical model for Numerical Case Study 3. The proposed analytical model is able to capture the signature of fault reactivation and subsequent transitional fault properties until late-time equilibrium is reached in the compartmentalized system.

In summary, we conclude that the proposed workflow that utilizes the proposed analytical model, along with early and late-time asymptotic solutions, to detect fault reactivation and characterize the evolution of fault properties when directional fault permeability is pressure-dependent, has been successfully validated.

4.9. Discussion

The analytical solution introduced in this study was derived on the ground of infinite-acting flow conditions. Results from numerical simulation case 2, however, suggest that, if the reservoir is relatively small, pressure-transient response would rapidly shift from the initial transitional flow regime, caused by the sudden enhancement in directional fault permeability at the onset of fault reactivation, to another transitional flow regime induced by boundary effects. In despite of the assumption of infinite-acting reservoir being violated after the end of the first transitional flow regime, anisotropic fault permeability can still be characterized using pressure data from the aforementioned flow regime (see Figure 4.15).

Similar scenarios would be an initially leaky fault undergoing reactivation and boundary-dominated flow regime being achieved before fault reactivation occurs. In either case, fault properties can still be characterized during the transitional flow period induced by fault reactivation. In fact, we have proved through Numerical Case 3 that, even in fault properties are pressure-dependent (i.e., fault is self-healing), the proposed analytical model can readily capture the transitional nature of fault properties, from their initial enhanced value to late-time (stabilized) properties.

Although the analytical fault reactivation model discussed herein is based on constant-rate fluid withdrawal, it can be readily extended to an injection well simply by reversing the sign of q in the definition of dimensionless pressure (Equation A-1). Given that analytical solutions introduced in this work are dimensionless, the full analytical as well as early and late-time asymptotic solutions apply for the injection well scenario.

Lastly, be aware that numerical Laplace inversion of Equation 5 generates $N - 1$ additional convolution integrals, making the estimation of p_{1D} and p_{2D} (if needed) computationally expensive, particularly at early times after the onset of fault reactivation when convolution integrals dominate the transitional flow regime (i.e., $t'_D \approx 0^+$). Nevertheless, if infinite-acting flow conditions are held for roughly 1 to 1-1/2 log-cycles after the onset of fault reactivation, we can use the late-time asymptotic solution to estimate enhanced fault properties.

4.10. Conclusions

We introduce a new analytical model that enables the detection of fault reactivation, estimation of the onset time of fault slip and estimation of enhanced fault permeability using typical PTA techniques such as diagnostic plots and type-curves matching. The proposed model is based on the hypothesis that fault reactivation can be represented as a sudden change in anisotropic fault permeability occurring at the onset of fault slip.

For the development of the analytical model we assume that the well is producing at constant rate and the fault is initially sealing and becomes linear-lateral leaky when the onset of fault reactivation is reached. Furthermore, we consider the onset time to be a history-matching parameter hence it must be estimated from either diagnostic PTA plots or type-curves matching methods.

We prove that fault reactivation induces a new transient flow regime in which the reservoir undergoes infinite-acting flowing conditions and pressure communication between fault blocks and along the fault is governed by the convolution between reservoir conditions before and after the onset of fault reactivation. This flow regime is analytically governed by convolution integrals arising during the inversion of the proposed model from Laplace-Fourier domain into time-space domain. We verified our analytical solution against the most relevant leaky fault models from the literature.

Furthermore, we were able to unveil the characteristic or signature transient response of bottomhole pressure and pressure-derivative to a sudden change in directional fault permeability. In the former case, fault reactivation is seen as a sudden drop in dimensionless pressure occurring at the onset of fault slip, whereas it is detected as a rapid, abrupt drop and rebound in dimensionless pressure-derivative in the latter. The transient pressure-derivative behavior undergoes a transitional flow regime which lasts for about 1 to 1-1/2 log-cycles to finally reach late-time equilibrium with the transient response of a leaky fault.

We setup several numerical simulation cases to demonstrate the applicability of the proposed analytical solution. The analytical workflow followed in each simulation case was: 1) estimation of the onset of fault reactivation, 2) examination of early and late-time pressure behavior, and 3) characterization of fault properties, either during the transitional flow regime or at late times. In all simulation cases, our analytical approach proved accurate and was in close agreement with the synthetic pressure data.

5. Discussion

Analytical models for pressure-transient analysis of three impactful reservoir models—MFHW performance in stress-sensitive composite formations, detection and assessment of frac hits in multi-well pads, and detection of fault reactivation and characterization of enhanced fault properties—were developed and studied in this dissertation. Single-phase fluid-flow and the absence of gravitational effects were considered in all models.

The development of the definition and subsequent inclusion of fracture skin into the MFHW model enables the detection and characterization of damage over the fracture face through the application of diagnostic plots and type-curves to well-test data. In a similar fashion, modeling frac hits as a valve connecting two wells enables the application of type-curves for detection and assessment of frac hits in a multi-well pad. Furthermore, the proposed fault reactivation model, originally devised as a low-cost alternative to seismic monitoring in compartmentalized reservoirs, allows the use of the well-testing interpretation techniques previously mentioned to characterize fault properties before, during, and after a fault reactivation event.

The combined application of advanced mathematical techniques, such as Laplace-Fourier transform, numerical integration of multidimensional convolution integrals and use of an iterative algorithm, facilitated the implementation of efficient computational scripts that allowed run most of the calculations for MFHW performance analysis within seconds. However, numerical evaluation of the convolution integrals in the fault reactivation model would often take up to ~ 5 minutes per time step, thus making the evaluation of pressure-transient response shortly after fault reactivation the most computationally expensive.

Shortcomings of each model are discussed in Section 2.13, Section 3.12 and Section 4.9. Similarly, future work related to each work is discussed in Chapter 7.

6. Conclusions

This dissertation focuses on the development of analytical reservoir models related to MFHW performance forecast in stress-sensitive composite systems, detection and assessment of frac hits in multi-well pads, and detection of fault reactivation and characterization of enhanced fault properties in compartmentalized reservoirs. Analytical solution for these models were successfully validated against synthetic pressure data. These results are presented in the form of pressure-transient diagnostic plots and type-curves that can be readily utilized for well-test interpretation.

To begin with, we have demonstrated that pressure-dependent rock and fluid properties can be incorporated into MFHW models without the need for using pseudo-functions. In fact, the analytical approach proposed in this dissertation allows for each region in the MFHW to have its own pressure-dependent rock properties. This is a more realistic scenario than merely assume that porosity and permeability vary with pressure at the same rate throughout the MFHW, as dictated by the pseudo-pressure approach. In addition, the proposed MFHW model accounts for damage over the fracture surface. From the validation cases, we conclude that the proposed MFHW model is accurate, computationally efficient and can be easily implemented in well-testing software.

In addition, we confirmed the hypothesis that pressure tends to reach equilibrium across MFHWs when frac hits are present. In this sense, we observe that detection and estimation of the fraction of frac hits between MFHWs can be achieved by analyzing pressure data in the form of pressure differential rather than individual bottomhole pressure. Based on this observation, we developed an analytical approach to model frac hits as a boundary condition that can partially connect two or three wells through hydraulic fractures. As a result, we obtained the analytical definition of the frac hits skin factor which enables the estimation of the fraction of frac hits. The final analytical solution to pressure-transient response of the multi-well pad was successfully validated against numerical simulations. Type-curves for various well configurations were generated and history-matched against numerical data. From the history-matching results, we observed that the required well-test time for the assessment of frac hits is typically less than 3 days therefore the proposed model can be used with transient data from the flowback period. Furthermore, the resulting analytical solution is computationally efficient thus can be readily extended to field applications.

Finally, we have proved that fault reactivation can be detected from diagnostic plots as a sudden, sharp drop in pressure-derivative occurring at the onset of fault reactivation. This is followed by a rapid rebound in the pressure-derivative response with a final trend to reach late-time equilibrium with the transient response expected from an initially-leaky fault with the same directional permeability than that corresponding to the enhanced fault properties resulting from fault reactivation. This new transient flow period, induced by fault reactivation, lasts for roughly 1 to $1 - 1/2$ log-time cycles. Therefore, we conclude that late-time asymptotic solution can be used for fault characterization purposes. The proposed analytical solution was compared against common leaky fault models from the literature. Furthermore, the fault reactivation model was validated against numerical simulations for various scenarios, including a scenario where fault permeability is pressure-dependent and self-healing after the onset of fault reactivation. In all cases, the proposed analytical model seems in good agreement with synthetic pressure data. Unlike the proposed analytical models for unconventional reservoirs previously discussed, the analytical solution for the fault reactivation problem is computationally expensive, particularly when analyzing pressure data shortly after the onset of fault reactivation. Nonetheless, the implementation of early and late-time asymptotic solutions improves the process of fault characterization dramatically.

7. Future Work

7.1. Pressure-Dependent MFHW model

The natural extension to the nonlinear MFHW model is the examination of rate-transient behavior for the case of constant-pressure production. Because neither the fluid-flow model nor the analytical solution procedure should change in this case, the mathematical development discussed in Chapter 2 still holds valid, except for the definitions of normalized pressure and the constant-pressure boundary condition. Additionally, the use of material balance time will be necessary for rate-normalized pressure-transient analysis using diagnostic plots and type-curves.

This scenario is precursory to the more general case of variable-rate/variable-pressure history. The complexity associated with this production scenario lies in the mandatory use of the convolution integral as the analytical solution to rate-transient behavior (Lee et al., 2003). Nonetheless, since the integration would likely be performed numerically, one may utilize the same time step for both the iterative algorithm and integration scheme to determine the evolution of pressure and rate in the MFHW.

Another possible extension to the current nonlinear MFHW model is to develop a general fluid-flow model that enables the incorporation of pressure-dependent properties that are not necessarily exponential. Given that the iterative algorithm proposed in Chapter 2 is not limited to exponential functions, it is feasible to implement a pressure-dependent diffusivity constant as the nonlinear scaling parameter. In this way, any kind of pressure-dependent function for rock and fluid properties could be inserted into the governing equations. However, this would require a fresh derivation of the governing equations and boundary conditions. Moreover, one must be aware that pressure should be normalized in such a way that it will produce a null initial condition.

7.2. Frac Hits Model

There are three main extensions to the current constant-rate frac hits model. First, to develop the constant-pressure solution to the model. Second, we acknowledge that the assumption of equal initial pressure in the multi-well pad may be inaccurate because typically offset wells had been producing for some time before infill wells are drilled

and completed. Therefore, initial pressure may actually vary from well to well (see Figure 3.1). Thus, another plausible extension to the present model is the incorporation of initial pressure on a per-MFHW basis.

Another potential extension to the present frac hits model is the incorporation of MFHWs landed in stacked plays (see Figure 3.2). Modeling vertical connectivity MFHWs through hydraulic fractures may be achieved in the same manner proposed Chapter 3. However, contrary to fully-overlapping fractures, which are interconnected via high-conductivity frac hits, partially-intersecting fractures may be modeled as being interconnected via low-conductivity frac hits. The validity of fracture and SRV linear flow assumptions should be verified, though.

Lastly, pressure connectivity due to frac hits may decrease with time as pressure declines. Therefore, it would be useful to incorporate this time-dependent process into the frac hits model by assigning pressure or time-dependent conductivity to the frac hits. An iterative scheme, as the one discussed in Chapter 2, may be required for this case. Furthermore, since the purpose of this model would be production forecast, SRV dimensions should lie within the recommended limits to avoid producing inaccurate predictions, specially at late times.

7.3. Fault Reactivation Model

A significant addition to the fault permeability enhancement model would be the incorporation of up-fault, or vertical, leakage into the fluid-flow model. This is a relevant feature to examine as pressure communication between the target zone and neighboring reservoirs can also take place across multiple over and underlying formations (Zeidouni, 2012). To keep the fluid-flow model simple and mathematically tractable, one can assume that up-fault flow is not influenced by transience effects hence vertical leakage is solely controlled by the pressure differential between formations and vertical-fault transmissibility (Shan et al., 1995).

Since transience effects on up-fault leakage are negligible, vertical-fault flow may be added into the governing equation following the flux-source approach. In this manner, fluid-flow along the fault will be the only component that would experience transience effects, just as proposed by Rahman et al. (2003). Consequently, the application of Laplace-Fourier transform onto the resulting governing equation would yield a time-independent, linear expression for pressure at the fault interface.

Another significant addition to the current model would be accounting for pressure or time-dependent effects directional fault properties. From the mathematical perspective, this objective would be challenging to accomplish because fault permeability would automatically become spatio-temporal dependent. This implies the development of averaging and/or nonlinear techniques that were not discussed in this dissertation.

Finally, extension of the current constant-rate method to constant-pressure fluid withdrawal/injection would enable the use of rate-transient analysis techniques to detect fault reactivation and characterize enhanced fault properties.

References

- Abass, H., Sierra, L., and Tahini, A. (2009). Optimizing Proppant Conductivity and Number of Hydraulic Fractures in Tight Gas Sand Wells. In *SPE Saudi Arabia Section Technical Symposium*, page 15. Society of Petroleum Engineers.
- Abbaszadeh, M. and Cinco-Ley, H. (1995). Pressure-Transient Behavior in a Reservoir With a Finite-Conductivity Fault. *SPE Formation Evaluation*, 10(01):26–32.
- Agarwal, R. G., Al-Hussainy, R., and Ramey Jr, H. (1970). An Investigation of Wellbore Storage and Skin Effect in Unsteady Liquid Flow: I. Analytical Treatment. *Society of Petroleum Engineers Journal*, 10(03):279–290.
- Ajani, A. A. and Kelkar, M. G. (2012). Interference Study in Shale Plays. In *SPE Hydraulic Fracturing Technology Conference*. Society of Petroleum Engineers.
- Algadi, O. A., Filyukov, R. V., and Luna, D. (2014). Multistage Hydraulic Fracturing using Coiled Tubing-activated Frac Sleeves: Case Study from the Permian Basin. In *SPE Annual Technical Conference and Exhibition*. Society of Petroleum Engineers.
- Ambastha, A., McLeroy, P., and Grader, A. (1989). Effects of a Partially Communicating Fault in a Composite Reservoir on Transient Pressure Testing. *SPE Formation Evaluation*, 4(02):210–218.
- Awada, A., Santo, M., Loughheed, D., Xu, D., and Virues, C. (2016). Is That Interference? A Work Flow for Identifying and Analyzing Communication Through Hydraulic Fractures in a Multiwell Pad. *SPE Journal*, 21(05):1,554–1,566.
- Bateman, H. (1954). *Tables of Integral Transforms [Volumes I & II]*. McGraw-Hill Book Company.
- Bergman, T. L., Incropera, F. P., DeWitt, D. P., and Lavine, A. S. (2011). *Fundamentals of Heat and Mass Transfer*. John Wiley & Sons.
- Berumen, S. and Tiab, D. (1996). Effect of Pore Pressure on Conductivity and Permeability of Fractured Rocks. In *SPE Western Regional Meeting*. Society of Petroleum Engineers.

- Bixel, H. C., Larkin, B. K., and Van Poolen, H. K. (1963). Effect of Linear Discontinuities on Pressure Build-Up and Drawdown Behavior. *Journal of Petroleum Technology*, 15(08):885–895.
- Bommer, P., Bayne, M., Mayerhofer, M., Machovoe, M., and Staron, M. (2017). Redesigning from Scratch and Defending Offset Wells: Case Study of a Six-Well Bakken Zipper Project, McKenzie County, ND. In *SPE Hydraulic Fracturing Technology Conference and Exhibition*. Society of Petroleum Engineers.
- Bourdet, D., Ayoub, J., and Pirard, Y. (1989). Use of Pressure Derivative in Well Test Interpretation. *SPE Formation Evaluation*, 4(02):293–302.
- Bourdet, D., Whittle, T., Douglas, A., and Pirard, Y. (1983). A New Set of Type Curves Simplifies Well Test Analysis. *World Oil*, 196(6):95–106.
- Bourouis, S. and Bernard, P. (2007). Evidence for coupled seismic and aseismic fault slip during water injection in the geothermal site of Soultz (France), and implications for seismogenic transients. *Geophysical Journal International*, 169(2):723–732.
- Brown, M. (2009). *Analytical Trilinear Pressure Transient Model for Multiply Fractured Horizontal Wells in Tight Shale Reservoirs*. Thesis, M. Sc. Thesis, Colorado School of Mines, Golden.
- Brown, M., Ozkan, E., Raghavan, R., and Kazemi, H. (2011). Practical Solutions for Pressure-Transient Responses of Fractured Horizontal Wells in Unconventional Shale Reservoirs. *SPE Reservoir Evaluation & Engineering*, 14(06):663–676.
- Buijze, L., van den Bogert, P. A., Wassing, B. B., Orlic, B., and ten Veen, J. (2017). Fault reactivation mechanisms and dynamic rupture modelling of depletion-induced seismic events in a Rotliegend gas reservoir. *Netherlands Journal of Geosciences*, 96(5):131–148.
- Caine, J. S., Evans, J. P., and Forster, C. B. (1996). Fault zone architecture and permeability structure. *Geology*, 24(11):1025–1028.
- Cao, R., Li, R., Girardi, A., Chowdhury, N., and Chen, C. (2017). Well Interference and Optimum Well Spacing for Wolfcamp Development at Permian Basin. In *Unconventional Resources Technology Conference, Austin, Texas*, pages 2756–2766. Society of Exploration Geophysicists, American Association of Petroleum Geologists, Society

of Petroleum Engineers.

- Cappa, F. and Rutqvist, J. (2011). Modeling of coupled deformation and permeability evolution during fault reactivation induced by deep underground injection of CO₂. *International Journal of Greenhouse Gas Control*, 5(2):336–346.
- Cerón, M. R., Walls, J. D., and Diaz, E. (2013). Comparison of Reservoir Quality from La Luna, Gacheta and Eagle Ford Shale Formations Using Digital Rock Physics. *Search and Discovery*, 50875.
- Chan, A. W. and Zoback, M. D. (2007). The role of hydrocarbon production on land subsidence and fault reactivation in the Louisiana coastal zone. *Journal of Coastal Research*, pages 771–786.
- Chen, D., Pan, Z., and Ye, Z. (2015). Dependence of gas shale fracture permeability on effective stress and reservoir pressure: Model match and insights. *Fuel*, 139:383–392.
- Chen, H. K. and Brigham, W. E. (1978). Pressure Buildup for a Well with Storage and Skin in a Closed Square. *Journal of Petroleum Technology*, 30(01):141–146.
- Chen, Z. (2007). *Reservoir Simulation: Mathematical Techniques in Oil Recovery*, volume 77. Society for Industrial and Applied Mathematics (SIAM).
- Cho, Y., Ozkan, E., and Apaydin, O. G. (2013). Pressure-Dependent Natural-Fracture Permeability in Shale and Its Effect on Shale-Gas Well Production. *SPE Reservoir Evaluation & Engineering*, 16(02):216–228.
- Cipolla, C., Lolon, E., Erdle, J., and Rubin, B. (2010). Reservoir Modeling in Shale-Gas Reservoirs. *SPE Reservoir Evaluation & Engineering*, 13(04):638–653.
- Cipolla, C. and Wallace, J. (2014). Stimulated Reservoir Volume: A Misapplied Concept? In *SPE Hydraulic Fracturing Technology Conference*. Society of Petroleum Engineers.
- Dake, L. P. (1983). *Fundamentals of Reservoir Engineering*, volume 8. Elsevier.
- Daneshy, A. A. (2014). Fracture Shadowing: Theory, Applications and Implications. In *SPE Annual Technical Conference and Exhibition*. Society of Petroleum Engineers.
- Davies, R. K., An, L., Jones, P., Mathis, A., and Cornette, C. (2003). Fault-seal analysis

- south Marsh Island 36 field, Gulf of Mexico. *AAPG Bulletin*, 87(3):479–491.
- Economides, M. J., Hill, A. D., Ehlig-Economides, C., and Zhu, D. (2013). *Petroleum Production Systems*. Pearson Education.
- El-sgher, M., Aminian, K., and Ameri, S. (2018). The Impact of Stress on Propped Fracture Conductivity and Gas Recovery in Marcellus Shale. In *SPE Hydraulic Fracturing Technology Conference and Exhibition*. Society of Petroleum Engineers.
- Ellsworth, W. L. (2013). Injection-induced earthquakes. *Science*, 341(6142):1225942.
- Fisher, M., Heinze, J., Harris, C., Davidson, B., Wright, C., and Dunn, K. (2004). Optimizing Horizontal Completion Techniques in the Barnett Shale using Microseismic Fracture Mapping. In *SPE Annual Technical Conference and Exhibition*. Society of Petroleum Engineers.
- Frohne, K.-H. and Mercer, J. C. (1984). Fractured Shale Gas Reservoir Performance Study—An Offset Well Interference Field Test. *Journal of Petroleum Technology*, 36(02):291–300.
- Gala, D. P., Manchanda, R., and Sharma, M. M. (2018). Modeling of Fluid Injection in Depleted Parent Wells to Minimize Damage Due to Frac-Hits. In *Unconventional Resources Technology Conference*, pages 4118–4131. Society of Exploration Geophysicists, American Association of Petroleum Geologists, Society of Petroleum Engineers.
- Garza, M., Baumbach, J., Prosser, J., Pettigrew, S., and Elvig, K. (2019). An Eagle Ford Case Study: Improving an Infill Well Completion Through Optimized Refracturing Treatment of the Offset Parent Wells. In *SPE Hydraulic Fracturing Technology Conference and Exhibition*. Society of Petroleum Engineers.
- Gringarten, A. C. (2008). From Straight Lines to Deconvolution: The Evolution of the State of the Art in Well Test Analysis. *SPE Reservoir Evaluation & Engineering*, 11(01):41–62.
- Gringarten, A. C., Bourdet, D. P., Landel, P. A., and Kniazeff, V. J. (1979). A Comparison Between Different Skin and Wellbore Storage Type-Curves for Early-Time Transient Analysis. In *SPE Annual Technical Conference and Exhibition*. Society of Petroleum Engineers.

- Guglielmi, Y., Cappa, F., Avouac, J.-P., Henry, P., and Elsworth, D. (2015). Seismicity triggered by fluid injection–induced aseismic slip. *Science*, 348(6240):1224–1226.
- Guo, T., Zhang, S., Gao, J., Zhang, J., and Yu, H. (2013). Experimental Study of Fracture Permeability for Stimulated Reservoir Volume (SRV) in Shale Formation. *Transport in Porous Media*, 98(3):525–542.
- Healy, J., Rubey, W., Griggs, D., and Raleigh, C. (1968). The Denver Earthquakes. *Science*, 161(3848):1301–1310.
- Horner, D. (1951). Pressure build-up in wells. In *3rd World Petroleum Congress*. World Petroleum Congress.
- Hsieh, P. A. and Bredehoeft, J. D. (1981). A reservoir analysis of the denver earthquakes: A case of induced seismicity. *Journal of Geophysical Research: Solid Earth*, 86(B2):903–920.
- Huang, J., Fu, P., Hao, Y., Morris, J., Settghost, R., and Ryerson, F. (2019). Three-Dimensional Effects of Reservoir Depletion on Hydraulic Fracture Propagation. In *SPE Hydraulic Fracturing Technology Conference and Exhibition*. Society of Petroleum Engineers.
- Jacobs, T. (2017a). Frac Hits Reveal Well Spacing May be Too Tight, Completion Volumes Too Large. *Journal of Petroleum Technology*, 69(11):35–38.
- Jacobs, T. (2017b). Oil and Gas Producers Find Frac Hits in Shale Wells a Major Challenge. *Journal of Petroleum Technology*, 69(04):29–34.
- Jacobs, T. (2018). Fighting Water With Water: How Engineers are Turning the Tides on Frac Hits. *Journal of Petroleum Technology*, 70(12):34–38.
- Jeanne, P., Guglielmi, Y., Rutqvist, J., Nussbaum, C., and Birkholzer, J. (2018). Permeability Variations Associated With Fault Reactivation in a Claystone Formation Investigated by Field Experiments and Numerical Simulations. *Journal of Geophysical Research: Solid Earth*, 123(2):1694–1710.
- Jha, B. and Juanes, R. (2014). Coupled multiphase flow and poromechanics: A computational model of pore pressure effects on fault slip and earthquake triggering. *Water Resources Research*, 50(5):3776–3808.

- Jia, P., Cheng, L., Clarkson, C. R., Qanbari, F., Huang, S., and Cao, R. (2017). A Laplace-Domain Hybrid Model for Representing Flow Behavior of Multifractured Horizontal Wells Communicating Through Secondary Fractures in Unconventional Reservoirs. *SPE Journal*, 22(06):1–856.
- Jolley, S., Fisher, Q., and Ainsworth, R. (2010). Reservoir compartmentalization: an introduction. *Geological Society, London, Special Publications*, 347(1):1–8.
- Keranen, K. M., Savage, H. M., Abers, G. A., and Cochran, E. S. (2013). Potentially induced earthquakes in Oklahoma, USA: Links between wastewater injection and the 2011 Mw 5.7 earthquake sequence. *Geology*, 41(6):699–702.
- Keranen, K. M., Weingarten, M., Abers, G. A., Bekins, B. A., and Ge, S. (2014). Sharp increase in central Oklahoma seismicity since 2008 induced by massive wastewater injection. *Science*, 345(6195):448–451.
- King, G. E., Rainbolt, M. F., and Swanson, C. (2017). Frac Hit Induced Production Losses: Evaluating Root Causes, Damage Location, Possible Prevention Methods and Success of Remedial Treatments. In *SPE Annual Technical Conference and Exhibition*. Society of Petroleum Engineers.
- Knipe, R. J., Jones, G., and Fisher, Q. (1998). Faulting, fault sealing and fluid flow in hydrocarbon reservoirs: an introduction. *Geological Society, London, Special Publications*, 147(1):vii–xxi.
- Lawal, H., Jackson, G., Abolo, N., and Flores, C. (2013). A Novel Approach to Modeling and Forecasting Frac Hits in Shale Gas Wells. In *EAGE Annual Conference & Exhibition incorporating SPE Europec*. Society of Petroleum Engineers.
- Lee, J., Rollins, J. B., and Spivey, J. P. (2003). *Pressure Transient Testing*, volume 9. Society of Petroleum Engineers.
- Luo, W., Liu, P., Tian, Q., Tang, C., and Zhou, Y. (2017). Effects of Discrete Dynamic-Conductivity Fractures on the Transient Pressure of a Vertical Well in a Closed Rectangular Reservoir. *Scientific Reports*, 7(1):15537.
- Marongiu-Porcu, M., Lee, D., Shan, D., and Morales, A. (2015). Advanced Modeling of Interwell Fracturing Interference: An Eagle Ford Shale Oil Study. In *SPE Annual Technical Conference and Exhibition*. Society of Petroleum Engineers.

- Mayerhofer, M. J., Lolon, E., Warpinski, N. R., Cipolla, C. L., Walser, D. W., and Rightmire, C. M. (2010). What Is Stimulated Reservoir Volume? *SPE Production & Operations*, 25(01):89–98.
- McGarr, A., Bekins, B., Burkardt, N., Dewey, J., Earle, P., Ellsworth, W., Ge, S., Hickman, S., Holland, A., Majer, E., et al. (2015). Coping with earthquakes induced by fluid injection. *Science*, 347(6224):830–831.
- Minkoff, S. E., Stone, C. M., Bryant, S., Peszynska, M., and Wheeler, M. F. (2003). Coupled fluid flow and geomechanical deformation modeling. *Journal of Petroleum Science and Engineering*, 38(1-2):37–56.
- Molina, O. M. and Zeidouni, M. (2017a). Analytical model for multifractured systems in liquid-rich shales with pressure-dependent properties. *Transport in Porous Media*, 119(1):1–23.
- Molina, O. M. and Zeidouni, M. (2017b). Analytical Model to Estimate the Fraction of Fracture Hits in a Multi-Well Pad. In *SPE Liquids-Rich Basins Conference-North America*. Society of Petroleum Engineers.
- Molina, O. M. and Zeidouni, M. (2018). Analytical Model to Detect Fault Permeability Alteration Induced by Fault Reactivation in Compartmentalized Reservoirs. *Water Resources Research*, 54(8):5841–5855.
- Morton, R. A. and Purcell, N. A. (2001). Wetland subsidence, fault reactivation, and hydrocarbon production in the U. S. Gulf Coast region. Report 091-01, U.S. Geological Survey.
- Nur, A. and Yilmaz, O. (1985). *Pore Pressure in Fronts in Fractured Rock Systems*. Thesis, Stanford University.
- Orangi, A., Nagarajan, N. R., Honarpour, M. M., and Rosenzweig, J. J. (2011). Unconventional Shale Oil and Gas-Condensate Reservoir Production, Impact of Rock, Fluid, and Hydraulic Fractures. In *SPE Hydraulic Fracturing Technology Conference*. Society of Petroleum Engineers, Society of Petroleum Engineers.
- Palacio, J. and Blasingame, T. (1993). Decline Curve Analysis Using Type Curves—Analysis of Gas Well Production Data. *SPE*, 25909.

- Palisch, T. T., Duenckel, R. J., Bazan, L. W., Heidt, J. H., and Turk, G. A. (2007). Determining Realistic Fracture Conductivity and Understanding Its Impact on Well Performance—Theory and Field Examples. In *SPE Hydraulic Fracturing Technology Conference*. Society of Petroleum Engineers.
- Peirce, A. and Bunger, A. (2015). Interference Fracturing: Nonuniform Distributions of Perforation Clusters that Promote Simultaneous Growth of Multiple Hydraulic Fractures. *SPE Journal*, 20(02):384–395.
- Raghavan, R. and Chin, L. (2004). Productivity Changes in Reservoirs With Stress-Dependent Permeability. *SPE Reservoir Evaluation & Engineering*, 7(04):308–315.
- Rahman, N., Miller, M. D., and Mattar, L. (2003). Analytical Solution to the Transient-Flow Problems for a Well Located Near a Finite-Conductivity Fault in Composite Reservoirs. In *SPE Annual Technical Conference and Exhibition*. Society of Petroleum Engineers.
- Rodionov, Y., Defeu, C., Gakhar, K., Mullen, K., Mayo, J. T., Shan, D., Usoltsev, D., and Ejofodomi, E. A. (2017). Optimization of Infill Well Development Using a Novel Far-Field Diversion Technique in the Eagle Ford Shale. In *Unconventional Resources Technology Conference*, pages 1160–1172. Society of Exploration Geophysicists, American Association of Petroleum Geologists, Society of Petroleum Engineers.
- Roussel, N. P. and Sharma, M. M. (2010). Quantifying Transient Effects in Altered-Stress Refracturing of Vertical Wells. *SPE Journal*, 15(03):770–782.
- Rubinstein, J. L., Ellsworth, W. L., McGarr, A., and Benz, H. M. (2014). The 2001–present induced earthquake sequence in the raton basin of northern new mexico and southern colorado. *Bulletin of the Seismological Society of America*, 104(5):2162–2181.
- Rubinstein, J. L. and Mahani, A. B. (2015). Myths and Facts on Wastewater Injection, Hydraulic Fracturing, Enhanced Oil Recovery, and Induced Seismicity. *Seismological Research Letters*, 86(4):1060–1067.
- Rutqvist, J., Rinaldi, A. P., Cappa, F., and Morigidis, G. J. (2013). Modeling of fault reactivation and induced seismicity during hydraulic fracturing of shale-gas reservoirs. *Journal of Petroleum Science and Engineering*, 107:31–44.
- Sardinha, C. M., Petr, C., Lehmann, J., Pyecroft, J. F., and Merkle, S. (2014). Deter-

- mining interwell connectivity and reservoir complexity through frac pressure hits and production interference analysis. In *SPE/CSUR Unconventional Resources Conference–Canada*. Society of Petroleum Engineers.
- Seth, P., Manchanda, R., Zheng, S., Gala, D., and Sharma, M. (2019). Poroelastic Pressure Transient Analysis: A New Method for Interpretation of Pressure Communication Between Wells During Hydraulic Fracturing. In *SPE Hydraulic Fracturing Technology Conference and Exhibition*. Society of Petroleum Engineers.
- Shan, C., Javandel, I., and Witherspoon, P. A. (1995). Characterization of leaky faults: Study of water flow in aquifer-fault-aquifer systems. *Water Resources Research*, 31(12):2897–2904.
- Sharma, M. and Manchanda, R. (2015). The Role of Induced Un-propped (IU) Fractures in Unconventional Oil and Gas Wells. In *SPE Annual Technical Conference and Exhibition*. Society of Petroleum Engineers.
- Sibson, R. H. (1985). A note on fault reactivation. *Journal of Structural Geology*, 7(6):751–754.
- Smith, M. B. and Montgomery, C. (2015). *Hydraulic Fracturing*. CRC Press.
- Song, B. and Ehlig-Economides, C. A. (2011). Rate-Normalized Pressure Analysis for Determination of Shale Gas Well Performance. In *North American Unconventional Gas Conference and Exhibition*. Society of Petroleum Engineers, Society of Petroleum Engineers.
- Spivey, J. P. and Lee, W. J. (2013). *Applied Well Test Interpretation*. Richardson, TX.: Society of Petroleum Engineers.
- Stalgorova, E. and Mattar, L. (2013). Analytical Model for Unconventional Multifractured Composite Systems. *SPE Reservoir Evaluation & Engineering*, 16(03):246–256.
- Stalgorova, E. and Mattar, L. (2016). Analytical Methods for Single-Phase Oil Flow: Accounting for Changing Liquid and Rock Properties. In *SPE Europec Featured at 78th EAGE Conference and Exhibition*. Society of Petroleum Engineers.
- Stegent, N. A., Ferguson, K., and Spencer, J. (2011). Comparison of Frac Valves vs. Plug-and-perf Completion in the Oil Segment of the Eagle Ford Shale: A Case Study.

- In *Canadian Unconventional Resources Conference*. Society of Petroleum Engineers.
- Stehfest, H. (1970). Algorithm 368: Numerical inversion of Laplace transforms [D5]. *Communications of the ACM*, 13(1):47–49.
- Stewart, G. (2011). *Well Test Design and Analysis*. PennWell.
- Suarez-Rivera, R., Burghardt, J., Edelman, E., Stanchits, S., and Surdi, A. (2013). Geomechanics Considerations for Hydraulic Fracture Productivity. In *47th US Rock Mechanics/Geomechanics Symposium*. American Rock Mechanics Association.
- Tabatabaie, S. H., Pooladi-Darvish, M., Mattar, L., and Tavallali, M. (2016). Analytical Modeling of Linear Flow in Pressure-Sensitive Formations. *SPE Reservoir Evaluation & Engineering*.
- Tang, H., Chai, Z., Yan, B., and Killough, J. (2017). Application of multi-segment well modeling to simulate well interference. In *Unconventional Resources Technology Conference*, pages 419–429. Society of Exploration Geophysicists, American Association of Petroleum Geologists, Society of Petroleum Engineers.
- Vidma, K., Abivin, P., Dunaeva, A., Panga, M., Nikolaev, M., Usoltsev, D., and Mayo, J. (2018). Far-Field Diversion Technology to Prevent Fracture Hits in Tightly Spaced Horizontal Wells. In *SPE Annual Technical Conference and Exhibition*. Society of Petroleum Engineers.
- Vidma, K., Abivin, P., Fox, D., Reid, M., Ajisafe, F., Marquez, A., Yip, W., and Still, J. (2019). Fracture Geometry Control Technology Prevents Well Interference in the Bakken. In *SPE Hydraulic Fracturing Technology Conference and Exhibition*. Society of Petroleum Engineers.
- Warpinski, N. (2009). Microseismic Monitoring: Inside and Out. *Journal of Petroleum Technology*, 61(11):80–85.
- Warpinski, N., Kramm, R. C., Heinze, J. R., and Waltman, C. K. (2005). Comparison of Single-and Dual-Array Microseismic Mapping Techniques in the Barnett Shale. In *SPE Annual Technical Conference and Exhibition*. Society of Petroleum Engineers.
- Weaver, J. D., Rickman, R. D., and Luo, H. (2010). Fracture-Conductivity Loss Caused by Geochemical Interactions Between Man-made Proppants and Formations. *SPE*

Journal, 15(01):116–124.

- Wilson, K. (2015). Analysis of Drawdown Sensitivity in Shale Reservoirs Using Coupled-Geomechanics Models. In *SPE Annual Technical Conference and Exhibition*. Society of Petroleum Engineers.
- Wiprut, D. and Zoback, M. D. (2000). Fault reactivation and fluid flow along a previously dormant normal fault in the northern north sea. *Geology*, 28(7):595–598.
- Yadav, H. and Motealleh, S. (2017). Improving Quantitative Analysis of Frac-Hits and Refracs in Unconventional Plays Using RTA. In *SPE Hydraulic Fracturing Technology Conference and Exhibition*. Society of Petroleum Engineers.
- Yao, S., Zeng, F., and Liu, H. (2016). A Semi-Analytical Model for Hydraulically Fractured Horizontal Wells with Stress-Sensitive Conductivities. *Environmental Earth Sciences*, 75(1):34.
- Yaxley, L. (1987). Effect of a Partially Communicating Fault on Transient Pressure Behavior. *SPE Formation Evaluation*, 2(04):590–598.
- Yu, W., Wu, K., Zuo, L., Tan, X., and Weijermars, R. (2016). Physical Models for Inter-Well Interference in Shale Reservoirs: Relative Impacts of Fracture Hits and Matrix Permeability. In *Unconventional Resources Technology Conference*, pages 1535–1558. Society of Exploration Geophysicists, American Association of Petroleum Geologists, Society of Petroleum Engineers.
- Yu, W., Xu, Y., Weijermars, R., Wu, K., and Sepehrnoori, K. (2018). A Numerical Model for Simulating Pressure Response of Well Interference and Well Performance in Tight Oil Reservoirs with Complex-Fracture Geometries using the Fast Embedded-Discrete-Fracture-Model Method. *SPE Reservoir Evaluation & Engineering*, 21(02):489–502.
- Zakian, V. (1969). Numerical inversion of Laplace transform. *Electronics Letters*, 5(6):120–121.
- Zeidouni, M. (2012). Analytical model of leakage through fault to overlying formations. *Water Resources Research*, 48(12).
- Zhang, J., Cramer, D. D., McEwen, J., White, M., and Bjornen, K. (2019). Utilization

of Far Field Diverters to Mitigate Parent and Infill Well Fracture Interaction in Shale Formations. In *SPE Hydraulic Fracturing Technology Conference and Exhibition*. Society of Petroleum Engineers.

Zhang, J., Kamenov, A., Hill, A. D., and Zhu, D. (2014). Laboratory Measurement of Hydraulic-Fracture Conductivities in the Barnett Shale. *SPE Production & Operations*, 29(03):216–227.

Zhu, L., Liao, X., Chen, Z., and Cheng, X. (2018). Pressure-Transient Analysis of a Vertically Fractured Well in a Tight Oil Reservoir with Rectangular Stimulated Reservoir Volume. *SPE Production & Operations*, 33(04):21.

A. Analytical Frac Hits Model

A.1. General Definitions

$$\eta_j = 2.637 \times 10^{-4} \frac{k_j}{\mu(\phi c_t)_j} \quad (\text{A.1})$$

$$q'_j = \left(\frac{q_{\text{well}}}{\delta_p n_f} \right)_j \quad (\text{A.2})$$

$$q'_t = \left(\frac{q_{\text{well}}}{\delta_p n_f} \right)_A + \left(\frac{q_{\text{well}}}{\delta_p n_f} \right)_B + \left(\frac{q_{\text{well}}}{\delta_p n_f} \right)_C \quad (\text{A.3})$$

A.2. Dimensionless Parameters Group

$$p_{jD} = \frac{k_{1A} h \Delta p_j}{141.2 q'_t \mu B} \quad (\text{A.4})$$

$$\eta_{jD} = \frac{\eta_j}{\eta_{1A}} \quad (\text{A.5})$$

$$t_D = \frac{\eta_{1A}}{x_{fA}^2} t \quad (\text{A.6})$$

$$q_{jD} = \frac{q'_j}{q'_t} \quad (\text{A.7})$$

$$x_{fjD} = \frac{x_{fj}}{x_{fA}} \quad (\text{A.8})$$

$$(F'_{CD})_j = \frac{(k_1 x_f)_j}{(k_1 x_f)_A} (F_{CD})_j \quad (\text{A.9})$$

A.3. Normalized Coordinates

A.3.1 Normalized Coordinates for Well A

$$x_D \equiv x_{AD} = \frac{x}{x_{fA}} \quad (\text{A.10})$$

$$y_D \equiv y_{AD} = \frac{y}{x_{fA}} \quad (\text{A.11})$$

A.3.2 Normalized Coordinates for Wells B and C

$$x_{BD} = x_{CD} = x_D \quad (\text{A.12})$$

$$y_{BD} = y_D - \frac{L_{AB}}{x_{fA}} \quad (\text{A.13})$$

$$y_{CD} = y_D + \frac{L_{AC}}{x_{fA}} \quad (\text{A.14})$$

A.4. Normalized Dimensions

A.4.1 Normalized Dimensions for Well A

$$w_{AD} = \frac{w_A}{x_{fA}} \quad (\text{A.15})$$

$$x_{eAD} = \frac{x_{eA}}{x_{fA}} \quad (\text{A.16})$$

$$y_{eOAD} = \frac{L_{AB}}{x_{fA} + x_{fB}} \quad (\text{A.17})$$

$$y_{eIAD} = \frac{L_{AC}}{x_{fA} + x_{fC}} \quad (\text{A.18})$$

$$(\text{A.19})$$

A.4.2 Normalized Dimensions for Well B

$$w_{BD} = \frac{w_B}{x_{fA}} \quad (\text{A.20})$$

$$x_{eBD} = \frac{x_{eB}}{x_{fA}} \quad (\text{A.21})$$

$$x_{fBD} = \frac{x_{fB}}{x_{fA}} \quad (\text{A.22})$$

$$y_{eOBD} = \frac{y_{eOB}}{x_{fA}} \quad (\text{A.23})$$

$$y_{eIBD} = x_{fBD} \left(\frac{L_{AB}}{x_{fA} + x_{fB}} \right) \quad (\text{A.24})$$

A.4.3 Normalized Dimensions for Well C

$$w_{CD} = \frac{w_C}{x_{fA}} \quad (\text{A.25})$$

$$x_{eCD} = \frac{x_{eC}}{x_{fA}} \quad (\text{A.26})$$

$$x_{fCD} = \frac{x_{fC}}{x_{fA}} \quad (\text{A.27})$$

$$y_{eOCD} = \frac{y_{eOC}}{x_{fA}} \quad (\text{A.28})$$

$$y_{eICD} = x_{fCD} \left(\frac{L_{AC}}{x_{fA} + x_{fC}} \right) \quad (\text{A.29})$$

B. Analytical Fault Reactivation Model

B.1. Dimensionless Parameters Group

We use the following normalized parameters with rock and fluid properties as well as distances and time being given in oil field units:

$$p_{jD} = \frac{k_1 h_1}{141.2 q \mu B} (p_i - p_j) \quad (\text{B.1})$$

$$x_D = \frac{x}{b} \quad (\text{B.2})$$

$$y_D = \frac{y}{b} \quad (\text{B.3})$$

$$x_{wD} = 1 - \frac{r_w}{b} \quad (\text{B.4})$$

$$h_D = \frac{h_2}{h_1} \quad (\text{B.5})$$

$$t_D = \frac{2.637 \times 10^{-4} k_1}{\mu (\phi c_t)_1 b^2} t \quad (\text{B.6})$$

$$t_{sD} = \frac{2.637 \times 10^{-4} k_1}{\mu (\phi c_t)_1 b^2} t_s \quad (\text{B.7})$$

$$\eta_j = \frac{2.637 \times 10^{-4} k_j}{\mu (\phi c_t)_j} \quad (\text{B.8})$$

$$\eta_D = \frac{\eta_2}{\eta_1} = \frac{k_2 (\phi c_t)_1}{k_1 (\phi c_t)_2} \quad (\text{B.9})$$

$$\eta_{fD} = \frac{\eta_f}{\eta_1} = \frac{k_{fl} (\phi c_t)_1}{k_1 (\phi c_t)_f} \quad (\text{B.10})$$

$$s_f = \frac{k_1 / b}{k_f / w_f} = \alpha^{-1} \quad (\text{B.11})$$

$$F_{CD} = \frac{k_{fl} w_f}{k_1 b} \quad (\text{B.12})$$

$$M = \frac{k_2}{k_1} \quad (\text{B.13})$$

$$T_D = M h_D \quad (\text{B.14})$$

$$F_s = \frac{(\phi c_t)_2}{(\phi c_t)_1} \quad (\text{B.15})$$

Vita

Oscar Mauricio Molina Ortiz, born in Barrancabermeja, Colombia, worked as a facilities and process engineer after receiving his bachelor's degree in mechanical engineering from Universidad Pontificia Bolivariana. As his interest in petroleum reservoir engineering grew, he decided to enter the Department of Petroleum Engineering at Louisiana State University, where he obtained his master's degree. He is currently working towards his Ph.D. degree and plans to graduate in August 2019. He plans to join the oil and gas industry as a reservoir engineer.